JOINT TRANSPORTATION RESEARCH PROGRAM

INDIANA DEPARTMENT OF TRANSPORTATION
AND PURDUE UNIVERSITY

Implementing an Advanced Friction Testing Program for Seamless Coverage of INDOT System

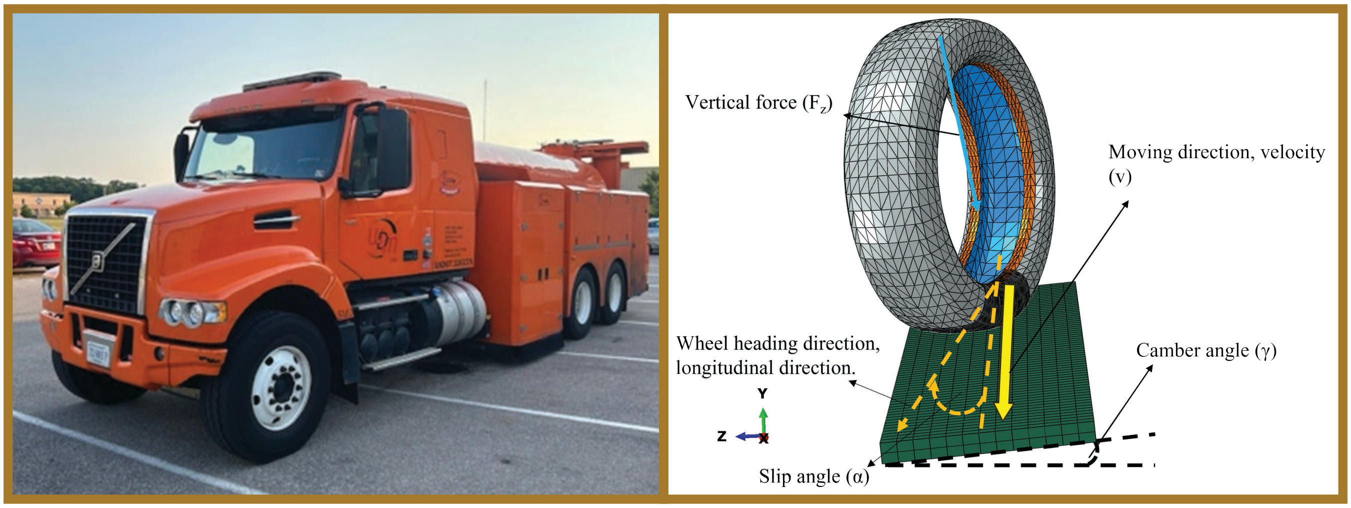

Chengcheng Tao, Yizhou Lin, Junyi Duan, Cheng Peng, Jieyi Bao, Yi Jiang, and Shuo Li

SPR-4940 • Report Number: FHWA/IN/JTRP-2025/22 • DOI: 10.5703/1288284317908

RECOMMENDED CITATION

Tao, C., Lin, Y., Duan, J., Peng, C., Bao, J., Jiang, Y., & Li, S. (2025). *Implementing an advanced friction testing program for seamless coverage of INDOT system* (Joint Transportation Research Program Publication No. FHWA/IN/JTRP-2025/22). West Lafayette, IN: Purdue University. https://doi.org/10.5703/1288284317908

AUTHORS

Chengcheng Tao, PhD
Assistant Professor
Purdue University
School of Construction Management
(765) 494-2454
tao133@purdue.edu
Corresponding Author

Yizhou Lin
Graduate Research Assistant
Purdue University
School of Construction Management

Junyi Duan
Graduate Research Assistant
Purdue University
School of Construction Management

Cheng Peng
Graduate Research Assistant
Purdue University
School of Construction Management

Jieyi Bao, PhD
Assistant Professor
Florida Gulf Coast University
Stock Development Department of Construction Management

Yi Jiang, PhD, PE
Professor
Purdue University
School of Construction Management

Shuo Li, PhD, PE
Research Engineer
Indiana Department of Transportation
Division of Research and Development

ACKNOWLEDGMENTS

This work was supported by the Joint Transportation Research Program (JTRP) administered by the Indiana Department of Transportation and Purdue University. The authors would like to thank the Study Advisory Committee (SAC) members: Samy Noureldin, Tim Wells, Dave Boruff, Taylor Ruble, and Isabel Lintner of INDOT for their technical guidance. Thanks are also extended to Mary Kay Salerno-Cahn and Dalton Ford of Potters Industries for their generous support in supplying materials used in this study.

JOINT TRANSPORTATION RESEARCH PROGRAM

The Joint Transportation Research Program serves as a vehicle for INDOT collaboration with higher education institutions and industry in Indiana to facilitate innovation that results in continuous improvement in the planning, design, construction, operation, management and economic efficiency of the Indiana transportation infrastructure. Learn more at engineering.purdue.edu/JTRP.

Published reports of the Joint Transportation Research Program are available at docs.lib.purdue.edu/jtrp/.

NOTICE

TECHNICAL REPORT DOCUMENTATION PAGE

1. Report No. FHWA/IN/JTRP-2025/22	**2. Government Accession No.**	**3. Recipient's Catalog No.**
4. Title and Subtitle Implementing an advanced friction testing program for seamless coverage of INDOT system		**5. Report Date** July 31, 2025 **6. Performing Organization Code**
7. Author(s) Chengcheng Tao, PhD (https://orcid.org/0000-0003-2708-0912) Yizhou Lin (https://orcid.org/0009-0006-7865-6888) Junyi Duan (https://orcid.org/0009-0002-5997-2608) Cheng Peng (https://orcid.org/0000-0002-6452-4431) Jieyi Bao, PhD (https://orcid.org/0000-0002-4677-4664) Yi Jiang, PhD, PE Shuo Li, PhD, PE (https://orcid.org/0000-0003-1070-9155)		**8. Performing Organization Report No.** FHWA/IN/JTRP-2025/22
9. Performing Organization Name and Address Joint Transportation Research Program Hall for Discovery and Learning Research (DLR), Suite 204 207 S. Martin Jischke Drive West Lafayette, IN 47907		**10. Work Unit No.** **11. Contract or Grant No.** SPR-4940
12. Sponsoring Agency Name and Address Indiana Department of Transportation (SPR) State Office Building 100 North Senate Avenue Indianapolis, IN 46204		**13. Type of Report and Period Covered** Final Report **14. Sponsoring Agency Code**
15. Supplementary Notes Conducted in cooperation with the U.S. Department of Transportation, Federal Highway Administration.		

16. Abstract

The interaction between tires and the road surface is crucial for maintaining vehicle stability and safety. The frictional forces at the tire-road interface, along with the coefficient of friction, affect vehicle dynamics, influencing transportation safety. Rapid advancements in transportation technology, infrastructure demands, and safety regulations pose complex transportation challenges, requiring adaptive solutions. The goal of this study is to provide actionable insights for highway agencies, offering improved friction assessment methodologies that support safer and more effective roadway maintenance and design. This study investigates and verify Locked Wheel Skid Tester (LWST) friction measurement on horizontal curves using Sideway-force Coefficient Routine Investigation Machine (SCRIM), pavement friction performance adjustment factor through a numerical approach incorporating thermomechanical finite element analysis (FEA), and advanced pavement marking assessments. The research aims to enhance friction measurement accuracy and improve roadway safety by integrating predictive modeling and field validation. Machine learning algorithms refine the interpretation of friction data, enabling the development of adjustment factors for various road geometries and speeds. Additionally, optimized pavement marking materials, including angular glass beads and ceramic particles, are explored to enhance long-term durability and friction performance.

17. Key Words friction, LWST, SCRIM, pavement marking, finite element analysis, data analysis, machine learning		**18. Distribution Statement** No restrictions. This document is available through the National Technical Information Service, Springfield, VA 22161.	
19. Security Classif. (of this report) Unclassified	**20. Security Classif. (of this page)** Unclassified	**21. No. of Pages** 201, including appendices	**22. Price**

Form DOT F 1700.7 (8-72) Reproduction of completed page authorized

EXECUTIVE SUMMARY

Introduction

The Joint Transportation Research Program (JTRP) project SPR-4646, *Advancing INDOT's Friction Test Program for Seamless Coverage of System* from Bao et al. (2024), has achieved its study objectives successfully and yielded first-hand data, valuable insights, and actionable recommendations for addressing potential safety issues associated with emerging roadway facilities, especially pavement markings, color surface treatments (red bus and green bike lanes), common aggregates, and horizontal curves. The approved implementation plan has developed a roadmap to ensure that all valuable findings of SPR-4646 will be implemented. This proposal further outlines the tasks and activities for successfully executing the implementation plan and incorporating additional tests on new pavement marking materials, as recommended by the JTRP Study Advisory Committee (SAC).

Findings

Assessment and Comparison of Locked Wheel Skid Trailer (LWST) and Sideway-Force Coefficient Routine Investigation Machine (SCRIM) Field Test

Polynomial regression effectively modeled nonlinear relationships between SCRIM Skid Resistance (SR), SCRIM mean profile depth (MPD), curve radius, and cross slope, with straight roads exhibiting stronger correlations than curved roads. Straight roads demonstrated the highest correlation for SR = f(MPD) ($R^2 = 0.245$), while curved roads had lower correlations. For friction number (FN) = f(SR), all pavements had the best correlations, with random forest ($R^2 = 0.374$) performing best, followed by polynomial regression ($R^2 = 0.357$). In FN = f(SR & MPD), polynomial regression provided the highest correlation, particularly on straight roads ($R^2 = 0.581$), while curved roads showed the second-best correlation. However, random forest struggled with complex surfaces due to overfitting. For FN = f(SR, MPD, curve radius, and cross slope), random forest achieved the highest correlation across different curvature types, with straight roads ($R^2 = 0.753$) and all roads ($R^2 = 0.746$) showing strong relationships, while polynomial regression struggled with curved roads ($R^2 = 0.159$), indicating greater variability.

Development of Adjustment Factors for Friction Tests on Horizontal Curves

A three-dimensional (3D) thermomechanical coupled finite element analysis (FEA) model is developed in Abaqus to simulate tire–pavement interactions. The model is calibrated using field test data from Indiana Department of Transportation (INDOT) test tracks and highways (e.g., S.R. 26, S.R. 47, and Purdue Airport roadways) to accurately establish the relationship between friction coefficients and temperature. Speed and vertical force influence friction performance, with higher speeds reducing friction numbers. Slip angle and superelevation on curved roads have pronounced effects, and the model capture the complex dynamics of tires during turns. Machine learning techniques are used to expand the dataset, creating a comprehensive friction adjustment factor database. This supports accurate friction performance predictions under various road geometries and speeds, enhancing safety assessments and road design.

Additional Tests on New Pavement Marking Materials

The incorporation of ceramic particles and angular glass particles of various sizes significantly improves the initial friction performance of pavement marking surfaces under both dry and wet conditions. Furthermore, the incorporation of ceramic particles and angular glass particles effectively enhances the dynamic friction at speed 40 km/h (DF40) and the friction number calibrated wet friction at 60 km/h (F60) values of pavement markings both during and after polishing. Angular glass particles are more effective in preserving the durability of the pavement surface. In contrast, specimens incorporating ceramic particles and Type 4 glass beads exhibited greater particle detachment during the polishing process and contributed to the accelerated deterioration of the pavement markings. The influence of thickness on friction performance remains uncertain, and further research is necessary to clarify its effect. This study also seeks to establish a connection between laboratory polishing tests and vehicle-induced wear on pavement markings through FEA. One LWST wheel rotation equals 4.4–11.3 three-wheel polishing device (TWPD) cycles, and a passenger car tire equals 15.7–40.3, based on corresponding friction coefficients.

Implementation

This study presents a structured implementation framework for enhancing INDOT's friction testing program, integrating thermomechanical FEA modeling, SCRIM test parameter analysis, and improved pavement marking evaluations. A key aspect of this implementation is the verification of LWST friction measurements on horizontal curves using SCRIM, ensuring consistency and accuracy in evaluating road safety performance. The implementation plan emphasizes the integration of predictive modeling tools, enabling accurate friction adjustment factors for various road geometries and speeds. Field data validation from LWST and SCRIM tests, combined with machine learning, refines friction performance predictions, supporting more informed roadway safety decisions. Additionally, optimized pavement marking, including angular glass beads and ceramic particles, are introduced to enhance durability and friction retention over time. The practical application of these findings benefits highway agencies and motorists by contributing to safer roadway design.

CONTENTS

LIST OF TABLES

LIST OF FIGURES

1. INTRODUCTION

1.1 Background

Pavement friction is a critical factor in roadway safety and a key performance indicator for Indiana Department of Transportation (INDOT). Joint Transportation Research Program (JTRP) project SPR-4646 from Bao et al. (2024) successfully advanced INDOT's friction testing program, providing essential data and recommendations for improving pavement markings, color surface treatments, and friction evaluation on horizontal curves. INDOT's Research and Development Division has been actively addressing safety challenges, including mitigating wet-pavement crashes, ensuring long-term friction retention, and improving pavement marking durability. However, emerging roadway features, evolving transportation technologies, and regulatory updates present new challenges that necessitate innovative solutions.

One challenge is friction testing on horizontal curves, where crash rates are three times higher than on straight road segments. Traditional Locked Wheel Skid Trailer (LWST) methods (ASTM International [ASTM], 2015b) are primarily designed for straight, flat sections and do not account for critical roadway features such as superelevation and varying curve radii. Bao et al. (2024) introduced adjustment factors to improve friction accuracy on curves, but these factors require further validation on real-world roadways with diverse geometric conditions. To address this, integrating GoPro vision technology, supervised machine learning (ML), and finite element analysis (FEA) can enhance friction predictions and adjustment models. Additionally, collaboration with Sideway-force Coefficient Routine Investigation Machine (SCRIM) program will help validate the proposed adjustments and refine INDOT's research goal.

Another challenge is the evaluation of pavement marking friction, particularly for emerging materials that balance durability and skid resistance. The 11th edition of the *Manual on Uniform Traffic Control Devices for Streets and Highways* (MUTCD) from the Federal Highway Administration (FHWA; 2023) mandates a minimum standard for pavement marking retroreflectivity, requiring agencies to adopt maintenance methods within 4 years. In response, the industry has developed innovative materials that enhance retroreflectivity without compromising durability or other key performance properties (FHWA, 2023). Despite these advancements, standardized friction testing methods for pavement markings remain limited, requiring further research.

Given that 23% of fatal crashes occur on horizontal curves, despite curves comprising only 5% of the national roadway network, upgrading INDOT's friction testing program is essential. The proposed implementation plan builds on the findings of SPR-4646 (Bao et al., 2024) by integrating ML, FEA, and expanded field testing to ensure comprehensive friction evaluation across Indiana's roadways. This initiative will not only improve friction performance assessments but also enhance roadway safety for autonomous vehicles.

1.2 Literature Review

Tire friction forces and the road–tire interface coefficient of friction are fundamental determinants of vehicle motion, critically influencing vehicle handling evaluation, control system design, and safety measures. However, these forces and the coefficient of friction are influenced by a multitude of uncontrollable factors, including pavement condition, temperature variations, speed, tire vertical force, slip angle, superelevation, tire pressure, and more (Alcázar Vargas et al., 2022; Bruzelius et al., 2014; Ray, 1997). To account for these complexities, optimizing tire design necessitates the development of computational models. Simulating tire experiments under realistic operating conditions provides an effective alternative that can reduce the overall design and development cycle time (Narasimha Rao & Krishna Kumar, 2007). This optimization is achievable through advanced numerical methods, such as Finite Element (FE) techniques.

This method allows for detailed simulations under various operating conditions, enabling predictions of stress, strain, and deformation patterns that affect friction forces. FEA has been widely employed in tire modeling to understand tire friction forces and their interaction with road surfaces. For instance, a robust model was developed for radial tires using incompressible elements and the Mooney-Rivlin elastomer framework, alongside a variable constraint method for accurate tire–ground interactions (Yan, 2003). Abaqus software (Dassault Systèmes, 2023) was employed to model the steady-state rolling behavior of a steel-belted radial tire, focusing on the influence of belt angles under slip conditions. Using a mixed Lagrangian-Eulerian approach, Ghoreishy (2006) revealed that belt angle variation affects contact pressure, lateral force, and interlayer shear stress, critical for optimizing tire performance during cornering. A comprehensive review of FEA methodologies was applied to rolling tires, highlighting their importance in predicting tire–road interaction, rolling resistance, and deformation patterns (Ghoreishy, 2008). The Arbitrary Lagrangian-Eulerian framework facilitates the modeling of rolling contact by decomposing the motion into rigid body movement and material deformation. This approach simplifies the treatment of large deformations, particularly in nonlinear viscoelastic materials (Nackenhorst, 2004). It is important to emphasize the critical role of experimentally determined material parameters in enhancing the accuracy of thermal predictions in rolling tires. By integrating dynamic mechanical analysis and FE simulations, Fathi et al. (2024) demonstrated that using experimentally validated properties improves the prediction of steady-state temperature distributions compared to relying solely on literature values. FEA was utilized to model a passenger car tire, validating results through static and dynamic tests to evaluate vertical stiffness, cornering stiffness, and rolling resistance. Such studies demonstrate the effectiveness of FEA in optimizing tire design and analyzing the critical parameters influencing tire–road interaction (Fathi et al., 2024).

INDOT utilizes data collected through its LWST for evaluating pavement friction. This testing adheres to the ASTM E274 standard method, which involves dragging a locked test tire over a wetted pavement surface to measure the frictional force and calculate the Friction Number (FN; ASTM, 2015b). The tire used for these tests is specified under ASTM E524, which defines the material, design, and performance standards for the smooth tires required for consistent and accurate skid-resistance measurements (ASTM, 2015a). By leveraging these standardized methods and equipment, INDOT ensures the reliability and comparability of its pavement friction data, supporting informed decisions for roadway safety and maintenance. SCRIM provides continuous data on pavement friction and texture, which is integral to understanding tire–pavement interaction under diverse road conditions. Studies leveraging SCRIM data have explored the relationships between surface texture, side friction resistance, friction resistance, mean profile depth (MPD), and other related factors.

Several studies, including Artamendi et al. (2013), S. Li et al. (2005), and Rabari et al. (2018) have examined key factors influencing skid resistance, surface texture, and vehicle stability. S. Li et al. (2005) analyzed friction variations in network pavement testing using the smooth tire. They found it more sensitive to pavement texture than the ribbed tire. Using data from INDOT since 1996, S. Li et al., (2005) examined system errors, seasonal effects, and spatial-temporal variations, emphasizing the need for proper calibration and test adjustment. The skid resistance and texture depth of proprietary asphalt mixes were examined, revealing that quartz granite (Polished Stone Value [PSV] 55) outperformed porphyry (PSV 60) in skid resistance, challenging the reliability of PSV as a predictor of in-service performance. Artamendi et al. (2013) demonstrated that the Wehner-Schulze test effectively correlated with in-situ SCRIM and GripTester measurements, making it a valuable tool for evaluating asphalt mixes comprehensively. The influence of superelevation and side friction factors was investigated on horizontal curve safety, using rural highway curves in Gujarat, India, as a case study (Artamendi et al., 2013). Rabari (2018) revealed that real-world side friction demands often differ from theoretical values, with passenger cars more prone to skidding and heavy vehicles more likely to roll over at low speeds. Stephenson (2018) emphasized the importance of selecting high PSV aggregates and high friction surfacing to meet safety targets while acknowledging performance variability. Evidence from New Zealand demonstrates the effectiveness of such strategies, with a 20% reduction in rural wet crash rates, underscoring the need for data-driven approaches to manage safety risk (Stephenson, 2018). The relationship between SCRIM data (wet skid resistance) and texture depth (macrotexture) was investigated, revealing a minimal direct correlation between the two. However, using random forest regression, Lai et al. (2022) demonstrated that combining texture depth with factors like region information, traffic volume, speed limits, and annual rainfall improved SCRIM coefficient prediction, achieving an R^2 of 0.82 for open-graded asphalt (Lai et al., 2022). Rosta and Gáspár (2023) conducted a comprehensive review of the skid resistance of asphalt pavements was conducted, evaluating measurement techniques and the influence of aggregate properties on skid resistance. Gu et al. (2023) evaluated the repeatability of friction measurements from the LWST and the SCRIM on 14 asphalt pavement sections at the NCAT Test Track. Gu et al. (2023) found that both devices were most consistent at a test speed of 50 mph on straight sections, with LWST measurements in the late afternoon and SCRIM readings at noon showing higher reliability. A strong correlation ($R^2 = 0.65$) was observed between LWST skid number and SCRIM reading, with test speed, air temperature, mean profile depth, and pavement type influencing friction measurements (Gu et al., 2023).

The friction performance of pavement marking surfaces is crucial in ensuring roadway safety, especially for vulnerable road users, like pedestrians, bicyclists, and motorcyclists. Several studies have investigated the friction, durability, and effectiveness of pavement markings across different materials and conditions. Anderson and Henry (1980) evaluated the wet friction of 39 pavement-marking formulations across 11 types and found that skid resistance varies by material thickness, with thicker markings being less affected by pavement texture. Various surface conditions can also impact the friction performance of pavement markings. Nassiri (2018) evaluated the friction performance of three marking types, thermoplastics, preformed tape, and waterborne paint, under dry, wet, and icy conditions. All three pavement markings exhibit the highest friction in dry conditions, decreasing in wet and icy conditions. Regarding the friction performance of pavement markings under varying conditions, preformed tape and waterborne paint demonstrate superior skid resistance compared to thermoplastic markings. Bao et al. (2024) conducted a comprehensive study on six types of pavement markings, waterborne paint, preformed tapes, epoxy paint, polyurea paint, methacrylate paint, and thermoplastics, to evaluate their friction performance under varying conditions. In wet environments, waterborne paint demonstrated higher wet friction than polyurea and Methyl Methacrylate (MMA), while epoxy exhibited the lowest initial friction. Among durable markings, preformed tape showed the highest initial friction, followed by polyurea, MMA, and epoxy, whereas thermoplastics had the lowest friction performance. Under dry conditions, the initial friction of all pavement markings remained relatively stable.

One fundamental function of pavement markings is to enhance road visibility and provide guidance to road users. Glass beads are typically applied to liquid pavement markings or embedded in premanufactured markings to enhance their reflective properties and improve visibility (Bowman & Kowshik, 1994). However, the addition of glass beads typically modified the surface texture of pavement markings, thereby affecting surface friction, particularly under wet conditions (Bao et al., 2025). For example, larger glass beads have been found to reduce the friction performance of wet pavement marking surfaces (Bao et al., 2024). Bao et al. (2024) added both ceramic particles and glass beads and found that ceramic particles can increase the surface friction of pavement marking significantly. Different combinations of pavement markings, glass beads, and other additives influence friction performance over time as traffic wear gradually polishes the surface. Coves-Campos et al. (2018) tested 18 types of pavement markings with various combinations of drop-on materials on a rural highway under real traffic conditions. Their study found that skid resistance and visibility exhibited an inverse relationship after a period of traffic exposure. As traffic wear increases, the rough surface texture accumulates dirt and rubber particles, leading to diminished visibility and a darker appearance. The three-wheel polishing device (TWPD) is commonly used in laboratory settings to simulate polishing conditions. Currently, a few studies have utilized TWPD to investigate the degradation and variation of pavement marking friction during polishing. Kassem et al. (2021) examined the characteristics of waterborne paint, thermoplastics, and MMA as bicycle lane markings by subjecting them to 100,000 polishing cycles. During the polishing process, the International Friction Index (IFI) of MMA gradually decreased, while that of thermoplastic remained relatively unchanged. In contrast, the IFI of waterborne paint gradually increased. Waterborne paint is a nondurable pavement marking. At a typical thickness of 15–25 mil (0.381–0.635 mm), it can withstand no more than 5,000 polishing cycles, whereas durable materials such as polyurea, MMA, and thermoplastic can endure up to 100,000 polishing cycles (Bao et al., 2024). The specific friction performance and durability depend on the thickness and the size, as well as the type of the added beads and particles. Bao et al. (2024) found that the addition of large glass beads and ceramic particles reduces the durability of pavement markings during the polishing process. For waterborne markings, samples with larger beads and ceramic particles showed a faster decrease in IFI values compared to those with smaller beads. Although the IFI values of markings with smaller beads were higher after application and polishing, the differences were not significant. For liquid durable markings, samples with small-sized glass beads did not exhibit superior friction performance compared to large-sized glass beads during the polishing process. However, while the addition of ceramic particles reduced durability, it significantly improved the IFI throughout the polishing process. Additionally, the friction performance of the performed tapes gradually declined during the polishing process, whereas thermoplastics maintained a stable friction level. However, the IFI values of thermoplastics remained lower than those of other marking materials (Bao et al., 2024).

1.3 Main Tasks

The following tasks are accomplished in this study:

1. *Assessment and comparison of LWST and SCRIM field test*: Conduct field measurements using an LWST and FHWA's SCRIM. SCRIM offers continuous data on pavement friction and texture which is crucial for understanding the dynamics of tire–pavement interaction across various road conditions.
2. *Development of adjustment factor for friction tests on horizontal curves*: Continue developing and refining the thermomechanical FEA simulation. This includes improving model accuracy by integrating an FN adjustment mechanism to provide engineers with insights into the adjustments required for FNs between curved and straight road segments.
3. *Additional material tests on new pavement marking materials*: Investigate the performance of new pavement marking materials with a focus on their effects on frictional properties and durability of pavement markings. This evaluation includes testing angular glass particles of varying sizes and spherical ceramic particles to assess their efficiency in improving pavement safety.

2. ASSESSMENT AND COMPARISON OF LWST AND SCRIM FIELD TEST

2.1 Background

SCRIM is a device that measures the side friction coefficient of road surfaces. Skid resistance and road surface characteristics are critical parameters for assessing pavement safety and performance. During the test, the SCRIM machine operates at a certain speed while dragging a wheel, usually at a specific angle, across the road surface. It measures the sideways friction force between the wheel and the road. The results help engineers evaluate the skid resistance of the pavement and determine whether maintenance or improvements are needed to reduce the risk of traffic accidents (Kumar et al., 2023).

Lai et al. (2022) explored the relationship between SCRIM measurements and pavement texture depths. For instance, research in Western Australia found a minimal direct correlation between SCRIM data and texture depth. However, predictive modeling indicated that combining texture with other factors, such as region information, annual rainfall, speed limit, and traffic volume, could effectively predict skid resistance. Findings on cross slope and texture depth impact drainage and hydroplaning risk offer insights into the friction number computed at test speed 40 mph (FN40) and skid resistance (SR) variability across segments. Their work emphasizes how design factors like slope and texture transitions influence frictional properties (Güven, O., & Melville, 1999; Lai et al., 2022). De León Izeppi et al. (2019) found that SCRIM's strong correlation with ribbed tire FN40 from LWSTs was noted, emphasizing its sensitivity to microtexture. Weaker correlations with FN40 on a smooth tire underline macrotexture's role. De León Izeppi et al. (2019) advocate integrating macrotexture data for improved pavement safety analysis.

In this report, we analyze the data from SCRIM tests on 11 road segments located in and around Indianapolis, Indiana. The roads span across different regions of Indiana, covering areas around Lafayette, Bloomington, Columbus, and within Indianapolis itself. Each of these road sections represents a distinct section where the SCRIM test measured friction and related parameters like FN40, curve radius, MPD, and SR.

We investigate the relationship between SCRIM SR and SCRIM MPD, as well as the relationship between CrossSlope and FN. Specifically, we look at the four correlations of the following parameters through curve fitting and ML algorithms.

1. SR = f(MPD)
2. FN = f(SR)
3. FN = f(SR, CurveRadius)
4. FN = f(SR, MPD, CurveRadius, CrossSlope)

2.2 Methodology

2.2.1 Statistics Analysis Approach

The correlation map, also known as a heatmap, is a graphical representation of two-dimensional (2D) data that uses colors to illustrate the degree of correlation between variables. This visual aid is invaluable for conveying statistical or data-driven information efficiently (Khalil et al., 2024). In this study, a heatmap is employed to illustrate the sensitivity of different parameters in the friction analysis, streamlining the visualization by eliminating unnecessary factors in the system. The purpose is to provide a clear, visual representation of how various elements interconnect, aiding in understanding, planning, and decision-making within a given context.

The friction analysis for the tire–pavement system focuses on the frictional number, speed, vertical force, slip angle, camber angle, and curving radius. The longitudinal frictional number is intricately linked to both vertical force and longitudinal horizontal force. To simplify the experimental system and remove unnecessary variables, the correlation map excludes the independent inclusion of horizontal force.

An additional consideration is the curve radius. The field-testing data from the Purdue Airport runways, as well as State Road (S.R.) 26, S.R. 75, and S.R. 47 concludes both left and right turns, thus the sign of the slip angle, is recorded accordingly. As the sensor is fixed on one side of the tire, the vertical force records for left and right turns are influenced by the shift in gravity. To address this, a correlation map is established using data from straight and curved roads along with the slip angle or camber angle separately. Additionally, the analysis data for slip angles are chosen to be positive values in this sensitivity analysis.

The statistical relationships included in the “Regression Equation” and “R^2 (R-squared Value)” are also provided. The linear regression equation helps in understanding the strength and nature of the relationship between two variables in SCRIM test (Lai et al., 2022). R^2 is used to evaluate how well a regression model fits the objective data. A higher R^2 value indicates a better fit with the study parameter, FN (Plonsky & Ghanbar, 2018).

2.2.2 *LWST Frictional Test*

INDOT utilizes data collected through its LWST for evaluating highway pavement friction performance at a routine network level. This testing adheres to the ASTM E274 standard method, which involves dragging a locked test tire over a wetted pavement surface for a constant period of time to measure the frictional force and calculate the FN (ASTM, 2015b). The standard test speed of LWST is 40 mph. Therefore, FN test results measured under a different speed will be converted to standard FN40 for comparison, which requires accurate measurement of tire testing speed. During each LWST test, the experimental tester first delivers a layer of water in front of the test tire on the left. Approximately 0.5 s later, the test wheel will be fully locked in friction test. Then, a 0.4-s waiting time is used before the LWST force transducer starts to measure the average dual-axis tire forces in a fixed 1 s of test time interval (Peng et al., 2024).

The test smooth tire used for these tests is specified under ASTM E524, which defines the material, design, and performance standards for the smooth tires required for consistent and standardized skid-resistance measurements (ASTM, 2015a). Field LWST test data were collected on Indiana S.R. 26, S.R. 47, S.R. 75, and the Purdue Airport roadways, as shown Figure 2.1. A rigidly mounted camera is facing down capturing the movement of the pavement surface in front of the test tire. With camera calibration, the tracked pavement 2D motion in the camera region of interest can be considered the apparent test tire planar motion. In this way, a real-time recording of test tire speed and tire sideslip angle time series is realized with high accuracy. During each cornering friction test, this upgraded LWST utilizes a vision-based method to capture the locked wheel sideslip angle in addition to the original tire forces (Peng et al., 2024). Road camber is manually measured onsite for each tested horizontal curve. All the LWST information can be further referred to in Appendix A and Appendix B.

2.2.3 *SCRIM Frictional Test*

SCRIM (Figure 2.2) provides continuous data on pavement friction and texture, which is integral to understanding tire–pavement interaction under diverse road conditions. Skid resistance and road surface characteristics are critical parameters for

(a) (b) (c)

Figure 2.1 LWST Measuring Process: (a) LWST Setup on the Purdue Airport; (b) A Vision-Based Method to Collect Slip Angle Values (Peng et al., 2024); (c) Camber Measurement.

Figure 2.2 SCRIM Friction Test Devices.

assessing pavement safety and performance. During the test, SCRIM operates at a certain speed while dragging a wheel (usually at a specific angle) across the road surface.

2.2.4 Pavement Material and Road Curvature Categorization

We categorize data based on two key criteria: road type and pavement type. For road type, the data are categorized into straight roads and curved roads. For pavement type, all asphalt roads from R1 to R9 are filtered into a single "asphalt" category, resulting in three pavement categorizations: asphalt, concrete pavement with longitudinal texture, and concrete pavement with transverse texture. The labels R1 through R9 refer to different road segments, as defined in Appendix E, which correspond to individual video-recorded test sections.

To determine the road pavement conditions, we used the Global Positioning System (GPS) coordinates recorded in the SCRIM test data to locate the corresponding dashcam images. By reviewing the sequence of dashcam images along the test route, we identified specific points where notable changes in pavement type and condition occurred. For example, Figure 2.3 represents typical transition points for the R3 pavement type. A clear change in the road surface texture can be observed, indicating a shift point in pavement type. This method allows us to correlate the visual road conditions with the GPS data from the SCRIM test, providing an assessment of pavement transitions along the route.

(a) (b)

Figure 2.3 Dashcam Images Showing Transition Points for R3 Pavement Type Along the SCRIM Test Route. (a) From "Asphalt (Grey) With Some Patching" to "Asphalt (Grey) on the Bridge"; (b) From "Asphalt (Grey) With Some Patching" to "Concrete."

In American Association of State Highway and Transportation Officials (AASHTO, 2018) guidelines, the distinction between straight roads and curved roads is often based on the presence or absence of superelevation. However, our dataset does not include superelevation data. Additionally, references rarely provide clear methodologies for distinguishing straight roads from curved roads using the curve radius alone. Therefore, in this section, we categorize road types based on visual observation using maps and adopt a threshold of 1,500 ft as the standard. Roads with a curve radius below 1,500 ft are categorized as curved roads, while those with a radius above 1,500 ft are categorized as straight roads. Detailed information on pavement identification is provided in Appendix E. For pavement-type categorization, we relied on dashcam footage captured during testing. This footage allowed us to visually identify and categorize pavements into three types: asphalt and concrete pavements.

2.2.5 Machine Learning Algorithms With and Without Road Type Categorization

We investigate correlations by applying three different ML algorithms: (1) Support Vector Machine, (2) Neural Network, and (3) Random Forest Regression, and then compare the R^2 with the polynomial regression function. We also investigate the improvement of different data processing methods, such as standardization and normalization (Ali et al., 2014).

Standardization: $$z = \frac{x - \mu}{\sigma} \qquad \text{Equation 2.1}$$

Normalization: $$z = \frac{x - x_{min}}{x_{max} - x_{min}} \qquad \text{Equation 2.2}$$

For the evaluation of the entire dataset without segmenting by road sections, R^2 is calculated on a test set comprising 20% of the overall data to prevent overfitting, as shown in Equation 2.3. However, for individual road sections, the dataset is further split, reducing the already limited data. Since the individual analysis uses only polynomial regression with an order of two, the risk of overfitting is relatively low. However, this approach can result in inflated R^2 values when there are too few data points, as the regression may overly conform to the limited data and fail to reflect the true variability. To address this, R^2 for individual road sections is calculated using the entire dataset, as shown in Equation 2.4.

$$R^2_{test} = 1 - \frac{\sum_{i=1}^{n.test}\left(y_i - \hat{y}_i\right)^2}{\sum_{i=1}^{n.full}\left(y_i - \bar{y}_{test}\right)^2} \qquad \text{Equation 2.3}$$

$$R^2_{full} = 1 - \frac{\sum_{i=1}^{n.full}\left(y_i - \hat{y}_i\right)^2}{\sum_{i=1}^{n.full}\left(y_i - \bar{y}_{full}\right)^2} \qquad \text{Equation 2.4}$$

2.3 Results and Discussion

2.3.1 Correlation Map

Figure 2.4 illustrates the correlation matrix for all road segments, showing the relationships between FN40, CrossSlope, MPD, SR, and Curve Radius. The strength of the correlation is represented by the color intensity, with darker shades of brown indicating stronger positive correlations and darker shades of blue representing stronger negative correlations. The data are selected from SCRIM and matched with LWST data from the same GPS coordination, as FN40 data are not originally available in the SCRIM dataset.

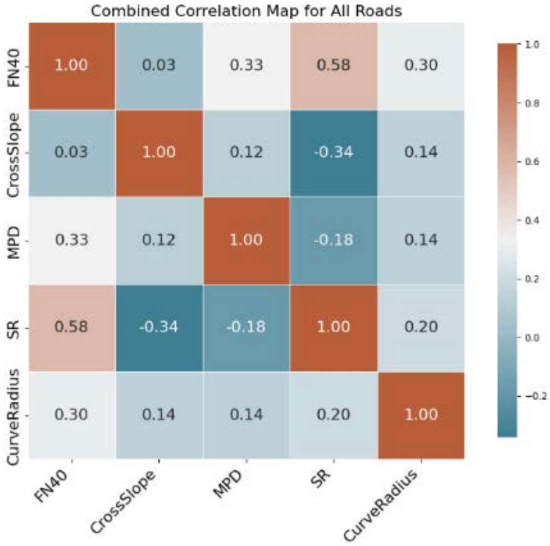

Figure 2.4 Correlation Map for Selected SCRIM Test Points for Key Road Parameters.

FN40 and CrossSlope have a very weak positive correlation (0.03), indicating almost no relationship between the two variables. FN40 and MPD have a moderate positive correlation (0.33), suggesting that as the MPD increases, FN40 tends to increase as well. FN40 and SR show a strong positive correlation (0.58), meaning that higher side resistance is closely associated with higher FN40 values.

FN40 and Curve Radius have a moderate positive correlation (0.30), indicating that larger curve radii are slightly related to increased FN40 values. In summary, FN40 has the strongest relationship with SR, followed by MPD and Curve Radius, while CrossSlope shows almost no correlation. The correlation coefficient between SR and MPD is –0.18, as indicated in the heatmap. This value suggests a weak negative correlation, meaning that as MPD increases, SR tends to decrease slightly, but the relationship is not strong. However, the summary of the correlation map may have a bias, as the sensitivity analysis on left and right run effects has been discussed before. Thus, we also conducted a correlation study on each road segment to verify accuracy.

The correlation maps for each road segment in Figure 2.5 show that the relationship between Curve Radius and FN40 fluctuates across different roads. In some roads, such as R3 and R6, the correlation between Curve Radius and FN40 is moderately positive (0.42 and 0.43, respectively), indicating a stronger relationship. However, in others like R8 and R10, the correlation is weaker or even negative (–0.29 and –0.43, respectively), showing no consistent trend.

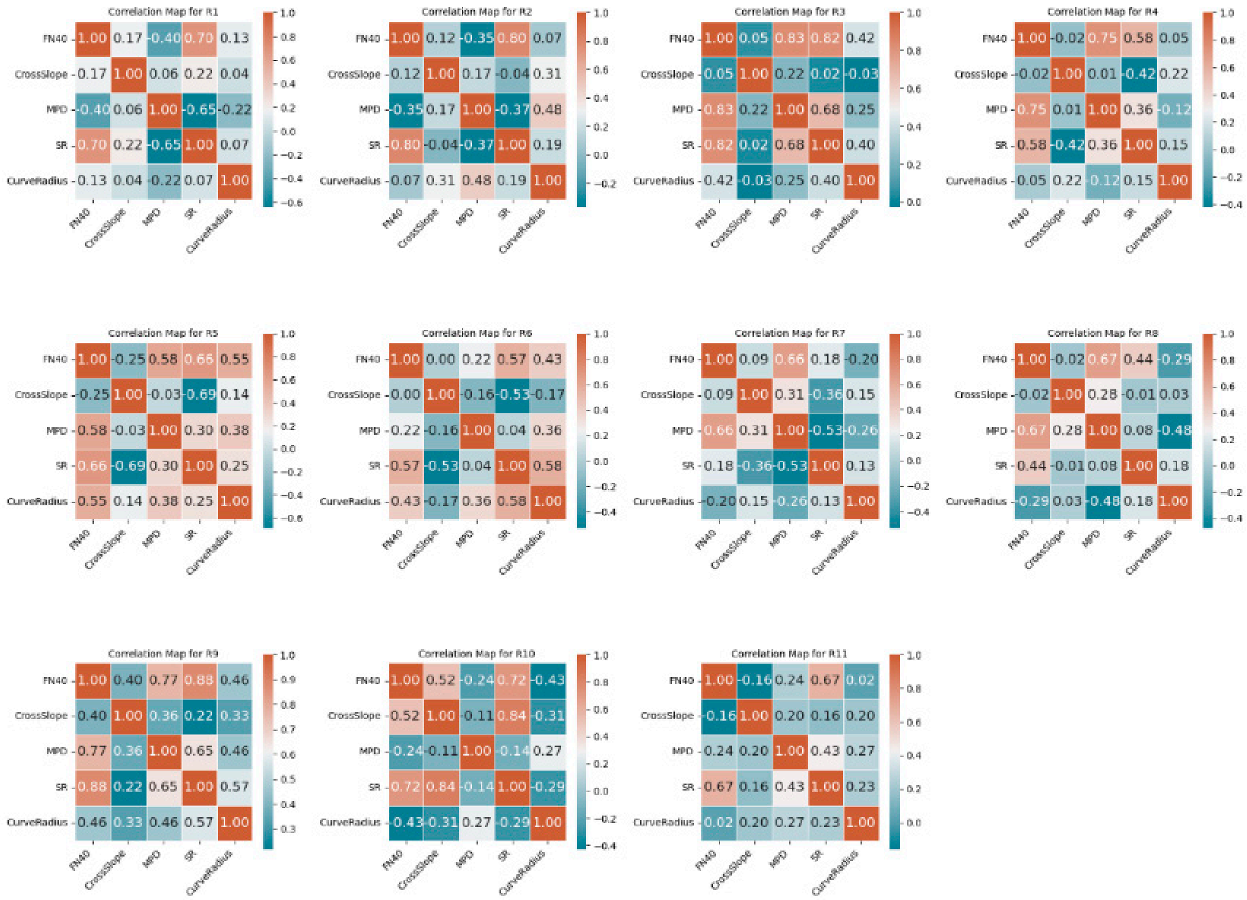

Figure 2.5 Correlation Map of Selected SCRIM Test Points for All Road Segments From R1 to R11.

Similarly, the relationships between FN40 and other parameters like CrossSlope, also vary across the segments. For instance, FN40 shows a relatively strong positive correlation with CrossSlope in some segments (e.g., R9 at 0.40 and R10 at 0.52), while CrossSlope in most cases generally shows no correlations, sometimes even negative (e.g., R10 at –0.24). SR and FN40 remain consistently aligned with each other. This indicates that SR has a strong, reliable relationship with FN40 across different road segments, as SR is a key factor influencing FN40 values.

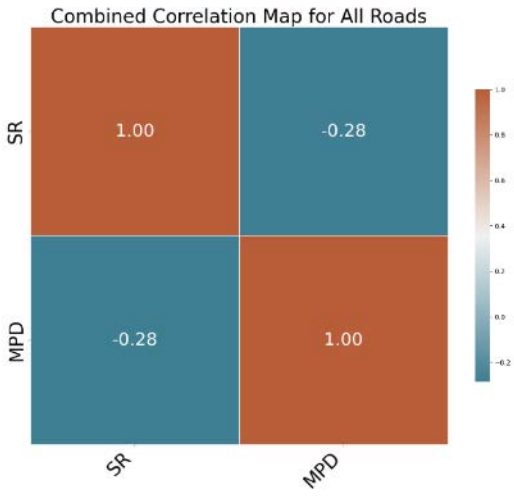

Figure 2.6 Correlation Map for Original SCRIM Test for All Roads.

2.3.2 LWST Frictional Test

This section primarily focuses on examining experimental results to investigate the influence of different parameters on FN data, providing further validation for the FEA results.

2.3.2.1 Sensitivity Analysis Without Considering Left and Right Turns. First, we analyze the overall LWST experimental data's impact on FN without considering turning effects. Figure 2.8 illustrates the correlation maps and statistical relationship with the field testing data at S.R. 26.

The central variable in this correlation analysis is the longitudinal FN, a pivotal parameter in the study. The correlation map in Figure 2.8 highlights the highest negative correlation between the longitudinal friction coefficient and speed (–0.71) and a weaker negative correlation between FN and vertical force (–0.29). R^2 results in 0.514 in the statistical relationship between FN and velocity, suggesting the highest correlation among the

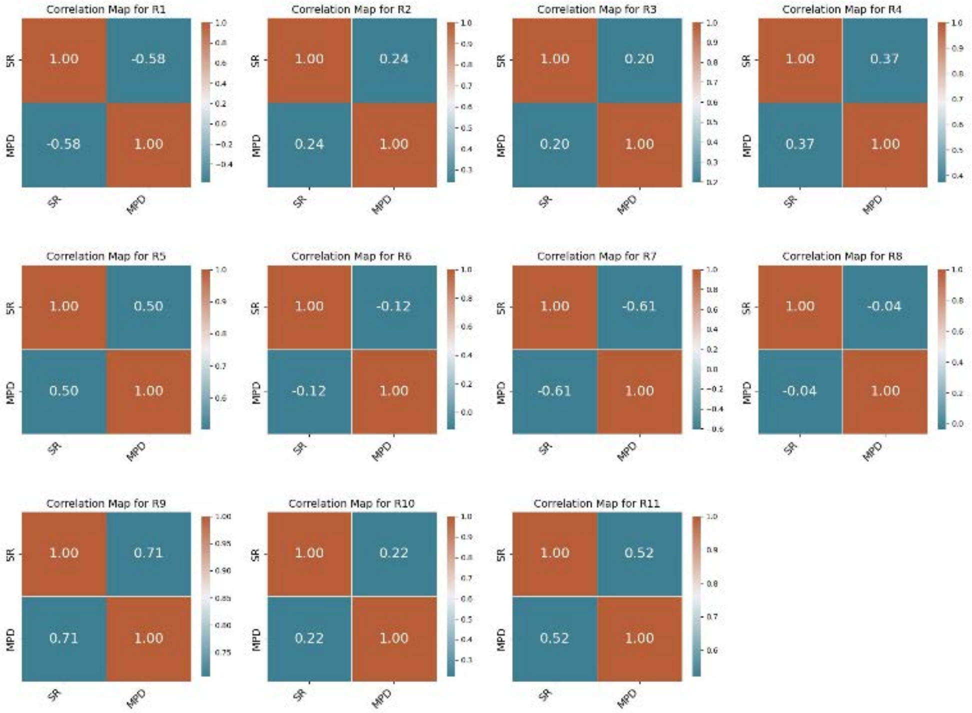

Figure 2.7 Correlation Map of Original SCRIM Test Points for All Road Segments from R1 to R11.

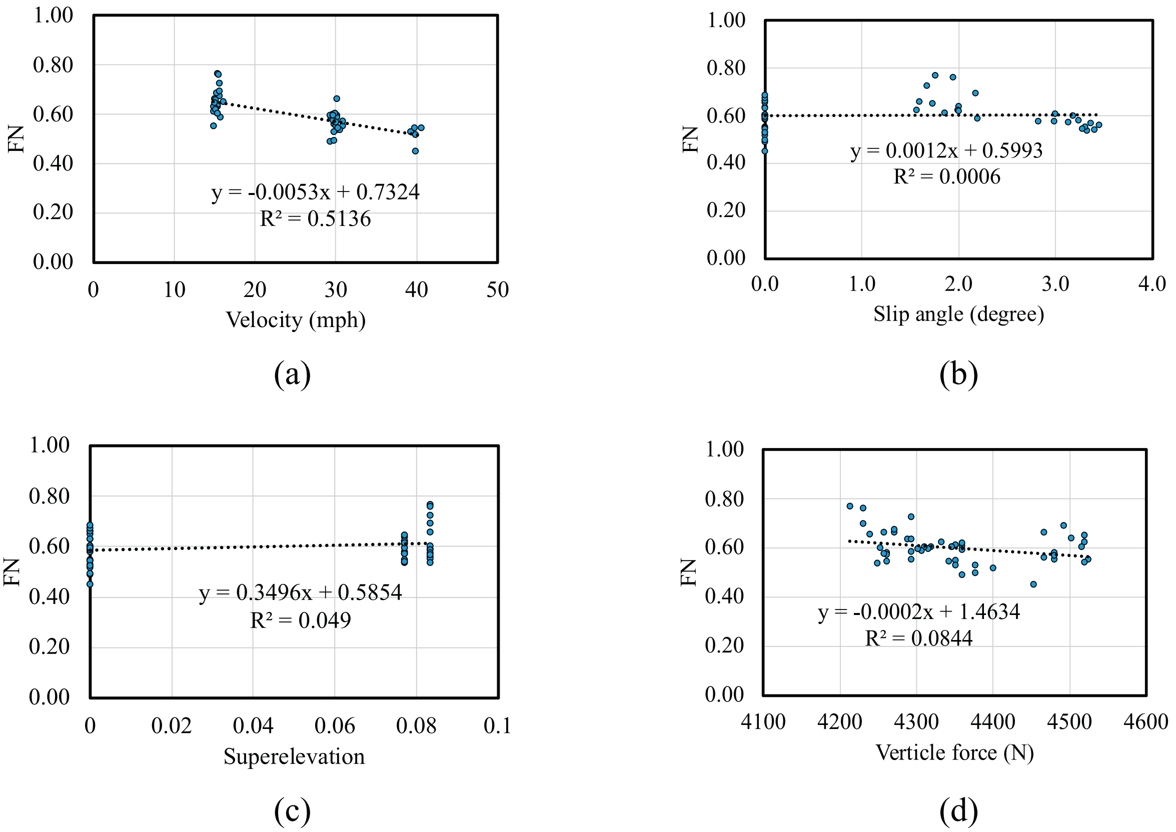

Figure 2.8 Sensitivity Analysis on S.R. 26. The Statistical Relationship Between FN and (a) Velocity; (b) Slip Angle; (c) Superelevation; (d) Vertical Force; and (e) Correlation Map From Field-Testing Data.

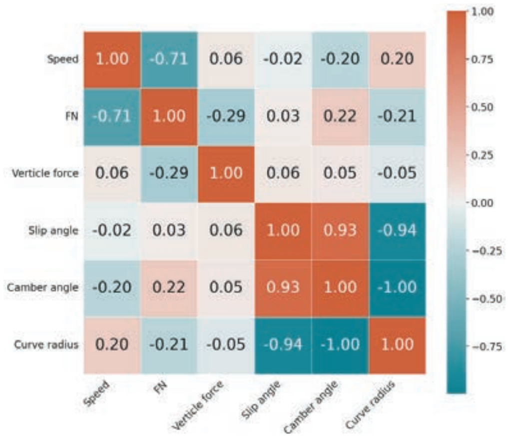

	Speed	FN	Verticle force	Slip angle	Camber angle	Curve radius
Speed	1.00	-0.71	0.06	-0.02	-0.20	0.20
FN	-0.71	1.00	-0.29	0.03	0.22	-0.21
Verticle force	0.06	-0.29	1.00	0.06	0.05	-0.05
Slip angle	-0.02	0.03	0.06	1.00	0.93	-0.94
Camber angle	-0.20	0.22	0.05	0.93	1.00	-1.00
Curve radius	0.20	-0.21	-0.05	-0.94	-1.00	1.00

(e)

Figure 2.8 Continued

parameters studied. This indicates that velocity is a significant factor affecting FN with high correlations. Figure 2.9 illustrates the correlation maps and statistical relationship with the field testing data at Purdue University Airport.

Similarly, the data from the road friction test reveals a –0.78 correlation value between longitudinal friction and speed and a –0.14 correlation value between longitudinal friction and vertical force. This relationship is also confirmed by other researchers that as the vehicle's speed increases, the longitudinal frictional number decreases accordingly (Gillespie, 2021).

Another important independent variable in the Airport dataset is the curving radius, with three different radii measured at 165 ft, 136 ft, and 146 ft. Different curving radii result in varied vertical forces, especially during right turns when the vehicle's center of gravity shifts, influencing the measured vertical force on the left-side tires. Consequently, this variation affected the slip angle value, demonstrating a correlation of –0.91. A correlation value of –0.12 between the slip angle and FN is found in this correlation map in Figure 2.9, which contrasts with the positive value of 0.03 observed in S.R. 26. Additionally, the R^2 value for slip angle and FN is 0.0155 in the Airport field test and 0.0006 in the S.R. 26 field test, indicating a poor fit with FN. Thus, the slip angle shows an unclear relationship based on these results.

S.R. 75 and S.R. 47 exhibit similar test results for FN. This similarity is possibly due to the same road surface textures and the fact that the tests are conducted in the same temperature conditions. Table 2.1 illustrates the correlation maps and statistical relationship with the field testing data at S.R. 47 and S.R. 75.

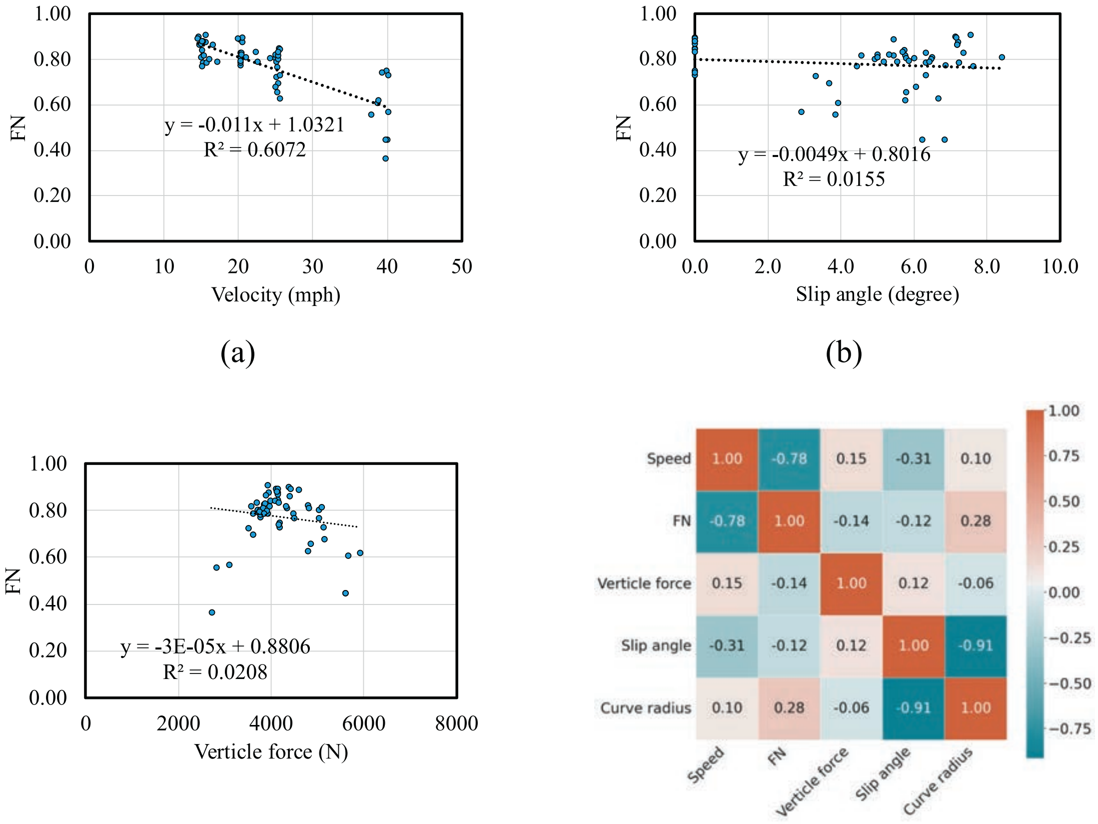

	Speed	FN	Verticle force	Slip angle	Curve radius
Speed	1.00	-0.78	0.15	-0.31	0.10
FN	-0.78	1.00	-0.14	-0.12	0.28
Verticle force	0.15	-0.14	1.00	0.12	-0.06
Slip angle	-0.31	-0.12	0.12	1.00	-0.91
Curve radius	0.10	0.28	-0.06	-0.91	1.00

(a)

(b)

(c)

(d)

Figure 2.9 Sensitivity Analysis on Purdue University Airport. The Statistical Relationship Between FN and (a) Velocity; (b) Slip Angle; (c) Vertical Force; and (d) Correlation Map From Field-Testing Data.

TABLE 2.1
Sensitivity Analysis on S.R. 47 and S.R. 75.

Statistical Relationship Between FN and:	S.R. 47	S.R. 75
Velocity	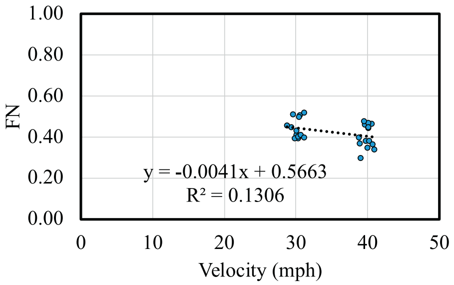	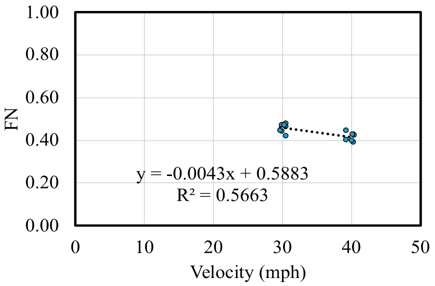
Slip Angle	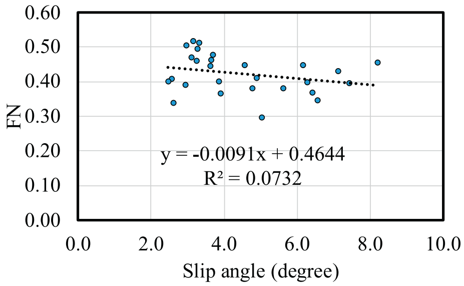	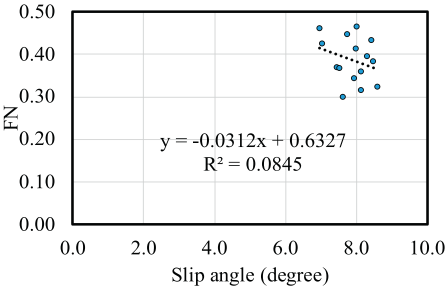
Superelevation	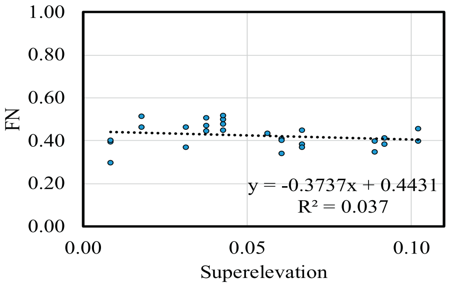	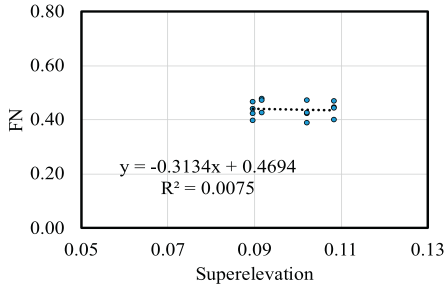
Vertical Force	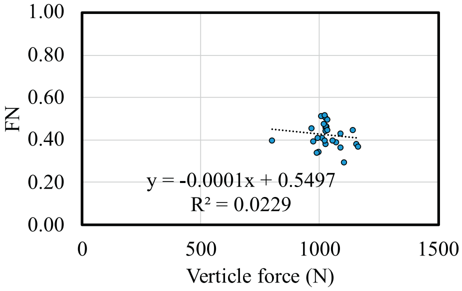	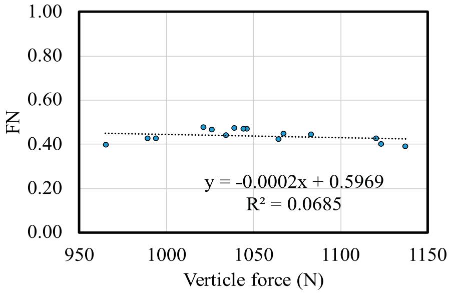
Correlation Map	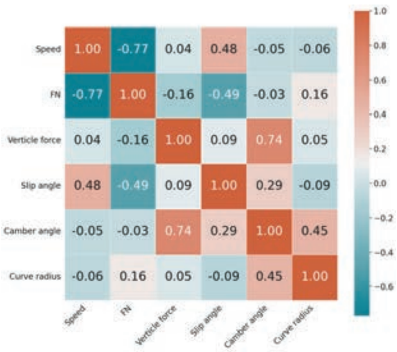	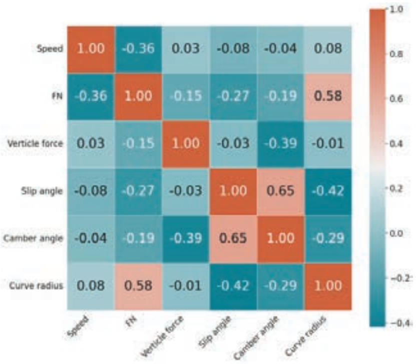

	Speed	FN	Verticle force	Slip angle	Camber angle	Curve radius
Speed	1.00	-0.77	0.04	0.48	-0.05	-0.06
FN	-0.77	1.00	-0.16	-0.49	-0.03	0.16
Verticle force	0.04	-0.16	1.00	0.09	0.74	0.05
Slip angle	0.48	-0.49	0.09	1.00	0.29	-0.09
Camber angle	-0.05	-0.03	0.74	0.29	1.00	0.45
Curve radius	-0.06	0.16	0.05	-0.09	0.45	1.00

	Speed	FN	Verticle force	Slip angle	Camber angle	Curve radius
Speed	1.00	-0.36	0.03	-0.08	-0.04	0.08
FN	-0.36	1.00	-0.15	-0.27	-0.19	0.58
Verticle force	0.03	-0.15	1.00	-0.03	-0.39	-0.01
Slip angle	-0.08	-0.27	-0.03	1.00	0.65	-0.42
Camber angle	-0.04	-0.19	-0.39	0.65	1.00	-0.29
Curve radius	0.08	0.58	-0.01	-0.42	-0.29	1.00

The data from the S.R. 47 and S.R. 75 road friction tests reveal correlation values of −0.36 and −0.77, respectively, between longitudinal friction and speed. Corresponding R^2 values are 0.131 on S.R. 47 and 0.567 on S.R. 75. This confirms that higher speeds result in lower friction values. It is essential to emphasize that the slip angle contributes to a negative correlation with FN, as indicated by both S.R. 47 and S.R. 75 correlation maps. The correlation value of slip indicates −0.27 on S.R. 47 and −0.49 on S.R. 75. However, the R^2 values are much lower, with 0.07 on S.R. 47 and 0.0845 on S.R. 75. Comparing the correlation maps from S.R. 26 and the Purdue Airport with those from S.R. 47 and S.R. 75 reveals a significant difference in the relationship between the FN and slip angle. Notably, S.R. 47 and S.R. 75 lack straight-road testing data, particularly on S.R. 75; the high average slip angle of the testing data may introduce some bias. This may be a possible reason for observing an obvious difference in the impact of the slip angle on FN in different testing conditions.

Similarly, the superelevation of S.R. 47 and S.R. 75 shows a negative correlation value toward FN, while S.R. 26 shows a positive correlation value. Since S.R. 26 has very limited data on superelevation, this may also introduce bias in the sensitivity test. On the other hand, the correlation value between vertical force and FN remains consistent across the tests. With increased vertical forces, FN values decrease, the same trend is confirmed by other researchers as well, such as Anupam et al. (2014).

2.3.2.2 Left and Right Turn Effects. The sensor detector, installed on the left wheel, records data that includes both negative and positive slip angle values. Negative slip angle values indicate left turns, while positive values indicate right turns. In the previous sensitivity analysis, we converted all cases to absolute values, combining straight and curved road data into a single analysis. However, in this section, we focus exclusively on curved roads, distinguishing between left and right turns.

Figure 2.10 illustrates the relationship between FN and slip angle for S.R. 26. Compared to the sensitivity analysis presented for S.R. 26, the correlations for left and right turns in the Purdue Airport exhibit lower values of −0.81 and −0.88, respectively, indicating a negative impact on FN as the slip angle increases. This reduction in correlation is likely due to the exclusion of straight-road data. There is no significant difference between the correlations for left and right turns on S.R. 26.

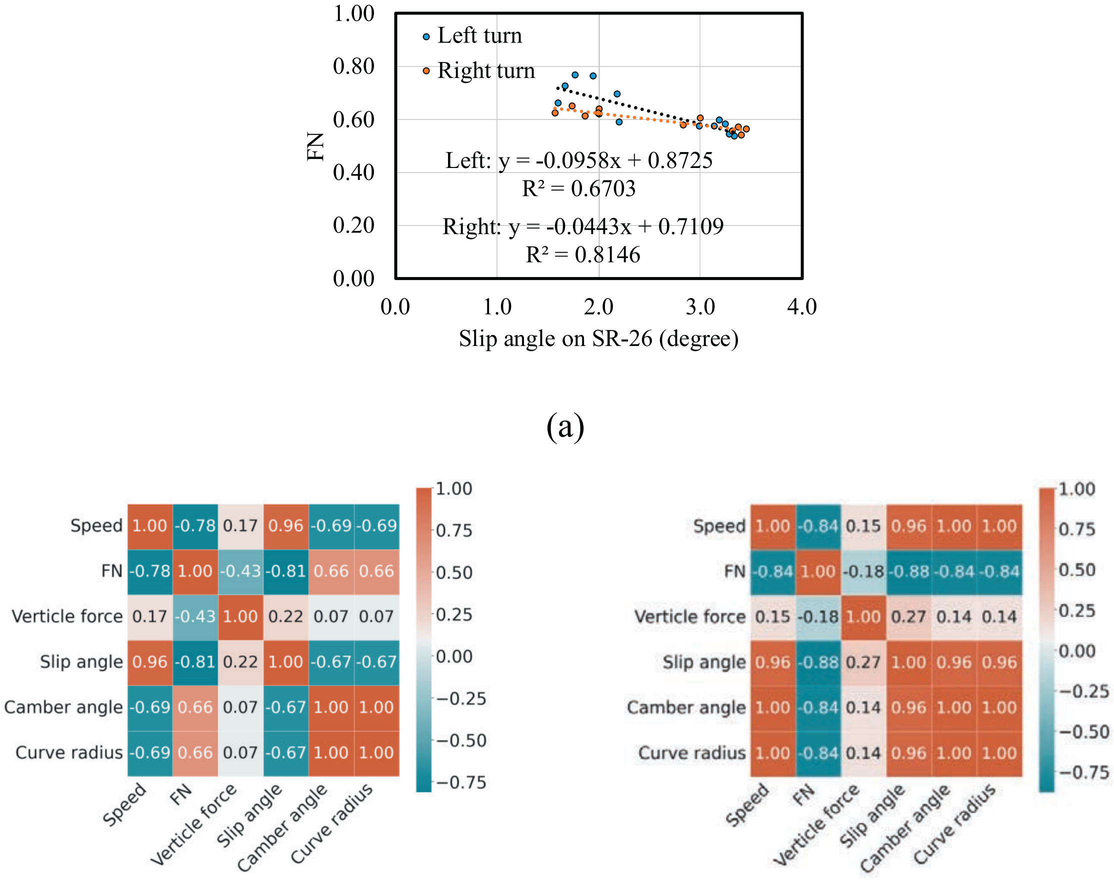

(a)

	Speed	FN	Verticle force	Slip angle	Camber angle	Curve radius
Speed	1.00	-0.78	0.17	0.96	-0.69	-0.69
FN	-0.78	1.00	-0.43	-0.81	0.66	0.66
Verticle force	0.17	-0.43	1.00	0.22	0.07	0.07
Slip angle	0.96	-0.81	0.22	1.00	-0.67	-0.67
Camber angle	-0.69	0.66	0.07	-0.67	1.00	1.00
Curve radius	-0.69	0.66	0.07	-0.67	1.00	1.00

(b)

	Speed	FN	Verticle force	Slip angle	Camber angle	Curve radius
Speed	1.00	-0.84	0.15	0.96	1.00	1.00
FN	-0.84	1.00	-0.18	-0.88	-0.84	-0.84
Verticle force	0.15	-0.18	1.00	0.27	0.14	0.14
Slip angle	0.96	-0.88	0.27	1.00	0.96	0.96
Camber angle	1.00	-0.84	0.14	0.96	1.00	1.00
Curve radius	1.00	-0.84	0.14	0.96	1.00	1.00

(c)

Figure 2.10 (a) The Statistical Relationship S.R. 26 Between FN and Slip Angle With a Left and Right Turn; (b) Sensitivity Analysis on S.R. 26 for the Left Turn; (c) Sensitivity Analysis on S.R. 26 for the Right Turn.

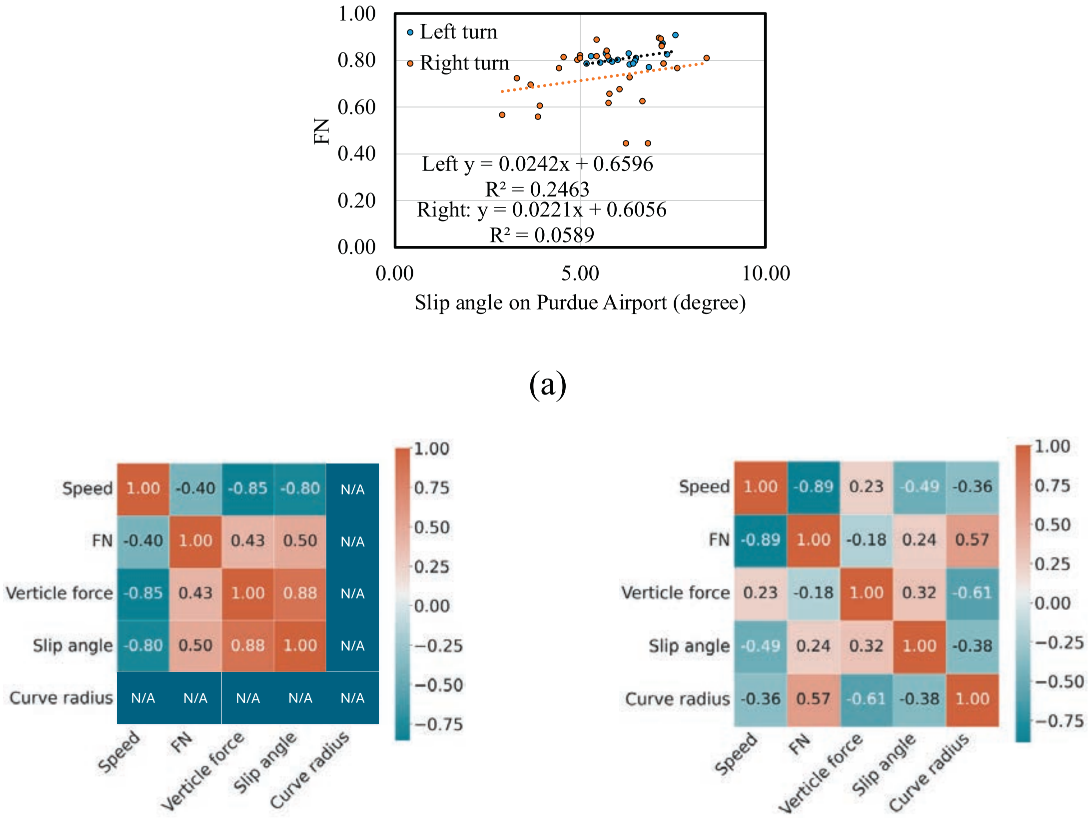

(a)

(b)

(c)

Figure 2.11 (a) The Statistical Relationship on the Purdue Airport Between FN and Slip Angle With a Left and Right Turn; (b) Sensitivity Analysis on the Purdue Airport for the Left Turn (Under the Same Curve Radius); (c) Sensitivity Analysis on the Purdue Airport for the Right Turn.

Figure 2.11 illustrates the relationship between FN and slip angle for the Purdue Airport. Since the curve radius for left turns remains constant, the sensitivity analysis does not include the curve radius parameter for left turns. Compared to the mixed data from straight and curved roads, the correlation value between FN and slip angle exhibits a positive value for both left and right turns. This is also due to the exclusion of straight-road data. Overall, the Purdue Airport field test includes 18 curved road test results for left turns and 27 for right turns, making it the largest curved road data group for the INDOT test field.

The correlation between FN and slip angle follows a similar trend to the previous values shown in Figure 2.12 for S.R. 47, as the field test on S.R. 47 lacks straight-road test data. There is not a significant difference between the left turn (–0.3) and right turn (–0.24) correlations. S.R. 75 shows a correlation between FN and slip angle, with values of –0.81 for the left turn and –0.02 for the right turn. However, the sensitivity analysis on S.R. 75 might be biased due to the limited number of data points, with only eight for each turning direction. Overall, its impact on FN generally remains the same level for left and right turns for all test fields.

In this section, the most significant impact on the left and right turn analysis is the vertical force. With different turning directions, vertical force affects FN, slip angle, and curve radius to varying degrees, as observed from the Purdue Airport, S.R. 47, and S.R. 75 tests.

2.3.2.3 Impact of Curve Radius. To gain a more direct understanding of the FN on vehicles, we aim to study the impact of curve radius in this section from LWST data and SCRIM data. Figure 2.13 summarizes the statistical relationship between curve radii and slip angles for all INDOT curve road tests.

The largest dataset from the Purdue Airport illustrates the negative impact of curve radius on slip angle within the range of 136–165 ft. Due to the narrow data range and the sharp curves, the slip angle may be influenced by other factors, such as instable vehicle maneuver. Similarly, the second-largest dataset from S.R. 47 demonstrates a negative correlation, where an increasing curve radius results in a decreasing slip angle.

Since the Purdue Airport data lack superelevation information, it is excluded from this section. Consequently, the largest dataset now comes from S.R. 47, which shows a negative impact of curve radius on superelevation. The other two datasets, S.R. 26 and S.R. 75, exhibit a positive impact of curve radius on superelevation. These results collected from test samples illustrate that a large superelevation rate is not guaranteed for a sharp curve with small radius of curvature in real-world construction, as illustrated in Figure 2.14.

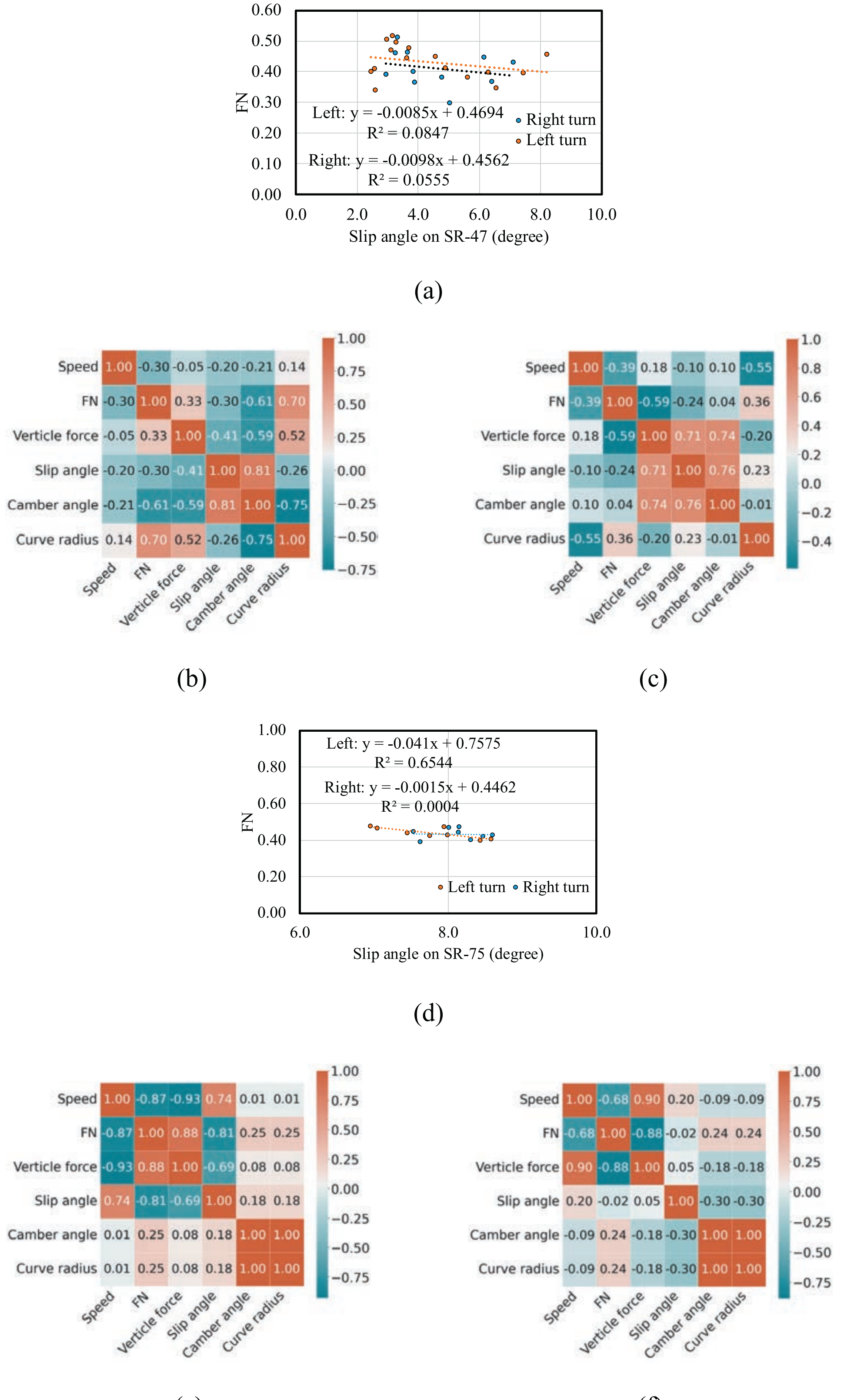

(a)

	Speed	FN	Verticle force	Slip angle	Camber angle	Curve radius
Speed	1.00	-0.30	-0.05	-0.20	-0.21	0.14
FN	-0.30	1.00	0.33	-0.30	-0.61	0.70
Verticle force	-0.05	0.33	1.00	-0.41	-0.59	0.52
Slip angle	-0.20	-0.30	-0.41	1.00	0.81	-0.26
Camber angle	-0.21	-0.61	-0.59	0.81	1.00	-0.75
Curve radius	0.14	0.70	0.52	-0.26	-0.75	1.00

(b)

	Speed	FN	Verticle force	Slip angle	Camber angle	Curve radius
Speed	1.00	-0.39	0.18	-0.10	0.10	-0.55
FN	-0.39	1.00	-0.59	-0.24	0.04	0.36
Verticle force	0.18	-0.59	1.00	0.71	0.74	-0.20
Slip angle	-0.10	-0.24	0.71	1.00	0.76	0.23
Camber angle	0.10	0.04	0.74	0.76	1.00	-0.01
Curve radius	-0.55	0.36	-0.20	0.23	-0.01	1.00

(c)

(d)

	Speed	FN	Verticle force	Slip angle	Camber angle	Curve radius
Speed	1.00	-0.87	-0.93	0.74	0.01	0.01
FN	-0.87	1.00	0.88	-0.81	0.25	0.25
Verticle force	-0.93	0.88	1.00	-0.69	0.08	0.08
Slip angle	0.74	-0.81	-0.69	1.00	0.18	0.18
Camber angle	0.01	0.25	0.08	0.18	1.00	1.00
Curve radius	0.01	0.25	0.08	0.18	1.00	1.00

(e)

	Speed	FN	Verticle force	Slip angle	Camber angle	Curve radius
Speed	1.00	-0.68	0.90	0.20	-0.09	-0.09
FN	-0.68	1.00	-0.88	-0.02	0.24	0.24
Verticle force	0.90	-0.88	1.00	0.05	-0.18	-0.18
Slip angle	0.20	-0.02	0.05	1.00	-0.30	-0.30
Camber angle	-0.09	0.24	-0.18	-0.30	1.00	1.00
Curve radius	-0.09	0.24	-0.18	-0.30	1.00	1.00

(f)

Figure 2.12 (a) The Statistical Relationship on S.R. 47 Between FN and Slip Angle With a Left and Right Turn; (b) Sensitivity Analysis on S.R. 47 for the Left Turn; (c) Sensitivity Analysis on S.R. 47 for the Right Turn; (d) The Statistical Relationship on S.R. 75 Between FN and Slip Angle with a Left and Right Turn; (e) Sensitivity Analysis on S.R. 75 for the Left Turn; (f) Sensitivity Analysis on S.R. 75 for the Right Turn.

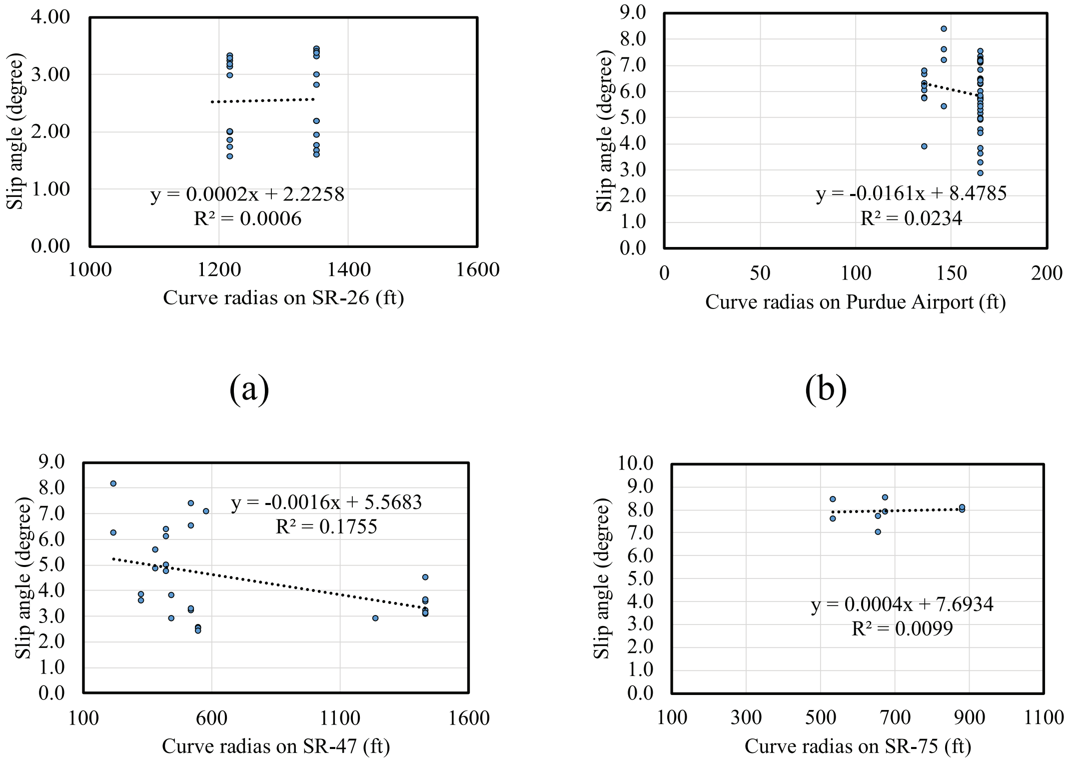

(a) (b)

(c) (d)

Figure 2.13 (a) The Statistical Relationship Between Curve Radius and Slip Angle on (a) S.R. 26; (b) the Purdue Airport; (c) S.R. 47; (d) S.R. 75.

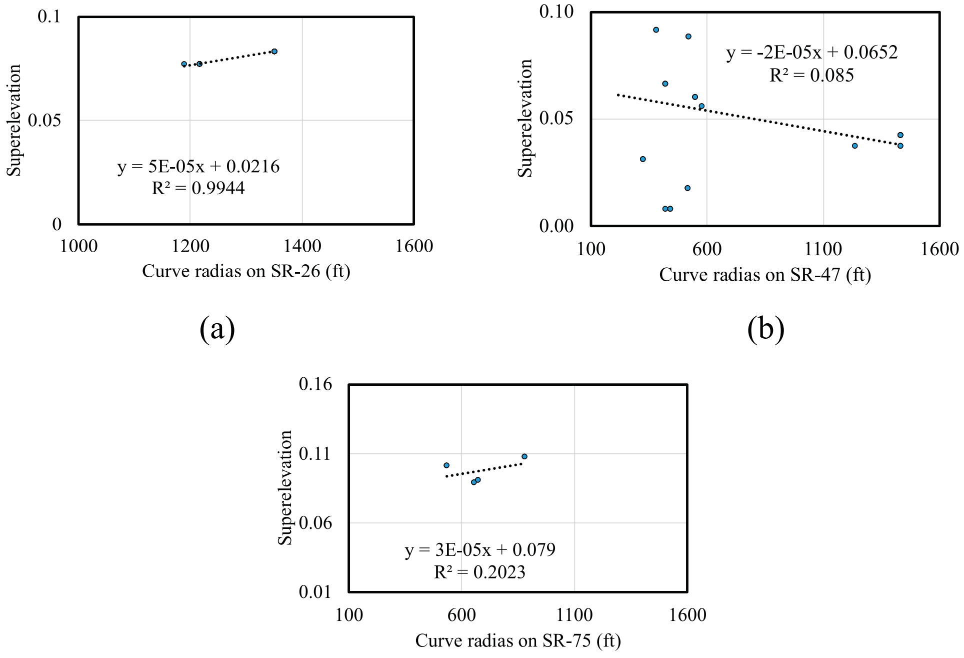

(a) (b)

(c)

Figure 2.14 (a) The Statistical Relationship Between Curve Radius and Superelevation on (a) S.R. 26; (b) S.R. 47; (c) S.R. 75.

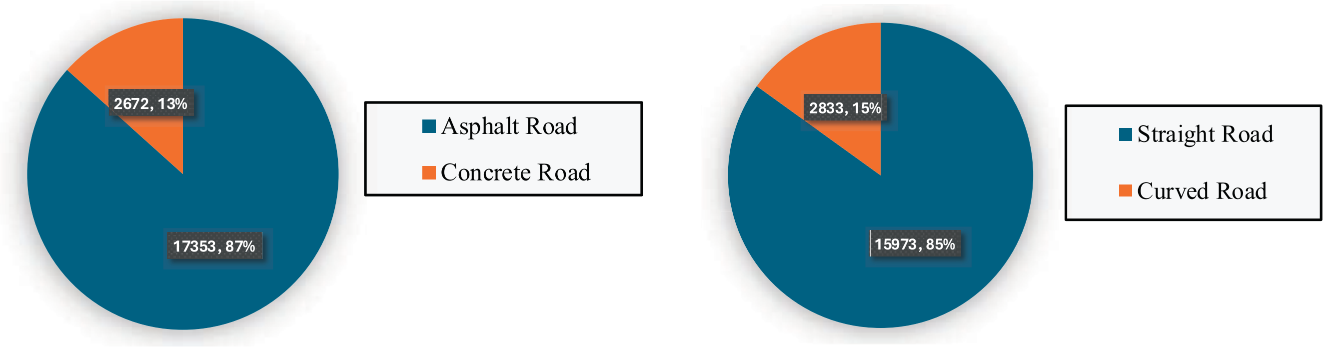

(a) (b)

Figure 2.15 Pie Charts for All Roads (a) Pavement Material Categorization and (b) Road Categorization.

2.3.3 SCRIM Frictional Test

2.3.3.1 Pavement Material and Road Curvature Categorization. We categorize all roads from R1 to R11. By using GPS coordinates recorded in the SCRIM test data, we match each coordinate with corresponding dashcam images, allowing us to visually inspect and confirm the pavement type and condition for each section. This systematic approach enables us to accurately identify transitions and categorize each segment based on pavement characteristics. As we move along the route, each change in pavement type is documented and aligned with the GPS data, ensuring a consistent and detailed record of road conditions across all segments. Straight and curved roads are categorized based on a curve radius threshold of 1,500 ft. Table 2.2 summarizes the road material and type information of the 11 SCRIM test roads. Figure 2.15 illustrates the total count of recorded points from testing vehicles and the corresponding percentages of R1 pavement type and road type: 87% of the roads are asphalt roads, 13% of roads are concrete, 85% of roads are straight roads, and 15% of roads are curved roads.

Overall, the correlation values, both from selected matched points and original points, tend to show negative values in some

TABLE 2.2
Correlation Values in Different Highway Route Segments.

Route ID	Route	Pavement Material Type	Road Type
1	US 52	90.23% Asphalt 9.77% Concrete	98.95% Straight 1.05% Curved
2	S.R. 32a	100.00% Asphalt	94.84% Straight 5.16% Curved
3	S.R. 32b	98.66% Asphalt 1.34% Concrete	99.44% Straight 0.56% Curved
4	S.R. 39	99.16% Asphalt 0.84% Concrete	82.95% Straight 17.05% Curved
5	S.R. 46a	98.70% Asphalt 1.30% Concrete	69.24% Straight 30.76% Curved
6	S.R. 135	99.18% Asphalt 0.82% Concrete	58.83% Straight 41.17% Curved
7	S.R. 46b	99.32% Asphalt 0.68% Concrete	88.49% Straight 11.51% Curved
8	S.R. 46c	100.00% Asphalt	93.34% Straight 6.66% Curved
9	S.R. 240	97.77% Asphalt 2.23% Concrete	91.84% Straight 8.16% Curved
10	I-65a	2.56% Asphalt 97.44% Concrete	97.88% Straight 2.12% Curved
11	I-65b	3.24% Asphalt 96.76% Concrete	96.93% Straight 3.07% Curved
All	All	Total: 86.66% Asphalt 13.34% Concrete	Total: 84.94% Straight 15.06% Curved

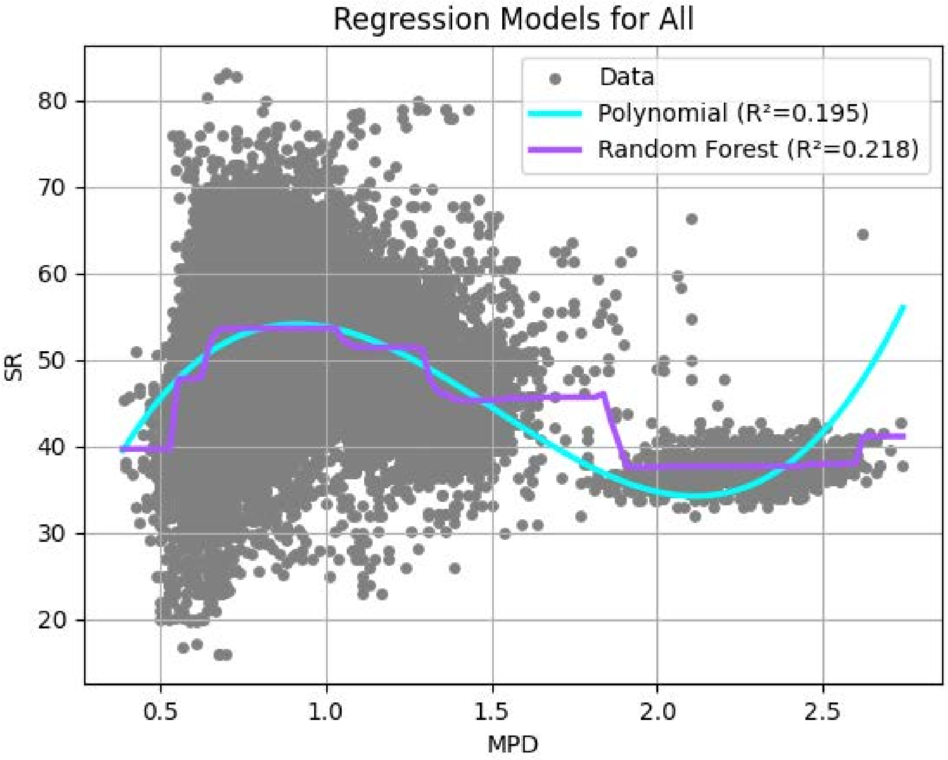

Figure 2.16 Comparison of Different Correlation Methods for SR = f(MPD).

routes. These overall correlations may be influenced by the imparts of different pavement types, concrete groove textures (longitudinal and transverse direction) and road curvature within the dataset. For instance, previous research found that pavement grooves can be oriented longitudinally (parallel to the centerline), transversely, or at a skewed angle. Most state highways have implemented longitudinal grooving, which is believed to enhance lateral stability and assist vehicles in navigating critical curves (Beaton et al., 1969). Hoerner et al. (2003) also indicate that transverse grooves offer higher surface friction and reduce splash and spray, while longitudinal grooves enhance directional control, resist lateral movement, produce less tire noise, and are easier to implement. However, this current report mainly focuses on road curvature analysis to provide a more accurate understanding of the four study relationships.

2.3.4 Machine Learning Algorithms With and Without Road Type Categorization

2.3.4.1 SR = f(MPD). Figure 2.16 shows the comparison of polynomial regression with three ML algorithms. Table 2.3 shows the R^2 values of different correlation methods with and without data preprocessing.

Figure 2.18 shows the two-dimensional (2D) plot of the polynomial regression for SR and MPD. Table 2.4 shows the polynomial regression functions SR = f(MPD) for individual and entire road data with R^2, Mean Squared Error (MSE), and Root Mean Squared Error (RMSE) values.

Figure 2.18 shows the comparison of polynomial regression with three algorithms for road categorization. Table 2.5 and Table 2.6 show the R^2 values and polynomial equations of each categorization.

2.3.4.2 FN = f(SR). Figure 2.19 shows the comparison of polynomial regression with three ML algorithms. Table 2.7 shows the R^2 values of different correlation methods with and without data preprocessing.

Figure 2.20 shows the 2D plot of the polynomial regression for FN and SR. Table 2.8 shows the polynomial regression functions FN = f(SR) for individual and entire road data with R^2, MSE, and RMSE values.

TABLE 2.3
R^2 Values of Different Correlation Methods With and Without Data Preprocessing.

Method	Original Data	Standardization	Normalization
Polynomial regression	0.113	0.113	0.113
Random forest regression	0.116	0.116	0.116

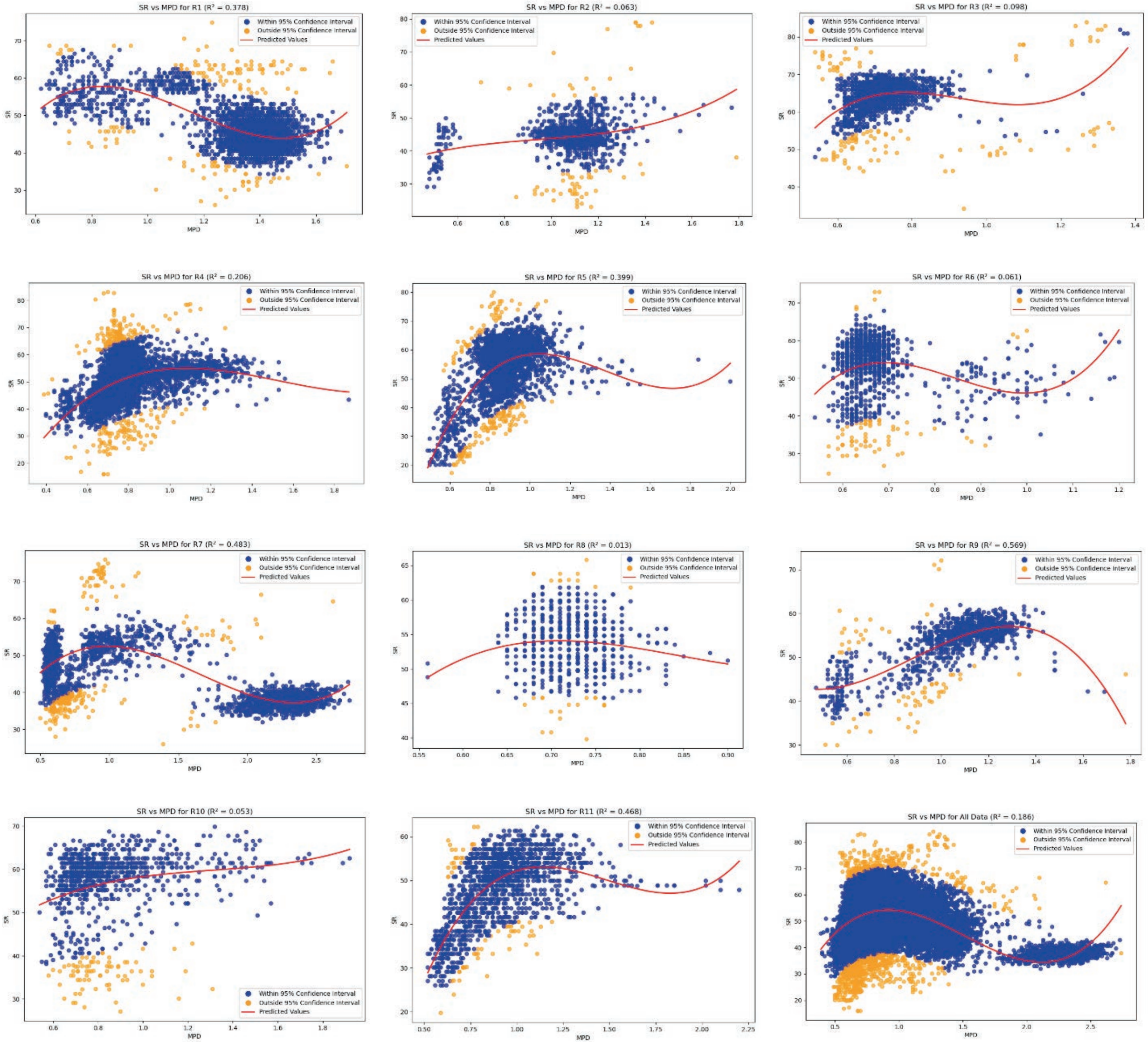

Figure 2.17 Polynomial Regression of SR and MPD for Individual and Entire Road Data (R1–R11).

TABLE 2.4
Polynomial Regression Functions SR = f(MPD) for Individual and Entire Road Data.

Road	Polynomial Regression Equation	MSE	RMSE	R^2
R1	$SR = 46.2008 - 24.8058 \times MPD + 48.9146 \times MPD^2 + 105.3162 \times MPD^3$	27.3918	5.2337	0.3778
R2	$SR = 44.2747 + 6.6745 \times MPD + 7.4391 \times MPD^2 + 16.9466 \times MPD^3$	31.4453	5.6076	0.0633
R3	$SR = 64.8303 + 13.1270 \times MPD - 142.3944 \times MPD^2 + 231.7913 \times MPD^3$	18.9899	4.3577	0.0976
R4	$SR = 51.6369 + 26.0879 \times MPD - 57.5665 \times MPD^2 + 26.6203 \times MPD^3$	51.7999	7.1972	0.2055
R5	$SR = 55.5245 + 36.7216 \times MPD - 125.0008 \times MPD^2 + 81.7397 \times MPD^3$	67.7470	8.2309	0.3993
R6	$SR = 54.0788 + 7.7092 \times MPD - 293.3172 \times MPD^2 + 596.0423 \times MPD^3$	56.0187	7.4846	0.0611
R7	$SR = 51.4964 - 8.9313 \times MPD - 17.1735 \times MPD^2 + 12.3031 \times MPD^3$	29.1363	5.3978	0.4828
R8	$SR = 54.0461 - 4.7350 \times MPD - 157.4131 \times MPD^2 + 440.0310 \times MPD^3$	16.3183	4.0395	0.0129
R9	$SR = 53.6583 + 22.9677 \times MPD - 24.2633 \times MPD^2 - 53.9709 \times MPD^3$	14.9025	3.8604	0.5694
R10	$SR = 57.0273 + 10.6761 \times MPD - 15.3174 \times MPD^2 + 11.2307 \times MPD^3$	64.2071	8.0129	0.0535
R11	$SR = 50.4843 + 24.2994 \times MPD - 65.1611 \times MPD^2 + 37.7147 \times MPD^3$	35.3176	5.9429	0.4685
All Roads (raw data)	$SR = 1.7466 + 133.5758 \times MPD - 104.2513 \times MPD^2 + 22.8848 \times MPD^3$	69.9104	8.3612	0.1857
All Roads (data transformation)	$SR = 54.1509 - 0.4825 \times MPD - 0.8446 \times MPD^2 + 0.0747 \times MPD^3$	69.9104	8.3612	0.1857

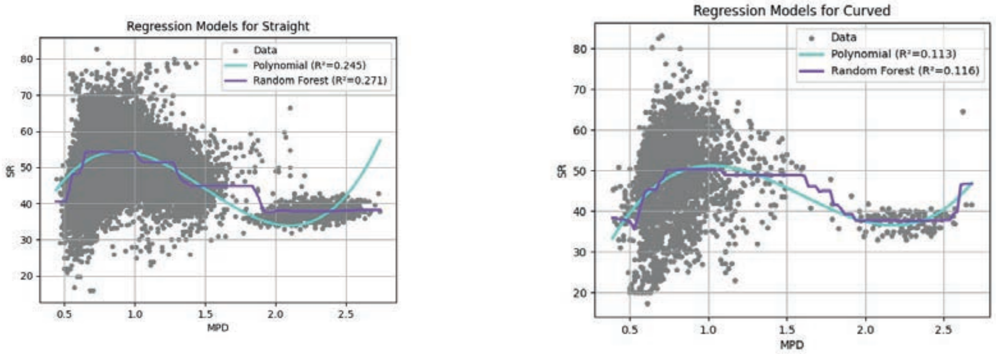

(a) (b)

Figure 2.18 Comparison of Different Correlation Methods for SR = f(MPD): (a) Straight Roads; (b) Curved Roads.

TABLE 2.5
R^2 Values of Different Correlation Methods With Road Type Categorization.

Road Type	Polynomial R^2	Random Forest R^2
Straight	0.245	0.271
Curved	0.113	0.116
All	0.195	0.218

TABLE 2.6
Polynomial Regression Equation With Road Type Categorization.

Road/Pavement	Polynomial Regression Equations
Straight	$SR = -126.788 + 659.998 \times MPD^1 - 891.637 \times MPD^2 + 563.028 \times MPD^3 - 171.123 \times MPD^4 + 20.218 \times MPD^5$
Curved	$SR = -1.574 + 122.460 \times MPD^2 - 87.840 \times MPD^3$
All	$SR = 586.0171 \times MPD - 781.8936 \times MPD^2 + 490.5209 \times MPD^3 - 149.1656 \times MPD^4 + 17.7324 \times MPD^5 - 109.6375$

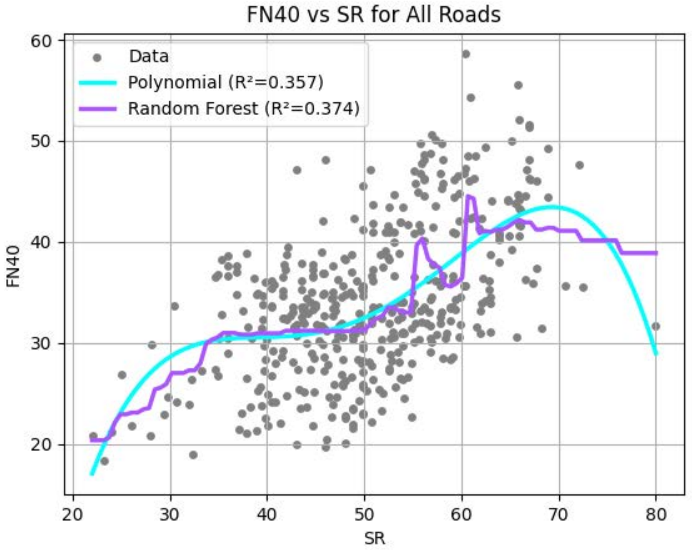

Figure 2.19 Comparison of Different Correlation Methods for FN = f(SR).

TABLE 2.7
R^2 Values of Different Correlation Methods With and Without Data Preprocessing.

Method	Original Data	Standardization	Normalization
Polynomial regression	0.357	0.357	0.357
Random forest regression	0.374	0.374	0.374

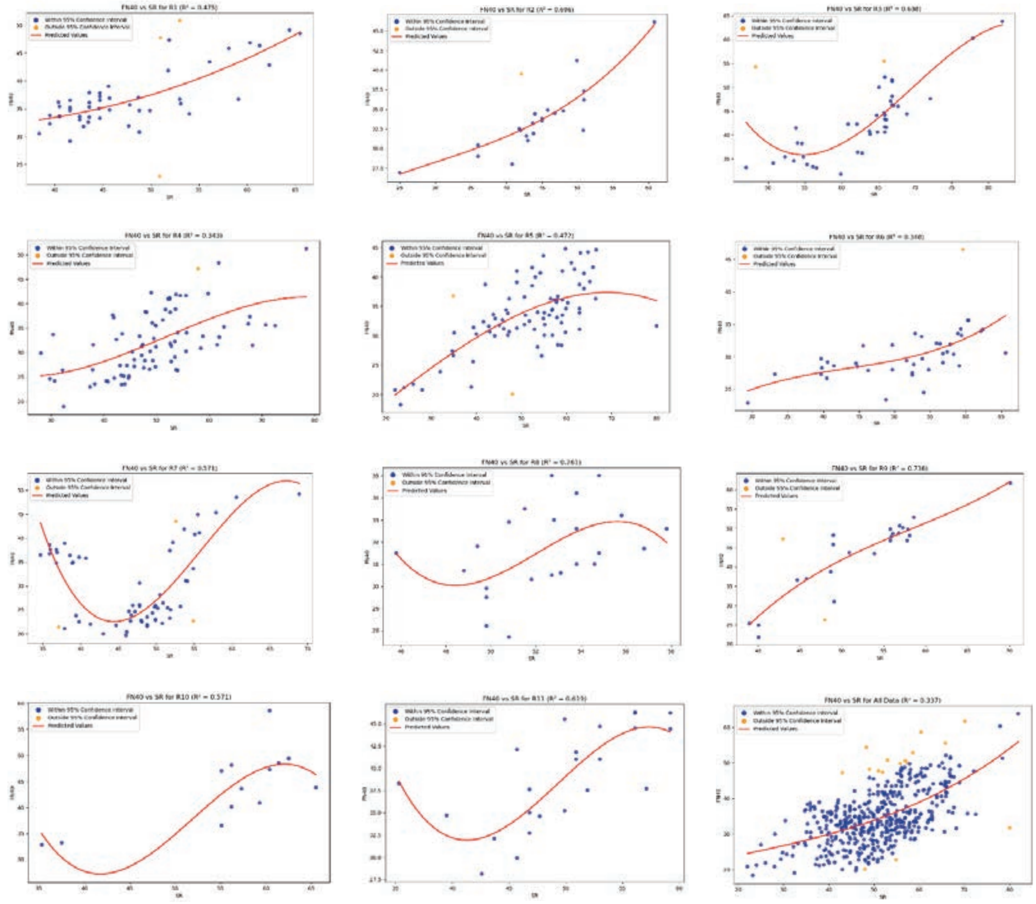

Figure 2.20 Polynomial Regression of FN Versus SR for Individual and Entire Road Data (R1–R11).

TABLE 2.8
Polynomial Regression Functions FN = f(SR) for Individual and Entire Road Data.

Road	Polynomial Regression Equation	MSE	RMSE	R^2
R1	FN40 = 36.4590 + 3.3454 × ((Matched_SR) – 47.9531)/7.0605 + 0.6070 × (((Matched_SR) – 47.9531)/7.0605)^2 + 0.0133 × (((Matched_SR) – 47.9531)/7.0605)^3	17.3627	4.1669	0.4749
R2	FN40 = 33.3585 + 3.1982 × ((Matched_SR) – 44.3136)/6.7409 + 0.5558 × (((Matched_SR) – 44.3136)/6.7409)^2 + 0.0868 × (((Matched_SR) – 44.3136)/6.7409)^3	5.5010	2.3454	0.6961
R3	FN40 = 40.7119 + 7.9425 × ((Matched_SR) – 62.6333)/7.2197 + 2.3319 × (((Matched_SR) – 62.6333)/7.2197)^2 – 0.8105 × (((Matched_SR) – 62.6333)/7.2197)^3	20.0121	4.4735	0.6376
R4	FN40 = 32.2291 + 4.4237 × ((Matched_SR) – 49.5812)/9.7223 + 0.1378 × (((Matched_SR) – 49.5812)/9.7223)^2 – 0.1984 × (((Matched_SR) – 49.5812)/9.7223)^3	27.4151	5.2359	0.3431
R5	FN40 = 34.2767 + 3.6532 × ((Matched_SR) – 51.3741)/11.0995 – 0.9177 × (((Matched_SR) – 51.3741)/11.0995)^2 – 0.0964 × (((Matched_SR) – 51.3741)/11.0995)^3	18.8468	4.3413	0.4720
R6	FN40 = 29.8328 + 2.1062 × ((Matched_SR) – 51.6902)/8.3922 + 0.7111 × (((Matched_SR) – 51.6902)/8.3922)^2 + 0.2403 × (((Matched_SR) – 51.6902)/8.3922)^3	10.1161	3.1806	0.3483
R7	FN40 = 23.7352 + 5.8178 × ((Matched_SR) – 47.1694)/7.0772 + 6.4679 × (((Matched_SR) – 47.1694)/7.0772)^2 – 1.7668 × (((Matched_SR) – 47.1694)/7.0772)^3	28.1119	5.3021	0.5709
R8	FN40 = 31.7173 + 1.6452 × ((Matched_SR) – 52.4174)/2.7602 – 0.1392 × (((Matched_SR) – 52.4174)/2.7602)^2 – 0.3266 × (((Matched_SR) – 52.4174)/2.7602)^3	2.6111	1.6159	0.2606
R9	FN40 = 43.8604 + 7.3451 × ((Matched_SR) – 51.9360)/7.1995 – 1.0342 × (((Matched_SR) – 51.9360)/7.1995)^2 + 0.3926 × (((Matched_SR) – 51.9360)/7.1995)^3	25.8652	5.0858	0.7360
R10	FN40 = 43.2025 + 11.7805 × ((Matched_SR) – 55.5538)/8.6949 – 4.1622 × (((Matched_SR) – 55.5538)/8.6949)^2 – 3.3045 × (((Matched_SR) – 55.5538)/8.6949)^3	20.5161	4.5295	0.5714
R11	FN40 = 38.7851 + 7.1914 × ((Matched_SR) – 49.7348)/6.0675 – 0.2970 × (((Matched_SR) – 49.7348)/6.0675)^2 – 1.3769 × (((Matched_SR) – 49.7348)/6.0675)^3	11.2559	3.3550	0.6194
All Roads (raw data)	FN40 = 18.0777 + 0.3371 × Matched_SR – 0.0035 × Matched_SR^2 + 0.0001 × Matched_SR^3	40.8174	6.3888	0.3370

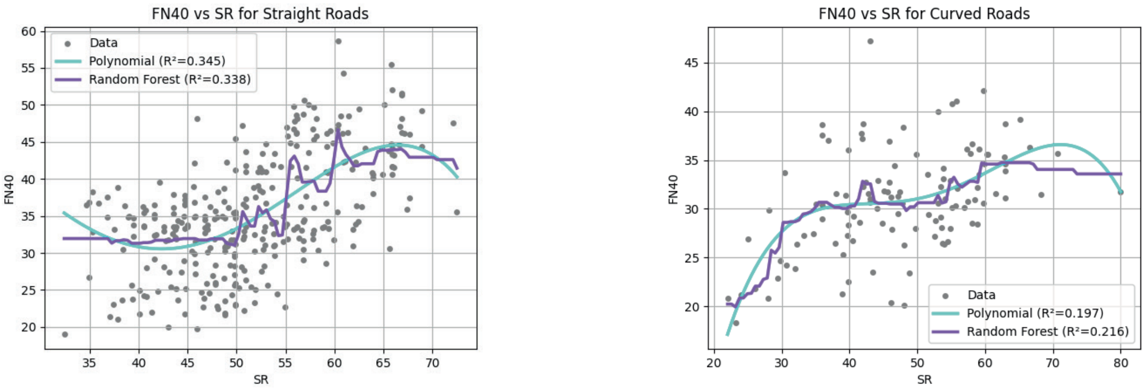

(a) (b)

Figure 2.21 Comparison of Different Correlation Methods for FN = f(SR): (a) Straight Roads; (b) Curved Roads.

Figure 2.18 shows the comparison of polynomial regression with three ML algorithms for road categorization. Table 2.9 and Table 2.10 show the R^2 values and polynomial equations of each categorization.

2.3.4.3 FN = f(SR & CurveRadius). Figure 2.22 shows the comparison of polynomial regression with three ML algorithms. Table 2.11 shows the R^2 values of different correlation methods with and without data preprocessing. There is a significant improvement in the support vector regression (SVR) algorithm after data normalization compared to the data without any preprocessing.

Figure 2.23 shows the three-dimensional (3D) plot of the polynomial regression for FN, SR, and Curve Radius. Table 2.12 shows the polynomial regression functions FN = f(SR, CurveRadius) for individual and entire road data.

TABLE 2.9
R^2 Values of Different Correlation Methods With Road Type Categorization.

Road Type	Polynomial R^2	Random Forest R^2
Straight	0.345	0.338
Curved	0.197	0.216
All	0.357	0.374

TABLE 2.10
Polynomial Regression Equation With Road Type Categorization.

Road	Polynomial Regression Equations
Straight	$FN40 = 16.683 + 5.961 \times SR - 0.325 \times SR^2 + 0.006 \times SR^3 - 0.000 \times SR^4$
Curved	$FN40 = -127.470 + 13.029 \times SR - 0.397 \times SR^2 + 0.005 \times SR^3 - 0.000 \times SR^4$
All	$FN40 = -185.317 + 19.199 \times SR - 0.628 \times SR^2 + 0.009 \times SR^3 - 0.000 \times SR^4$

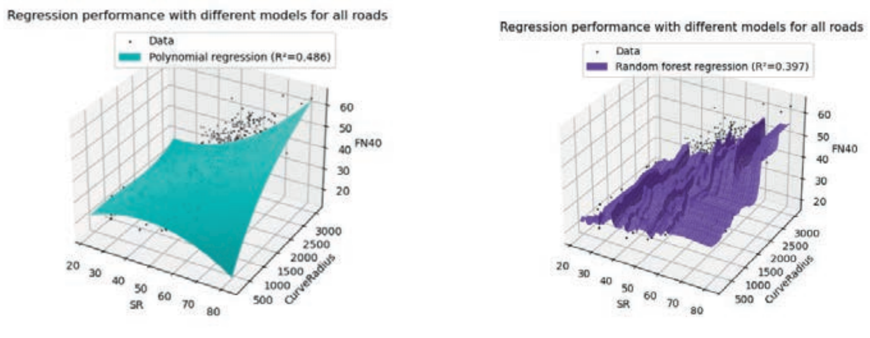

Figure 2.22 Comparison of Different Correlation Methods for FN = f(SR & MPD).

TABLE 2.11
R^2 Values of Different Correlation Methods With and Without Data Preprocessing.

Method	Original Data	Standardization	Normalization
Polynomial regression	0.486	0.486	0.486
Random forest regression	0.397	0.398	0.398

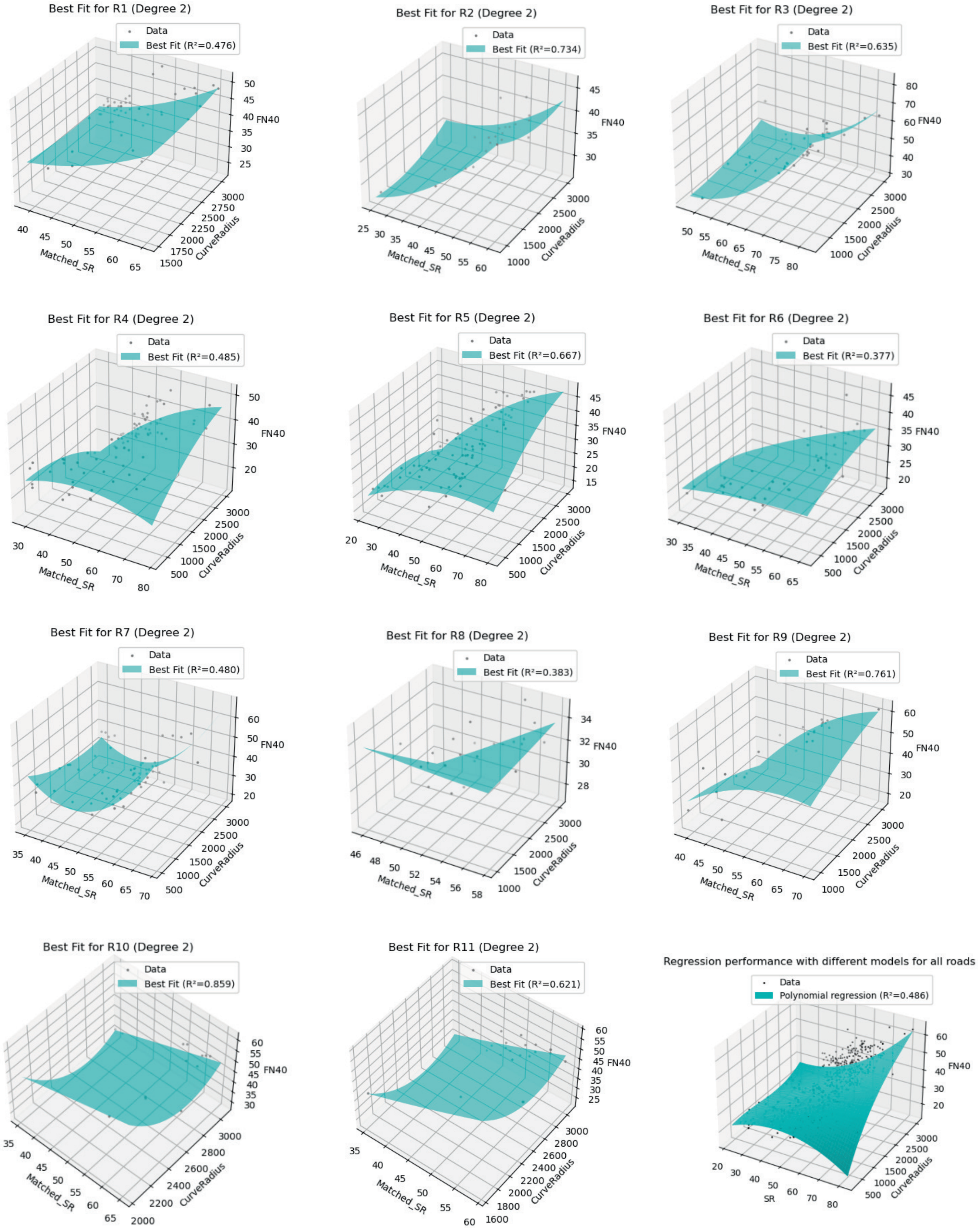

Figure 2.23 Polynomial Regression of FN Versus SR and CurveRadius for Individual and Entire Road Data (R1–R11).

TABLE 2.12
Polynomial Regression Functions FN = f(SR, CurveRadius) for Individual and Entire Road Data.

Road	Polynomial Regression Equation	R^2
R1	$FN40 = -0.7623\ SR - 0.0082\ CR + 0.0112\ SR^2 + 0.0001\ SR \times CR + 52.9367$	0.4765
R2	$FN40 = -0.1668\ SR - 0.0028\ CR + 0.0094\ SR^2 - 0.0001\ SR \times CR + 28.5488$	0.7336
R3	$FN40 = -3.1797\ SR + 0.0109\ CR + 0.0372\ SR^2 - 0.0003\ SR \times CR + 101.6421$	0.6350
R4	$FN40 = 0.7375\ SR - 0.0057\ CR - 0.0079\ SR^2 + 0.0002\ SR \times CR + 11.7798$	0.4851
R5	$FN40 = 0.6028\ SR + 0.0015\ CR - 0.0052\ SR^2 + 0.0002\ SR \times CR + 7.5286$	0.6670
R6	$FN40 = 0.3231\ SR - 0.0037\ CR - 0.0029\ SR^2 + 0.0001\ SR \times CR + 18.5256$	0.3775
R7	$FN40 = -6.4006\ SR - 0.0172\ CR + 0.0677\ SR^2 + 0.0001\ SR \times CR + 190.8823$	0.4804
R8	$FN40 = -0.5666\ SR - 0.0174\ CR + 0.0020\ SR^2 + 0.0003\ SR \times CR + 58.8672$	0.3832
R9	$FN40 = 3.1010\ SR - 0.0151\ CR - 0.0274\ SR^2 + 0.0004\ SR \times CR - 48.8929$	0.7614
R10	$FN40 = 0.2122\ SR - 0.2287\ CR - 0.0006\ SR^2 + 0.0001\ SR \times CR + 327.1206$	0.8587
R11	$FN40 = 0.5724\ SR - 0.0943\ CR + 0.0032\ SR^2 + 119.7628$	0.6206
All Roads	$FN = 0.9207\ SR + 0.0066\ CR - 0.0108\ SR^2 - 0.0002\ SR \times CR + 7.0008$	0.486

Figure 2.18 shows the comparison of polynomial regression with three ML algorithms for pavement material and road categorization. Table 2.13 and Table 2.14 show the R^2 values and polynomial equations of each categorization.

2.3.4.4 FN = f(SR, MPD, CurveRadius, CrossSlope). Table 2.15 shows the R^2 values of different correlation methods with and without data preprocessing.

TABLE 2.13
R^2 Values of Different Correlation Methods With Road Type Categorization.

Road Type	Polynomial R^2	Random Forest R^2
Straight	0.581	0.580
Curved	0.543	0.426
All	0.486	0.397

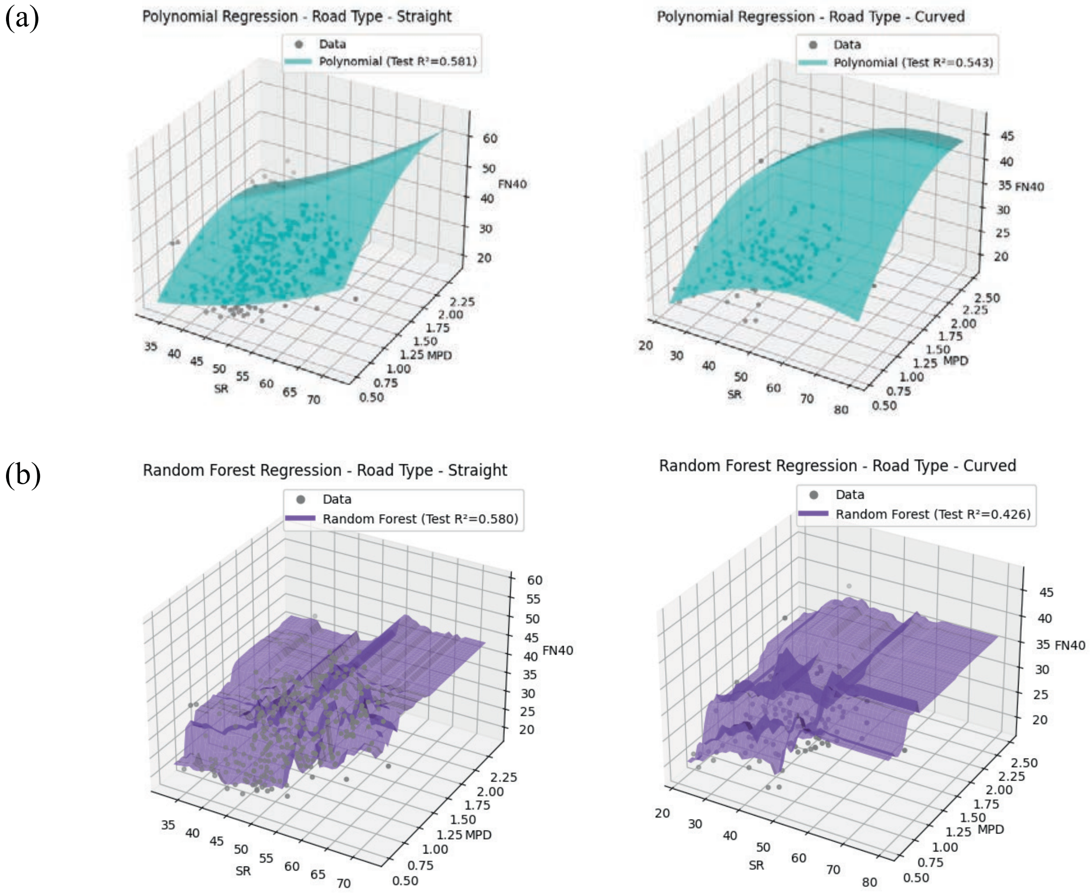

Figure 2.24 Comparison of Different Correlation Methods for FN = f(SR & MPD): (a) Polynomial Regression on Straight Roads and Curved Roads, and (b) Random Forest Regression on Straight Roads and Curved Roads.

TABLE 2.14
Polynomial Regression Equation With Road Type Categorization.

Road/Pavement	Polynomial Regression Equations
Straight	$FN40 = 3.856 - 0.282 \times SR + 35.932 \times MPD + 0.0084 \times SR^2 + 0.0130 \times SR \times MPD - 10.7028 \times MPD \times SR$
Curved	$FN40 = -10.3624 + 0.6817 \times SR + 35.1989 \times MPD + -0.0045 \times SR^2 - 0.0861 \times SR \times MPD - 8.4040 \times MPD \times SR$
All	$FN40 = 0.9207\ SR + 0.0066\ CR - 0.0108\ SR^2 - 0.0002\ SR \times CR + 7.0008$

TABLE 2.15
R^2 Values of Different Correlation Methods With and Without Data Preprocessing.

Method	Original Data	Standardization	Normalization
Polynomial regression	0.709	0.710	0.709
Random forest regression	0.746	0.746	0.747

TABLE 2.16
Polynomial Regression Functions FN = f(SR, MPD, CurveRadius, CrossSlope) for Individual and Entire Road Data.

Road	Polynomial Regression Equation	R^2
R1	$FN40 = -4.3417\ SR - 0.2348\ CR + 9.7824\ MPD + 145.3118\ CS - 0.0245\ SR^2 + 0.0033\ SR \times CS - 1.8618\ SR \times MPD - 0.1368\ SR \times CS + 0.0563\ CR \times MPD - 0.0369\ CR \times CS - 42.4307\ MPD^2 + 5.4576\ MPD \times CS - 8.5623\ CS^2 + 314.1912$	0.6192
R2	$FN40 = -1.8977\ SR + 0.0144\ CR - 69.6624\ MPD - 4.6316\ CS + 0.0240\ SR^2 - 0.0007\ SR \times CR + 1.5626\ SR \times MPD - 0.0643\ SR \times CS - 0.0040\ CR \times MPD - 0.0005\ CR \times CS + 4.3645\ MPD^2 + 7.7721\ MPD \times CS - 0.3173\ CS^2 + 88.4889$	0.9230
R3	$FN40 = -4.4441\ SR + 0.0423\ CR + 256.8905\ MPD - 58.2518\ CS + 0.0356\ SR^2 - 0.0003\ SR \times CR - 0.5409\ SR \times MPD + 0.7828\ SR \times CS - 0.0165\ CR \times MPD + 0.0002\ CR \times CS - 77.6740\ MPD^2 - 6.9065\ MPD \times CS + 2.3196\ CS^2 + 63.8554$	0.8885
R4	$FN40 = 0.9550\ SR - 0.0037\ CR + -8.2747\ MPD + 1.6277\ CS - 0.0138\ SR^2 + 0.0001\ SR \times CR + 0.7390\ SR \times MPD - 0.0320\ SR \times CS + 0.0026\ CR \times MPD - 0.0003\ CR \times CS - 5.9634\ MPD^2 + 0.5608\ MPD \times CS + 0.0503\ CS^2 - 3.1159$	0.7542
R5	$FN40 = -0.4491\ SR + 0.0056\ CR + 1.8556\ MPD - 2.2133\ CS - 0.0013\ SR^2 + 0.0001\ SR \times CR + 0.7378\ SR \times MPD + 0.0008\ SR \times CS - 0.0063\ CR \times MPD - 0.0001\ CR \times CS - 6.3794\ MPD^2 + 2.6503\ MPD \times CS + 0.0019\ CS^2 + 24.0506$	0.7735
R6	$FN40 = -2.0414\ SR - 0.0107\ CR - 388.8256\ MPD - 4.4194\ CS - 0.0072\ SR^2 + 0.0002\ SR \times CR + 4.6716\ SR \times MPD - 0.0058\ SR \times CS - 0.0003\ CR \times MPD + 0.0001\ CR \times CS + 127.5445\ MPD^2 + 7.6182\ MPD \times CS + 0.0501\ CS^2 + 194.9694$	0.7140
R7	$FN40 = -0.5514\ SR + 0.0000\ CR + 38.5424\ MPD + 2.8179\ CS + 0.0118\ SR^2 + 0.0000\ SR \times CR + 0.0961\ SR \times MPD - 0.0535\ SR \times CS - 0.0011\ CR \times MPD + 0.0000\ CR \times CS + -10.1882\ MPD^2 - 0.2677\ MPD \times CS - 0.0352\ CS^2 + 1.8405$	0.9281
R8	$FN40 = 6.7182\ SR - 0.0134\ CR - 111.2836\ MPD + 2.6253\ CS - 0.0297\ SR^2 - 0.0003\ SR \times CR - 3.7951\ SR \times MPD + 0.0113\ SR \times CS + 0.0355\ CR \times MPD - 0.0001\ CR \times CS + 189.9660\ MPD^2 - 4.7602\ MPD \times CS + 0.2715\ CS^2 - 113.7797$	0.8172
R9	$FN40 = -0.9587\ SR - 0.0143\ CR + 181.2769\ MPD - 9.5420\ CS + 0.0222\ SR^2 + 0.0010\ SR \times CR - 3.8630\ SR \times MPD + 0.1678\ SR \times CS + 0.0051\ CR \times MPD + 0.0007\ CR \times CS + 8.7274\ MPD^2 + 1.5908\ MPD \times CS - 0.0599\ CS^2 - 0.1507$	0.9773
R10	$FN40 = -1.0470\ SR - 0.2796\ CR - 3.9905\ MPD + 3.7822\ CS + 0.0773\ SR^2 - 0.0006\ SR \times CR - 6.4437\ SR \times MPD - 0.3041\ SR \times CS + 0.1024\ CR \times MPD - 0.0049\ CR \times CS - 3.8628\ MPD^2 + 37.1911\ MPD \times CR - 0.8353\ CS^2 + 430.0987$	1.0000
R11	$FN40 = 1.2861\ SR - 0.1692\ CR - 132.9574\ MPD + 7.8563\ CS + 0.0133\ SR^2 - 0.0008\ SR \times CR + 0.5569\ SR \times MPD + 0.0843\ SR \times CS + 0.0950\ CR \times MPD - 0.0034\ CR \times CS - 89.6274\ MPD^2 - 2.0166\ MPD \times CS + 0.2278\ CS^2 + 250.1692$	0.7896
All Roads	$FN = -0.0646\ SR - 0.0063\ CR + 50.3149\ MPD - 1.5305\ CS + 0.0035\ SR^2 + 0.0002\ SR \times CR - 0.1925\ SR \times MPD + 0.0365\ SR \times CS - 0.0003\ CR \times MPD - 0.0001 CR \times CS - 12.5384\ MPD^2 + 0.1233\ MPD \times CS + 0.0371\ CS^2 + 0.4257$	0.709

Table 2.16 shows the polynomial regression function FN = f(SR, MPD, CurveRadius, CrossSlope) for individual and entire road data.

Table 2.17 and Table 2.18 show the R^2 values and polynomial equations of each categorization.

TABLE 2.17
R^2 Values of Different Correlation Methods With Road Type Categorization.

Road Type	Polynomial R^2	Random Forest R^2
Straight	0.733	0.753
Curved	0.159	0.271
All	0.709	0.746

TABLE 2.18
Polynomial Regression Equation with Road Type Categorization.

Road	Polynomial Regression Equations
Straight	$FN40 = 45.886 - 0.684 \times SR + 37.221 \times MPD - 0.025 \times CurveRadius - 3.029 \times CrossSlope + 0.007 \times SR^2 - 0.047 \times SR \times MPD + 0.064 \times SR \times CrossSlope - 11.987 \times MPD^2 + 0.002 \times MPD \times CurveRadius - 0.125 \times MPD \times CrossSlope$
Curved	$FN40 = -19.189 + 1.076 \times SR + 42.629 \times MPD - 0.017 \times CurveRadius + 0.686 \times CrossSlope - 0.008 \times SR^2 - 0.353 \times SR \times MPD - 0.011 \times SR \times CrossSlope - 10.041 \times MPD^2 + 0.011 \times MPD \times CurveRadius + 0.007 \times MPD \times CrossSlope + 0.011 \times CrossSlope^2$
All	$SR = 586.0171 \times MPD - 781.8936 \times MPD^2 + 490.5209 \times MPD^3 - 149.1656 \times MPD^4 + 17.7324 \times MPD^5 - 109.6375$

2.4 Summary

The analysis of pavement friction performance using polynomial regression and ML models provided valuable understandings into the relationships between SR, MPD, curve radius, and cross slope across different road types. Polynomial regression effectively captured nonlinear trends in the data, offering reliable predictions, though R^2 values remained relatively low for certain datasets.

The key conclusions can be drawn as follows:

1. Polynomial regression performs well on the original data, providing reliable predictions.
2. Data preprocessing techniques like standardization and normalization do not improve the performance of polynomial regression and random forest regression.
3. Key findings from the correlation analysis include:
   a. *SR = f(MPD)*: Straight roads demonstrated the highest correlation ($R^2 = 0.245$), while all roads outperformed curved roads.
   b. *FN = f(SR)*: All pavements demonstrated the highest correlation across all methods, with random forest network ($R^2 = 0.374$) showing the best performance, followed by polynomial regression ($R^2 = 0.357$).
   c. *FN = f(SR & MPD)*: Polynomial regression provides the best correlation, especially on straight roads ($R^2 = 0.581$), while curved roads show the second-best correlation. Random forest performs poorly for complex surfaces with overfitting.
   d. *FN = f(SR, MPD, curve radius, and cross slope)*: Random forest provides the highest correlation across different curvature types, with straight roads ($R^2 = 0.753$) and all roads ($R^2 = 0.746$) showing stronger relationships. However, curved roads exhibit greater variability with R^2 0.159 for polynomial regression.

3. DEVELOPMENT OF ADJUSTMENT FACTORS FOR FRICTION TESTS ON HORIZONTAL CURVES

3.1 Problem Statement

The interaction between tires and pavement is a critical aspect of vehicle performance and road safety (Anupam et al., 2013; Canudas-de-Wit, 2022; N. Xu et al., 2020; Yu et al., 2017). Traditional experimental methods for analyzing tire–pavement interactions, while accurate, often require substantial investments of time, labor, and resources. FEA offers a more efficient alternative, enabling the simulation of tire–pavement interactions under a wide range of conditions without the extensive costs associated with physical testing. The process involves the creation of a 3D tire model. FEA allows detailed simulation of complex behaviors such as tire deformation, frictional heat generation, and energy dissipation, providing insights that are difficult to achieve through experimental methods alone.

3.2 Theoretical Equations of Vehicle Dynamics

Since our study aims to derive an adjustment factor by utilizing measurable data collected on real roads, we address the need for practicality in tire friction analysis. Accurately measuring vertical force and slip angle under practical, real-world conditions poses challenges. Typical vehicles in daily driving do not provide direct readings for vertical force and slip angle in real-world conditions. To address this limitation, we propose replacing these two parameters with equations that relate them to more readily measurable variables, such as speed, curve radius, and superelevation. This approach ensures that the model remains practical and applicable to real road conditions. Before proceeding, we need to determine which variables will be inputs and which will be outputs, as well as identify the constants to be fixed throughout the simulations. The following Table 3.1 shows the summary of inputs for FEA, the required inputs for the adjustment factor, and the parameter conversion relationships.

TABLE 3.1
Independent Variable and Dependent Variable Parameters Studied Relationships.

Relationship	Section/Equation
$F_x = F_x$ (v, F_z, α, γ, Temp-FN relationship)	Section 3.3
FN(T) = FN (v, F_z, α, γ)	Section 3.4.1
$F_z = F_z$ (v, γ, R)	Section 3.2.1
α = α (m, v, R, γ)	Section 3.2.2
$F_x = F_x$ (v, γ, R, Temp-FN relationship)	Section 3.4

3.2.1 Parameter Conversion on Vertical Load

To achieve parameter conversion on vertical load, a rollover concept, in which a vehicle tips over onto its side or roof, is utilized. This typically occurs when a vehicle's center of gravity shifts excessively during a sharp turn, sudden maneuver, or impact, causing it to lose stability and flip over. The rollover force is typically defined by the difference in vertical (normal) tire loads between the left and right sides of the vehicle (B. Li & Bei, 2019). However, since the forces on the left inner (F_{zi}) and right outer (F_{zo}) tires are difficult to measure directly, the rollover force is estimated to use roll dynamic models (Rajamani, 2012).

The slope of the road is assumed to be zero. This assumption enables the system to achieve a static state, as shown in Figure 3.1 By taking moments of the contact point of the inner wheel,

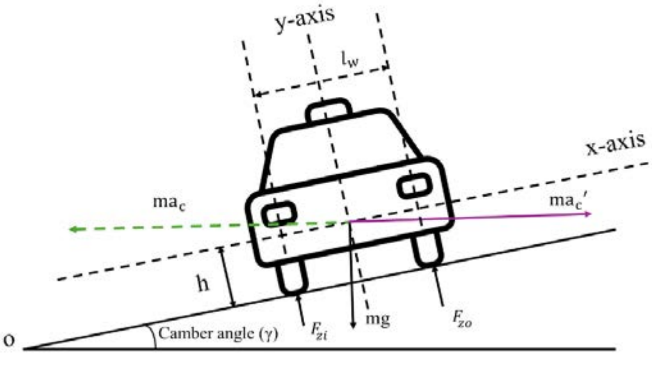

Figure 3.1 Schematic Drawing of Roll Moment Stability During Steady-State Cornering at a Camber Angle.

the moment balance can be calculated. In these models, a_c represents the vehicle's lateral acceleration, with F_{zi} and F_{zo} denoting the support loads on the left (inner) and right (outer) tires, respectively (Rajamani, 2012). Based on the actual special testing vehicle only has two wheels, now the expression becomes:

The moment equilibrium:

$$ma_c h + F_{zo} l_w - mg\frac{l_w}{2} = 0 \qquad \text{Equation 3.1}$$

The force equilibrium on the vertical axis is:

$$\sum Force = F_{zi} + F_{zo} = mg \qquad \text{Equation 3.2}$$

Thus, the forces on the inner and outer tire wheels can be written as:

$$F_{zi} = \frac{mg}{2} + \frac{ma_c h}{l_w} \qquad \text{Equation 3.3}$$

$$F_{zo} = \frac{mg}{2} - \frac{ma_c h}{l_w} \qquad \text{Equation 3.4}$$

$$a_c = \frac{V^2}{R} \qquad \text{Equation 3.5}$$

where a_c represents lateral or centripetal acceleration; l_w stands for the track width (distance between the wheels); h represents the height of the vehicle's center of gravity; V is the vehicle speed; m is the mass of the vehicle. Since the equations in the references are based on a 2D plot, the actual vehicle in 3D should have dual wheels in the lateral direction. m is the vehicle's mass. F_{zi} and F_{zo} denote the support loads on the left (inner) and right (outer) tires, respectively.

According to the ASTM (2015a) Standard Specification for Standard Smooth Tire for Pavement Skid-Resistance Tests (E524) each tire supports approximately 1085 lb, which means the mass of the special testing vehicle is about 984.3 kg. Other than the weight transfer due to the rolling moment and stability when a car is positioned on a slope, the partial lateral force and partial gravity force oppose the centripetal force. This dynamic requires assuming an opposing partial centripetal force acting on the vehicle to counterbalance the tipping force (Peng et al., 2024). The new balance can be written as:

$$F_{zi} = \frac{mg}{2}\cos(\gamma) + \frac{m\left(\frac{V^2}{R}\right)}{2}sin(\gamma) + \frac{m\left(\frac{V^2}{R}\right)h}{l_w}\cos(\gamma) - \frac{mgh}{l_w}\sin(\gamma)$$

Equation 3.6

$$F_{zo} = \frac{mg}{2}\cos(\gamma) + \frac{m\left(\frac{V^2}{R}\right)}{2}sin(\gamma) - \frac{m\left(\frac{V^2}{R}\right)h}{l_w}\cos(\gamma) + \frac{mgh}{l_w}\sin(\gamma)$$

Equation 3.7

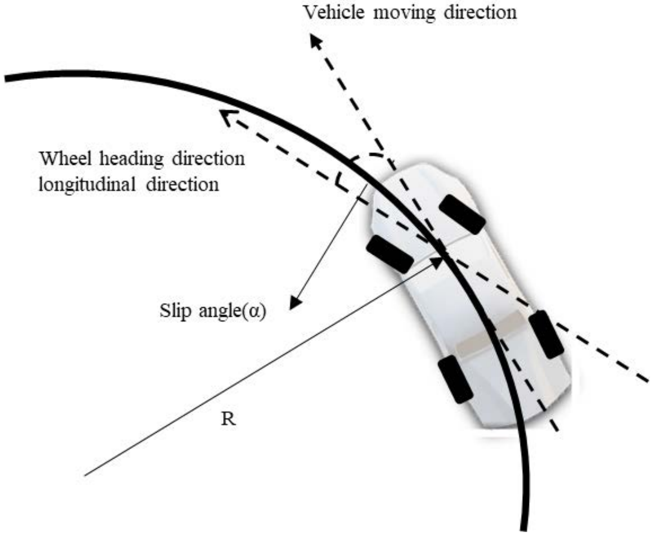

Figure 3.2 Schematic Drawing for Vehicle's Slip Angle Model.

3.2.2 Parameter Conversion on Slip Angle

This section describes the relationship between slip angle and curve radius. We will use a "bicycle model" as a dynamic model to determine the relationship between the slip angle and curve radius. The bicycle model is a simplification of a vehicle's dynamics where the front and rear wheels on each side are combined into a single front and rear wheel. This model captures the essential lateral dynamics of a vehicle with two degrees of freedom: lateral velocity (side-to-side movement) and yaw rate (rotation around the vehicle's vertical axis; Belrzaeg et al., 2021; Rajamani, 2012). Figure 3.2 shows the schematic drawing for the vehicle model with a slip angle.

A steady-state slip angle can be expressed as follows:

$$\alpha = \frac{l_r}{R} - \frac{l_f}{2C_{\alpha r}\left(l_f + l_r\right)}\frac{mV^2}{R} \qquad \text{Equation 3.8}$$

where α is the total slip angle of the vehicle, ℓ_f is the distance from the vehicle's front axle to the center of mass (front overhang length, ℓ_r is the distance from the vehicle's rear axle to the center of mass (rear overhang length; $C_{\alpha r}$ is the cornering stiffness of the rear axle tires (reflecting the tire's ability to generate lateral force); m is the mass of the vehicle; V is the speed of the vehicle, and R is the curve radius.

3.3 FEA Tire Friction Model Setup

This section introduces the setup of developing a thermomechanical FEA model to simulate tire–pavement friction interactions during tire full brake. The model, implemented in Abaqus software (Dassault Systèmes, 2023), captures the effects of temperature, vertical load, slip angle, and other factors on the frictional performance of tires. The FEA approach allowed for a detailed examination of the friction forces under simulated conditions, providing insights into tire behavior on various

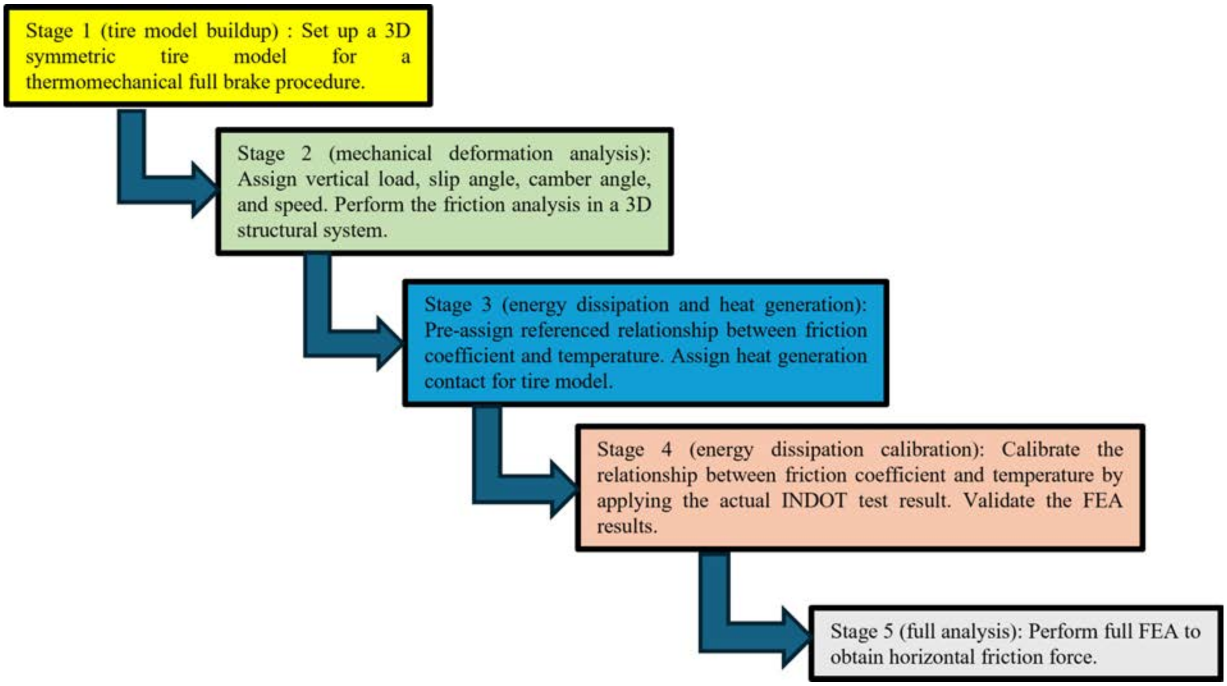

Figure 3.3 Workflow of the Tire–Pavement Thermomechanical Friction Simulation.

pavement surfaces. Using Abaqus for complex 3D modeling, we can predict real-world tire friction conditions by altering road geometry or pavement designs (Z. Li et al., 2023). Our simulation utilizes a thermomechanical 3D full brake procedure, where energy dissipation primarily results from frictional heat generation. Anupam et al. (2014) and Srirangam et al. (2012) have performed friction performance studies by using the same method as well.

Various steps, including mechanical deformation analysis, energy dissipation analysis, and temperature-friction coefficient calibration are systematically performed to examine the tire friction force on the tire. The workflow for thermomechanical tire simulation in Abaqus is illustrated in Figure 3.3, showing the sequential steps as a comprehensive analysis.

In Stage 1, the simulation model step is selected to be "Coupled with a temperature-displacement analysis," utilizing a coupled temperature-displacement mesh element. Similar to the simulation study by Wang et al. (2014), the road is modeled as a nondeformable flat surface to enhance computational efficiency and stability. The dimensions of the simulating tire are as follows: tread width of 5.85 in., tire outer diameter of 27.68 in., and cross-section width of 8.35 in. These tire dimensions match the experimental tire dimension according to test standard E524 (ASTM, 2015a). Tire size and type can influence contact area, pressure distribution, and slip behavior, although the impact is moderate. Both the experimental tests and the FEA are conducted using the same tire size specified in ASTM E524, using the same tire dimension to ensure consistency and more reliable results. Figure 3.4 illustrates the assembly of components constituting the 3D simulation tire, tread, belt, carcass, and bead. Abaqus 3D model forms the foundation for subsequent analyses, which contains the essential elements influencing tire mechanical deformation behavior.

The material properties of different tire components, including the tread, belt, carcass, and bead have been assigned in the FEA, as shown in Table 3.2. These material properties are referenced from previous research studies, including Srirangam et al. (2012), Tönük and Ünlüsoy (2001), and Abdelkarim et al. (2024).

3.3.1 FE Mechanical Deformation Model

Following the establishment of the 3D tire model, Stage 2 involves vertical load assignment and inflation analysis within the 3D tire structural system. For the 3D FEA tire model, vertical force and inter-tire pressure are predefined before the full tire brake analysis (Zhang et al., 2023). The vertical force of 1,085 lb has been established as the standard loading condition in tire friction testing. FEA is assigned the overall body load on the tire bead and maintains a consistent internal tire pressure of 0.165 MPa (ASTM, 2015a). Figure 3.5 visually demonstrates the application of vertical load and internal pressure distribution in the cross-section. The rib tire model in this section is adjusted to achieve a smooth tire profile in alignment with the specifications set by INDOT. To optimize computational resources for the FEA, the simulation concluded with a total of 37,390 4-node, linear, thermally coupled, tetrahedral solid element (C3D4T), with a denser mesh in the contact area with the pavement. A static thermal coupled temperature-displacement is set to analyze the overall horizontal force and temperature variation. Surface-to-surface interaction with "Hard Contact" of "Finite Sliding" contact property is applied between the tire

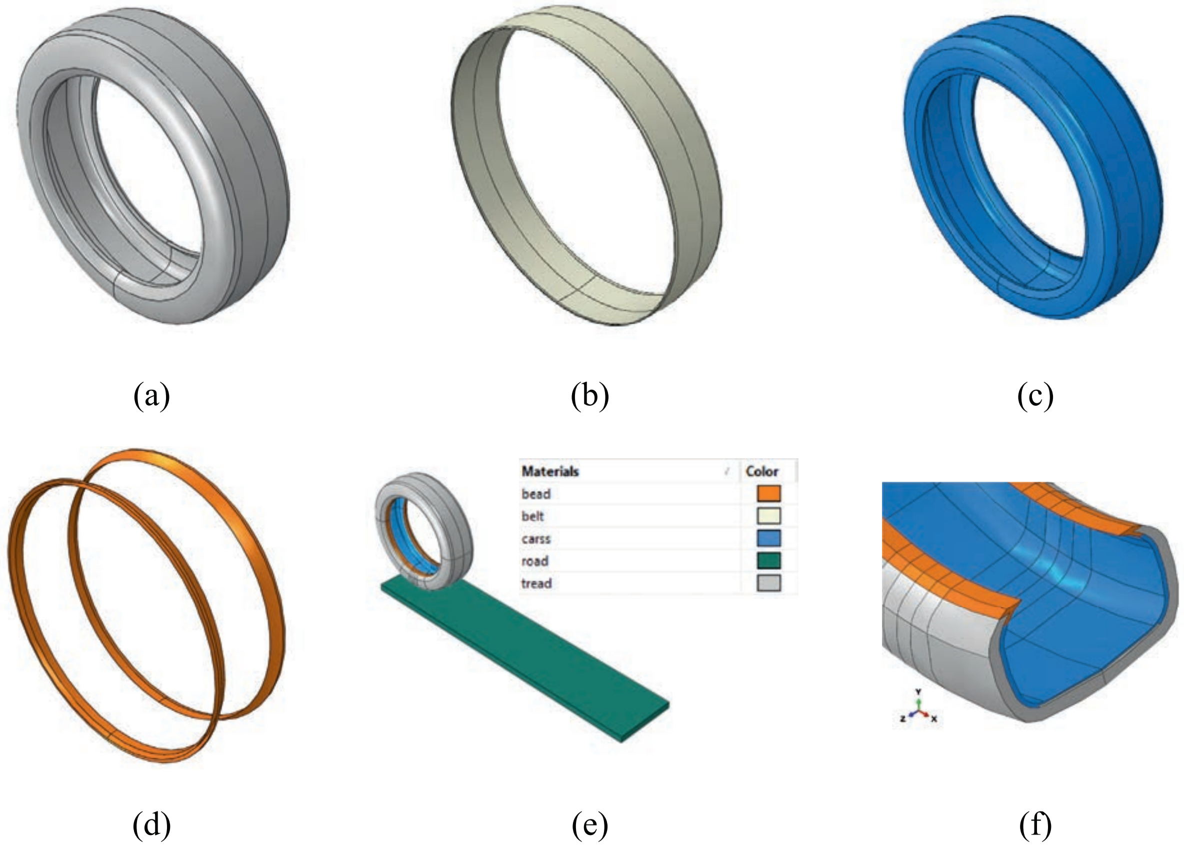

(a) (b) (c)

(d) (e) (f)

Figure 3.4 Essential Tire Components for 3D Tire Model. (a) Tread; (b) Belt; (c) Carcass; (d) Bead; (e) Full Brake Process for the Tire on the Pavement; (f) Cross-Section of Tire Component.

TABLE 3.2
Material Properties for Tire Components.

Tire Section	Type of Material	Young's Modulus (MPa)	Poisson's Ratio	Density (kg/m^3)
Tread	Visco Elastic	10	0.45	1200
Belt	Elastic	3,400	0.3	6500
Carcass	Elastic	9,500	0.3	1200
Bead	Elastic	200,000	0.2	7850

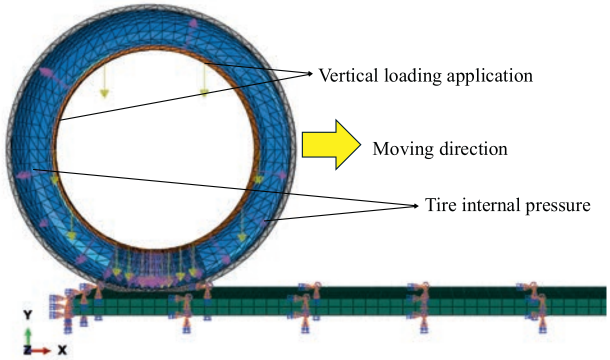

Figure 3.5 Detail of Loading Application on 3D Tire Model.

tread and the pavement (Jagadeesh et al., 2025; Z. Li et al., 2023; Yu et al., 2017).

In the tire simulation model, four main input factors are considered in the mechanical part: the vertical force perpendicular to the road (F_z), slip angle (α), camber angle (γ), and velocity (v). The slip angle is defined as the angle between the wheel heading direction and the moving direction. The output of this model is the horizontal frictional force acting along the direction of the tire's movement. Figure 3.6 illustrates assigned inputs in detail. Additionally, since the model incorporates a thermodynamic component, the sliding distance of the tire impacts the final temperature distribution. To capture these effects, we set the total sliding duration to 0.07 seconds (Narasimha Rao & Krishna Kumar, 2007). During this simulation, the longitudinal

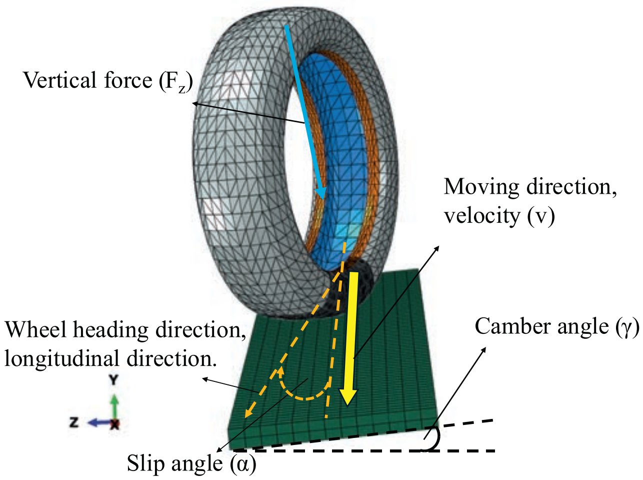

Figure 3.6 Visualization of Details of F_z, α, γ, and v on 3D Tire Model.

horizontal force ("Horizontal Force," F_x) aligned with the wheel heading direction is recorded at the final time step.

The loading process for full brake analysis is conducted by establishing a reference point at the center of the tire to facilitate its connection. Velocity is applied to the tire through the same reference point, directed towards the positive global X-axis. Vertical force is then applied to the bead of the tire, causing vertical deformation by lowering the tire's center of gravity towards the rigid road surface.

3.3.2 FE Thermomechanical Interaction Model

After the mechanical deformation analysis phase, dissipated energy and the rate of heat generation are integrated numerically over the viscoelastic tire rubber model (Anupam et al., 2013). In Stage 3, energy dissipation analysis is conducted by calculating the energy dissipation at each Gauss point across the whole tire model (Anupam et al., 2014). During the full brake stage, a heat flux is generated from the relative speed between the tire and the road. The heat generation ultimately led to a change in the temperature at the contact area between the tire and the road. Several factors can influence this final temperature change. For example, the vertical load and inflation pressure affect this temperature. Specifically, a decrease in the load on the tire or an increase in inflation pressure results in a drop in temperature (Anupam et al., 2014). Conversely, thermal conductivity and specific heat on material properties also affect the rate of heat flux. As the contact temperature varies, the friction coefficient responds differently to the corresponding temperature changes (Anupam et al., 2013; Anupam et al., 2014; Jung et al., 2018; Korunović et al., 2011; Rafei et al., 2018; Srirangam et al., 2012). In the static FEA model, the friction coefficient is originally treated as a fixed value. By contrast, with the introduction of energy dissipation settings, it can be transformed into a temperature-dependent model. By employing this method, we can evaluate the impact of different factors on the friction coefficient. However, a correlation between temperature and FN must be predefined in FEA. Since this study lacks an established relationship between friction and tire temperature, we utilize a reference correlation based on previous research findings to incorporate it into Abaqus. Then we calibrate the relationship based on the previous INDOT experimental results on different test conditions.

3.3.3 Machine Learning Algorithms in Friction Adjustment Factor

3.3.3.1 Friction Adjustment Factor Definition. To evaluate the difference in friction performance between curved and straight road conditions, we define a parameter: "friction adjustment factor," or FAF. The FAF represents the ratio of the friction performance under curved road conditions (with superelevation, slip angle and different vertical forces) to the friction performance observed under straight leveling road conditions, as illustrated in Equation 3.9.

$$\text{Friction Adjustment Factor}_v = \frac{FN_{v,\text{curve}}}{FN_{v,\text{straight}}} \qquad \text{Equation 3.9}$$

where $FN_{v,\text{curve}}$ represents the measured FN on a curved road segment influenced by factors such as curve radius, superelevation, and slip angle at specific speeds (e.g., 30, 40, or 50 mph).

$FN_{v,\text{straight}}$ is the baseline FN measured on a straight, level road segment under identical speed conditions without the influence of curves, superelevation, or slip angle.

By comparing $FN_{v,\text{curve}}$ and $FN_{v,\text{straight}}$, the FAF highlights the impact of geometric road features and driving dynamics on tire–road friction. This comparison provides an understanding of how curved and straight road variables affect vehicle handling and safety under real-world conditions. For example, at 40 mph, if the measured FN on a straight road is 0.50 and the FAF is 0.70, the estimated FN on a curved road can be calculated as 0.50 × 0.70 = 0.35. This shows a 30% reduction in friction due to the effects of curve geometry and lateral dynamics. Once the straight-line FN is known, the curved-road friction can be directly estimated using the FAF.

3.3.3.2 Machine Learning Algorithms. To expand the dataset and enhance its comprehensiveness, we used ML to generate additional entries, resulting in finer input values across these parameters. The expanded dataset in FEA now includes nine speeds (30 mph, 32.5 mph, 35 mph, 37.5 mph, 40 mph, 42.5 mph, 45 mph, 47.5 mph, and 50 mph), a broader set of 12 curve radii (150 ft, 300 ft, 450 ft, 600 ft, 750 ft, 800 ft, 900 ft, 1,050 ft, 1,150 ft, 1,200 ft, 1,350 ft, and 1,500 ft), and 11 superelevation rates (0, 0.01, 0.02, 0.03, 0.04, 0.05, 0.06, 0.07, 0.08, 0.09, and 0.10). This expansion results in a total of 1,188 unique configurations on curved roads in the dataset. Additionally, by including data for both the inner and outer tires under each configuration, we double the dataset to encompass 2,376 cases in total, allowing for a comprehensive analysis of conditions across both sides of the tire on curved roads.

In this section, we developed a predictive model to estimate horizontal force values using multiple ML, including a multilayer perceptron neural network (MLP), random forest, gradient boosting, and Gaussian process regression (GPR). GPR is a nonparametric, Bayesian approach to regression in ML. Unlike traditional parametric models that assume a specific form for the underlying function, GPR defines a distribution over possible functions that fit the observed data, allowing for flexible modeling of complex relationships (MathWorks, n.d.; sci-kitlearn, n.d.; Shields, 2021). Gradient boosting is a ML method that constructs a predictive model by sequentially combining multiple weak learners, typically decision trees. Each new model aims to correct the errors made by the combination of all previous models, effectively reducing the overall prediction error (Badirli, et al., 2020; Natekin & Knoll, 2013). Gradient boosting can handle different types of data and loss functions, making it suitable for both regression and categorization. It fits a new decision tree to the residuals. This decision tree focuses on capturing the patterns in the residuals, effectively addressing the error. The use of decision trees as base learners allows for better interpretability of the model's structure (Breiman, 2001; Cutler et al., 2012; Friedman, 2001). Random forests offer more interpretability and can be considered "grey box" models. Random forests allow for easier feature importance tracking because individual decision trees provide interpretable paths, whereas neural networks lack this transparency (Harris & Grzes, 2019).

We selected specific variables, speed, slip angle, vertical forces, and camber angle, as input features, with the FEA horizontal force as the output. The data are split into a 75% training set and a 25% testing set (validation set). Each model is trained on the 75% training set, and R^2 and MSE are calculated on the testing set to evaluate performance (Hansen et al., 2019; Nadkarni et al., 2023). Predictions are then generated on a separate test set, with the same scaling applied for consistency. Additionally, we visualized each model's performance by calculating the residual error (%).

$$\text{Residual error}\left(\%\right)=\frac{\text{Predictable value}-\text{Ture value}}{\text{Ture value}}\times 100\%$$

Equation 3.10

3.4 Results and Discussion

In this section, the results and discussion are presented to analyze key findings.

3.4.1 Calibration of FEA

The calibration of the FEA temperature function for the 3D tire–pavement model is conducted by comparing FEA results with field testing results on highway S.R. 26, S.R. 47, S.R. 75, INDOT track, and the Purdue Airport roadways, considering both straight and curved roads. The input parameters for the FEA model include the vertical force (F_z), slip angle (α), camber angle (γ), velocity (v), and the relationship between FN and temperature, while the output calculated by the FEA model is the F_x.

3.4.1.1 FN-Temperature Relationship Calibration. The calibration process for the friction coefficient-temperature relationship in Abaqus involved iterative steps to ensure simulation accuracy. A reference relationship from Oliver et al. (1989) is predefined in the FEA model, and simulations are run for specific road segments (e.g., S.R. 47 and S.R. 75) under conditions similar to INDOT experiments. The results are compared with experimental data, and discrepancies reveal inaccuracies in the initial relationship. Adjustments are made to the friction–temperature relationship, and simulations are rerun to reduce errors. This iterative process of modifying the relationship continued until the calibrated results aligned within an acceptable error range. Figure 3.7a shows the iterative calibration process used to refine the FN-temperature relationship for FEA simulations. Figure 3.7b illustrates the results of the friction coefficient against tire temperature from other research and a calibrated relationship for the INDOT test on S.R. 47 and S.R. 75 as one example (Oliver et al., 1989).

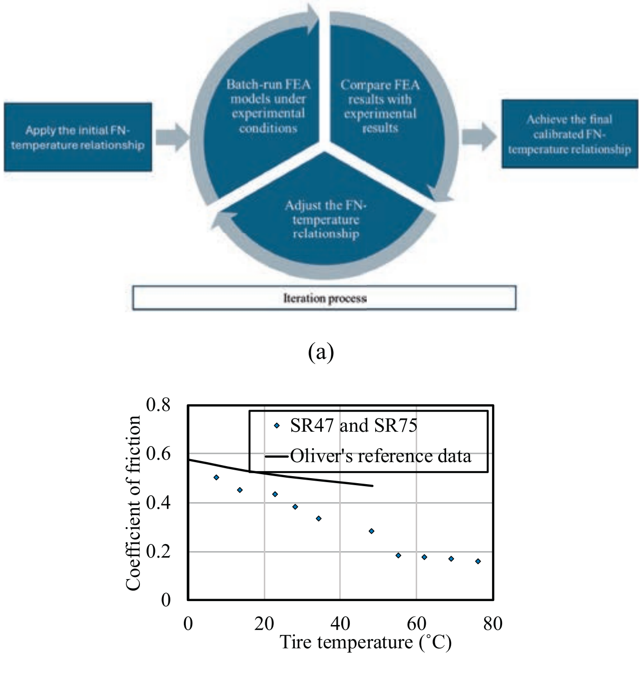

(a)

(b)

Figure 3.7 (a) Calibration Process for FN-Temperature Relationship in FEA Models, (b) The Plot of Friction Coefficient Against Tire Temperature From Reference and After Calibration in S.R. 47 and S.R. 75 INDOT Test (Oliver et al., 1989).

3.4.1.2 Straight Road Analysis. Straight road tire friction testing is conducted on the INDOT friction test track, the Purdue Airport, and S.R. 26, covering three distinct pavement surfaces: bituminous, tined concrete, and slick concrete on the INDOT track. Given that most of the S.R. 26 tests are conducted on straight roads, with some on curved roads, we decided to include all S.R. 26 field test results in this section to compare the results. The relationships between the FN and temperature are finally calibrated accordingly, as shown in Figure 3.8, based on the different road conditions.

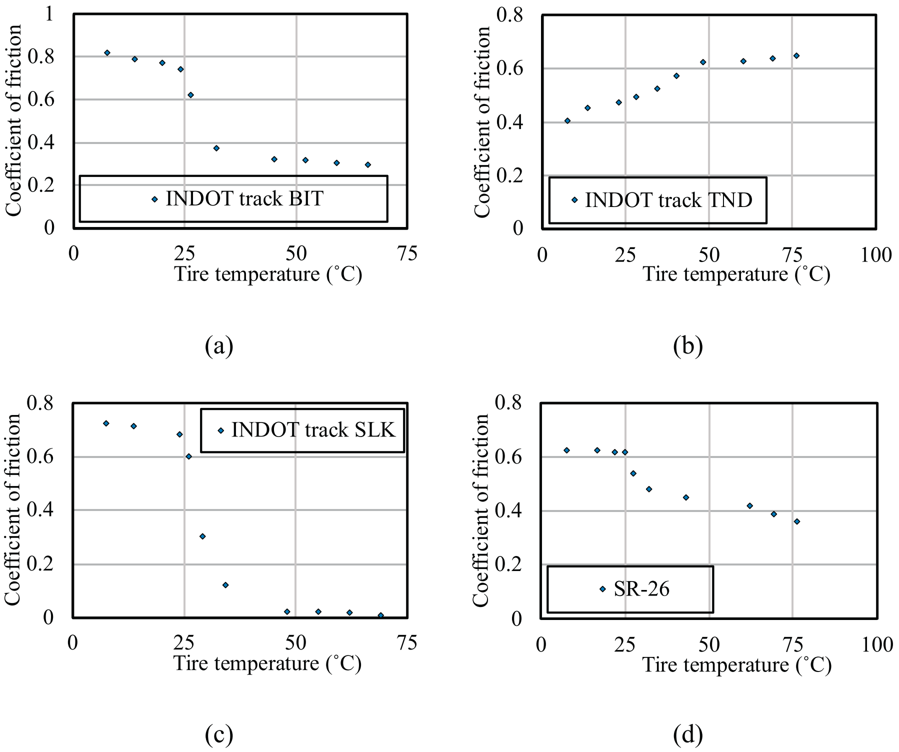

Figure 3.8 The Plot of Friction Coefficient Against Tire Temperature on (a) INDOT Track Bituminous (BIT) Surface; (b) INDOT Track Tined Concrete (TND) Surface; (c) INDOT Track Slick Concrete (SLK) Surface; (d) S.R. 26.

After calibrating the friction coefficient-temperature relationship, one exception is observed: the friction coefficient increases when tire temperature rises on INDOT tined. It is an inverse relationship compared to other field tests. As a result, an increase in tire speed results in a higher horizontal force, as matched in the INDOT track-tined concrete surface field test result. The tined surface may have had different groove depths or patterns, leading to more tire–groove engagement at higher temperatures. This effect is likely site specific, not a general trend.

The 3D tire model successfully validated six results from the INDOT smooth test track and five physical testing results from highway S.R. 26. In total, 11 physical tests were confirmed by the 3D tire FEA results, as outlined in Table 3.3. The disparities between the FEA model and physical testing results range from –5.6–3.33%. For case No. 1 on the bituminous INDOT track, Figure 3.9 displays the temperature and contact pressure distributions at the contact interface between the tire and the road.

3.4.1.3 Curved Road Analysis. In addition to straight road segment analysis, a curved road analysis is conducted to examine changes in friction during turns, incorporating slip angle and camber angle as two crucial variables for understanding tire behavior under different turning conditions. This

TABLE 3.3
FEA Calibration With Field Testing on INDOT Friction Test Track (05/2023) and S.R. 26 (05/2023).

No.	Surface/Road	Road	Speed (mph)	Vertical Force (lb)	Horizontal Force (lb)	Slip angle (degrees)	Camber	FEA Horizontal Force (lb)	Difference (%)
1	Bituminous	INDOT track	29.75	1010	505	0	0	496.2	–1.75
2	Bituminous		15.24	984	703	0	0	670.0	–4.70
3	Tined concrete		29.59	977	643	0	0	643.2	0.03
4	Tined concrete		14.51	1002	579	0	0	570.0	–1.61
5	Slick concrete		29.60	1063	232	0	0	240.6	3.69
6	Slick concrete		15.29	984	550	0	0	681.1	–2.71
7	Straight/Curved Road	S.R. 26	30.11	971	585	0	0	554.0	–5.60
8			14.87	964	611	0	0	627.2	2.59
9			29.69	989	513	0	0	516.2	0.62
10			15.08	958	549	1.57	0.077	567.9	3.33
11			15.08	958	632	0.00	0.000	623.4	–1.38

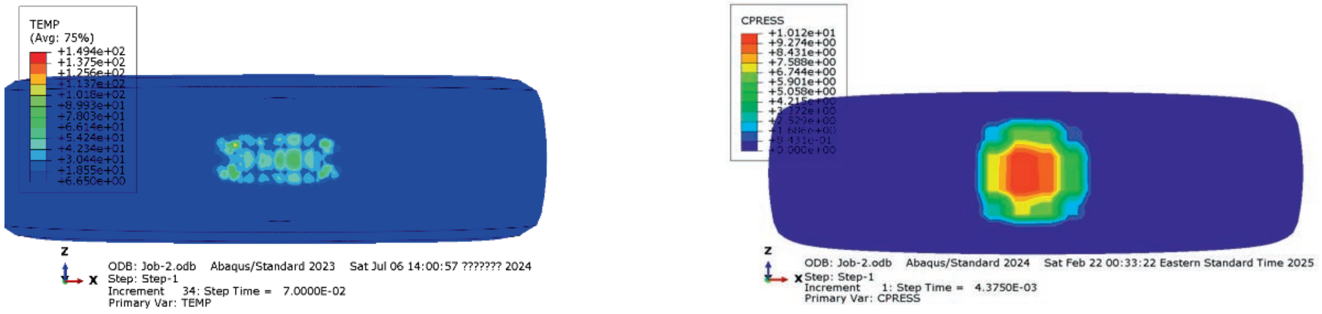

(a) (b)

Figure 3.9 Straight Road FEA No. 1 Results on Bituminous INDOT Friction Test Track: (a) Temperature Distribution and (b) Contact Pressure.

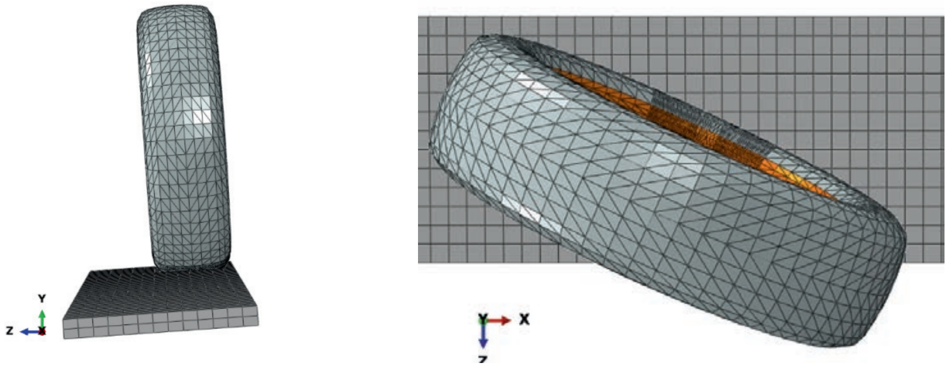

(a) (b)

Figure 3.10 (a) Front View of 3D Tire With Camber; (b) Top View of 3D Tire With Slip Angle.

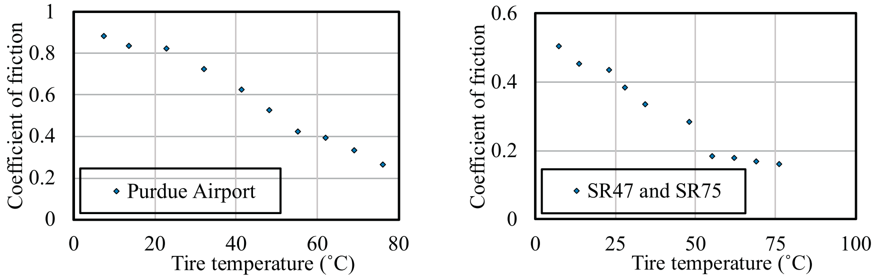

(a) (b)

Figure 3.11 The Plot of Friction Coefficient Against Tire Temperature on (a) the Purdue Airport; (b) S.R. 47 and S.R. 75.

includes four key elements on FEA setup: (1) the incorporation of slip angle; (2) the camber angle set on roads; (3) the application of the appropriate vehicle load acting on the tire; and (4) the sliding speed with assigned slip angle direction. Figure 3.10 illustrates the 3D FEA model for the tire with the slip angle and camber angle, respectively. Similarly, in the curved road simulation, the relationships between FN and temperature are also calibrated accordingly, as shown in Figure 3.11.

Field friction measurements were conducted on curved runways at Purdue University Airport in April and October 2023, and S.R. 75 and S.R. 47 in May 2024. The test results are incorporated into the simulation model to calibrate the curved FEA tire–pavement friction model. A total of 20 field testing results are compared, with a speed range of 15.2–40.69 mph, a slip angle range of 0–8.3 degrees, and a superelevation range of 0–11%. The comparison results are presented in Table 3.4.

TABLE 3.4
FEA Calibration With Field Testing on the Purdue Airport (04/2023 and 10/2023) and S.R. 75 and S.R. 47 (05/2024).

No.	Road	Speed (mph)	Vertical Force (lb)	Horizontal Force (lb)	Slip angle (degrees)	Camber	FEA Horizontal Force (lb)	Difference (%)
1	Purdue Airport	15.2	895	752	5.7	0	757.6	0.75
2		25.2	787	569	3.3	0	630.6	10.83
3		38.9	1328	821	5.8	0	852.5	3.84
4		25.17	838	661	5.54	0	658.7	–0.34
5		20.49	866	717	6.32	0	698.1	–2.64
6		15.65	888	776	7.22	0	757.0	–2.45
7		39.89	941	704	0	0	699.4	–0.65
8		25.53	932	788	0	0	774.7	–1.68
9	S.R. 47	39.8	1025	392	5.61	0.09	398.6	1.7
10		40.27	1152	440	4.77	0.07	464.6	5.6
11		38.96	1161	429	6.41	0.07	466.9	8.8
12		38.8	799	319	6.27	0.10	331.4	3.9
13		40.69	1087	399	3.88	0.03	455.4	14.1
14		40.63	1028	477	3.64	0.03	440.7	–7.6
15		39.59	1024	472	3.24	0.02	437.9	–7.2
16	S.R. 75	29.96	1034	456	7.45	0.09	431.0	–5.5
17		30.49	1026	478	7.04	0.09	428.5	–10.3
18		29.7	1067	476	7.53	0.11	436.0	–8.4
19		29.91	1044	491	8.01	0.11	431.2	–12.2
20		30.49	1021	488	6.96	0.09	422.1	–13.5

The differences between the field test results and FEA results range from –2.64–10.83% at the Purdue Airport. In contrast, at S.R. 47 and S.R. 75, the differences range of –13.5–14.1% indicates a misalignment between the FEA predictions and the physical testing data. S.R. 47 and S.R. 75 exhibit a wider range of camber and slip angles compared to S.R. 26, which likely contributed to the larger differences observed. The uncertainty of the slip angle may cause this discrepancy in the physical tests, and the topic of slip angle will be discussed in the next sensitivity analysis section. Overall, the FEA demonstrates the thermal-mechanical model's capability to provide a range of horizontal force results caused by different factors. It shows a reasonable deviation from the field-testing data. Figure 3.12 presents the FEA temperature and contact pressure distributions at the contact interface between the tire and the road and footprint analysis results in curved road analysis.

3.4.2 Validation of FEA

In this section and its subsections, the main results from FEA and experimental fields are presented and discussed.

3.4.3 Experimental Result Analysis

3.4.3.1 SCRIM Experimental Data. The relationship FN = f(CurveRadius) from SCRIM results is shown in Figure 3.13. The R^2 values are compared with those from the polynomial regression function. Table 3.5 presents the corresponding ML results.

For left turns, the expected relationship is a decreasing trend in FN40 with increasing CurveRadius, as larger radii reduce friction demand due to decreased lateral force requirements. However, the polynomial regression equation suggests an inconsistent trend, with FN40 slightly increasing in certain regions. The scatterplot and fitted curves highlight fluctuations in FN40, particularly over longer test routes. A major factor contributing to these inconsistencies is likely the variation in pavement conditions across the extended test route, causing the FN40 values to fluctuate instead of following the anticipated trend. It is recommended to either segment the test route into smaller sections with uniform pavement or account for pavement variability during analysis to achieve a more accurate trend representation. For right turns, the polynomial equation aligns more closely with the data, showing a mild upward trend in FN40 as CurveRadius increases. This corresponds to the expected physical behavior, as friction demand may slightly increase for smaller radii due to increased vertical force.

Based on the analysis results, it can be concluded that for both left and right turns, the SVR model demonstrates the best performance, achieving a near-perfect fit with $R^2 = 0.996$ for left turns and $R^2 = 0.956$ for right turns. This indicates that SVR effectively captures the nonlinear relationship between FN40 and CurveRadius. In contrast, polynomial regression performs poorly, with R^2 values of 0.204 and 0.123 for left and right turns, respectively. Random forest and gradient boosting models show moderate performance, with random forest slightly outperforming gradient boosting for right turns ($R^2 = 0.501$ versus $R^2 = 0.442$) but exhibiting similar performance for left turns ($R^2 = 0.420$ versus $R^2 = 0.285$).

3.4.4 Sensitivity Study of Impact on Single Variable Analysis for FEA

By focusing on one variable at a time, the FEA study can isolate the specific impact on its results without interference from other factors. This helps in understanding the direct relationship

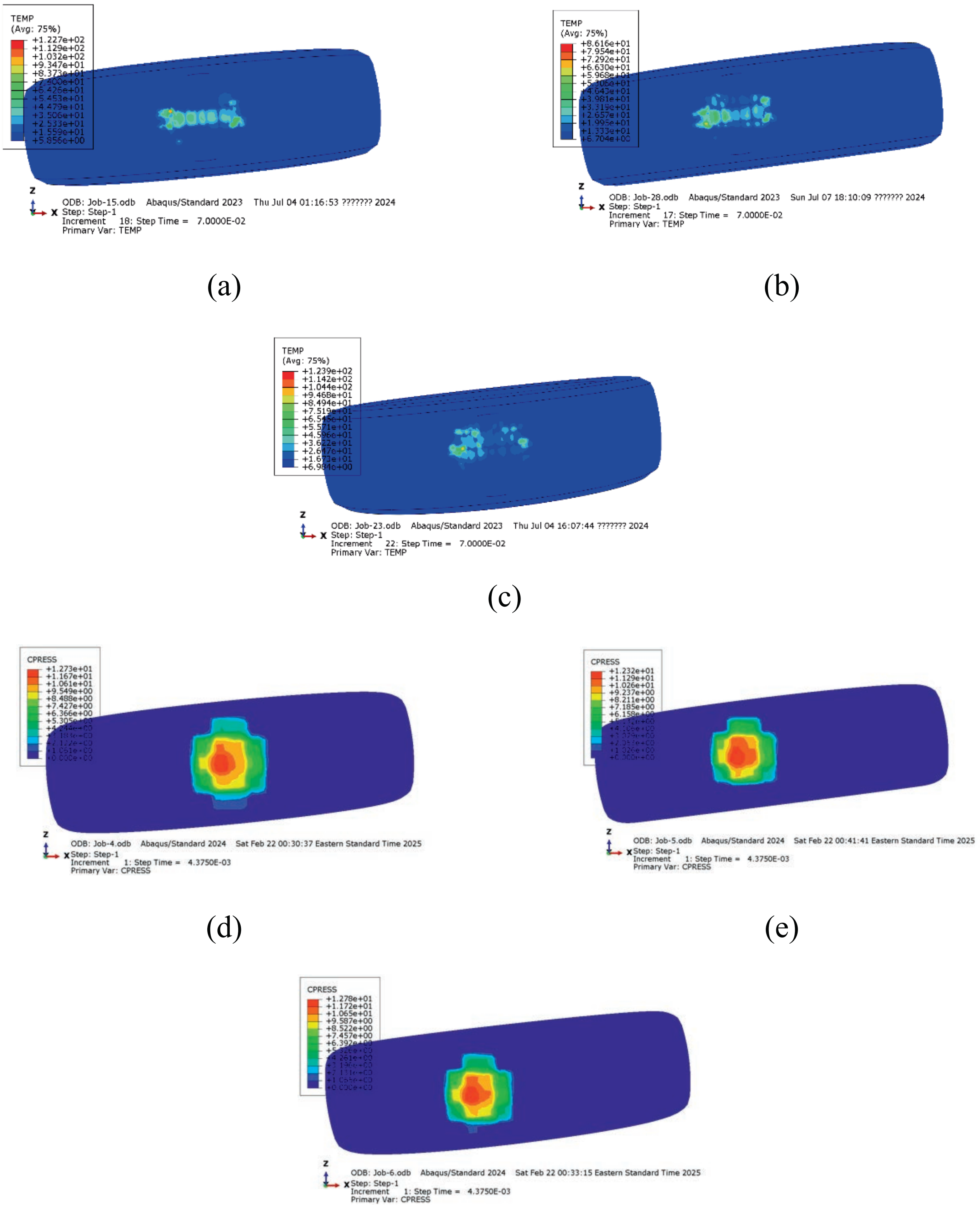

(a) (b)

(c)

(d) (e)

(f)

Figure 3.12 Curved Road FEA Results: (a) and (d) Temperature and Contact Pressure Distribution for No.4 With a Slip Angle of 5.54°. (b) and (e) Temperature Contact Pressure Distribution for No.6 With a Slip Angle of 7.22°. (c) and (f) Temperature Contact Pressure Distribution for No.14 With a Slip Angle of 6.1° and Superelevation of 0.07.

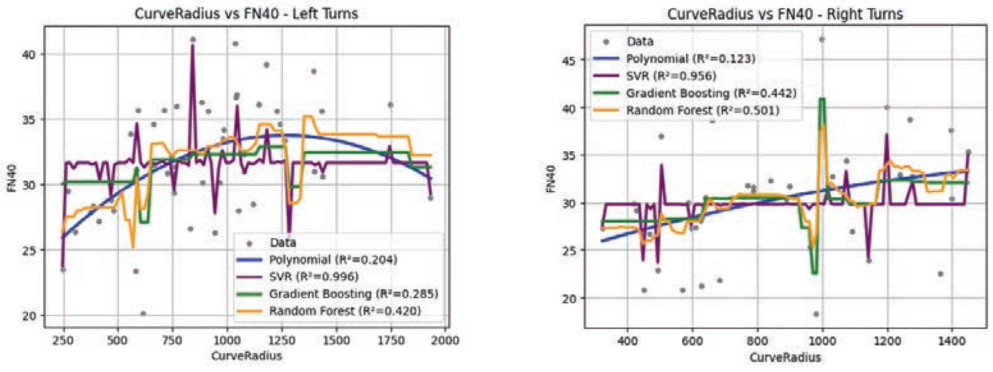

(a) (b)

Figure 3.13 Comparison of FN40 and CurveRadius Trends: (a)Left Turn (Outer Tire) and (b) Right Turn (Inner Tire).

TABLE 3.5
R^2 Values and Polynomial Equations of Different Correlation Methods for Left and Right Turns.

Road Type	Polynomial Equation	Polynomial R^2	SVR R^2	Gradient Boosting R^2	Random Forest R^2
Left turn (outer tire)	FN40 = 21.703 + 0.019 × CurveRadius −0.00001 × CurveRadius^2	0.204	0.996	0.285	0.420
Right turn (inner tire)	FN40 = 22.543 + 0.011 × CurveRadius	0.123	0.956	0.442	0.501

between the variable and the outcome. To understand the impact of a single variable in our experiment, we decided to keep all other input variables in the model constant while only changing one variable at a time. This approach allows us to isolate and observe the effect of altering a single variable through FEA, providing clear insights into how this change influences the overall model behavior. The inputs and results for the single variable analysis are shown in Table 3.6. The graphs in Figure 3.14 include horizontal force versus time plots and scatter plots, which visually illustrate the impact of different parameters on FN using the results from the Table 3.6. The sensitivity analysis reveals that higher speed and vertical force negatively influence

TABLE 3.6
Inputs and Results for Single Variable Analysis FEA.

Study Parameter	Speed (mph)	Vertical Force (lb)	Slip Angle (degrees)	Camber	Horizontal Force (lb)	FN
Speed	10	1000	0	0.00	513	0.513
	20	1000	0	0.00	498	0.498
	30	1000	0	0.00	469	0.469
	40	1000	0	0.00	443	0.443
	50	1000	0	0.00	429	0.429
Vertical force	20	600	0	0.00	307	0.512
	20	1000	0	0.00	498	0.498
	20	1400	0	0.00	655	0.468
	20	1800	0	0.00	784	0.436
	20	2200	0	0.00	886	0.403
Slip angle	20	1000	0	0.00	498	0.498
	20	1000	2.5	0.00	488	0.488
	20	1000	5.0	0.00	490	0.490
	20	1000	7.5	0.00	498	0.498
	20	1000	10	0.00	500	0.500
Camber	20	1000	0	0.00	498	0.498
	20	1000	0	0.025	484	0.484
	20	1000	0	0.05	472	0.472
	20	1000	0	0.075	467	0.467
	20	1000	0	0.1	441	0.441

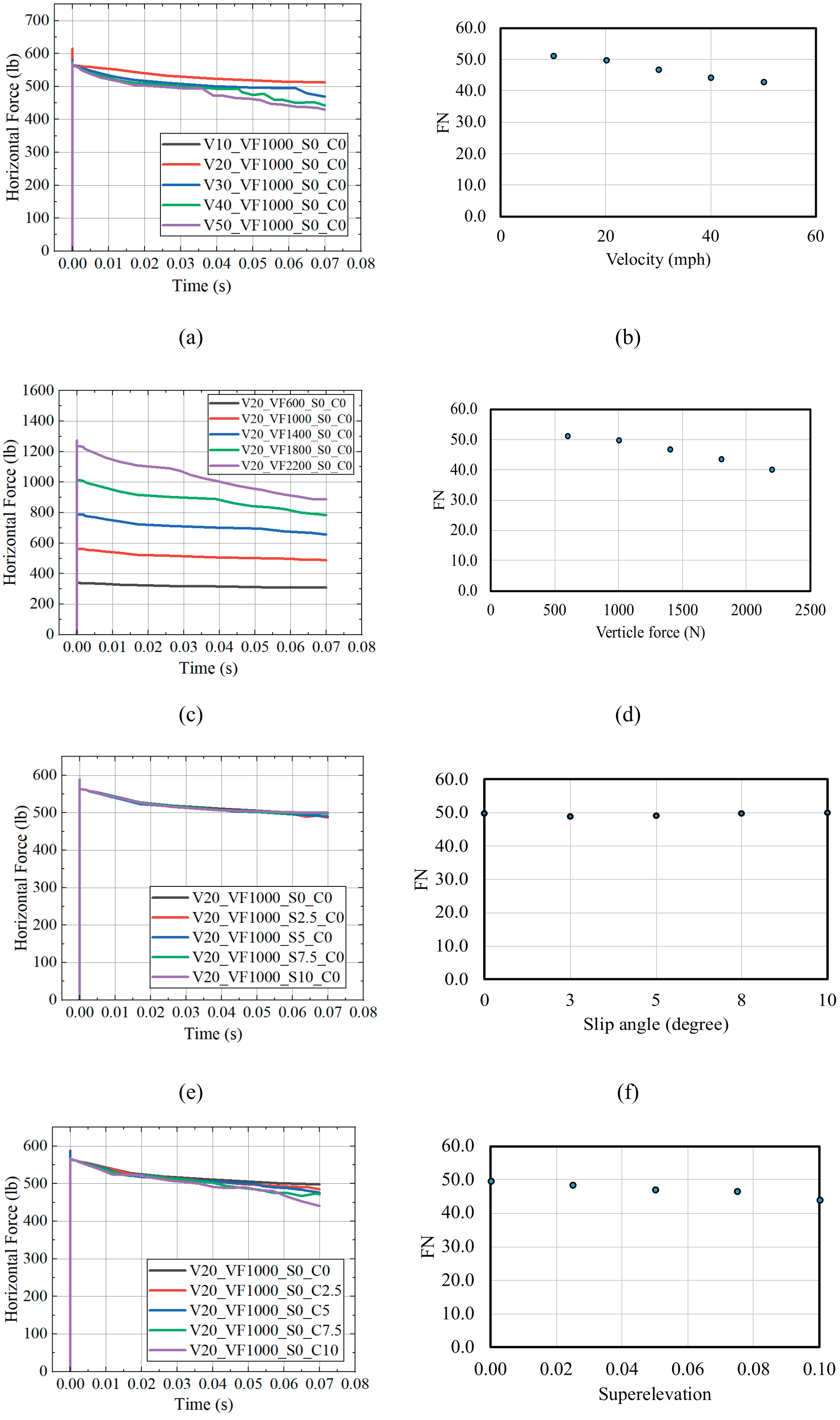

(a)

(b)

(c)

(d)

(e)

(f)

(g)

(h)

Figure 3.14 Horizontal Force and FN Results by Changing Different Parameters on (a) and (b) Velocity; (c) and (d) Slip Angle; (e) and (f) Vertical Force; and (g) and (h) Superelevation.

the frictional performance of tire–pavement interactions (Wang et al., 2014; J. Xu et al. 2023). As speed increases, both the horizontal force and FN steadily decrease, with FN dropping from 0.513 at 10 mph to 0.429 at 50 mph. Similarly, higher vertical forces result in a decline in FN, from 0.512 at 600 lb to 0.403 at 2,200 lb, despite an increase in horizontal force. In contrast, variations in slip angle from 0° to 10° exhibit negligible changes in FN, maintaining a range of 0.498–0.500. Camber, though less impactful than speed or vertical force, shows a gradual reduction in FN as it increases, with FN declining from 0.498 at 0.00 camber to 0.441 at 0.1 camber. These findings highlight the dominant roles of speed and vertical force in influencing tire–pavement friction, while other parameters like slip angle and camber have relatively smaller effects. “V20_VF1000V_S2_C2” represents 20 mph speed, 1,000 lb vertical force, 2° slip angles, and 2% camber angle.

Figure 3.14a and Figure 3.14b show that as velocity increases, the FN decreases. This indicates a negative correlation between velocity and FN, meaning that higher speeds result in lower friction. Figure 3.14c and Figure 3.14d show that an increase in vertical force generates higher horizontal forces but causes a decrease in the FN, indicating a negative correlation. Figure 3.14e and Figure 3.14f illustrate the relationship between the slip angle and FN, where FN initially dips slightly before rising again, suggesting some fluctuation but with an overall minimal impact on FN within the observed range. Overall, an increase in slip angle causes a nonlinear fluctuation in horizontal force Figure 3.14g and Figure 3.14h show that as superelevation increases, horizontal force, and FN decrease, indicating a negative correlation where a greater road superelevation reduces the frictional effectiveness.

The components shown in Figure 3.15 display FEA simulations illustrating the temperature distribution on a tire under varying velocities, vertical forces, slip angles, and camber angles. Figure 3.15a–c show that as the velocity increases from 10 mph to 50 mph, the tire’s temperature rises and the heat spreads more extensively across the surface. Similarly, Figure 3.15d–f illustrate that increasing the vertical force from 600 lb to 2,200 lb results in higher temperatures and a broader heat distribution. These simulations illustrate the significant impact of both velocity and vertical force on the thermal behavior of the tire. The effect of slip angles is shown in Figure 3.15g–i. As the slip angle increases from 0° to 10°, the temperature distribution shifts and becomes more asymmetrical, with higher temperatures observed at greater slip angles. The impact of camber angles is demonstrated in Figure 3.15j–l. As the camber angle increases from 0%

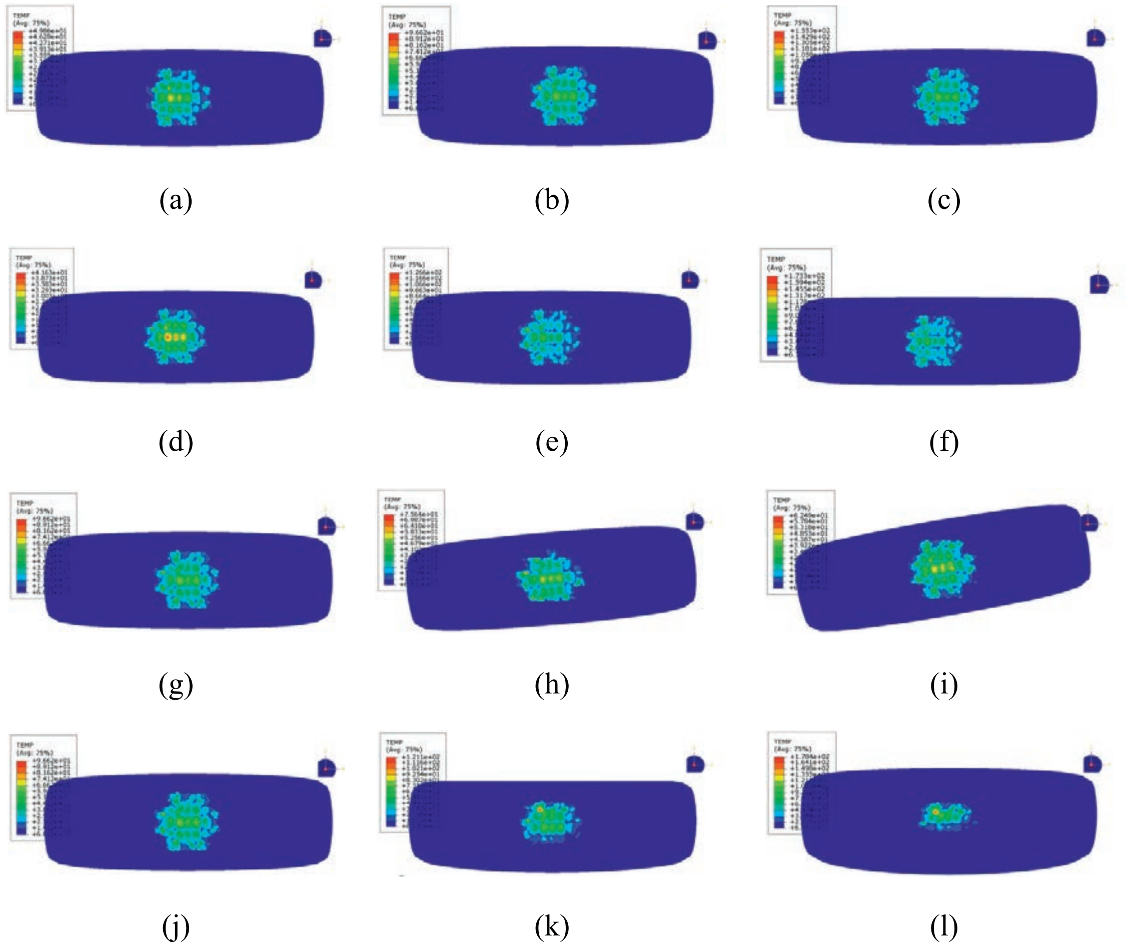

(a) (b) (c)

(d) (e) (f)

(g) (h) (i)

(j) (k) (l)

Figure 3.15 Temperature Distribution on Tire Surface Under Varying Conditions of (a–c) Velocity From 10 to 50 mph; (d–f) F_z From 600 to 2200 lb; (g–i) α From 0° to 10°, and (j–l) γ From 0 to 0.1.

TABLE 3.7
FEA Validation With Field Testing on the Purdue Airport (04/2023 and 10/2023) and S.R. 75 and S.R. 47 (05/2024).

No.	Road	Speed (mph)	Vertical Force (lb)	Horizontal Force (lb)	Slip angle (degrees)	Camber	FEA Horizontal Force (lb)	Difference (%)
1	Airport	20.54	931	816	0	0	810.0	−0.73
2		15.24	925	812	0	0	799.5	−1.54
3	S.R. 47	39.95	993	345	6.55	0.09	395.6	14.7
4		40.06	1024	457	3.61	0.04	425.1	−7.0
5		40.11	1025	482	3.10	0.04	423.5	−12.1
6		30.12	1010	417	4.87	0.09	432.4	3.7
7		29.34	1139	510	6.14	0.07	477.8	6.3
8		30.23	1039	490	7.9	0.09	432.6	−11.7
9	S.R. 75	40.27	1120	478	8.60	0.10	417.1	−12.8
10		40.27	1137	443	7.6	0.10	415.1	−6.3
11		40.06	965	384	8.4	0.09	377.5	−1.7
12		40.37	994	422	7.75	0.09	385.8	−8.6

to 10%, the temperature becomes more concentrated on one side of the tire, indicating an increase in thermal gradient. These simulations emphasize how both slip and camber angles influence the tire's thermal characteristics, with higher camber angles leading to more localized and elevated temperatures.

3.4.5 FEA Validation Results

Following the completion of model calibration, additional data points are selected to validate the straight and curved FEA tire–pavement friction models. This validation process involved 12 field testing results, covering a speed range of 15.24–40.69 mph, a slip angle range of 0–8.6 degrees, and a superelevation range of 0–10%. The validation results, comparing the simulation outputs with the newly selected field data, are presented in Table 3.7.

The validation results show that the FEA horizontal force predictions generally align with the actual test results but exhibit varying accuracy depending on road conditions, slip angles, and camber. For the Purdue Airport data with low slip angles and no camber, the FEA model performed well, with minimal differences of −0.73% and −1.54%. However, at S.R. 47, where slip angles range from 2.59–6.55° and camber values are minimal, discrepancies are more pronounced, with differences from −12.1–14.7%. At S.R. 75, which includes higher slip angles (up to 8.6°) and noticeable camber, the model tends to underestimate horizontal forces, with deviations up to −12.8%.

3.4.6 Data Generation from FEA

This section presents the completed process of creating a dataset using FEA simulations and subsequently expanding it through ML. The dataset, generated by FEA, includes key factors such as v, α, Fmatamata, FN, γ, and the relationship between FN and temperature.

3.4.6.1 Theoretical Result of Vehicle Dynamics. Table 3.8 contains data obtained from actual measurements of LWST, which will be used in the calculations for vertical force and slip angle. Figure 3.16 illustrates the schematic drawing with the dimensions of the special testing vehicle. In the actual testing process, the vehicle is towed by a truck.

It is important to note that the theoretical slip angle formula does not account for the effect of superelevation, despite it being a crucial factor. This became apparent when analyzing the

TABLE 3.8
Vehicle Dynamics Parameters for Theoretical Equation Calculations.

Parameters	Value
m (kg)	984.3
l_w (mm)	1524
h (mm)	864
l_f (mm)	762
l_r (mm)	7310
$C_{\alpha r}$ (N/Rad)	3438

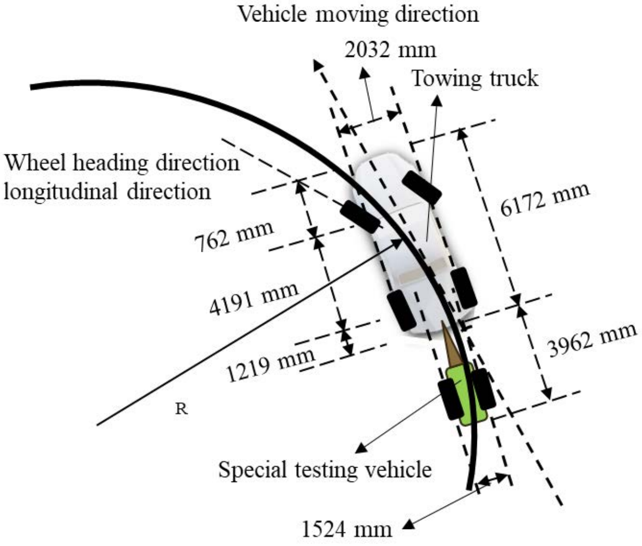

Figure 3.16 Schematic Drawing With Dimensions of the Special Testing Vehicle.

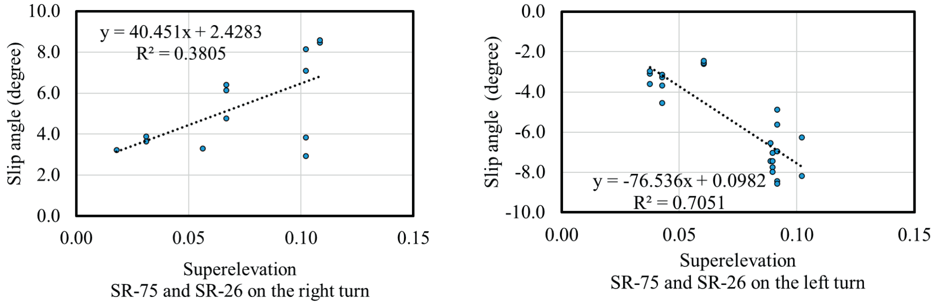

(a) (b)

Figure 3.17 Correlation Between Camber and Slip Angle on S.R. 75 and S.R. 26 for (a) Left Turns and (b) Right Turns.

earlier correlation map, where the camber angle and slip angle values, such as 0.93 on S.R. 26 and 0.65 on S.R. 47, indicated that superelevation plays an important role. Since the theoretical relationship cannot directly incorporate the influence of superelevation, we introduced test data from S.R. 47 and S.R. 75 to develop a regression line. We decided to use the data from S.R. 47 and S.R. 75 because their camber angle ranges cover the broadest range, allowing for a more comprehensive inclusion of all relevant conditions. Since the recorded slip angles for left and right turns have different positive and negative values, we conducted two separate regression lines to account for each direction. This regression is then applied to adjust the theoretical formula, thereby better reflecting the impact of superelevation and improving the overall accuracy of the model. Figure 3.17 illustrates the regression results from S.R. 47 and S.R. 75.

The data for left turns shows a stronger and more reliable relationship between superelevation and slip angle, with a higher R^2 value (0.71), indicating that superelevation is a good predictor for slip angle. The data for right turns shows a much weaker correlation, with a lower R^2 value (0.38). The regression lines from the two sets of data still show some differences in the coefficient factors, indicating that the relationship between superelevation and slip angle varies between right and left turns. After further analysis of the recorded experimental data, we calibrated the results to obtain the most accurate estimates of the actual slip angle. The final regression function below, which reflects the best fit for the experimental data, is used for the final adjustment of the slip angle values.

If camber presents:

$$\alpha\ (degree)_{correlation} = 30\,\gamma + 2; \qquad \text{Equation 3.11}$$

Combined with the previous equation, now becomes:
If camber presents:

$$\alpha\left(degree\right)_{correlation} = 30\times\left(\frac{l_r}{R} - \frac{l_f}{2C_{\alpha r}\left(l_f+l_r\right)}\frac{mV^2}{R}\right)+2;$$

Equation 3.12

If no camber presents:

$$\alpha\ (degree)_{correlation} = \alpha$$

Table 3.9, Table 3.10, and Table 3.11 compare the vertical force and slip angle between experiments and theoretical results

TABLE 3.9
The Theoretical Force and Slip Comparison for Airport.

Road	Speed (mph)	Experiment Fz (lb)	Calculated Vertical Force (lb)	Difference (%)	Experiment Slip Angle (degree)	Calculated Slip Angle (degree)	Differences (%)	Superelevation	Radius Curve (ft)
Airport 2023-10-18	24.3	832	792	4.9	5.79*	5.69	1.6	0	165
	22.7	811	829	2.2	5.17*	5.94	15	0	165
	25.1	845	772	8.6	6.02*	5.56	7.5	0	165
	22.4	826	835	1.1	5.70*	5.98	5	0	165
	25.2	838	770	8.2	5.54*	5.55	0.1	0	165
	25.1	803	772	3.8	5.31*	5.56	4.8	0	165
	20.3	863	880	2	7.35*	6.28	14.5	0	165
	20.4	846	878	3.8	6.86*	6.27	8.6	0	165
	20.5	866	876	1.2	6.32*	6.26	1	0	165
	20.3	848	879	3.7	6.33*	6.28	0.8	0	165
	20.4	859	878	2.3	6.50*	6.27	3.5	0	165
	20.3	840	879	4.7	5.85*	6.28	7.2	0	165
	15.7	882	963	9.2	7.56*	6.84	9.6	0	165
	15.8	882	962	9	7.24*	6.83	5.8	0	165

Note: * Means it is an Outer Tire.

TABLE 3.10
The Theoretical Force and Slip Comparison for S.R. 47.

Road	Speed (mph)	Experiment Fz (lb)	Calculated Vertical Force (lb)	Difference (%)	Experiment Slip Angle (degree)	Calculated Slip Angle (degree)	Differences (%)	Superelevation	Radius Curve (ft)
S.R. 47	39.8	1025	875	14.7	5.61*	5.87	4.6	0.09	382
	40.27	1152	1331	15.5	4.77	4.66	2.4	0.07	422
	38.96	1161	1310	12.8	6.41	5.06	21	0.07	422
	38.8	799	678	15.2	6.27*	10.12	61.2	0.1	219
	40.69	1087	1472	35.4	3.88	4.11	5.9	0.03	326
	40.63	1028	1471	43.1	3.64	4.13	13.5	0.03	326
	39.59	1024	1314	28.3	3.24	3.2	1.3	0.02	519
	39.95	993	955	3.8	6.55*	4.73	27.8	0.09	521
	39.06	1103	1374	24.5	5.03	3.26	35.1	0.01	422
	40.95	987	917	7.1	2.59*	3.76	45	0.06	549
	40.06	1024	1041	1.7	3.61*	2.57	28.8	0.04	1434
	40.11	1025	1041	1.6	3.10*	2.56	17.2	0.04	1434
	30.12	1010	1013	0.3	4.87*	9.51	95.3	0.09	382
	29.34	1139	1177	3.4	6.14	7.62	24.1	0.07	422

Note: * Means it is an Outer Tire.

TABLE 3.11
The Theoretical Force and Slip Comparison for SR - 75.

Road	Speed (mph)	Experiment Fz (lb)	Calculated Vertical Force (lb)	Difference (%)	Experiment Slip Angle (degree)	Calculated Slip Angle (degree)	Differences (%)	Superelevation	Radius Curve (ft)
S.R. 75	29.96	1034	875	14.7	7.45*	6.34	14.9	0.09	655
	30.49	1026	1331	15.5	7.04*	6.24	11.4	0.09	655
	29.7	1067	1310	12.8	7.53	5.76	23.5	0.11	880
	29.91	1044	678	15.2	8.01	5.73	28.5	0.11	880
	30.49	1021	1472	35.4	6.96*	6.19	11	0.09	674
	30.23	1039	1471	43.1	7.94*	6.24	21.5	0.09	674
	40.27	1120	1314	28.3	8.6	4.85	43.6	0.1	533
	40.27	1137	955	3.8	7.63	4.85	36.4	0.1	533
	40.06	965	1374	24.5	8.43*	4.16	50.7	0.09	655
	40.37	994	917	7.1	7.75*	4.08	47.4	0.09	655
	39.17	1123	1041	1.7	8.3	4.04	51.4	0.11	880
	39.22	1083	1041	1.6	8.13	4.03	50.5	0.11	880
	40.21	989	1013	0.3	7.99*	4.09	48.8	0.09	674
	40.21	986	1177	3.4	8.58*	4.09	52.3	0.09	674

Note: * Means it is an Outer Tire.

in the Purdue Airport and S.R. 47. The values marked with an asterisk (*) in the slip angle column indicate a left turn, which tests the inner tire. The difference between previous theoretical values and experimental values is obtained using Equation 3.13.

$$\text{Difference}\,(\%) = \left|\frac{\text{Theoredical value} - \text{Experimental measurement}}{\text{Experimental measurement}}\right| \times 100\%$$

Equation 3.13

Based on the data in both tables, it shows that the vertical force differences between experimental and calculated values remain relatively small across most cases, while the slip angle differences are more pronounced, especially under conditions with higher superelevation. On S.R. 47, vertical force deviations are modest, such as −14.7% at 39.8 mph with 0.09 superelevation and −43.1% at 40.63 mph with 0.03 superelevation. However, slip angle discrepancies are substantial, with a 61.2% difference at 38.8 mph with 0.10 superelevation and 35.1% at 39.06 mph with 0.01 superelevation. Similarly, on S.R. 75, vertical force differences stay minimal, such as 5.3% at 29.96 mph with 0.09 superelevation. In contrast, slip angle deviations are considerably larger, including 50.7% at 40.06 mph with 0.09 superelevation.

This variation is possibly due to the true dynamic conditions. In reality, tire–road interaction is highly nonlinear, particularly when superelevation is involved. The theoretical equations are based on steady-state conditions, which may fail to capture the true dynamics, especially at high speeds and steep superelevation. Additionally, this study involves an articulated vehicle with two jointed vehicle bodies and three axles. Due to differences in the vehicle's structural system, slip angle calculations may deviate from theoretical model predictions.

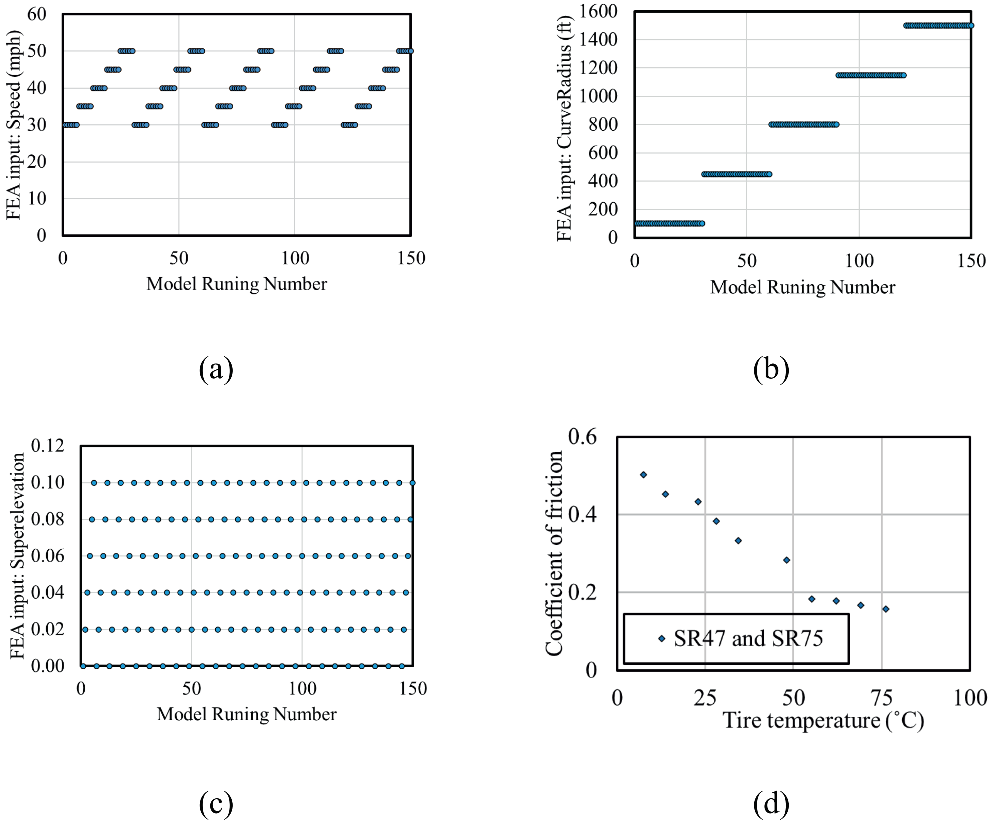

Figure 3.18 The Input Plots of 150 Runs of FEA Inputs for Each Side of the Tire on Curved Roads: (a) Speed; (b) Curve Radius; (c) Superelevation; (d) FN and Temperature Relationship on S.R. 47 and S.R. 75.

3.4.6.2 FEA Batch Running Result. In this section, we account for the variability in the relationship between FN and temperature, which depends on road conditions and the initial temperatures of both the road and tire. To standardize our analysis, we assume that the FN and temperature relationship is consistent with that of S.R. 47 and S.R. 75, where the most representative experimental data on a normal highway is available for calibrating this relationship.

To accurately determine the adjustment factor curves for varying speeds, curve radii, and camber angles within our required range, a comprehensive database is created. This database is designed to simulate the outcomes of different combinations of a practical range of variables, enabling a comparison between the actual FN and longitudinal FN with the corresponding real-world values.

For constructing this database, we selected five sets of speeds (30 mph, 35 mph, 40 mph, 45 mph, and 50 mph), five sets of curve radii (150 ft, 450 ft, 800ft, 1150ft, and 1,500ft, six sets of superelevation (0, 0.02, 0.04, 0.06, 0.08, and 0.10; AASHTO, 2018). Additionally, for straight-line conditions, only five different speeds (30 mph, 35 mph, 40 mph, 45 mph, and 50 mph) are considered, adding another five datasets. This brings the total to 155 datasets. In total, 155 datasets are simulated for each side of the tire, resulting in 310 datasets overall for both sides. Due to the large number of simulations required and the complexity of each model, we have edited the Abaqus Python code to use batch runs for database generation. This approach allows us to control each variable in the simulation process efficiently, ensuring that the extensive modeling tasks are managed systematically.

Figure 3.18 shows the input distributions for velocity, slip angle, and vertical force in the FEA model on curved roads. The FEA inputs consist of a dataset with 150 data points on each side of the tire, evenly distributed across a spectrum of velocity, vertical force, slip angle, and camber values, as these inputs are aligned with the range of required designed curves.

The inputs and results in Appendix D provide inputs such as speed, vertical force, slip angle, camber, and curve radius and outputs like FN and FAF. The FEA FN values for both inner and outer tires generally decrease as speed increases, with higher values at lower speeds and lower values at higher speeds. For a fixed speed, FN remains stable or slightly increases with small slip angles but decreases significantly as slip angle grows, particularly at higher speeds. This behavior shows the sensitivity of FEA FN to both speed and slip angle, with large slip angles and high speeds reducing lateral force effectiveness and stability. For the outer tire, positive vertical forces at lower speeds (30–40 mph) allow for meaningful friction calculations. However, at higher speeds (45–50 mph), vertical forces sometimes become negative, causing the tire to lose contact with the road, invalidating friction force calculations and highlighting the critical role of maintaining sufficient vertical load for stability.

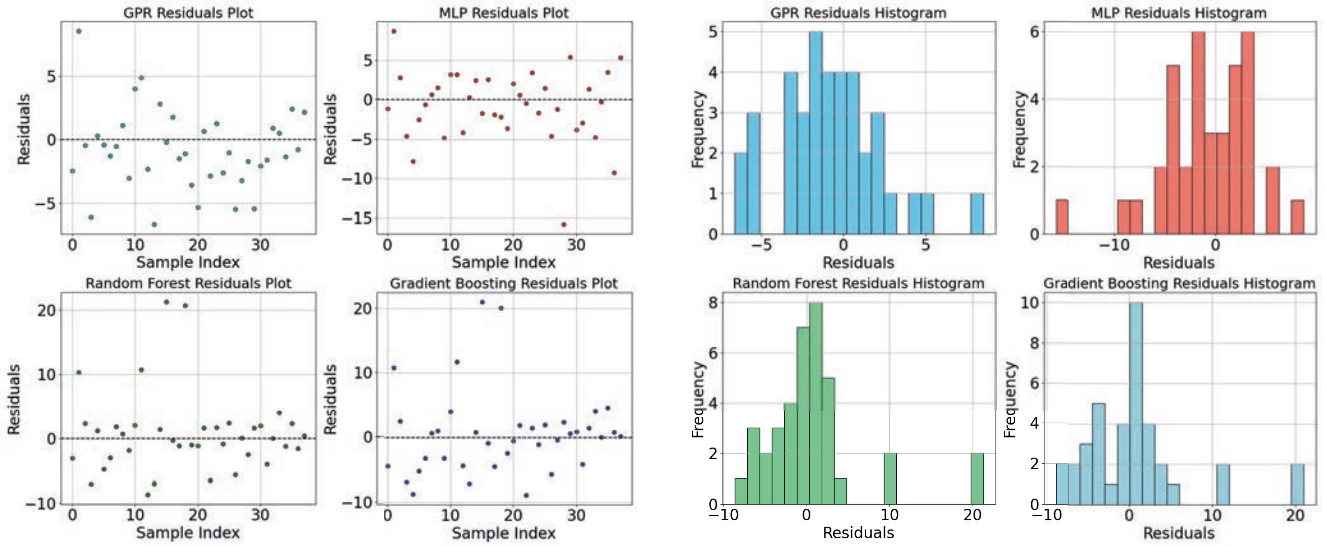

(a) (b)

Figure 3.19 Comparison of Predicted Versus True FEA Horizontal Force Values Across Different Machine Learning Models on the Inner Tire Model: (a) Gaussian Process Regression; (b) Random Forest Prediction; (c) Gradient Boosting Prediction. (d) Neural Network.

3.4.7 FAF from ML-Based Algorithm

Predicted and true values on the validation set are compared through scatter plots, as shown Figure 3.19 and Figure 3.20, providing an assessment of each model's effectiveness in predicting horizontal force values.

Table 3.12 and Table 3.13 provide a comparison of the predictive performance of four models, GRP, MLP, random forest, and gradient boosting, on the validation set for estimating FEA horizontal force. The metrics used for evaluation are R^2 and MSE, separated by training (75%) and validation (25%) set.

Table 3.12 presents the performance of various ML models in predicting FEA horizontal force on the inner tire. The GPR model with WhiteKernel function stands out with the highest R^2 (validation) at 0.97 and the lowest MSE (validation) of 215.3, indicating the best fit to the predictive values. The MLP model follows with a good R^2 (validation) of 0.915, though its MSE (validation) of 613.1 is higher, suggesting lower prediction accuracy compared to GPR. The gradient boosting model has an R^2 (validation) of 0.840 and a higher MSE (validation) of 1156.7, showing that it underperforms relative to GPR and Gradient Boosting. Lastly, the random forest model has an R^2(validation) of 0.856 and an MSE (validation) of 1039.3, placing it between gradient boosting and the neural network in terms of predictive accuracy. Overall, GPR is the best performer, followed by neural network.

Table 3.13 presents the performance of various ML models in predicting FEA horizontal force on the outer tire. The GPR model with WhiteKernel function demonstrates the highest performance with an R^2 (validation) of 0.997 and the lowest MSE (validation) of 28.8. The MLP model follows with an R^2 (validation) of 0.993 and an MSE (validation) of 59.0. The random forest model shows similar effectiveness with an R^2 (validation) of 0.985 and an MSE (validation) of 127.1. Finally, the gradient boosting model achieves an R^2 (validation) of 0.986 but has an MSE (validation) of 124.9. Overall, GPR performs best for both inner and outer tires, followed by neural network and random forest. Therefore, we utilized GPR to perform data expansion for both inner and outer tires.

The ML results in Appendix D align well with the trends observed in the previous FEA analysis, showing consistent patterns across key parameters including speed, superelevation, and

TABLE 3.12
Validation Performance Evaluation for ML Models in Predicting FEA Horizontal Forces on the Inner Tires.

Model	Input	Output	R^2 (Train)	MSE (Train)	R^2 (Validation)	MSE (Validation)
GPR	Speed, slip angle, vertical forces, and camber angle	FEA horizontal force	0.744	1909.2	0.970	215.3
MLP			0.830	1268.1	0.915	613.1
Random Forest			0.965	257.0	0.856	1039.3
Gradient Boosting			0.991	66.5	0.840	1156.7

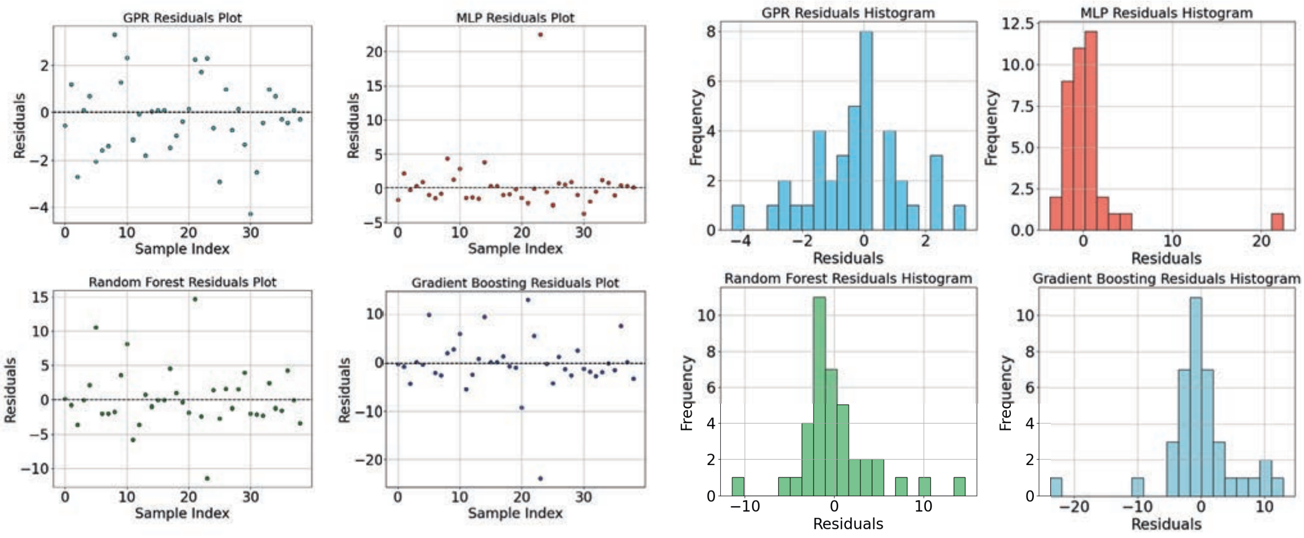

(a) (b)

Figure 3.20 Comparison of Predicted and True FEA Horizontal Force Residuals Across Different ML Models for the Outer Tire Model: GPR, MLP, Random Forest, and Gradient Boosting. (a) The Residual Plots (Percentage Error Versus Sample Index) and (b) the Residual Distribution Histograms.

TABLE 3.13
Validation Performance Evaluation for ML Models in Predicting FEA Horizontal Forces on the Outer Tire.

Model	Input	Output	R^2 (Train)	MSE (Train)	R^2 (Validation)	MSE (Validation)
GPR	Speed, slip angle, vertical forces, and camber angle	FEA horizontal force	0.997	31.8	0.997	28.8
MLP			0.998	17.1	0.993	59.0
Random Forest			0.997	24.3	0.985	127.1
Gradient Boosting			1.000	2.2	0.986	124.9

curve radius. Similar to the FEA findings, the ML outputs capture the sensitivity of tire–road interactions to study parameters. With the inclusion of more curved radii data, the ML results offer a broader representation of tire–road dynamics, covering a wider range of scenarios for a LWST vehicle. This expanded dataset enhances the understanding of the effects of road curvature and other variables on tire performance, providing a more comprehensive database for predicting tire FAF under diverse conditions.

Users can follow the instructions below to check friction adjustment values between a curved road and a straight road for a LWST vehicle in Appendix D.

1. Determine the side of tire for evaluation: The inner tire table represents the inner tire on the vehicle during turning, while the outer tire table represents the opposite-side tire during turning.
2. Locate the FAF: Identify the vehicle inputs (speed, superelevation, and turning curve radius). If there is no exact match on the table, use the closest available row.
3. Read the FAF factor: The corresponding FAF value determines how much FN alters between a curved road and a straight road condition.

3.5 Summary

This modeling section demonstrated the application of FEA in simulating tire–pavement frictional interactions under diverse conditions, including variations in speed, vertical force, slip angle, and camber. By calibrating and validating the FEA model with experimental data, the model showcased its capability to predict longitudinal horizontal forces and FNs.

The experimental results analysis reveals differences between left turns and right turns in terms of their impact on FN and related parameters. In general, the correlation between FN and slip angle shows similar trends for both directions, but specific variations are noted across different test sites:

1. *Slip Angle and FN*: On S.R. 26, left turns exhibit a correlation of –0.81 between FN and slip angle, while right turns show a slightly stronger negative correlation of -0.88. The negative impact on FN as slip angle increases is consistent for both directions due to the exclusion of straight-road data. However, these correlations indicate that slip angle has a greater influence during right turns than left turns on S.R. 26.

2. *Curve Radius and FN*: Across different sites, vertical force and curve radius play significant roles in influencing FN during left and right turns. For example, tighter curve radii tend to increase vertical forces on inner tires, leading to reduced FN. This effect is observed consistently, although the exact magnitude of the reduction varies by site and turn direction.
3. *Superelevation and Slip Angle*: Superelevation data further highlight differences between left and right turns. While curve radius and superelevation exhibit varying impacts, limited test samples constrain the broader applicability of these observations.

The integration of thermomechanical FEA analysis in this study has a total of 320 cases. FEA sensitivity results demonstrate the influence of speed, vertical force, slip angle, and camber on tire–pavement frictional performance. Key findings from FEA include:

1. *Speed Influence*: As speed increases, the FN and horizontal force consistently decline. For example, FN drops from 0.513 at 10 mph to 0.429 at 50 mph from FEA sensitivity analysis. This indicates that higher speeds significantly reduce frictional performance.
2. *Vertical Force Impact*: Changes in vertical force reveal a nonlinear relationship with FN. Higher vertical forces, such as 2,200 lb, result in a notable decrease in FN to 0.403 compared to 0.512 at 600 lb from FEA sensitivity analysis, despite an increase in horizontal force. Excessive vertical loads further amplify FN reductions.
3. *Slip Angle Effect*: Variations in slip angle (0–10°) exhibit minimal influence on FN, maintaining a stable range from 0.498–0.500 from FEA sensitivity analysis, indicating its relatively smaller role compared to speed and vertical force.
4. *Camber Influence*: Increasing camber leads to a gradual reduction in FN. For instance, FN decreases from 0.498 at 0.00 camber to 0.441 at 0.1 camber from FEA sensitivity analysis, underscoring its modest but consistent effect.
5. *Curve Radius Effect*: Tighter curve radii increase vertical forces on inner tires, leading to a noticeable reduction in FN. For example, smaller curve radii induce higher vertical forces, which amplify FN reduction compared to larger radii.

To expand the utility of the FEA results, ML techniques are employed, enabling the creation of a comprehensive dataset. GPR was used to integrate 320 FEA simulations into an expanded 2,376 cases that encompasses a wide range of conditions, including varying speeds, curve radii, and superelevation. The ML-enhanced database facilitated the prediction of FAF across diverse conditions, providing users with a practical tool to account for different road and vehicle dynamics. The generated dataset allowed for the development of more FAF curves, enabling efficient evaluations without the need for additional simulations. This integration of experimental evaluation, advanced modeling, and ML-based data expansion ensures the practicality of the study, offering a practical guidance for optimizing tire–pavement frictional performance.

4. ADDITIONAL TESTS ON NEW PAVEMENT MARKING MATERIALS

4.1 Problem Statement

Pavement markings play a crucial role in regulating traffic flow and enhancing road safety regulating traffic flow and enhancing road safety by providing clear guidance and improving visibility, particularly at night. The newest *MUTCD* (11th ed.) proposed a minimum standard for pavement marking retroreflectivity to ensure the safety of roadways, especially under dark conditions (FHWA, 2023). Over the years, research on pavement markings has predominantly focused on visibility and reflectivity, with limited investigation into surface friction. In Europe, skid resistance is recognized as a key performance indicator of pavement markings, with established evaluation standards in place (British Standards Institution, 2018). In contrast, attention to pavement skid resistance in the United States has only recently increased. While the *MUTCD* emphasizes the need to minimize traction loss and tripping hazards (FHWA, 2023), there remains no clear guidance for evaluating pavement marking skid resistance.

The higher requirements for pavement marking materials' visibility and frictional performance require further research. Traditionally, achieving both high visibility and adequate friction in pavement markings using only glass beads has been difficult. Previous research has found that while larger glass beads enhance visibility (Bowman & Kowshik, 1994), they may also reduce surface friction (Bao et al., 2024). Therefore, testing new marking material is crucial to achieving both adequate friction and visibility while ensuring long-term performance that meets FHWA roadway safety standards.

This section builds upon previous research (i.e., SPR-4646 [Bao et al., 2024]) to further investigate the effects of different materials on pavement marking skid resistance and provide a reference for standard development. By integrating existing pavement marking regulations with experimental findings, Bao et al. (2024) recommend that the wet British Pendulum Number (BPN) for sidewalks, signs, and letters should be no less than 40–45. However, epoxy and thermoplastics do not meet this requirement. Thermoplastics are premanufactured with glass beads and particles embedded during production, whereas in epoxy markings, particles are applied to the surface after the epoxy is laid. When glass beads, regardless of size, are added, the wet BPN falls below 40. Building on this, this section examines the effect of ceramic particles on the skid resistance of epoxy pavement markings. Furthermore, the skid resistance performance of new marking materials (angular glass particles) was evaluated to identify materials that can simultaneously enhance friction, durability, and visibility, addressing current challenges in pavement marking. The findings are compared with the results from SPR-4646 (Bao et al., 2024) to provide further insights into material performance and potential improvements in pavement marking durability and safety.

Therefore, this section aims to achieve the following objectives:

1. Assess the impact of ceramic particles and angular glass particles on epoxy skid resistance, including friction and surface texture, before and after polishing.
2. Evaluated the effects of different materials on the durability of pavement markings based on the conditions of slabs after polishing.
3. Compared findings with SPR-4646 results to provide insights into material performance and potential improvements in pavement marking durability and safety.
4. Established a connection between laboratory polishing tests and vehicle-induced wear on pavement markings through FEA.

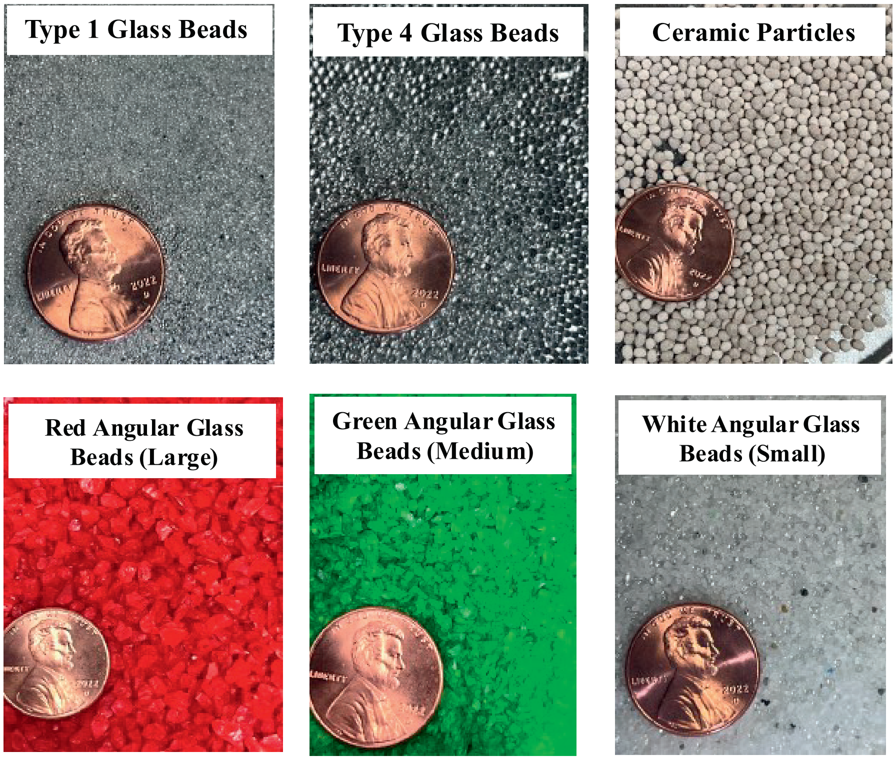

Figure 4.1 Glass Beads, Ceramic Particles, and Angular Glass Particles.

4.2 Experiment Devices

4.2.1 Materials

The materials used in this study include liquid epoxy marking and various particles, such as AASHTO M247 Type 1 glass beads (AASHTO, 2013), ceramic particles, and angular glass particles of different sizes. Figure 4.1 presents the particles used in this study, with AASHTO M247 Type 4 glass particles included for comparison. Table 4.1 presents the gradation and particle size distributions of the tested materials. The particle sizes, ordered from smallest to largest, are: Type 1 glass beads, Type 4 glass beads, large red angular glass particles, medium green angular glass particles, small white angular glass particles, and ceramic particles. Type 1 and Type 4 glass beads are commonly used in pavement markings to enhance their retroreflectivity. To ensure optimal retroreflective performance, glass beads are typically dropped or sprayed onto freshly applied liquid pavement markings. Ceramic particles consist of microcrystalline ceramic beads partially embedded within composite cores. These particles are typically applied to pavement markings at a minimum thickness of 25 mils (0.635 mm) before glass beads. The ceramic particles were designed to enhance the retroreflective properties of pavement marking surfaces. Moreover, Bao et al. (2024) indicate that these particles improve skid resistance, while they may also reduce the durability of pavement markings. The angular glass particles are manufactured from recycled pulverized glass. For the large sized angular glass particles (1.0–3.36 mm), the recommended wet firm thickness is 40–50 mils (1.016–1.27 mm). For the middle-sized angular glass particles (0.59–1.68 mm), this recommended wet film is 35–40 mils (0.889–1.016 mm). For the small-sized angular glass particles (0.59–1.00 mm), the recommended wet firm thickness is 20–25 mils (0.508–0.635 mm). The bright colors of the angular glass particles improve lane visibility while providing clearer guidance to road users. Figure 4.1 shows the concrete slab with applied epoxy pavement marking.

Figure 4.2 Epoxy Painting.

TABLE 4.1
Gradation or Size of Glass Beads and Ceramic Particles.

Sieve Size		Mass % Passing			Particle Size		
Standard (mm)	Sieve No.	Type 1	Type 4	Ceramic Particles	Red	Green	White
2.00	10	–	100	95–100	1.0–3.36 mm	0.59–1.68 mm	0.59–1.00 mm
1.70	12	–	95–100	–			
1.40	14	–	80–95	0–40			
1.18	16	100	10–40	–			
1.00	18	–	0–5	–			
0.850	20	95–100	0–2	0–5			
0.600	30	75–95	–	–			
0.425	40	–	–	–			
0.300	50	15–35	–	–			
0.180	80	–	–	–			
0.150	100	0–5	–	–			

4.2.2 Devices for Measuring Surface Texture

A laser texture scanner (LTS) and a circular track meter (CTM) were utilized to measure the surface texture of the specimens. Figure 4.3 provides images of these instruments. The LTS measures surface texture depth within a rectangular area of 76.2 mm × 101.6 mm. It detects wavelengths ranging from 0.03–50 mm, allowing for the measurement of macrotexture and partial microtexture. Therefore, it is used to assess the surface texture depth of specimens before polishing and generating 3D surface representations. The CTM is utilized to measure the surface macrotexture both before and during polishing. It has a charge couple devices laser-displacement sensor and measures a circular ring with a diameter of 284 mm (ASTM, 2019a), aligning with the trajectory of the TWPD.

4.2.3 Devices for Measuring Surface Friction

Figure 4.4 illustrates the British Pendulum Tester (BPT) and Figure 4.5 shows the Dynamic Friction Tester (DFT) utilized in this study for surface friction evaluation. The BPT was specifically utilized to measure surface friction before polishing. It is widely used for surface friction testing in both laboratory and field settings due to its portability. Some regions have developed friction standards for pavement markings based on the BPN, the measurement obtained from the BPT. This device features a swinging pendulum with a rubber slider attached at its base. The rubber sliders are available in two standard sizes. In this study, the rubber with dimensions of 76 mm × 25 mm × 6 mm (3 in. × 1 in. × ¼ in.) was utilized (AASHTO, 2021). As the pendulum descends from an elevated horizontal position, the rubber slider

(a) (b)

Figure 4.3 Texture Measuring Device: (a) Laser Texture Scanner and (b) Circular Track Meter.

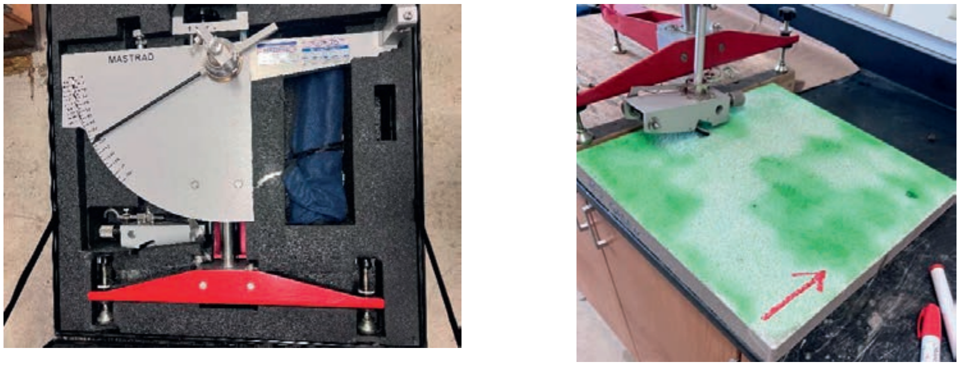

(a)

(b)

Figure 4.4 British Pendulum Tester.

(a)

(b)

Figure 4.5 Dynamic Friction Tester.

makes contact with the measurement surface and travels a specified distance, typically between 12.4–12.7 cm ($4\frac{7}{8}$ in. and 5 in.; AASHTO, 2021). This device includes two measurement scales, F-scale and main scale, and in this study, results were recorded from the main scale. For each specimen, testing was repeated multiple times until the difference between five consecutive readings was less than one unit, ensuring measurement stability and reliability.

The DFT was employed to measure surface friction before and during polishing. It features a horizontally spinning disk with three spring-loaded rubber sliders, which measure the dynamic friction coefficient on the trajectory aligned with the TWPD and CTM. During operation, water is supplied to the surface, and as the disk rotates, the rubber sliders contact the measurement surface to assess friction at different speeds (0, 12, 19, 25, and 37 mph, or 0, 20, 30, 40, and 60 km/h; ASTM, 2019b). The dynamic friction data, combined with the MPD measured by CTM, were used to calculate the IFI (ASTM, 2023).

4.2.4 TWPD

Figure 4.6 shows the TWPD utilized in this study to simulate traffic-induced polishing on pavement surfaces. It features a rotating plate with three rubber tires that maintain contact with the polishing surface, applying a total load of 217 lb. (approximately 98.5 kg; INDOT, 2018). The rotation rate of the plate is approximately 47 revolutions per min. During polishing, water is continuously sprayed onto the specimen surface to remove debris generated in the process. In this study, each specimen experienced 50,000 cycles of polishing.

Figure 4.6 Three-Wheel Polishing Device.

The IFI is calculated to characterize pavement surface friction properties by integrating measurements from different friction assessment devices. The IFI comprises two key parameters: F60 and speed constant of wet pavement friction (S_p). These parameters are derived from measurements of macrotexture (MPD) and wet friction, allowing for the standardization of friction values across different testing devices and speeds. Equations 4.1 and 4.2 display the formula to calculate the two parameters (ASTM, 2023). This approach ensures consistency in surface friction assessments, facilitating reliable comparisons and evaluations of pavement safety and performance.

$$S_p = 14.2 + 89.7\,MPD \qquad \text{Equation 4.1}$$

$$F_{60} = 0.081 + 0.732 DF \exp\left(-\frac{40}{S_p}\right) \qquad \text{Equation 4.2}$$

where DF is the dynamic friction measured under a specific speed. In this study, the coefficients of dynamic friction measured under 40 km/h were utilized.

4.3 Testing Sample

4.3.1 Specimen Preparation

Concrete slabs with dimensions of 20 × 20 × 2 in. (50.8 × 50.8 × 5.08 cm) were used as substrates for the test specimens. During epoxy application, a controlled volume is applied to the concrete slabs using a paint roller to achieve a thickness as close as possible to the required specification. Additives, including glass beads, ceramic particles, and angular glass particles, were immediately dropped onto the wet paint after its application. Figure 4.7 shows a sample specimen with the red angular glass particles dropped onto the epoxy marking.

Table 4.2 presents the specimen details evaluated in this study. All specimens were prepared under the same conditions to ensure reliability. The table provides information on marking materials, bead and particle types, particle application rates, coating thicknesses, and event quantity. Among these specimens, No.11 and No.12 were previously tested in SPR-4646, while No.25–29 are newly introduced in this study. The Group ID coding follows the continuation of SPR-4646, ensuring consistency in specimen identification.

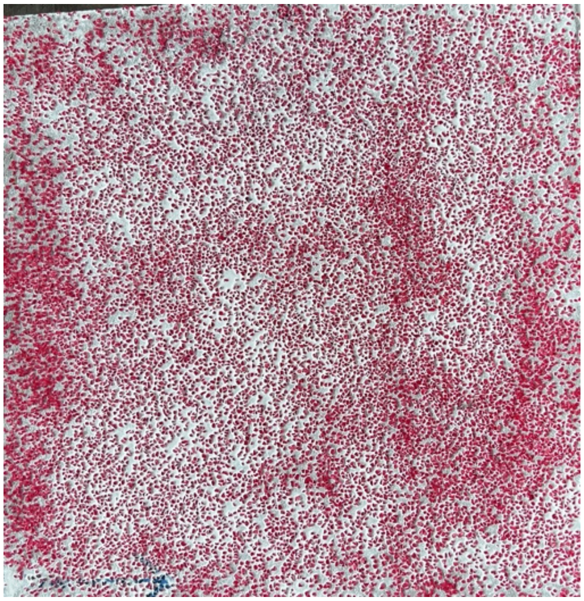

Figure 4.7 Sample Specimen With Red Angular Glass Particles.

4.4 Results and Analysis

4.4.1 Surface Friction Characteristics Before Polishing

Friction metrics, including BPN, macrotexture MPD, and DF40, were measured before polishing the specimens both under dry and wet conditions, as shown in Figure 4.8. The macrotexture MPDs were measured by both LTS and CTM, and the results are approaching. The following characteristics were observed:

- *Dry Friction Performance*: Specimens incorporating angular glass particles or ceramic particles (No.25–No.29) exhibited higher dry BPN compared to those containing only glass beads (No.11 and No.12).
- *Effect of Ceramic Particles on Wet Friction*: The addition of ceramic particles significantly improved the initial friction performance of epoxy. The wet BPN increased from less than 36 (No.11 and No.12) to 61 (No.29), while DF40 rose from a minimum of 0.21 (No.12) to 0.54 (No.29).
- *Effect of Angular Glass Particles on Wet Friction*: Specimens containing angular glass particles (No.25–No.28) exhibited

TABLE 4.2
Details of Test Specimens.

Product Group ID	Marking Material	Type of Bead/Particle	Bead and Particle Application Rate	Desired Thickness	No. of Specimens
No.11 (Bao et al., 2024)	Epoxy	Type 1	20 lb/gal	20 mils	2
No.12 (Bao et al., 2024)	Epoxy	Type 1 + Type 4	6 lb/100 ft^2 (Type 1) & 10 lb/100 ft^2 (Type 4)	20 mils	2
No.25	Epoxy	Large glass beads	25 lb/100 ft^2	40 mils	2
No.26	Epoxy	Medium glass beads	25 lb/100 ft^2	40 mils	2
No.27	Epoxy	Small glass beads	15 lb/100 ft^2	20 mils	1
No.28	Epoxy	Small glass beads	15 lb/100 ft^2	25 mils	1
No.29	Epoxy	Type 1 + ceramic particles	10 lb/100 ft^2 (Type 1) & 8 lb/100 ft^2 (Ceramic Particle)	25mils	2

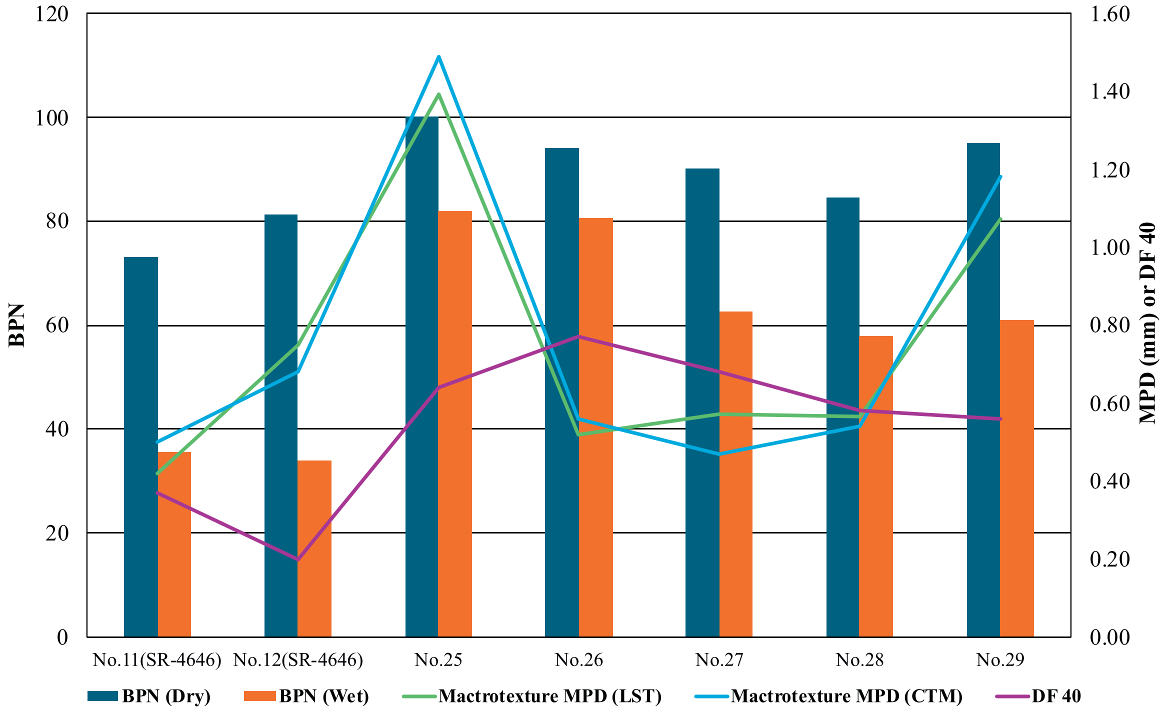

Figure 4.8 BPN, MPD, and DF40 Measurements of Markings Before Polishing.

significantly improved wet friction compared to those with only glass beads (No.11 and No.12). Larger and medium-sized angular glass particles (No.25 and No.26) resulted in higher wet BPN values (BPN > 80), while the wet BPN of smaller angular glass particles (No.27 and No.28) was compatible with that of specimens containing ceramic particles (No.29), around 60. In contrast, the DF40 values of specimens with large and small angular glass particles (No.25, No.27, and No.28) were lower than those with medium-sized particles (No.26), but all remained significantly higher than those of specimens containing only sphere glass beads (No.11 and No.12).

- *Macrotexture (MPD)*: Specimens containing large angular glass particles (No.25) exhibited a higher initial MPD, whereas those with medium- and small-sized particles (No.26–No.28) showed MPD values comparable to specimens with Type 1 glass beads (No.11). Although the particle sizes are similar to those of the ceramic particles, the MPD is significantly lower. This reduction may be attributed to the excessive binder thickness (40 mils for No.26), which limits particle exposure and leads to a comparatively smaller surface texture.
- *Thickness Influence*: Specimens No.27 and No.28 did not exhibit significant differences in MPD, suggesting that variations in thickness had a limited impact on surface texture and friction performance. The relationship between pavement marking thickness and friction remains inconclusive, and further research is needed to better understand this interaction.

For a complete record of all MPD and BPN measurement values, please refer to Table F.1 to Table F.3 in Appendix F.

Figure 4.9 presents the 3D surface plots generated from LTS scanning, offering a detailed visualization of the surface texture. Based on the figure, specimens No.25 and No.29 exhibit more pronounced surface projections, whereas the surfaces of specimens No.26–No.28 appear noticeably flatter.

4.4.2 Surface Friction Characteristics During and After Polishing

4.4.2.1 Durability. Durability refers to the ability of pavement markings to maintain their structural integrity and surface condition under repeated polishing or traffic-induced wear. Table 4.3 and Table 4.4 present close-up and overall views of the specimens before and after polishing. Although all specimens (No.25–No.29) underwent 55,000 polishing cycles, the condition of the surfaces after polishing—including binder loss, bead dislodgement, and surface wear—reflects the influence of different additives on the durability of the epoxy markings. Based on the observations from Table 4.3 and Table 4.4, a comparison between specimens No.25–No.29 and No.11 and No.12 reveals notable differences in surface condition after polishing. Specimens containing angular glass particles (No.25 and No.28) showed no visible wheel marks following polishing. Although wheel marks were present on specimens No.26 and No.27, surface inspection indicated that the particles remained embedded and did not detach. These are different from large beads, such as Type 4 glass beads and ceramic particles, which are more prone to detachment, which can accelerate the deterioration of pavement marking performance. In contrast, angular glass particles appear to mitigate this issue effectively. After 55,000 polishing cycles, the surface condition of specimens No.25–No.28 remained intact. In comparison, specimen No.29 exhibited significant surface damage and noticeable particle loss.

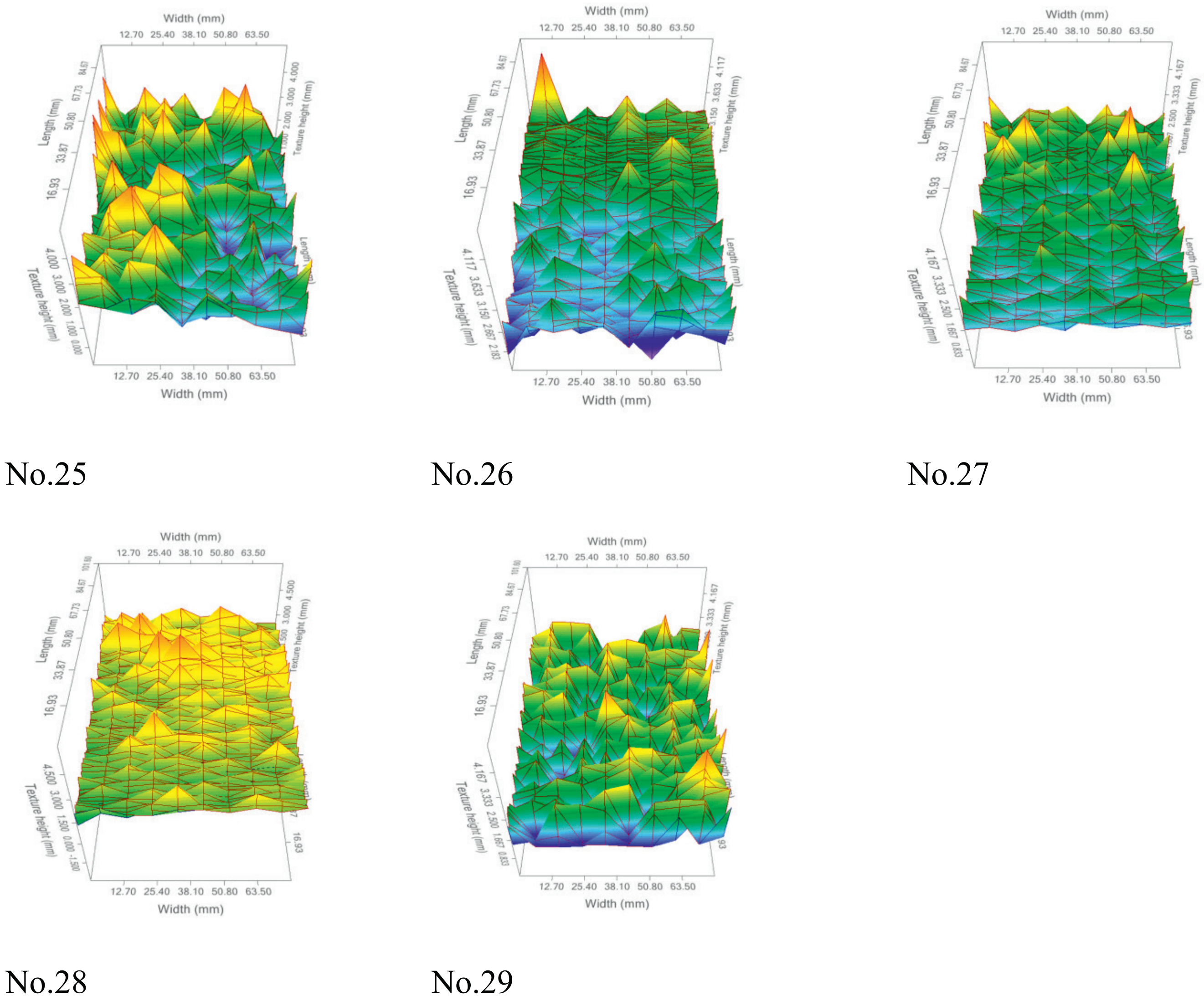

No.25

No.26

No.27

No.28

No.29

Figure 4.9 3D LTS Scanning Surface Plot for No.25–No.29.

In conclusion, although all specimens were subjected to the same number of polishing cycles, angular glass particles had a lesser impact on the durability of the pavement markings. In fact, their performance suggests potentially greater durability compared to specimens containing Type 1 glass beads, which underwent 60,000 polishing cycles. In contrast, the inclusion of ceramic particles significantly compromised the durability of the pavement markings.

4.4.2.2 Effects of Ceramic Particles. Figure 4.10 shows the MPD, DF40, and F60 values for specimens containing only glass beads (No.11 and No.12) and for those incorporating both Type 1 glass beads and ceramic particles (No. 29) throughout the polishing process. Specimens with ceramic particles (No.29) exhibited strong friction performance, with DF40 and F60 values approximately 1.5 times higher than those of specimens containing only Type 1 glass beads (No.11). Although a notable reduction in friction performance was observed after the first 1,500 polishing cycles, the values stabilized thereafter and remained substantially higher than those of specimens containing only glass beads. Epoxy has been found to exhibit lower friction performance compared to other pavement markings when using the same type and application rate of glass beads. The incorporation of ceramic particles effectively addresses limitations by improving the skid resistance of epoxy surfaces.

4.4.2.3 Effects of Angular Glass Particles. Figure 4.11 to Figure 4.14 illustrate the friction performance of epoxy markings incorporating angular glass particles of varying sizes through the polishing process. Epoxy with Type 1 glass beads (No.11) with large-sized angular glass particles (No.25) exhibit significantly higher MPD, DF40, and F60 values to those containing only Type 1 glass beads (No.11), as shown in Figure 4.11. The friction metrics values of No.25 specimens show a more pronounced decline during the initial stage of polishing compared to No.11, but the friction performance stabilized after

TABLE 4.3
Close-Up Detail Photos of an Epoxy Marking Specimen Surface Before and After Polishing.

Group No.	Before Polishing	After Polishing
No.11		
No.12		
No.25	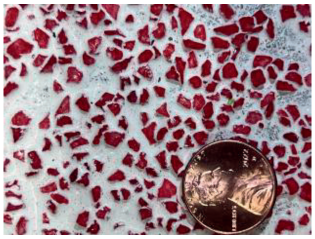	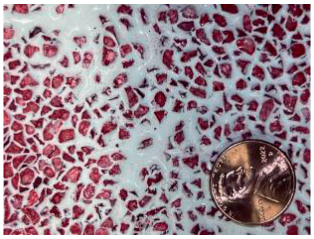
No.26	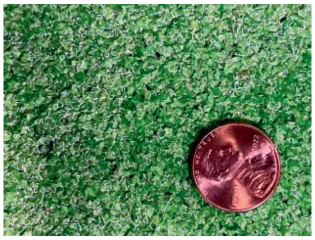	
No.27		
No.28		
No.29		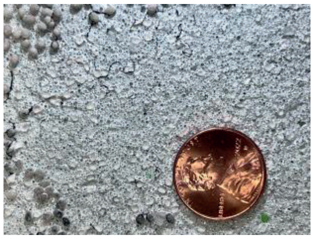

TABLE 4.4
Overall View Photos of an Epoxy Marking Specimen Surface Before and After Polishing.

Group No.	Before Polishing	After Polishing
No.25	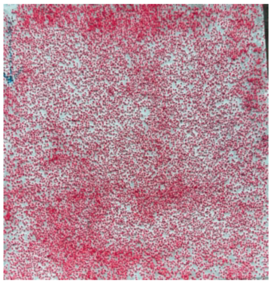	
No.26	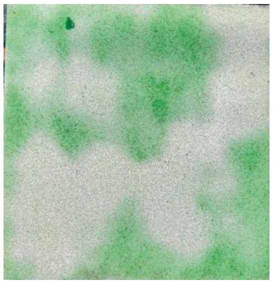	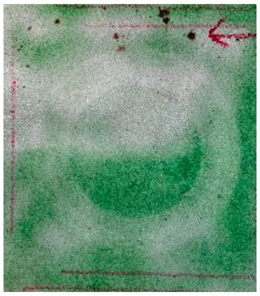
No.27		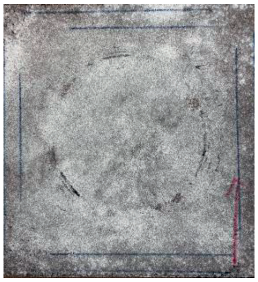
No.28		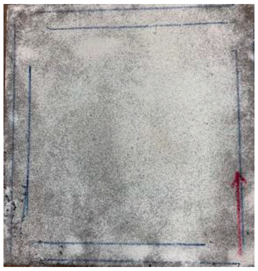
No.29		

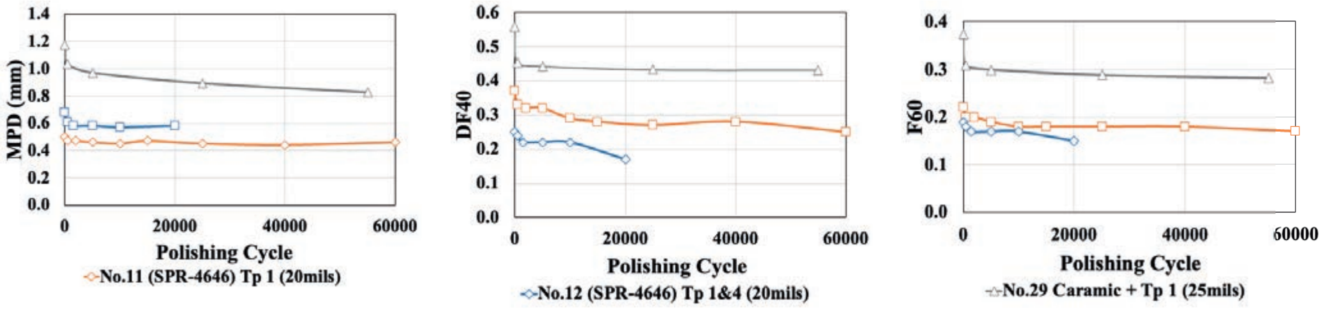

(a) (b) (c)

Figure 4.10 Effect of Polishing Cycles on the Surface Performance of Epoxy with Ceramic Particles: (a) MPD, (b) DF40, and (c) F60.

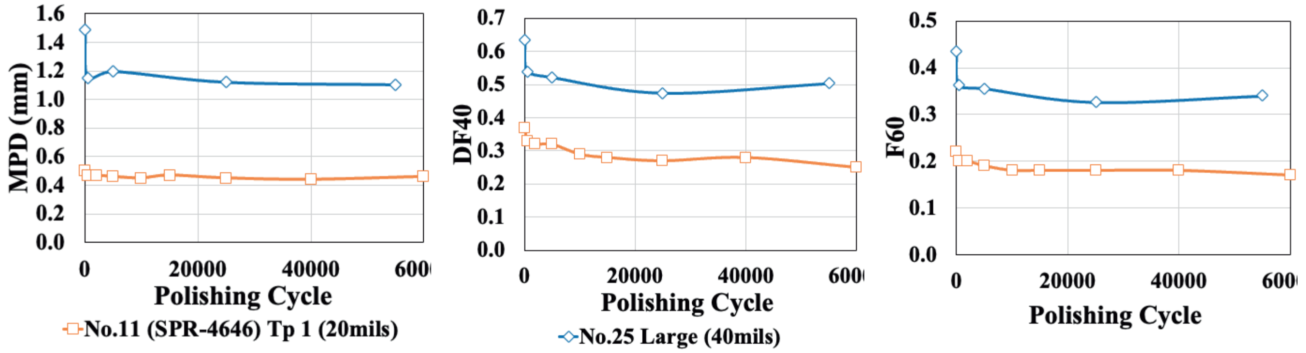

(a) (b) (c)

Figure 4.11 Effect of Polishing Cycles on the Surface Performance of Epoxy with Large Angular Glass Particles: (a) MPD, (b) DF40, and (c) F60.

approximately 500 polishing cycles. Throughout the polishing process, the DF40 and F60 values of the No.25 specimens remained approximately 1.7 times higher than those of No.11.

Compared to specimens with large-sized particles (No.25), those with medium and small angular particles (No.26–No.28) exhibited higher initial MPD values than the specimen containing only Type 1 glass beads (No.11). However, these MPD values declined to levels comparable to No.11 during the early stages of polishing. Furthermore, the DF40 and F60 values of specimens No.26–No.28 were significantly higher than those of No.11. Although a noticeable decline was observed during the initial polishing stage, the DF40 values of No.26–No.28 remained 1.4–1.8 times higher than those of No.11 after 5,000 polishing cycles and were maintained at this level through the reminder of the test. While the difference in F60 values between No.26–No.28 and No.11 was slightly smaller than that observed for DF40, specimens No.26–No.28 still demonstrated superior skid resistance. Moreover, no noticeable difference in friction performance was observed between specimens No.27 and No.28 during the polishing process. However, this does not imply that thickness has no influence on friction.

Figure 4.14 shows the friction performance of specimens No. 25, No.26, No. 27, and No.28. The MPD of the specimens with large-sized angular particles (No.25) is significantly higher than that of specimens with medium and small angular particles (No.26–28). During the polishing process, the DF40 value of the specimen with medium-sized angular particles (No.26) was superior to those of the other groups. However, the DF40 values of specimens No.25–No.28 did not differ significantly and consistently remained at a high level above 0.4. After polishing, specimens No.25 exhibited the highest DF40 value at 0.5, followed by No.26, No.27, and No.28 in descending order. Due to its higher MPD, specimen No.25 exhibited superior F60 performance, while the F60 values of specimens No.26–No.28 were largely similar. However, the different sizes of angular glass particles did not result in significant variation in DF40 values.

4.4.3 Equivalent Application of Three-Wheel Polishing

To convert the number of actual traffic applications to the equivalent number of three-wheel polishing applications, two scenarios were considered, including LWST and standard

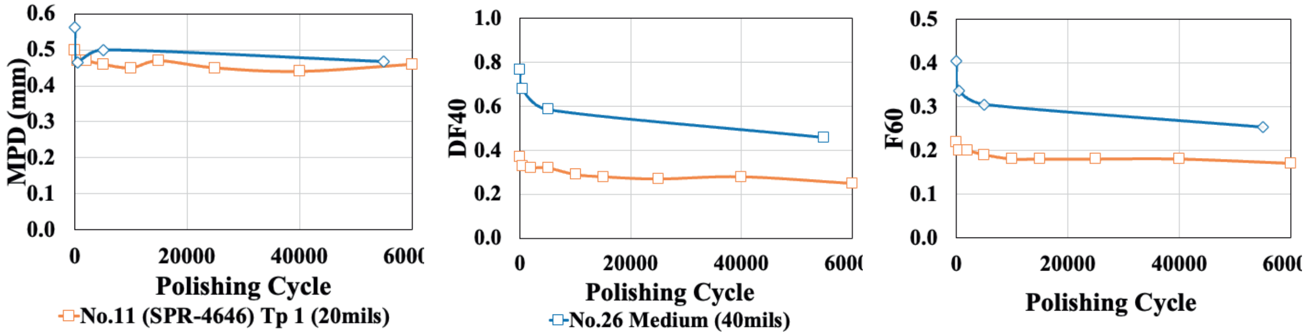

(a) (b) (c)

Figure 4.12 Effect of Polishing Cycles on the Surface Performance of Epoxy with Medium Angular Glass: (a) MPD, (b) DF40, and (c) F60.

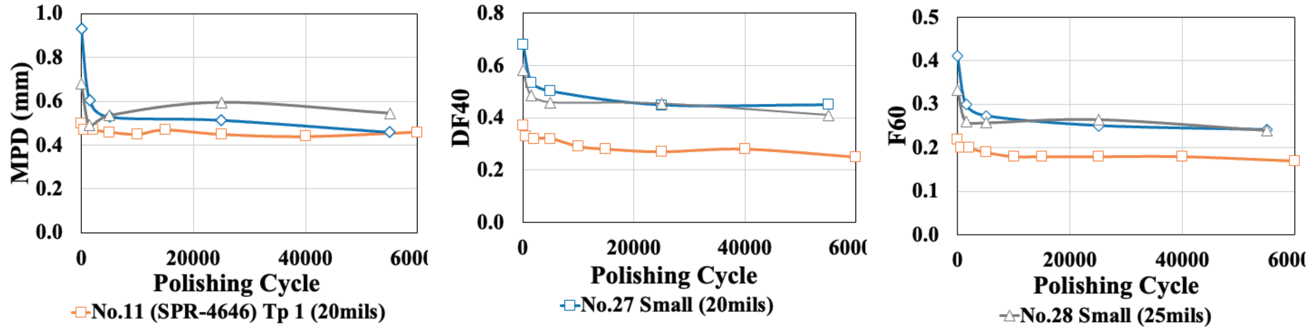

(a) (b) (c)

Figure 4.13 Effect of Polishing Cycles on the Surface Performance of Epoxy with Small Angular Glass: (a) MPD, (b) DF40, and (c) F60.

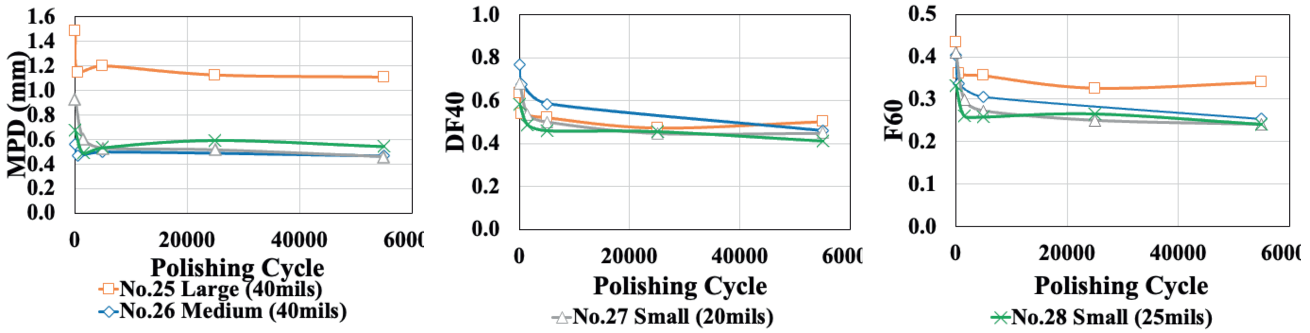

(a) (b) (c)

Figure 4.14 Effect of Polishing Cycles on the Surface Performance of Epoxy with Angular Glass: (a) MPD, (b) DF40, and (c) F60.

passenger car. The TWPD machine applies a vertical load *F* of 217 lb (98 kg) with three wheels, and the friction coefficient has been previously measured using the DFT to obtain an average DF40 value. From this, we can determine the tire frictional force for each wheel. With the TWPD's rotational diameter of 300 mm, as shown in Figure 4.15, the work done per revolution can be calculated for each wheel based on energy conservation principles in the following equation.

$$W = (F \times d \times \pi) \times n; \qquad \text{Equation 4.3}$$

where *W* represents the work for three wheels. *F* is the force applied for each wheel, *d* represents the rotational diameter over

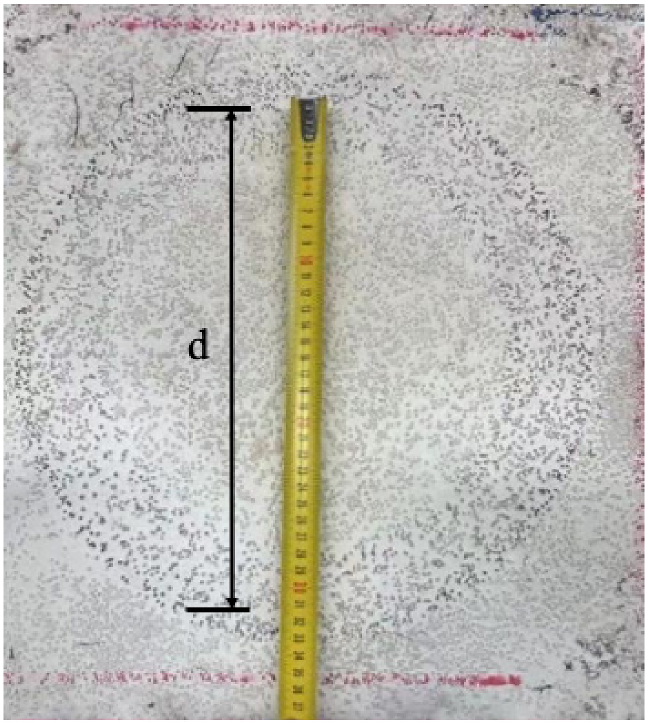

Figure 4.15 LWST Polishing Trajectory Measurement.

which the force is applied, and *n* is the number of wheels on TWPD.

In terms of average $F_{f.average}$ value, using only the initial and final values of friction force can oversimplify the actual degradation behavior, potentially overlooking critical transitions in friction loss. A more reliable method is the trapezoidal rule, as it offers a practical solution to this problem by numerically integrating discrete *DF40* data points, as shown in Equation 4.4 This method treats the friction-versus-polishing-cycle curve as a series of trapezoids, where each trapezoid represents the area between two consecutive data points (Trefethen & Weideman, 2014). By calculating the area under the curve and dividing it by the total polishing cycle length, it obtains the average DF40. By multiplying the average trapezoidal *DF40* value by the applied vertical load, shown in as shown in Equation 4.5. The average friction force experienced during the full polishing cycle can be obtained. This approach accounts for both the magnitude and variation of friction throughout the test, providing a more representative and accurate evaluation of friction durability.

$$DF40_{Trapezodial} = \frac{1}{x_n - x_1}\sum_{i=1}^{n-1}\frac{DF40_1 + DF40_{i+1}}{2}\left(x_{i+1} - x_i\right);$$

Equation 4.4

$$F_{f.average} = DF40_{Trapezodial} \times Vertical\ load;$$ Equation 4.5

x represents the interval polishing cycle during the polishing process.

In this study, we aim to determine how many TWPD tire cycles are equivalent to a single vehicle pass over a stop pavement marking, by matching the total energy applied to the marking surface. The pavement marking is set to a width of 12 inches (304.8 mm; FHWA, 2023). As illustrated in Figure 4.16, a four-wheel passenger vehicle is assumed; however, only one side of the vehicle (two wheels) is considered in the analysis, representing half of the vehicle passing over the pavement marking. The number of wheels and width of pavement marking are accounted for in the energy equivalence calculation. Table 4.5 presents the

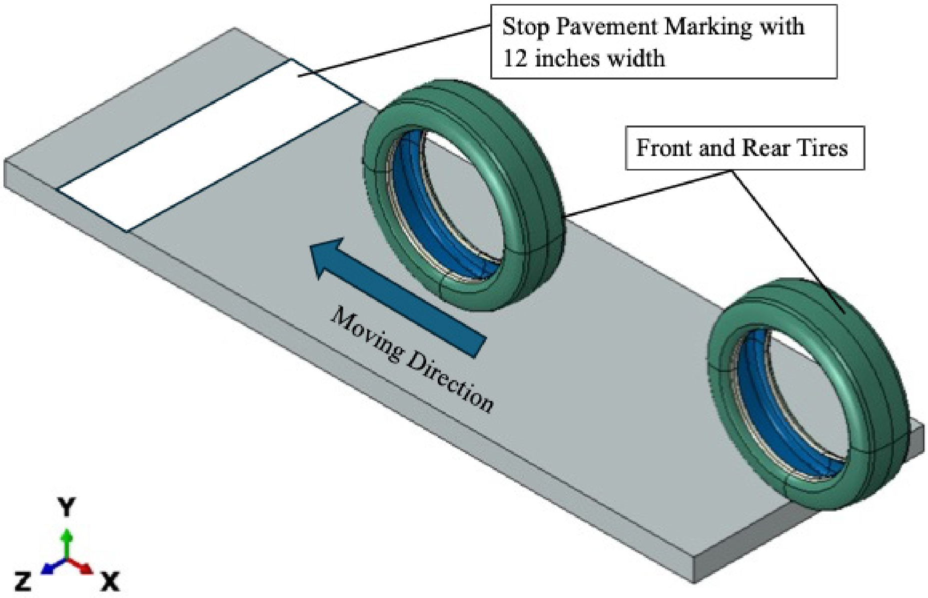

Figure 4.16 Schematic Drawing for a Two Wheels Car Passing Over the Stop Pavement Marking.

TABLE 4.5
Calculation of Equivalent Passes of LWST Corresponding to Each TWPD Cycle.

No.	Vertical Force (N)	DF 40 Trapezoidal	Friction force (N)	Distance (m)/Cycle	Energy (J)	LWST vertical force (N)	FN	Horizontal force (N)/ Each side	Pavement Marking Width (mm)	Equivalent TWPD polishing/ One LWST cycle
11	965.3	0.28	269.4	0.892	253.9	4826	0.47	2248.9	304.8	8.5
12	965.3	0.21	201.4	0.892	189.8	4826	0.47	2248.9	304.8	11.3
25	965.3	0.49	476.2	0.892	448.7	4826	0.47	2248.9	304.8	4.8
26	965.3	0.54	517.2	0.892	487.4	4826	0.47	2248.9	304.8	4.4
27	965.3	0.45	435.6	0.892	410.5	4826	0.47	2248.9	304.8	5.2
28	965.3	0.44	429.4	0.892	404.6	4826	0.47	2248.9	304.8	5.3
29	965.3	0.43	419.7	0.892	395.5	4826	0.47	2248.9	304.8	5.4

TABLE 4.6
Calculations of Equivalent Passes of a Passenger Vehicle Corresponding to Each TWPD Cycle.

Vehicle	No.	Number of tires on each side	Vertical Force (N)/Each Side	FN	Horizontal Force (N)/Each Side	Pavement Marking Width (mm)	Equivalent TWPD Polishing/One Passenger Vehicle Tire Cycle
Passenger Vehicle	11	2	16000	0.50	8000	711	30.2
	12	2	16000	0.50	8000	711	40.3
	25	2	16000	0.50	8000	711	17.1
	26	2	16000	0.50	8000	711	15.7
	27	2	16000	0.50	8000	711	18.6
	28	2	16000	0.50	8000	711	18.9
	29	2	16000	0.50	8000	711	19.4

calculation procedure to determine how many TWPD tire cycles are equivalent to one pass of the LWST in terms of pavement marking wear by matching the same amount of energy.

We also conducted an equivalent cycle analysis for a standard passenger car. The vertical forces acting on the tires were derived from existing references. For an average passenger vehicle under free rolling and cornering conditions, Srirangam et al. (2012) utilized a friction coefficient of 0.5 in P195/75R14 tire analysis when speed is 43.75 mph. Additionally, a central load of 8000 N was applied for each tire, with the inner side of the tire maintained at an inflation pressure of 1.3 bar (Mhaske et al., 2015). The results are shown in Table 4.6.

Users can refer to Table 4.6 to check the values of the equivalent passes of different vehicles (LWST and passenger vehicle) corresponding to the same energy caused by TWPD on different pavement marking samples. For instance:

- For Sample No.11, the equivalent TWPD Polishing per one LWST pass is 8.5. This means one pass of the LWST trailer corresponds to 8.5 TWPD cycles in terms of energy impact. If the LWST rotates 100 times, the equivalent TWPD polishing cycles would be:100 × 8.5 = 850 TWPD cycles.
- Similarly, for the passenger vehicle on Sample No.11, the equivalent TWPD passes per one standard vehicle pass is 30.2. So, if the vehicle tires roll 50 times over the same spot, it would have the same energy effect as: 50 × 30.4 = 1,520 TWPD cycles.

4.5 Summary

Building on project SPR-4646 (Bao et al., 2024), this section further investigates the effects of ceramic particles and angular glass particles of varying sizes on the friction performance of epoxy pavement markings. By systematically measuring and analyzing relevant friction metrics, the following conclusions can be drawn as follows:

- *Initial friction*: The incorporation of ceramic particles and angular glass particles of various sizes significantly improves the friction performance of pavement marking surfaces under both dry and wet conditions. In wet conditions, the BPN and DF40 values increased from a maximum of 35.5 and 0.36, respectively, with regular glass beads to a minimum of 58 and 0.54 following the addition of ceramic and angular glass particles.
- *Durability*: Angular glass particles are more effective in preserving the durability of the pavement surface. After polishing, specimens containing angular glass particles showed no visible wheel marks or significant particle loss. In contrast, specimens incorporating ceramic particles and Type 4 glass beads exhibited greater particle detachment during the polishing process, which contributed to the accelerated deterioration of the pavement markings.
- *Friction during and after polishing*: The incorporation of ceramic particles and angular glass particles effectively enhances the DF40 and F60 values of pavement markings both during and

after polishing. The addition of ceramic particles and large-sized angular glass particles resulted in a notable increase in MPD. Although medium- and small-sized angular glass particles did not significantly increase MPD, this had no adverse effect on the wet friction performance of the surface.

- *Thickness*: Based on the results obtained from the specimens in this study, variations in thickness alone did not produce a noticeable difference in friction performance. However, this does not imply that thickness has no influence. It is preliminarily understood that thickness, particle size, and application rate collectively contribute to the surface friction of pavement markings. Further research is necessary to clarify the interactions among these factors.
- *Equivalent application of TWPD*: The calculations of equivalent TWPD cycles corresponding to one full rotation of the LWST wheel are completed for different pavement marking samples, with values ranging from 4.4 to 11.3 TWPD cycles per LWST pass. Similarly, one rotation of a standard passenger vehicle tire (with a 16,000 N load and FN of 0.5) corresponds to 15.7 to 40.3 TWPD cycles, depending on the pavement surface. This indicates that both vehicle types impart significantly more energy per pass compared to the TWPD.

5. CONCLUSIONS

This study comprehensively analyzed pavement friction performance using polynomial regression, ML models, FEA, and experimental evaluations of pavement marking materials. The findings provide actionable insights for improving friction testing, modeling, and pavement material selection to enhance roadway safety. Major findings and conclusions are drawn as follows:

- Assessment and comparison of LWST and SCRIM field test (Task 1):
    - Polynomial regression effectively captured nonlinear relationships between SR, MPD, curve radius, and cross slope, with straight roads exhibiting stronger correlations than curved roads.
    - ML techniques, particularly random forest, improved predictive accuracy in complex conditions, while SVR and neural networks required additional data preprocessing to enhance performance.
    - SR = f(MPD): Straight roads had the highest correlation ($R^2 = 0.245$), with all roads performing better overall.
    - FN = f(SR): All pavement roads showed the strongest correlation, with random forest network ($R^2 = 0.374$) outperforming polynomial regression ($R^2 = 0.357$).
    - FN = f(SR & MPD): Polynomial regression performed best on straight ($R^2 = 0.581$) followed curved roads. Random forest performs poor for complex surfaces with overfitting.
    - FN = f(SR, MPD, curve radius, and cross slope): Random forest provided the best correlation ($R^2 = 0.753$) for straight roads, and random forest ($R^2 = 0.746$) performed well in all pavement roads.
- Development of an adjustment factor for friction tests on horizontal curves (Task 2):
    - FEA simulations demonstrated the impact of speed, vertical force, slip angle, and camber on tire–pavement interactions.
    - Increasing speed and vertical force significantly reduced FN, while smaller curve radii amplified FN reductions due to higher inner tire loads.
    - Left and right turn analysis revealed stronger negative correlations between FN and slip angle on right turns, highlighting directional influences.
    - A ML-enhanced GPR model expanded 320 FEA simulations into 2,376 cases, improving FAF predictions across varying conditions.
- Additional tests on new pavement marking materials (Task 3):
    - The incorporation of ceramic particles and angular glass particles of various sizes significantly improves the initial friction performance of pavement marking surfaces under both dry and wet conditions
    - The incorporation of ceramic particles and angular glass particles effectively enhances the DF40 and F60 values of pavement markings both during and after polishing.
    - Angular glass particles are more effective in preserving the durability of the pavement surface. In contrast, specimens incorporating ceramic particles and Type 4 glass beads exhibited greater particle detachment during the polishing process and contributed to the accelerated deterioration of the pavement markings.
    - One LWST pass equals 4.4–11.3 TWPD cycles, and a passenger car pass equals 15.7–40.3, based on load and friction. Since the effect of epoxy thickness on friction performance is not clear, future studies are necessary to investigate this effect and include it into the calculation.

In addition, a recommendation on the ratio of various particles can be provided with more future tests results on dry and wet reflectivity, durability, and skid resistance. Through the optimization of the test data, a minimum number of beads without compromising performance can be identified. Further studies are needed to establish recommendations for the optimal bead mix.

REFFERENCES

Abdelkarim,Y., Kim, T.-Y., & Skarpas, A. (2024). Finite element modelling of tire pavement interaction on miromechanical pavement surface. In K. Sennah (Ed.), *Proceedings of the 9th international conference on civil structural and transportation engineering, ICCSTE 2024*. Avestia Publishing. https://doi.org/10.11159/iccste24.163

Alcázar Vargas, M., Pérez Fernández, J., Sánchez Andrades, I., Cabrera Carrillo, J. A., & Castillo Aguilar, J. J. (2022). Modeling of the influence of operational parameters on tire lateral dynamics. *Sensors*, *22*(17), 6380. https://doi.org/10.3390/s22176380

Ali, P. J. M. & Faraj, R. H. (2014). Data normalization and standardization: A technical report. *Machine Learning Technical Reports*, *1*(1). https://doi.org/10.13140/RG.2.2.28948.04489

American Association of State Highway and Transportation Officials. (2013). *Standard specification for glass beads used in pavement markings* (M247) American Association of State Highway and Transportation Officials.

American Association of State Highway and Transportation Officials. (2018). *A policy on geometric design of highways and streets* (7th ed).

American Association of State Highway and Transportation Officials. (2021). *Standard practice for sample preparation and polishing of asphalt mixture specimens for dynamic friction* (pp. 104–21).

Anderson, D. A., & Henry, J. J. (1980). Wet-pavement friction of pavement-marking materials. *Transportation Research Record, 777*, 58–62.

Anupam, K., Srirangam, S. K., Scarpas, A., & Kasbergen, C. (2013). Influence of temperature on tire–pavement friction: Analyses. *Transportation Research Record*, *2369*(1), 114–124. https://doi.org/10.3141/2369-13

Anupam, K., Srirangam, S. K., Scarpas, A., Kasbergen, C., & Kane, M. (2014*)*. Study of cornering maneuvers of a pneumatic tire on asphalt pavement surfaces using the finite element method*. Transportation Research Record*, *2457*(1), 129–139. https://doi.org/10.3141/2457-14

Artamendi, I., Phillips, P., Allen, B., & Woodward, D. (2013). Development of UK proprietary asphalt surfacing skid resistance and texture*.* In I. L. Al-Qadi & S. Murrell (Eds.), *Airfield and highway pavement 2013: Sustainable and efficient pavements* (pp. 865–874). https://doi.org/10.1061/9780784413005.071

ASTM International. (2015a). *Standard specification for standard smooth tire for pavement skid-resistance tests* (ASTM E524-08 [2015]). https://doi.org/10.1520/E0524-08R15

ASTM International. (2015b). *Standard test method for skid resistance of paved surfaces using a full-scale tire* (ASTM E274-06). https://doi.org/10.1520/E0274-06

ASTM International. (2019a). *Standard test method for measuring pavement macrotexture properties using the circular track meter* (ASTM E2157-15). https://doi.org/10.1520/E2157-15

ASTM International. (2019b). *Standard test method for measuring surface frictional properties using the dynamic friction tester* (ASTM E1911-19). https://doi.org/10.1520/E1911-19

ASTM International. (2023). *Standard practice for calculating international friction index of a pavement surface* (ASTM E1960-07[2023]). https://doi.org/10.1520/E1960-07R23

Badirli, S., Liu, X., Xing, Z., Bhowmik, A., Doan, K., & Keerthi, S. S. (2020). *Gradient boosting neural networks: GrowNet*. arXiv preprint arXiv:2002.07971. https://doi.org/10.48550/arXiv.2002.07971

Bao, J., Hu, X., Peng, C., Duan, J., Lin, Y., Tao, C., Jiang, Y., & Li, S. (2024). *Advancing INDOT's friction test program for seamless coverage of system: Pavement markings, typical aggregates, color surface treatment, and horizontal curves* (Joint Transportation Research Program Publication No. FHWA/IN/JTRP-2024/09). Purdue University. https://doi.org/10.5703/1288284317734

Bao, J., Zhao, H., Jiang, Y., & Li, S. (2025). International perspectives on skid resistance requirements for pavement markings: A comprehensive synthesis and analysis. *Lubricants*, *13*(1), 29. https://doi.org/10.3390/lubricants13010029

Beaton, J. L., Zube, E., & Skog, J. (1969). Reduction of accidents by pavement grooving. *Highway Research Board Special Report*, *101*, 110–125. https://onlinepubs.trb.org/Onlinepubs/sr/sr101/101-011.pdf

Belrzaeg, M., Ahmed, A. A., Almabrouk, A. Q., Khaleel, M. M., Ahmed, A. A., & Almukhtar, M. (2021). Vehicle dynamics and tire models: An overview. *World Journal of Advanced Research and Reviews*, *12*(1), 331–348. https://doi.org/10.30574/wjarr.2021.12.1.0524

Bowman, B. L., & Kowshik, R. R. (1994). Comparative study of glass bead usage in pavement marking reflectorization. *Transportation Research Record*, *1442*, 57–64. http://onlinepubs.trb.org/Onlinepubs/trr/1994/1442/1442-007.pdf

Breiman, L. (2001). Random forests. *Machine Learning*, *45*(1), 5–32. https://doi.org/10.1023/A:1010933404324

British Standards Institution. (2018*). Road marking materials: Road marking performance for road users and test methods* (BS EN 1436:2018).

Bruzelius, F., Hjort, M., & Svendenius, J. (2014). Validation of a basic combined-slip tyre model for use in friction estimation applications. *Proceedings of the Institution of Mechanical Engineers, Part D: Journal of Automobile Engineering*, *228*(13), 1622–1629. https://doi.org/10.1177/0954407013511797

Canudas-de-Wit, C., Tsiotras, P., Velenis, E., Basset, M., & Gissinger, G. (2002). *Dynamic friction models for longitudinal road/tire interaction: Experimental results* [Paper presentation]. 21st IASTED Conference on Modelling, Identification and Control, Innsbruck, Austria. https://dcsl.gatech.edu/papers/iasted02b.pdf

Coves-Campos, A., Bañón, L., Coves-García, J. A., & Ivorra, S. (2018). In situ study of road marking durability using glass microbeads and antiskid aggregates as drop-on materials. *Coatings*, *8*(10), 371. https://doi.org/10.3390/coatings8100371

Cutler, A., Cutler, D. R., & Stevens, J. R. (2012). Random Forests. In C. Zhang & Y. Ma (Eds.), *Ensemble machine learning: Methods and applications* (pp. 157–175). Springer. https://doi.org/10.1007/978-1-4419-9326-7_5

Dassault Systèmes. (2023). *Abaqus/CAE user's manual*.

de León Izeppi, E., Flintsch, G., Katicha, S., McGhee, K., & McCarthy, R. (2019). *Locked-wheel and sideway-force continuous friction measurement equipment comparison and evaluation report* (Virginia Polytechnic Institute and State University Report No. FHWA-RC-19-001). Federal Highway Administration. https://www.fhwa.dot.gov/pavement/management/pubs/fhwarc19001.pdf

Fathi, H., El-Sayegh, Z., Ren, J., & El-Gindy, M. (2024). Modeling and validation of a passenger car tire using finite element analysis. *Vehicles*, *6*(1), 384–402. https://doi.org/10.3390/vehicles6010016

Federal Highway Administration. (2023). *Manual on uniform traffic control devices for streets and highways* (11th ed.). https://mutcd.fhwa.dot.gov/

Friedman, J. H. (2001). Greedy function approximation: A gradient boosting machine. *The Annals of Statistics*, *29*(5), 1189–1232. https://doi.org/10.1214/aos/1013203451

Ghoreishy, M. H. R. (2006). Finite element analysis of steady rolling tyre with slip angle: Effect of belt angle. *Plastics, Rubber and Composites*, *35*(2), 83–90. https://doi.org/10.1179/174328906X79905

Ghoreishy, M. H. R. (2008). A state-of-the-art review of the finite element modelling of rolling tyres. *Iranian Polymer Journal*, *17*(8), 571–597.

Gillespie, T. D. (2021). *Fundamentals of vehicle dynamics, Revised edition*. SAE International.

Gu, F., Chen, C., Heitzman, M., Potter, R., & Powell, B. (2023). Evaluation of locked-wheel skid trailer and SCRIM friction measurements at NCAT test track. *International Journal of Pavement Engineering*, *24*(2). https://doi.org/10.1080/10298436.2022.2124249

Güven, O., & Melville, J. G. (1999). Pavement cross slope design—A technical review. Auburn University: Highway Research Center. https://eng.auburn.edu/files/centers/hrc/IR-99-01.pdf

Hansen, C. B., Ali, A. M. M., Ethelberg, M. Z., & Wozniak, M. M. (2019). *Comparing random forest, XGBoost and neural networks with hyperparameter optimization by nested cross-validation* [Bachelor's thesis]. Roskilde University. https://rucforsk.ruc.dk/ws/files/64939887/Machine_Learning_Bachelor_2019.pdf

Harris, L., & Grzes, M. (2019). Comparing explanations between random forests and artificial neural networks [Conference proceeding]. In *2019 IEEE International Conference on Systems, Man and Cybernetics (SMC)* (pp. 2978–2985*)*. https://doi.org/10.1109/smc.2019.8914321

Hoerner, T. E., Smith, K. D., Larson, R. M., & Swanlund, M. E. (2003). Current practice of portland cement concrete pavement texturing. *Transportation Research Record*, *1860*(1), 178–186. https://doi.org/10.3141/1860-20

Indiana Department of Transportation. (2018). *Acceptance procedures for HMA surface mixture coarse aggregates for ESAL ≥ 10,000 (ITM no. 221-18).* https://www.in.gov/indot/doing-business-with-indot/files/221_testing.pdf

Jagadeesh, A., Premarathna, W. A. A. S., Kumar, A., Kasbergen, C., & Erkens, S. (2025). Finite element modelling of jointed plain concrete pavements under rolling forklift tire. *Engineering Structures*, *328*, 119705. https://doi.org/10.1016/j.engstruct.2025.119705

Jung, H. C., Park, W. C., & Jeong, K. M. (2018). Finite element analysis of tire traction using a rubber-ice friction model. *Open Journal of Applied Sciences*, *8*(11), 495–505. https://doi.org/10.4236/ojapps.2018.811040

Kassem, E., Lowry, M., Fanijo, E., & Mohamed, M. (2021). *Deterioration of green conflict paint for bicycle facilities* (Pacific Northwest Transportation Consortium Report No. 2018-S-UI-2). https://rosap.ntl.bts.gov/view/dot/58694

Khalil, N. Z., Kong, N., & Fricke, H. (2024). The influence of GNP on the mechanical and thermomechanical properties of epoxy adhesive: Pearson correlation matrix and heatmap application in data interpretation. *Polymer Composites*, *45*(10), 8997–9018. https://doi.org/10.1002/pc.28390

Korunović, N., Trajanović, M., Stojković, M., Mišić, D., & Milovanović, J. (2011). Finite element analysis of a tire steady rolling on the drum and comparison with experiment. *Strojniški vestnik –The Journal of Mechanical Engineering*, *57*(12), 888–897. https://doi.org/10.5545/sv-jme.2011.124

Kumar, A., Tang, T., Gupta, A., & Anupam, K. (2023). A state-of-the-art review of measurement and modelling of skid resistance: The perspective of developing nation. *Case Studies in Construction Materials*, *18*, e02126. https://doi.org/10.1016/j.cscm.2023.e02126

Lai, T. H. H., Cardell-Oliver, R., Hu, Y., & Beard, S. (2022). *Analysis of the relationship between SCRIM and texture depths* [Paper presentation]. CEED Seminar Proceedings 2022. https://ceed.wa.edu.au/wp-content/uploads/2022/09/Tim-Hok-Him-Lai-Seminar-Paper.pdf

Li, B., & Bei, S. (2019). Research method of vehicle rollover mechanism under critical instability condition. *Advances in Mechanical Engineering*, *11*(1). https://doi.org/10.1177/1687814018821218

Li, S., Zhu, K., Noureldin, S., & Harris, D. (2005). Identifying friction variations with the standard smooth tire for network pavement inventory friction testing. *Transportation Research Record*, *1905*(1), 157–165. https://doi.org/10.1177/0361198105190500117

Li, Z., Chen, W., Li, Y., & Wu, W. (2023). Finite element analysis of tyre contact interaction considering simplified pavement with different aggregate sizes. *Applied Sciences*, *13*(21), 12011. https://doi.org/10.3390/app132112011

MathWorks. (n.d.). *Gaussian process regression models*. https://www.mathworks.com/help/stats/gaussian-process-regression-models.html

Mhaske, P., Narwade, P.N., & Nagarkar, M. P. (2015). Analysis of vertical stiffness of passenger car tire at different pressure using FE model. *International Journal of Innovations in Engineering Research and Technology,* (2015:ICITDCEME). https://repo.ijiert.org/index.php/ijiert/article/view/712

Nackenhorst, U. (2004). The ALE-formulation of bodies in rolling contact. *Computer Methods in Applied Mechanics and Engineering*, *193*(39–41), 4299–4322. https://doi.org/10.1016/j.cma.2004.01.033

Nadkarni, S. B., Vijay, G. S., & Kamath, R. C. (2023). Comparative study of random forest and gradient boosting algorithms to predict airfoil self-noise. *Engineering Proceedings*, *59*(1), 24. https://doi.org/10.3390/engproc2023059024

Narasimha Rao, K. V., & Krishna Kumar, R. (2007). Simulation of tire dynamic behavior using various finite element techniques. *International Journal for Computational Methods in Engineering Science and Mechanics*, *8*(5), 363–372. https://doi.org/10.1080/15502280701471566

Natekin, A., & Knoll, A. (2013). Gradient boosting machines, a tutorial. *Frontiers in Neurorobotics*, *7*, 21. https://doi.org/10.3389/fnbot.2013.00021

Oliver, J. W. H., Tredrea, P. F., & Pratt, D. N. (1989). *Seasonal variation of skid resistance in Australia*. Australian Road Research Board.

Peng, C., Tao, C., Jiang, Y., & Li, S. (2024). Investigation of locked wheel skid tester practicability on horizontal curves: A camera-based field implementation. *Transportation Research Record*, *2678*(12), 848–863. https://doi.org/10.1177/03611981241248170

Plonsky, L., & Ghanbar, H. (2018). Multiple regression in L2 research: A methodological synthesis and guide to interpreting R^2 values. *The Modern Language Journal*, *102*(4), 713–731. https://doi.org/10.1111/modl.12509

Rabari, A., Gundaliya, P. J., & Gupta, D. (2018). Analysis of superelevation and side friction factor on horizontal curve. *International Research Journal of Engineering and Technology*, *5*(2), 1201–1205. https://irjet.net/archives/V5/i2/IRJET-V5I2259.pdf

Rafei, M., Ghoreishy, M. H. R., & Naderi, G. (2018). Thermo-mechanical coupled finite element simulation of tire cornering characteristics—Effect of complex material models and friction law. *Mathematics and Computers in Simulation*, *144*, 35–51. https://doi.org/10.1016/j.matcom.2017.05.011

Rajamani, R. (2012). *Vehicle dynamics and control* (2nd ed.). Springer. https://doi.org/10.1007/978-1-4614-1433-9

Ray, L. R. (1997). Nonlinear tire force estimation and road friction identification: Simulation and experiments. *Automatica*, *33*(10), 1819–1833. https://doi.org/10.1016/S0005-1098(97)00093-9

Rodin, H., III, Nassiri, S., & Yekkalar, M. (2018). *Evaluation of motorcyclists' and bikers' safety on wet pavement markings* (Pacific Northwest Transportation Consortium Report). https://rosap.ntl.bts.gov/view/dot/63404

Roe, P. G., & Sinhal, R. (2005). *Recent developments-to-the SCRIM measurement-technique in the UK*. TRL Limited.

Rosta, S., & Gáspár, L. (2023). *Skid resistance of asphalt pavements*. *Eng*, *4*(2), 1597–1615. https://doi.org/10.3390/eng4020091

scikit-learn. (n.d.). *Gaussian processes*. https://scikit-learn.org/stable/modules/gaussian_process.html

Shields, M. D. (2021). Gaussian process regression. *UQpy*. https://uqpyproject.readthedocs.io/en/latest/surrogates/gpr.html

Srirangam, S. K., Anupam, K., Scarpas, A., & Kösters, A. (2013). *Influence of temperature on tire-pavement friction-I: Laboratory tests and finite element modeling* [Paper presentation]. Transportation Research Board Annual Meeting, Washington, D.C.

Stephenson, M. (2018). Skidding resistance: Measurement and use of data. *The International Journal of Pavement Engineering and Asphalt Technology*, *19*(2). https://www.ljmu.ac.uk/-/media/files/ljmu/about-us/events/asphalt-conference/paper-3.pdf

Tönük, E., & Ünlüsoy, Y. S. (2001). Prediction of automobile tire cornering force characteristics by finite element modeling and analysis. *Computers and Structures*, *79*(13), 1219–1232. https://doi.org/10.1016/s0045-7949(01)00022-0

Trefethen, L. N., & Weideman, J. A. C. (2014). The exponentially convergent trapezoidal rule. *SIAM Review*, *56*(3), 385–458. https://doi.org/10.1137/130932132

Wang, H., Al-Qadi, I. L., & Stanciulescu, I. (2014). Effect of surface friction on tire–pavement contact stresses during vehicle maneuvering. *Journal of Engineering Mechanics*, *140*(4), 04014001. https://doi.org/10.1061/(ASCE)EM.1943-7889.0000691

Xu, J., Jia, M., Gao, C., & Lv, W. (2023). Limited response of curve safety level to friction factor and superelevation variation under repeated traffic loads. *Sustainability*, *15*(24), 16923. https://doi.org/10.3390/su152416923

Xu, N., Yang, Y., & Guo, K. (2020). A discrete tire model for cornering properties considering rubber friction. *Automotive Innovation*, *3*(2), 133–146. https://doi.org/10.1007/s42154-020-00097-y

Yan, X. (2003). Nonlinear three-dimensional finite element analysis of steady rolling radial tires. *Journal of Reinforced Plastics and Composites*, *22*(8), 733–750. https://doi.org/10.1177/0731684403022008004

Yu, M., Wu, G., Kong, L., & Tang, Y. (2017). Tire–pavement friction characteristics with elastic properties of asphalt pavements. *Applied Sciences*, *7*(11), 1123. https://doi.org/10.3390/app7111123

Zhang, Q., Shangguan, L., Li, T., Ma, X., Yin, Y., & Dong, Z. (2023). Tire–pavement interaction simulation based on finite element model and response surface methodology. *Computation, 11*(9), 186. https://doi.org/10.3390/computation11090186

APPENDICES

Appendix A. Locked Wheel Skid Trailer In-Situ Test Results From SPR-4646 (Bao Et Al., 2024)

Appendix B. Locked Wheel Skid Trailer In-Situ Test Results

Appendix C. FEA Friction Number Simulation Results

Appendix D. Machine Learning Result of Friction Adjustment Factor From FEA Simulations

Appendix E. Assessment and Comparison of LWST and SCRIM Field Test Route Details

Appendix F. Pavement Markings Lab Test Results and Photos

Appendix A. Locked-Wheel Skid Trailer In-Situ Test Results From SPR-4646 (Bao et al., 2024)

Table A.1 *Data Measurements from Airport Friction Tests (April 2024).*

Vertical Force F_Z (lb)	Longitudinal Friction Force F_x (lb)	Curvature Radius (ft)	Tire Speed (mph)	Test Tire Slip Angle (°)	Vehicle Articulation Angle (°)	Camber
892	729	165.13	13.66230	-5.751517852	5.2928181	0
895	752	165.13	13.74729	-5.726146019	4.599217996	0
808	561	165.13	23.02924	-3.666031082	2.703258334	0
787	569	165.13	23.62321	-5.745144632	2.959999527	0
631	351	165.13	34.44051	-3.85982	1.754519653	0
696	395	165.13	36.1126	-2.90578	5.137543164	0
974	788	146	12.59475	8.404424813	-4.867974419	0
1005	788	136.48	12.02413	7.241279617	-6.950920275	0
969	790	146	12.72534	5.442504961	-4.33522109	0
1008	773	136.48	12.17057	7.628625305	-5.991552728	0
1089	713	146	20.93595	5.781367789	-4.238160526	0
1154	840	136.48	19.51254	6.330145978	-6.365301812	0
1075	672	146	20.71231	6.679737144	-4.224539388	0
1156	782	136.48	18.40004	6.063244609	-5.693386612	0
1257	560	146	30.55440	6.227848857	-2.440121793	0
1257	559	146	31.67547	6.829862364	-2.872285621	0
1271	771	136.48	27.66835	3.924644506	-0.350547025	0
1328	821	136.48	28.16540	5.773564137	-0.831041917	0
941	704	infinity	39.83058	0.015058672	-	0
932	788	infinity	25.65141	-0.121037025	-	0
931	816	infinity	20.51910	0.093597293	-	0
925	812	infinity	14.54373	-0.607053664	-	0
938	682	infinity	39.94888	0.170594042	-	0
916	771	infinity	25.89180	-0.180506747	-	0
921	822	infinity	20.47434	0.212469698	-	0
931	807	infinity	14.72801	0.008509310	-	0
935	691	infinity	40.18021	-0.069424100	-	0
933	776	infinity	25.59718	0.116934659	-	0
928	826	infinity	20.66238	0.389093921	-	0
926	814	infinity	15.23819	-0.196714668	-	0

Vertical Force F_Z (lb)	Longitudinal Friction Force F_x (lb)	Curvature Radius (ft)	Tire Speed (mph)	Test Tire Slip Angle (°)	Vehicle Articulation Angle (°)	Camber
832	668	165.13	23.06859	-5.785903121	3.892268776	0
811	638	165.13	21.86412	-5.169643943	3.384584009	0
845	678	165.13	24.16971	-6.018679188	0.550418401	0
826	686	165.13	21.54012	-5.695343150	2.600247724	0
838	661	165.13	23.63146	-5.543233566	0.282279422	0
803	657	165.13	23.64312	-5.307909347	2.840125115	0
863	713	165.13	19.89829	-7.353181167	2.988668725	0
846	652	165.13	20.40975	-6.858642264	3.130534248	0
866	717	165.13	20.22881	-6.317005515	3.273073784	0
848	664	165.13	20.51237	-6.327960379	4.430516782	0
859	695	165.13	20.26141	-6.495695877	2.793164560	0
840	665	165.13	20.62991	-5.854898154	2.835494664	0
882	800	165.13	15.35101	-7.560528367	2.232561978	0
882	693	165.13	15.24876	-7.243853288	3.483546143	0
888	776	165.13	15.59926	-7.217522041	2.239600760	0
877	700	165.13	16.32777	-6.477944556	3.544947623	0
871	751	165.13	16.94923	-7.187550632	1.716512831	0
864	680	165.13	16.97430	-6.434215155	3.494911301	0
1132	905	165.13	22.56135	4.929394313	-6.145475214	0
1145	932	165.13	22.30079	4.554600981	-6.368956485	0
1130	866	165.13	23.19811	4.432694349	-5.861274600	0
1076	882	165.13	18.66951	4.997697087	-6.535332991	0
1083	876	165.13	19.51077	4.991446685	-6.176366622	0
1031	915	165.13	18.86636	5.438873886	-5.908810866	0
983	882	165.13	14.19641	7.128058162	-5.930055383	0
993	886	165.13	14.61059	7.164015896	-6.042474646	0
989	852	165.13	13.70036	7.190030794	-5.928043811	0

Table A.2 *Data Measurements from S.R. 26 Friction Tests.*

Vertical Force F_Z (lb)	Friction Force F_f (lb)	Curvature Radius (ft)	Tire Speed (mph)	Test Tire Slip Angle (°)	Vehicle Articulation Angle (°)	Camber
971	585	infinity	29.32223	0.00556	-0.03564	0.000
970	577	infinity	29.65789	0.01731	-0.06461	0.000
960	636	infinity	15.00631	0.05974	-0.11380	0.000
969	583	infinity	15.62535	0.11502	-0.08665	0.000
964	611	infinity	14.74244	0.08726	-0.10043	0.000
953	623	infinity	40.13993	0.07784	-0.04373	0.000
965	533	infinity	39.69890	0.04444	-0.07421	0.000
1001	452	2348	29.94574	2.99520	-0.53674	0.083
989	513	2348	30.08078	3.44900	-0.69473	0.083
980	594	2348	30.17151	-3.23930	1.01492	0.077
1004	564	2348	29.83766	-3.33020	0.97565	0.077
958	557	2348	14.93938	1.86060	-0.66798	0.077
955	513	2348	14.96021	2.00360	-0.68043	0.077
978	598	infinity	15.22523	0.06777	0.15600	0.000
1012	647	2348	14.74003	-1.76170	0.98463	0.083
1004	665	2348	14.85150	-2.19650	0.84431	0.083
947	727	infinity	14.98606	-0.00559	0.07802	0.000
968	569	infinity	40.85553	0.04102	-0.00176	0.000
960	647	infinity	30.08515	0.03727	-0.06896	0.000
978	535	infinity	28.27379	0.00357	-0.06871	0.000
980	481	2348	28.75471	3.31270	-0.63336	0.083
984	488	2348	28.81379	3.40120	-0.52222	0.083
1007	558	2348	28.74320	-3.12950	1.07141	0.077
1016	548	2348	29.18659	-2.99130	0.96256	0.077
958	549	2348	15.04770	1.56742	-1.14089	0.077
957	550	2348	15.25551	1.99080	-1.26840	0.077
974	608	infinity	14.79671	0.00752	0.13194	0.000
1016	634	2348	14.77189	-1.67165	0.47997	0.083
1015	612	2348	14.18153	-1.60001	0.39071	0.083
965	701	infinity	14.95686	-0.00306	-0.05554	0.000
957	632	infinity	29.18635	-0.04594	0.01034	0.000
965	611	infinity	29.64864	-0.01077	-0.00322	0.000
965	563	infinity	29.41965	0.02627	-0.01153	0.000
980	578	infinity	39.59928	0.01665	-0.00012	0.000

Vertical Force F_Z (lb)	Friction Force F_f (lb)	Curvature Radius (ft)	Tire Speed (mph)	Test Tire Slip Angle (°)	Vehicle Articulation Angle (°)	Camber
984	521	infinity	39.10395	0.01733	0.00494	0.000
976	533	2348	29.35742	2.82660	-0.71302	0.083
978	517	2348	29.39508	3.36960	-0.82328	0.083
1007	582	2348	28.72242	-3.17950	0.55886	0.077
1007	573	2348	29.91297	-3.28300	0.65475	0.077
956	572	2348	15.03217	2.00310	-0.54262	0.077
958	521	2348	15.03110	1.73640	-0.85200	0.077
980	606	infinity	15.32027	0.10946	0.11629	0.000
1016	660	2348	15.28421	-1.94558	0.79707	0.083
1010	695	2348	15.30922	-2.18195	0.21759	0.083
951	725	2348	15.37218	-0.35940	0.18130	0.000
951	662	infinity	30.42320	0.00325	0.01659	0.000
977	591	infinity	28.81360	-0.00233	0.01648	0.000
967	577	infinity	28.29820	-0.00184	0.01486	0.000

Appendix B. Locked-Wheel Skid Trailer In-Situ Test Results

Table B.1 *Data Measurements from Airport Friction Tests (October 2024).*

Vertical Force F_Z (lbs)	Longitudinal Friction Force F_x (lbs)	Curvature Radius (ft)	Tire Speed (mph)	Test Tire Slip Angle (°)	Camber
832	668	165	24.28	-5.79	0
811	638	165	22.67	-5.17	0
845	678	165	25.06	-6.02	0
826	686	165	22.41	-5.70	0
838	661	165	25.17	-5.54	0
803	657	165	25.06	-5.31	0
863	713	165	20.28	-7.35	0
846	652	165	20.38	-6.86	0
866	717	165	20.49	-6.32	0
848	664	165	20.33	-6.33	0
859	695	165	20.38	-6.50	0
840	665	165	20.33	-5.85	0
882	800	165	15.65	-7.56	0
882	693	165	15.76	-7.24	0
888	776	165	15.65	-7.22	0
877	700	165	16.17	-6.48	0
871	751	165	16.64	-7.19	0
864	680	165	17.16	-6.43	0
1132	905	165	25.38	4.93	0
1145	932	165	25.38	4.55	0
1130	866	165	25.32	4.43	0
1076	882	165	20.49	5.00	0
1083	876	165	21.11	4.99	0
1031	915	165	20.18	5.44	0
983	882	165	14.72	7.13	0
993	886	165	14.56	7.16	0
989	852	165	14.82	7.19	0
941	704	infinity	39.89	0	0
932	788	infinity	25.53	0	0
931	816	infinity	20.54	0	0
925	812	infinity	15.24	0	0
938	682	infinity	40.2	0	0
916	771	infinity	25.64	0	0

Table B.2 *Data Measurements from S.R. 47 Friction Tests.*

Vertical Force F_Z (lbs)	Friction Force F_f (lbs)	Curvature Radius (ft)	Tire Speed (mph)	Test Tire Slip Angle (°)	Camber
965	346	382	39.59	-3.77	0.092
1025	392	382	39.8	-5.61	0.092
1152	440	422	40.27	4.77	0.067
1161	429	422	38.96	6.41	0.067
905	385	219	39.59	-2.76	0.102
799	319	219	38.8	-6.27	0.102
1087	399	326	40.69	3.88	0.031
1028	477	326	40.63	3.64	0.031
1079	454	519	40.01	2.00	0.018
1024	472	519	39.59	3.24	0.018
955	327	521	39.06	-2.60	0.089
993	345	521	39.95	-6.55	0.089
1104	357	422	40.11	3.03	0.008
1103	329	422	39.06	5.03	0.008
987	336	549	40.95	-2.59	0.060
1030	445	1434	39.64	-1.54	0.038
1024	457	1434	40.06	-3.61	0.038
1025	482	1434	40.11	-3.10	0.038
1114	439	1257	39.8	1.53	0.043
1304	410	1257	39.8	4.27	0.043
1026	416	382	29.65	-3.71	0.092
1010	417	382	30.12	-4.87	0.092
1025	471	422	30.23	2.21	0.067
1139	510	422	29.34	6.14	0.067
1006	454	219	29.86	-4.12	0.102
965	441	219	28.76	-8.19	0.102
989	506	326	30.02	0.04	0.031
1016	473	326	30.33	1.09	0.031
1020	504	519	30.23	1.30	0.018
1007	516	519	29.55	3.31	0.018
979	397	521	29.86	-4.87	0.089
972	385	521	30.28	-7.43	0.089
1067	419	443	29.86	2.93	0.008
1053	422	443	30.28	3.84	0.008

Vertical Force F_Z (lbs)	Friction Force F_f (lbs)	Curvature Radius (ft)	Tire Speed (mph)	Test Tire Slip Angle (°)	Camber
989	405	549	30.64	-2.56	0.060
1021	409	549	31.17	-2.46	0.060
1006	513	1237	29.91	-0.52	0.038
1028	517	1237	30.17	-1.78	0.038
1023	517	1237	30.59	-2.95	0.038
1082	454	579	30.02	2.46	0.056
1088	470	579	30.02	7.10	0.056
1003	510	1434	30.12	-1.58	0.043
1030	512	1434	30.49	-3.26	0.043
1022	529	1434	31.12	-3.14	0.043
989	448	1434	39.64	-1.40	0.043
1015	485	1434	39.53	-3.68	0.043
1030	463	1434	40.06	-4.55	0.043

Table B.3 *Data Measurements from S.R. 75 Friction Tests.*

Vertical Force F_Z (lbs)	Friction Force F_f (lbs)	Curvature Radius (ft)	Tire Speed (mph)	Test Tire Slip Angle (°)	Camber
1046	465	533	30.17	4.37	0.102
1046	493	533	30.33	8.14	0.102
1064	449	533	30.44	8.47	0.102
1037	466	655	30.12	-3.35	0.090
1034	456	655	29.96	-7.45	0.090
1026	478	655	30.49	-7.04	0.090
1044	507	880	30.12	3.66	0.108
1067	476	880	29.7	7.53	0.108
1044	491	880	29.91	8.01	0.108
1008	499	674	30.12	-3.39	0.092
1021	488	674	30.49	-6.96	0.092
1039	490	674	30.23	-7.94	0.092
1095	466	533	40.21	3.82	0.102
1120	478	533	40.27	8.60	0.102
1137	443	533	40.27	7.63	0.102
1003	486	655	40.48	-0.39	0.090
965	384	655	40.06	-8.43	0.090
994	422	655	40.37	-7.75	0.090
1093	481	880	40.27	3.38	0.108
1123	451	880	39.17	8.30	0.108
1083	481	880	39.22	8.13	0.108
969	421	674	40.79	-3.93	0.092
989	423	674	40.21	-7.99	0.092
986	402	674	40.21	-8.58	0.092

Appendix C. FEA Friction Number Simulation Results

***Table C.1** Friction Numbers by Speed, Vertical Force, Slip Angle, and Camber Angle on the Inner Tire.*

Speed (mph)	Vertical Force (lb)	Slip Angle (degree)	Camber	Curve Radius (ft)	FEA Horizontal Force (lb)	FEA FN	Friction Adjustment Factor
30	1578.7	5.1	0	150	643.1	0.407	0.874
30	1559.3	5.1	0.02	150	636.5	0.408	0.876
30	1539.3	8.2	0.04	150	631.5	0.41	0.881
30	1518.7	11.2	0.06	150	624.2	0.411	0.882
30	1497.5	14.3	0.08	150	586.2	0.391	0.84
30	1475.9	17.4	0.1	150	550.1	0.373	0.8
35	1756.9	3.9	0	150	699.7	0.398	0.884
35	1739.5	4.4	0.02	150	676.3	0.389	0.863
35	1721.3	6.7	0.04	150	677.1	0.393	0.873
35	1702.5	9.1	0.06	150	636.5	0.374	0.83
35	1683.1	11.5	0.08	150	602.3	0.358	0.794
35	1663.1	13.8	0.1	150	561.5	0.338	0.749
40	1962.5	2.6	0	150	681.5	0.347	0.817
40	1947.3	3.5	0.02	150	700	0.359	0.845
40	1931.3	5.1	0.04	150	666.6	0.345	0.812
40	1914.6	6.6	0.06	150	605.8	0.316	0.744
40	1897.2	8.2	0.08	150	621.3	0.328	0.77
40	1879	9.7	0.1	150	564.2	0.3	0.706
45	2195.5	1	0	150	681	0.31	0.72
45	2182.9	2.6	0.02	150	691.2	0.317	0.735
45	2169.3	3.2	0.04	150	681.9	0.314	0.73
45	2155	3.8	0.06	150	679.8	0.315	0.733
45	2139.8	4.4	0.08	150	651.7	0.305	0.707
45	2123.8	5.1	0.1	150	639	0.301	0.699
50	2455.9	-0.7	0	150	688.8	0.28	0.668
50	2446.1	1.6	0.02	150	740.7	0.303	0.722
50	2435.3	1.1	0.04	150	687.5	0.282	0.673
50	2423.6	0.7	0.06	150	709.3	0.293	0.698
50	2411	0.3	0.08	150	703.5	0.292	0.695

Speed (mph)	Vertical Force (lb)	Slip Angle (degree)	Camber	Curve Radius (ft)	FEA Horizontal Force (lb)	FEA FN	Friction Adjustment Factor
50	2397.4	-0.1	0.1	150	684.6	0.286	0.681
30	1249.8	1.7	0	450	552.4	0.442	0.949
30	1226.8	3	0.02	450	528.4	0.431	0.925
30	1203.3	4.1	0.04	450	518	0.43	0.924
30	1179.4	5.1	0.06	450	505	0.428	0.919
30	1155	6.1	0.08	450	495.8	0.429	0.921
30	1130.3	7.1	0.1	450	477.9	0.423	0.908
35	1309.2	1.3	0	450	552.5	0.422	0.937
35	1286.8	2.8	0.02	450	531.6	0.413	0.917
35	1264	3.6	0.04	450	516.7	0.409	0.907
35	1240.6	4.4	0.06	450	500.1	0.403	0.895
35	1216.9	5.2	0.08	450	481	0.395	0.877
35	1192.7	5.9	0.1	450	468.5	0.393	0.872
40	1377.7	0.9	0	450	555.7	0.403	0.949
40	1356.1	2.5	0.02	450	544.5	0.402	0.944
40	1334	3	0.04	450	524.6	0.393	0.925
40	1311.3	3.5	0.06	450	526.5	0.401	0.944
40	1288.2	4.1	0.08	450	514	0.399	0.939
40	1264.7	4.6	0.1	450	487.4	0.385	0.906
45	1455.4	0.3	0	450	557.7	0.383	0.89
45	1434.6	2.2	0.02	450	540.7	0.377	0.875
45	1413.3	2.4	0.04	450	524	0.371	0.861
45	1391.4	2.6	0.06	450	524	0.377	0.875
45	1369.1	2.8	0.08	450	461.5	0.337	0.783
45	1346.3	3	0.1	450	485	0.36	0.837
50	1542.2	-0.2	0	450	561.7	0.364	0.868
50	1522.4	1.9	0.02	450	548.5	0.36	0.859
50	1502	1.7	0.04	450	557.4	0.371	0.885
50	1481	1.6	0.06	450	472.8	0.319	0.761
50	1459.5	1.4	0.08	450	524.4	0.359	0.856
50	1437.5	1.3	0.1	450	461.3	0.321	0.765
30	1177.9	1	0	800	533.3	0.453	0.972

Speed (mph)	Vertical Force (lb)	Slip Angle (degree)	Camber	Curve Radius (ft)	FEA Horizontal Force (lb)	FEA FN	Friction Adjustment Factor
30	1154	2.6	0.02	800	521.8	0.452	0.971
30	1129.8	3.2	0.04	800	494	0.437	0.939
30	1105.1	3.7	0.06	800	481.4	0.436	0.935
30	1080.1	4.3	0.08	800	452.1	0.419	0.899
30	1054.7	4.9	0.1	800	425.2	0.403	0.865
35	1211.3	0.7	0	800	532.6	0.44	0.976
35	1187.8	2.4	0.02	800	504	0.424	0.942
35	1163.9	2.9	0.04	800	496.2	0.426	0.946
35	1139.6	3.3	0.06	800	471.6	0.414	0.918
35	1114.9	3.8	0.08	800	455.3	0.408	0.906
35	1089.8	4.2	0.1	800	435.6	0.4	0.887
40	1249.8	0.5	0	800	531.4	0.425	1
40	1226.8	2.3	0.02	800	504.8	0.411	0.968
40	1203.3	2.6	0.04	800	482.8	0.401	0.944
40	1179.4	2.9	0.06	800	462.9	0.393	0.923
40	1155	3.2	0.08	800	463.9	0.402	0.945
40	1130.3	3.4	0.1	800	454.5	0.402	0.946
45	1293.5	0.2	0	800	520.9	0.403	0.935
45	1271	2.1	0.02	800	485.1	0.382	0.887
45	1247.9	2.2	0.04	800	485.2	0.389	0.903
45	1224.4	2.3	0.06	800	477.4	0.39	0.906
45	1200.5	2.5	0.08	800	466.3	0.388	0.902
45	1176.2	2.6	0.1	800	402.6	0.342	0.795
50	1342.3	-0.1	0	800	522.8	0.389	0.928
50	1320.3	1.9	0.02	800	493.7	0.374	0.891
50	1297.8	1.8	0.04	800	496.4	0.382	0.912
50	1274.8	1.8	0.06	800	470	0.369	0.879
50	1251.4	1.7	0.08	800	473.6	0.378	0.902
50	1227.5	1.6	0.1	800	411.9	0.336	0.8
30	1149.7	0.7	0	1150	534.8	0.465	0.999
30	1125.6	2.4	0.02	1150	511.1	0.454	0.975
30	1101	2.8	0.04	1150	492.4	0.447	0.96

Speed (mph)	Vertical Force (lb)	Slip Angle (degree)	Camber	Curve Radius (ft)	FEA Horizontal Force (lb)	FEA FN	Friction Adjustment Factor
30	1076.1	3.2	0.06	1150	472.6	0.439	0.943
30	1050.8	3.6	0.08	1150	440.1	0.419	0.899
30	1025.1	4	0.1	1150	418.4	0.408	0.876
35	1172.9	0.5	0	1150	504.5	0.43	0.955
35	1149.1	2.3	0.02	1150	497.1	0.433	0.96
35	1124.8	2.6	0.04	1150	485.8	0.432	0.959
35	1100.1	2.9	0.06	1150	462.8	0.421	0.934
35	1075	3.2	0.08	1150	448.3	0.417	0.926
35	1049.5	3.5	0.1	1150	423.5	0.403	0.895
40	1199.8	0.3	0	1150	513.5	0.428	1.007
40	1176.2	2.2	0.02	1150	485.8	0.413	0.971
40	1152.2	2.4	0.04	1150	468.1	0.406	0.956
40	1127.7	2.6	0.06	1150	450	0.399	0.939
40	1102.9	2.8	0.08	1150	433.1	0.393	0.924
40	1077.7	3	0.1	1150	438	0.406	0.956
45	1230.1	0.1	0	1150	512.6	0.417	0.968
45	1206.9	2.1	0.02	1150	471.8	0.391	0.908
45	1183.2	2.2	0.04	1150	474.8	0.401	0.932
45	1159.1	2.2	0.06	1150	449.3	0.388	0.9
45	1134.5	2.3	0.08	1150	442.4	0.39	0.906
45	1109.6	2.4	0.1	1150	390.5	0.352	0.817
50	1264.1	-0.1	0	1150	510	0.403	0.962
50	1241.2	1.9	0.02	1150	473	0.381	0.908
50	1217.9	1.9	0.04	1150	480.5	0.395	0.94
50	1194.1	1.8	0.06	1150	450.1	0.377	0.898
50	1169.9	1.8	0.08	1150	450.5	0.385	0.918
50	1145.3	1.7	0.1	1150	415.9	0.363	0.865
30	1134.7	0.5	0	1500	528.6	0.466	1
30	1110.4	2.3	0.02	1500	505.6	0.455	0.977
30	1085.7	2.6	0.04	1500	479.5	0.442	0.948
30	1060.6	2.9	0.06	1500	463.7	0.437	0.939
30	1035.1	3.2	0.08	1500	424.5	0.41	0.88

Speed (mph)	Vertical Force (lb)	Slip Angle (degree)	Camber	Curve Radius (ft)	FEA Horizontal Force (lb)	FEA FN	Friction Adjustment Factor
30	1009.3	3.5	0.1	1500	426.2	0.422	0.906
35	1152.5	0.4	0	1500	505.5	0.439	0.973
35	1128.4	2.2	0.02	1500	489.4	0.434	0.963
35	1103.9	2.5	0.04	1500	476.6	0.432	0.958
35	1079	2.7	0.06	1500	460.9	0.427	0.948
35	1053.7	2.9	0.08	1500	443.4	0.421	0.934
35	1028.1	3.2	0.1	1500	428.6	0.417	0.925
40	1173.1	0.3	0	1500	500.8	0.427	1.004
40	1149.2	2.2	0.02	1500	480.1	0.418	0.983
40	1124.9	2.3	0.04	1500	458.6	0.408	0.959
40	1100.2	2.5	0.06	1500	444.4	0.404	0.95
40	1075.1	2.6	0.08	1500	430.2	0.4	0.941
40	1049.7	2.8	0.1	1500	408.8	0.389	0.916
45	1196.4	0.1	0	1500	497.9	0.416	0.967
45	1172.7	2.1	0.02	1500	468.4	0.399	0.928
45	1148.7	2.1	0.04	1500	464.1	0.404	0.938
45	1124.2	2.2	0.06	1500	449.2	0.4	0.928
45	1099.4	2.2	0.08	1500	435.7	0.396	0.921
45	1074.1	2.3	0.1	1500	395.6	0.368	0.855
50	1222.4	-0.1	0	1500	496.8	0.406	0.969
50	1199.1	2	0.02	1500	468.9	0.391	0.932
50	1175.3	1.9	0.04	1500	474.9	0.404	0.963
50	1151.1	1.9	0.06	1500	436.7	0.379	0.904
50	1126.5	1.8	0.08	1500	431.7	0.383	0.913
50	1101.5	1.8	0.1	1500	411.8	0.374	0.891
30	1085	0	0	Infinity	505.6	0.466	1
35	1085	0	0	Infinity	489	0.451	1
40	1085	0	0	Infinity	461.4	0.425	1
45	1085	0	0	Infinity	467.3	0.431	1
50	1085	0	0	Infinity	455.4	0.42	1

Table C.2 *Friction Numbers by Speed, Vertical Force, Slip Angle, and Camber Angle on the Outer Tire.*

Speed (mph)	Vertical Force (lb)	Slip Angle (degree)	Camber	Curve Radius (ft)	FEA Horizontal Force (lb)	FEA FN	Friction Adjustment Factor
30	591.9	5.1	0	150	295.5	0.499	1.071
30	621.9	5.1	0.02	150	300.5	0.483	1.037
30	651.7	8.2	0.04	150	314.6	0.483	1.036
30	681.1	11.2	0.06	150	311.3	0.457	0.981
30	710.1	14.3	0.08	150	321.6	0.453	0.972
30	738.8	17.4	0.1	150	321.6	0.435	0.934
35	413.8	3.9	0	150	209.6	0.507	1.124
35	445.8	4.4	0.02	150	221.4	0.497	1.102
35	477.6	6.7	0.04	150	231.8	0.485	1.077
35	509.2	9.1	0.06	150	242.2	0.476	1.056
35	540.5	11.5	0.08	150	248.8	0.46	1.022
35	571.5	13.8	0.1	150	260.7	0.456	1.013
40	208.2	2.6	0	150	108	0.519	1.221
40	242.5	3.5	0.02	150	126	0.52	1.222
40	276.8	5.1	0.04	150	144.3	0.521	1.226
40	310.8	6.6	0.06	150	159.6	0.513	1.208
40	344.7	8.2	0.08	150	172	0.499	1.174
40	378.3	9.7	0.1	150	188.5	0.498	1.172
45	-24.8	1	0	150			
45	12.2	2.6	0.02	150	10.6	0.87	2.021
45	49.1	3.2	0.04	150	32.9	0.67	1.556
45	86	3.8	0.06	150	55.2	0.642	1.49
45	122.8	4.4	0.08	150	76.5	0.623	1.447
45	159.4	5.1	0.1	150	97.7	0.613	1.423
50	-285.2	-0.7	0	150			
50	-245.3	1.6	0.02	150			
50	-205.2	1.1	0.04	150			
50	-165.2	0.7	0.06	150			
50	-125.2	0.3	0.08	150			
50	-85.2	-0.1	0.1	150			
30	920.9	1.7	0	450	437.8	0.475	1.021

Speed (mph)	Vertical Force (lb)	Slip Angle (degree)	Camber	Curve Radius (ft)	FEA Horizontal Force (lb)	FEA FN	Friction Adjustment Factor
30	947.1	3	0.02	450	434	0.458	0.984
30	973	4.1	0.04	450	445.5	0.458	0.983
30	998.4	5.1	0.06	450	440.5	0.441	0.947
30	1023.4	6.1	0.08	450	446.2	0.436	0.936
30	1047.9	7.1	0.1	450	447.7	0.427	0.917
35	861.5	1.3	0	450	403.5	0.468	1.04
35	888.4	2.8	0.02	450	402.4	0.453	1.005
35	915	3.6	0.04	450	408.6	0.447	0.991
35	941.1	4.4	0.06	450	402.8	0.428	0.95
35	966.8	5.2	0.08	450	402	0.416	0.923
35	992.1	5.9	0.1	450	403.5	0.407	0.903
40	792.9	0.9	0	450	366.1	0.462	1.086
40	820.7	2.5	0.02	450	365.4	0.445	1.047
40	848	3	0.04	450	369.3	0.435	1.024
40	875	3.5	0.06	450	374	0.427	1.005
40	901.6	4.1	0.08	450	370.3	0.411	0.966
40	927.7	4.6	0.1	450	392.1	0.423	0.994
45	715.3	0.3	0	450	333.5	0.466	1.083
45	743.9	2.2	0.02	450	322.5	0.434	1.007
45	772.2	2.4	0.04	450	333.7	0.432	1.004
45	800.1	2.6	0.06	450	345.3	0.432	1.002
45	827.6	2.8	0.08	450	355.5	0.43	0.998
45	854.7	3	0.1	450	343.9	0.402	0.934
50	628.5	0	0	450	294.6	0.469	1.117
50	658.1	1.9	0.02	450	289.9	0.441	1.05
50	687.4	1.7	0.04	450	301.1	0.438	1.044
50	716.3	1.6	0.06	450	318.6	0.445	1.06
50	744.9	1.4	0.08	450	313.3	0.421	1.003
50	773.2	1.3	0.1	450	316.6	0.409	0.976
30	992.8	1	0	800	461	0.464	0.997
30	1018.3	2.6	0.02	800	470.5	0.462	0.992
30	1043.3	3.2	0.04	800	473.2	0.454	0.974

Speed (mph)	Vertical Force (lb)	Slip Angle (degree)	Camber	Curve Radius (ft)	FEA Horizontal Force (lb)	FEA FN	Friction Adjustment Factor
30	1067.8	3.7	0.06	800	473	0.443	0.951
30	1091.9	4.3	0.08	800	456.5	0.418	0.897
30	1115.5	4.9	0.1	800	445.4	0.399	0.857
35	959.4	0.7	0	800	444.4	0.463	1.028
35	985.2	2.4	0.02	800	429.6	0.436	0.968
35	1010.6	2.9	0.04	800	442	0.437	0.971
35	1035.6	3.3	0.06	800	442.2	0.427	0.948
35	1060.1	3.8	0.08	800	440.1	0.415	0.921
35	1084.1	4.2	0.1	800	434.8	0.401	0.89
40	920.9	0.5	0	800	416.6	0.452	1.064
40	947.1	2.3	0.02	800	410.9	0.434	1.02
40	973	2.6	0.04	800	416.8	0.428	1.007
40	998.4	2.9	0.06	800	411.4	0.412	0.969
40	1023.4	3.2	0.08	800	410.4	0.401	0.943
40	1047.9	3.4	0.1	800	429.8	0.41	0.965
45	877.2	0.2	0	800	391.5	0.446	1.036
45	903.9	2.1	0.02	800	380.1	0.42	0.977
45	930.3	2.2	0.04	800	394.3	0.424	0.984
45	956.3	2.3	0.06	800	397.5	0.416	0.965
45	981.8	2.5	0.08	800	399.1	0.407	0.944
45	1006.8	2.6	0.1	800	382.6	0.38	0.882
50	828.4	0	0	800	371.7	0.449	1.07
50	855.7	1.9	0.02	800	364.5	0.426	1.015
50	882.6	1.8	0.04	800	368.8	0.418	0.996
50	909.2	1.8	0.06	800	379.2	0.417	0.994
50	935.3	1.7	0.08	800	355.8	0.38	0.907
50	961	1.6	0.1	800	371.3	0.386	0.921
30	1021	0.7	0	1150	476.7	0.467	1.002
30	1046.1	2.4	0.02	1150	482.1	0.461	0.989
30	1070.8	2.8	0.04	1150	486	0.454	0.974
30	1095	3.2	0.06	1150	479.9	0.438	0.941
30	1118.7	3.6	0.08	1150	455.4	0.407	0.874

Speed (mph)	**Vertical Force (lb)**	**Slip Angle (degree)**	**Camber**	**Curve Radius (ft)**	**FEA Horizontal Force (lb)**	**FEA FN**	**Friction Adjustment Factor**
30	1141.9	4	0.1	1150	458.8	0.402	0.862
35	997.7	0.5	0	1150	447.3	0.448	0.995
35	1023.1	2.3	0.02	1150	446.6	0.437	0.969
35	1048.1	2.6	0.04	1150	449.8	0.429	0.952
35	1072.6	2.9	0.06	1150	458.5	0.427	0.949
35	1096.6	3.2	0.08	1150	451.5	0.412	0.914
35	1120.1	3.5	0.1	1150	452.1	0.404	0.896
40	970.9	0.3	0	1150	435.6	0.449	1.055
40	996.6	2.2	0.02	1150	428.6	0.43	1.011
40	1021.9	2.4	0.04	1150	425.7	0.417	0.98
40	1046.7	2.6	0.06	1150	424.1	0.405	0.953
40	1071.1	2.8	0.08	1150	423.5	0.395	0.93
40	1094.9	3	0.1	1150	445.3	0.407	0.957
45	940.5	0.1	0	1150	413.7	0.44	1.021
45	966.6	2.1	0.02	1150	399.4	0.413	0.96
45	992.2	2.2	0.04	1150	413.9	0.417	0.969
45	1017.4	2.2	0.06	1150	419.6	0.412	0.958
45	1042.1	2.3	0.08	1150	411.4	0.395	0.917
45	1066.4	2.4	0.1	1150	388.2	0.364	0.845
50	906.6	0	0	1150	407.5	0.449	1.071
50	933	1.9	0.02	1150	391.9	0.42	1.001
50	959	1.9	0.04	1150	399	0.416	0.992
50	984.6	1.8	0.06	1150	395.6	0.402	0.958
50	1009.8	1.8	0.08	1150	378.5	0.375	0.894
50	1034.4	1.7	0.1	1150	394.1	0.381	0.908
30	1036	0.5	0	1500	498.3	0.481	1.033
30	1060.9	2.3	0.02	1500	489.5	0.461	0.99
30	1085.5	2.6	0.04	1500	479.5	0.442	0.948
30	1109.5	2.9	0.06	1500	483.9	0.436	0.936
30	1133	3.2	0.08	1500	461.7	0.407	0.875
30	1156	3.5	0.1	1500	469.6	0.406	0.872
35	1018.2	0.4	0	1500	460.9	0.453	1.005

Speed (mph)	Vertical Force (lb)	Slip Angle (degree)	Camber	Curve Radius (ft)	FEA Horizontal Force (lb)	FEA FN	Friction Adjustment Factor
35	1043.3	2.2	0.02	1500	455.8	0.437	0.97
35	1068.1	2.5	0.04	1500	460.7	0.431	0.957
35	1092.3	2.7	0.06	1500	465.5	0.426	0.946
35	1116.1	2.9	0.08	1500	472	0.423	0.939
35	1139.3	3.2	0.1	1500	458	0.402	0.892
40	997.6	0.3	0	1500	446.5	0.448	1.053
40	1023	2.2	0.02	1500	429.8	0.42	0.988
40	1048	2.3	0.04	1500	435.4	0.415	0.977
40	1072.5	2.5	0.06	1500	435.4	0.406	0.955
40	1096.5	2.6	0.08	1500	435.1	0.397	0.933
40	1120	2.8	0.1	1500	453.3	0.405	0.952
45	974.3	0.1	0	1500	429.6	0.441	1.024
45	1000	2.1	0.02	1500	407.4	0.407	0.946
45	1025.2	2.1	0.04	1500	419.2	0.409	0.95
45	1050	2.2	0.06	1500	423.8	0.404	0.937
45	1074.3	2.2	0.08	1500	424.3	0.395	0.917
45	1098.1	2.3	0.1	1500	393.7	0.359	0.833
50	948.3	0	0	1500	410.6	0.433	1.032
50	974.2	2	0.02	1500	401.7	0.412	0.983
50	999.8	1.9	0.04	1500	413.3	0.413	0.985
50	1024.9	1.9	0.06	1500	409.9	0.4	0.953
50	1049.5	1.8	0.08	1500	401.8	0.383	0.913
50	1073.6	1.8	0.1	1500	404.9	0.377	0.899
30	1085	0	0	Infinity	505.6	0.466	1
35	1085	0	0	Infinity	489	0.451	1
40	1085	0	0	Infinity	461.4	0.425	1
45	1085	0	0	Infinity	467.3	0.431	1
50	1085	0	0	Infinity	455.4	0.42	1

Appendix D. Machine Learning Result of Friction Adjustment Factor From FEA Simulations

Table D.1 *Friction Numbers by Speed, Vertical Force, Slip Angle, and Camber Angle on the Inner Tire.*

Speed (mph)	Vertical Force (lb)	Slip Angle (degree)	Camber	Curve Radius (ft)	FEA Horizontal Force (lb)	FEA FN	Friction Adjustment Factor
30	1578.7	5.1	0	150	642.9	0.407	0.874
30	1570.7	3.5	0.01	150	620.5	0.395	0.848
30	1562.5	5.1	0.02	150	618.5	0.396	0.85
30	1554.2	6.6	0.03	150	615.4	0.396	0.85
30	1545.7	8.2	0.04	150	611.2	0.395	0.849
30	1537.1	9.7	0.05	150	606	0.394	0.846
30	1528.3	11.2	0.06	150	599.7	0.392	0.842
30	1519.3	12.8	0.07	150	592.5	0.39	0.837
30	1510.3	14.3	0.08	150	584.3	0.387	0.83
30	1501.1	15.8	0.09	150	575.3	0.383	0.823
30	1491.8	17.4	0.1	150	565.4	0.379	0.814
32.5	1664.4	4.6	0	150	650.7	0.391	0.852
32.5	1657.1	3.4	0.01	150	630.8	0.381	0.83
32.5	1649.7	4.7	0.02	150	627.9	0.381	0.83
32.5	1642.1	6.1	0.03	150	624.1	0.38	0.829
32.5	1634.3	7.5	0.04	150	619.4	0.379	0.826
32.5	1626.4	8.8	0.05	150	613.9	0.377	0.823
32.5	1618.3	10.2	0.06	150	607.5	0.375	0.819
32.5	1610.1	11.6	0.07	150	600.4	0.373	0.813
32.5	1601.7	12.9	0.08	150	592.6	0.37	0.807
32.5	1593.2	14.3	0.09	150	584.1	0.367	0.799
32.5	1584.5	15.7	0.1	150	574.9	0.363	0.791
35	1756.9	3.9	0	150	659.1	0.375	0.833
35	1750.5	3.2	0.01	150	642.3	0.367	0.814
35	1743.8	4.4	0.02	150	638.4	0.366	0.813
35	1737	5.5	0.03	150	633.8	0.365	0.81
35	1730	6.7	0.04	150	628.6	0.363	0.806

Speed (mph)	Vertical Force (lb)	Slip Angle (degree)	Camber	Curve Radius (ft)	FEA Horizontal Force (lb)	FEA FN	Friction Adjustment Factor
35	1722.9	7.9	0.05	150	622.6	0.361	0.802
35	1715.5	9.1	0.06	150	616.1	0.359	0.797
35	1708.1	10.3	0.07	150	608.9	0.356	0.791
35	1700.4	11.5	0.08	150	601.2	0.354	0.785
35	1692.6	12.6	0.09	150	593.1	0.35	0.778
35	1684.7	13.8	0.1	150	584.5	0.347	0.77
37.5	1856.3	3.3	0	150	668.1	0.36	0.804
37.5	1850.7	3	0.01	150	654.6	0.354	0.791
37.5	1844.9	4	0.02	150	649.8	0.352	0.787
37.5	1838.9	5	0.03	150	644.4	0.35	0.783
37.5	1832.8	5.9	0.04	150	638.4	0.348	0.779
37.5	1826.5	6.9	0.05	150	631.9	0.346	0.773
37.5	1820	7.9	0.06	150	625	0.343	0.768
37.5	1813.3	8.9	0.07	150	617.7	0.341	0.761
37.5	1806.5	9.9	0.08	150	610	0.338	0.755
37.5	1799.5	10.9	0.09	150	602	0.335	0.748
37.5	1792.3	11.8	0.1	150	593.8	0.331	0.74
40	1962.5	2.6	0	150	677.5	0.345	0.812
40	1957.8	2.8	0.01	150	667.8	0.341	0.802
40	1953	3.5	0.02	150	661.8	0.339	0.797
40	1947.9	4.3	0.03	150	655.5	0.336	0.792
40	1942.7	5.1	0.04	150	648.7	0.334	0.785
40	1937.2	5.9	0.05	150	641.6	0.331	0.779
40	1931.6	6.6	0.06	150	634.2	0.328	0.772
40	1925.8	7.4	0.07	150	626.5	0.325	0.765
40	1919.8	8.2	0.08	150	618.6	0.322	0.758
40	1913.6	8.9	0.09	150	610.5	0.319	0.75
40	1907.3	9.7	0.1	150	602.3	0.316	0.743
42.5	2075.6	1.8	0	150	686.8	0.331	0.756
42.5	2071.9	2.5	0.01	150	681.4	0.329	0.752
42.5	2068	3.1	0.02	150	674.3	0.326	0.745

Speed (mph)	Vertical Force (lb)	Slip Angle (degree)	Camber	Curve Radius (ft)	FEA Horizontal Force (lb)	FEA FN	Friction Adjustment Factor
42.5	2063.9	3.6	0.03	150	666.9	0.323	0.739
42.5	2059.6	4.2	0.04	150	659.2	0.32	0.732
42.5	2055.2	4.7	0.05	150	651.3	0.317	0.724
42.5	2050.5	5.3	0.06	150	643.2	0.314	0.717
42.5	2045.6	5.8	0.07	150	634.9	0.31	0.709
42.5	2040.5	6.4	0.08	150	626.5	0.307	0.702
42.5	2035.2	6.9	0.09	150	618	0.304	0.694
42.5	2029.7	7.5	0.1	150	609.5	0.3	0.686
45	2195.5	1	0	150	696	0.317	0.736
45	2192.9	2.3	0.01	150	695.3	0.317	0.736
45	2190	2.6	0.02	150	687	0.314	0.729
45	2187	2.9	0.03	150	678.4	0.31	0.72
45	2183.7	3.2	0.04	150	669.6	0.307	0.712
45	2180.2	3.5	0.05	150	660.6	0.303	0.704
45	2176.5	3.8	0.06	150	651.6	0.299	0.695
45	2172.6	4.1	0.07	150	642.5	0.296	0.687
45	2168.5	4.4	0.08	150	633.3	0.292	0.678
45	2164.1	4.8	0.09	150	624.1	0.288	0.67
45	2159.6	5.1	0.1	150	614.9	0.285	0.661
47.5	2322.3	0.2	0	150	704.4	0.303	0.71
47.5	2320.8	2.1	0.01	150	709.1	0.306	0.715
47.5	2319	2.1	0.02	150	699.4	0.302	0.706
47.5	2317.1	2.2	0.03	150	689.5	0.298	0.696
47.5	2314.8	2.2	0.04	150	679.4	0.293	0.687
47.5	2312.4	2.3	0.05	150	669.2	0.289	0.677
47.5	2309.7	2.3	0.06	150	659	0.285	0.668
47.5	2306.9	2.4	0.07	150	648.6	0.281	0.658
47.5	2303.7	2.4	0.08	150	638.3	0.277	0.648
47.5	2300.4	2.5	0.09	150	628	0.273	0.639
47.5	2296.9	2.5	0.1	150	617.8	0.269	0.629
50	2455.9	-0.7	0	150	711.9	0.29	0.691

Speed (mph)	Vertical Force (lb)	Slip Angle (degree)	Camber	Curve Radius (ft)	FEA Horizontal Force (lb)	FEA FN	Friction Adjustment Factor
50	2455.6	1.8	0.01	150	722.5	0.294	0.701
50	2455	1.6	0.02	150	711.3	0.29	0.691
50	2454.2	1.4	0.03	150	699.8	0.285	0.68
50	2453.1	1.1	0.04	150	688.2	0.281	0.669
50	2451.8	0.9	0.05	150	676.5	0.276	0.658
50	2450.2	0.7	0.06	150	664.7	0.271	0.647
50	2448.4	0.5	0.07	150	652.9	0.267	0.636
50	2446.4	0.3	0.08	150	641.1	0.262	0.625
50	2444.1	0.1	0.09	150	629.3	0.257	0.614
50	2441.6	-0.1	0.1	150	617.6	0.253	0.603
30	1332	2.6	0	300	574	0.431	0.925
30	1321.8	2.8	0.01	300	562.8	0.426	0.914
30	1311.5	3.5	0.02	300	555.6	0.424	0.909
30	1301.1	4.3	0.03	300	548.2	0.421	0.905
30	1290.5	5.1	0.04	300	540.8	0.419	0.9
30	1279.8	5.8	0.05	300	533.3	0.417	0.894
30	1269	6.6	0.06	300	525.8	0.414	0.889
30	1258.1	7.4	0.07	300	518.3	0.412	0.884
30	1247	8.2	0.08	300	511	0.41	0.88
30	1235.9	8.9	0.09	300	503.7	0.408	0.875
30	1224.6	9.7	0.1	300	496.6	0.406	0.871
32.5	1374.9	2.3	0	300	574.5	0.418	0.911
32.5	1365.1	2.7	0.01	300	564.8	0.414	0.902
32.5	1355.1	3.4	0.02	300	557.1	0.411	0.896
32.5	1345	4.1	0.03	300	549.2	0.408	0.89
32.5	1334.8	4.7	0.04	300	541.2	0.405	0.884
32.5	1324.5	5.4	0.05	300	533.3	0.403	0.878
32.5	1314	6.1	0.06	300	525.4	0.4	0.872
32.5	1303.4	6.8	0.07	300	517.5	0.397	0.866
32.5	1292.7	7.5	0.08	300	509.8	0.394	0.86
32.5	1281.9	8.2	0.09	300	502.2	0.392	0.854

Speed (mph)	Vertical Force (lb)	Slip Angle (degree)	Camber	Curve Radius (ft)	FEA Horizontal Force (lb)	FEA FN	Friction Adjustment Factor
32.5	1271	8.8	0.1	300	494.7	0.389	0.849
35	1421.1	2	0	300	575.6	0.405	0.899
35	1411.7	2.6	0.01	300	567.6	0.402	0.892
35	1402.2	3.2	0.02	300	559.2	0.399	0.885
35	1392.5	3.8	0.03	300	550.8	0.396	0.878
35	1382.6	4.4	0.04	300	542.4	0.392	0.871
35	1372.7	5	0.05	300	533.9	0.389	0.863
35	1362.6	5.5	0.06	300	525.5	0.386	0.856
35	1352.4	6.1	0.07	300	517.2	0.382	0.849
35	1342.1	6.7	0.08	300	509	0.379	0.842
35	1331.6	7.3	0.09	300	501	0.376	0.835
35	1321.1	7.9	0.1	300	493.2	0.373	0.829
37.5	1470.8	1.6	0	300	577.2	0.392	0.877
37.5	1461.8	2.5	0.01	300	571	0.391	0.873
37.5	1452.7	3	0.02	300	562.1	0.387	0.865
37.5	1443.4	3.5	0.03	300	553.1	0.383	0.856
37.5	1434	4	0.04	300	544.1	0.379	0.848
37.5	1424.5	4.5	0.05	300	535.1	0.376	0.84
37.5	1414.8	5	0.06	300	526.2	0.372	0.831
37.5	1405	5.4	0.07	300	517.4	0.368	0.823
37.5	1395.1	5.9	0.08	300	508.7	0.365	0.815
37.5	1385.1	6.4	0.09	300	500.3	0.361	0.807
37.5	1374.9	6.9	0.1	300	492	0.358	0.8
40	1523.9	1.3	0	300	579.4	0.38	0.894
40	1515.4	2.4	0.01	300	575.1	0.38	0.893
40	1506.7	2.8	0.02	300	565.6	0.375	0.883
40	1497.9	3.2	0.03	300	556	0.371	0.873
40	1489	3.5	0.04	300	546.5	0.367	0.863
40	1479.9	3.9	0.05	300	536.9	0.363	0.853
40	1470.7	4.3	0.06	300	527.5	0.359	0.844
40	1461.3	4.7	0.07	300	518.1	0.355	0.834

Speed (mph)	Vertical Force (lb)	Slip Angle (degree)	Camber	Curve Radius (ft)	FEA Horizontal Force (lb)	FEA FN	Friction Adjustment Factor
40	1451.8	5.1	0.08	300	508.9	0.351	0.825
40	1442.2	5.5	0.09	300	499.9	0.347	0.815
40	1432.4	5.9	0.1	300	491.1	0.343	0.807
42.5	1580.5	0.9	0	300	582.1	0.368	0.842
42.5	1572.4	2.3	0.01	300	579.9	0.369	0.843
42.5	1564.3	2.5	0.02	300	569.7	0.364	0.833
42.5	1555.9	2.8	0.03	300	559.6	0.36	0.822
42.5	1547.5	3.1	0.04	300	549.4	0.355	0.812
42.5	1538.8	3.4	0.05	300	539.3	0.35	0.801
42.5	1530.1	3.6	0.06	300	529.3	0.346	0.791
42.5	1521.2	3.9	0.07	300	519.4	0.341	0.78
42.5	1512.1	4.2	0.08	300	509.6	0.337	0.77
42.5	1502.9	4.5	0.09	300	500	0.333	0.76
42.5	1493.6	4.7	0.1	300	490.7	0.329	0.751
45	1640.4	0.5	0	300	585.2	0.357	0.829
45	1632.9	2.2	0.01	300	585.2	0.358	0.832
45	1625.3	2.3	0.02	300	574.5	0.353	0.821
45	1617.5	2.5	0.03	300	563.7	0.348	0.809
45	1609.5	2.6	0.04	300	552.9	0.344	0.798
45	1601.4	2.8	0.05	300	542.2	0.339	0.786
45	1593.1	2.9	0.06	300	531.5	0.334	0.775
45	1584.7	3.1	0.07	300	521	0.329	0.764
45	1576.1	3.2	0.08	300	510.7	0.324	0.753
45	1567.4	3.4	0.09	300	500.5	0.319	0.742
45	1558.5	3.5	0.1	300	490.6	0.315	0.731
47.5	1703.8	0.1	0	300	588.7	0.346	0.809
47.5	1696.9	2	0.01	300	591.1	0.348	0.815
47.5	1689.8	2.1	0.02	300	579.7	0.343	0.803
47.5	1682.5	2.1	0.03	300	568.3	0.338	0.79
47.5	1675.1	2.1	0.04	300	556.9	0.332	0.778
47.5	1667.5	2.1	0.05	300	545.5	0.327	0.766

Speed (mph)	Vertical Force (lb)	Slip Angle (degree)	Camber	Curve Radius (ft)	FEA Horizontal Force (lb)	FEA FN	Friction Adjustment Factor
47.5	1659.7	2.2	0.06	300	534.2	0.322	0.753
47.5	1651.8	2.2	0.07	300	523.1	0.317	0.741
47.5	1643.7	2.2	0.08	300	512.1	0.312	0.729
47.5	1635.5	2.2	0.09	300	501.4	0.307	0.717
47.5	1627.2	2.3	0.1	300	490.8	0.302	0.706
50	1770.6	-0.4	0	300	592.5	0.335	0.797
50	1764.3	1.9	0.01	300	597.4	0.339	0.807
50	1757.8	1.8	0.02	300	585.4	0.333	0.794
50	1751.1	1.7	0.03	300	573.3	0.327	0.78
50	1744.2	1.6	0.04	300	561.2	0.322	0.767
50	1737.1	1.5	0.05	300	549.2	0.316	0.754
50	1729.9	1.4	0.06	300	537.3	0.311	0.74
50	1722.6	1.2	0.07	300	525.5	0.305	0.727
50	1715	1.1	0.08	300	513.9	0.3	0.714
50	1707.4	1	0.09	300	502.5	0.294	0.701
50	1699.5	0.9	0.1	300	491.4	0.289	0.689
30	1249.8	1.7	0	450	550.6	0.441	0.946
30	1238.9	2.5	0.01	450	543.6	0.439	0.942
30	1227.9	3	0.02	450	534.5	0.435	0.935
30	1216.7	3.5	0.03	450	525.4	0.432	0.927
30	1205.4	4.1	0.04	450	516.4	0.428	0.92
30	1194	4.6	0.05	450	507.4	0.425	0.912
30	1182.5	5.1	0.06	450	498.5	0.422	0.905
30	1171	5.6	0.07	450	489.8	0.418	0.898
30	1159.3	6.1	0.08	450	481.3	0.415	0.891
30	1147.5	6.6	0.09	450	473	0.412	0.885
30	1135.6	7.1	0.1	450	465	0.41	0.879
32.5	1278.4	1.5	0	450	548.8	0.429	0.936
32.5	1267.7	2.5	0.01	450	542.8	0.428	0.934
32.5	1256.9	2.9	0.02	450	533.3	0.424	0.925
32.5	1246	3.4	0.03	450	523.9	0.42	0.917

Speed (mph)	Vertical Force (lb)	Slip Angle (degree)	Camber	Curve Radius (ft)	FEA Horizontal Force (lb)	FEA FN	Friction Adjustment Factor
32.5	1235	3.8	0.04	450	514.4	0.417	0.908
32.5	1223.8	4.3	0.05	450	505.1	0.413	0.9
32.5	1212.6	4.7	0.06	450	495.9	0.409	0.892
32.5	1201.2	5.2	0.07	450	486.9	0.405	0.884
32.5	1189.7	5.6	0.08	450	478	0.402	0.876
32.5	1178.2	6.1	0.09	450	469.5	0.398	0.869
32.5	1166.5	6.6	0.1	450	461.2	0.395	0.862
35	1309.2	1.3	0	450	547.5	0.418	0.928
35	1298.8	2.4	0.01	450	542.5	0.418	0.927
35	1288.3	2.8	0.02	450	532.7	0.413	0.918
35	1277.6	3.2	0.03	450	522.8	0.409	0.908
35	1266.9	3.6	0.04	450	513	0.405	0.899
35	1256	4	0.05	450	503.3	0.401	0.889
35	1245	4.4	0.06	450	493.8	0.397	0.88
35	1233.9	4.8	0.07	450	484.4	0.393	0.871
35	1222.6	5.2	0.08	450	475.2	0.389	0.863
35	1211.3	5.5	0.09	450	466.3	0.385	0.854
35	1199.9	5.9	0.1	450	457.7	0.381	0.847
37.5	1342.3	1.1	0	450	546.6	0.407	0.91
37.5	1332.2	2.3	0.01	450	542.8	0.407	0.911
37.5	1322	2.7	0.02	450	532.5	0.403	0.9
37.5	1311.6	3	0.03	450	522.3	0.398	0.89
37.5	1301.1	3.3	0.04	450	512.1	0.394	0.88
37.5	1290.5	3.6	0.05	450	502	0.389	0.87
37.5	1279.8	4	0.06	450	492.1	0.385	0.859
37.5	1268.9	4.3	0.07	450	482.4	0.38	0.85
37.5	1258	4.6	0.08	450	472.9	0.376	0.84
37.5	1246.9	5	0.09	450	463.6	0.372	0.831
37.5	1235.8	5.3	0.1	450	454.6	0.368	0.822
40	1377.7	0.9	0	450	546.1	0.396	0.932
40	1367.9	2.3	0.01	450	543.5	0.397	0.935

Speed (mph)	Vertical Force (lb)	Slip Angle (degree)	Camber	Curve Radius (ft)	FEA Horizontal Force (lb)	FEA FN	Friction Adjustment Factor
40	1358	2.5	0.02	450	532.9	0.392	0.923
40	1347.9	2.8	0.03	450	522.3	0.387	0.911
40	1337.7	3	0.04	450	511.7	0.383	0.9
40	1327.4	3.3	0.05	450	501.3	0.378	0.888
40	1317	3.5	0.06	450	491	0.373	0.877
40	1306.4	3.8	0.07	450	480.9	0.368	0.866
40	1295.8	4.1	0.08	450	471	0.363	0.855
40	1285	4.3	0.09	450	461.3	0.359	0.845
40	1274.1	4.6	0.1	450	452	0.355	0.835
42.5	1415.4	0.6	0	450	546.1	0.386	0.882
42.5	1406	2.2	0.01	450	544.8	0.388	0.886
42.5	1396.4	2.4	0.02	450	533.8	0.382	0.874
42.5	1386.6	2.5	0.03	450	522.8	0.377	0.862
42.5	1376.7	2.7	0.04	450	511.8	0.372	0.85
42.5	1366.7	2.9	0.05	450	501	0.367	0.838
42.5	1356.6	3.1	0.06	450	490.3	0.361	0.826
42.5	1346.4	3.3	0.07	450	479.8	0.356	0.815
42.5	1336	3.5	0.08	450	469.6	0.351	0.803
42.5	1325.5	3.6	0.09	450	459.6	0.347	0.793
42.5	1314.9	3.8	0.1	450	449.9	0.342	0.782
45	1455.4	0.3	0	450	546.6	0.376	0.872
45	1446.3	2.1	0.01	450	546.7	0.378	0.878
45	1437	2.2	0.02	450	535.2	0.372	0.865
45	1427.6	2.3	0.03	450	523.8	0.367	0.852
45	1418.1	2.4	0.04	450	512.5	0.361	0.839
45	1408.4	2.5	0.05	450	501.3	0.356	0.827
45	1398.6	2.6	0.06	450	490.2	0.35	0.814
45	1388.7	2.7	0.07	450	479.3	0.345	0.802
45	1378.6	2.8	0.08	450	468.7	0.34	0.79
45	1368.5	2.9	0.09	450	458.3	0.335	0.778
45	1358.2	3	0.1	450	448.2	0.33	0.767

Speed (mph)	Vertical Force (lb)	Slip Angle (degree)	Camber	Curve Radius (ft)	FEA Horizontal Force (lb)	FEA FN	Friction Adjustment Factor
47.5	1497.7	0.1	0	450	547.4	0.366	0.855
47.5	1488.9	2	0.01	450	549	0.369	0.863
47.5	1480	2	0.02	450	537.1	0.363	0.849
47.5	1471	2.1	0.03	450	525.3	0.357	0.836
47.5	1461.8	2.1	0.04	450	513.6	0.351	0.822
47.5	1452.5	2.1	0.05	450	502	0.346	0.809
47.5	1443	2.1	0.06	450	490.6	0.34	0.796
47.5	1433.5	2.1	0.07	450	479.3	0.334	0.783
47.5	1423.7	2.1	0.08	450	468.3	0.329	0.77
47.5	1413.9	2.2	0.09	450	457.6	0.324	0.757
47.5	1404	2.2	0.1	450	447.1	0.318	0.745
50	1542.2	-0.2	0	450	548.7	0.356	0.848
50	1533.8	1.9	0.01	450	551.7	0.36	0.857
50	1525.3	1.9	0.02	450	539.5	0.354	0.843
50	1516.7	1.8	0.03	450	527.3	0.348	0.829
50	1507.9	1.7	0.04	450	515.2	0.342	0.814
50	1498.9	1.6	0.05	450	503.3	0.336	0.8
50	1489.9	1.6	0.06	450	491.4	0.33	0.786
50	1480.6	1.5	0.07	450	479.8	0.324	0.772
50	1471.3	1.4	0.08	450	468.4	0.318	0.759
50	1461.8	1.4	0.09	450	457.3	0.313	0.746
50	1452.2	1.3	0.1	450	446.5	0.307	0.733
30	1208.7	1.3	0	600	539	0.446	0.957
30	1197.4	2.4	0.01	600	534.1	0.446	0.957
30	1186	2.8	0.02	600	524	0.442	0.948
30	1174.5	3.2	0.03	600	514	0.438	0.939
30	1162.9	3.5	0.04	600	504.1	0.433	0.931
30	1151.2	3.9	0.05	600	494.3	0.429	0.922
30	1139.3	4.3	0.06	600	484.7	0.425	0.913
30	1127.4	4.7	0.07	600	475.2	0.422	0.905
30	1115.4	5.1	0.08	600	466	0.418	0.897

Speed (mph)	Vertical Force (lb)	Slip Angle (degree)	Camber	Curve Radius (ft)	FEA Horizontal Force (lb)	FEA FN	Friction Adjustment Factor
30	1103.3	5.5	0.09	600	457.1	0.414	0.889
30	1091.1	5.8	0.1	600	448.4	0.411	0.882
32.5	1230.1	1.1	0	600	536	0.436	0.95
32.5	1219	2.3	0.01	600	531.8	0.436	0.951
32.5	1207.8	2.7	0.02	600	521.5	0.432	0.941
32.5	1196.5	3	0.03	600	511.2	0.427	0.932
32.5	1185	3.4	0.04	600	501	0.423	0.922
32.5	1173.5	3.7	0.05	600	491	0.418	0.912
32.5	1161.8	4.1	0.06	600	481	0.414	0.903
32.5	1150.1	4.4	0.07	600	471.4	0.41	0.894
32.5	1138.2	4.7	0.08	600	461.9	0.406	0.885
32.5	1126.3	5.1	0.09	600	452.7	0.402	0.876
32.5	1114.3	5.4	0.1	600	443.9	0.398	0.869
35	1253.2	1	0	600	533.5	0.426	0.945
35	1242.3	2.3	0.01	600	530	0.427	0.947
35	1231.3	2.6	0.02	600	519.4	0.422	0.936
35	1220.2	2.9	0.03	600	508.8	0.417	0.926
35	1209	3.2	0.04	600	498.4	0.412	0.915
35	1197.6	3.5	0.05	600	488	0.408	0.904
35	1186.1	3.8	0.06	600	477.9	0.403	0.894
35	1174.6	4.1	0.07	600	467.9	0.398	0.884
35	1162.9	4.4	0.08	600	458.2	0.394	0.874
35	1151.2	4.7	0.09	600	448.8	0.39	0.865
35	1139.3	5	0.1	600	439.7	0.386	0.857
37.5	1278.1	0.8	0	600	531.3	0.416	0.929
37.5	1267.4	2.2	0.01	600	528.7	0.417	0.932
37.5	1256.6	2.5	0.02	600	517.8	0.412	0.921
37.5	1245.7	2.7	0.03	600	506.9	0.407	0.91
37.5	1234.7	3	0.04	600	496.2	0.402	0.898
37.5	1223.5	3.2	0.05	600	485.6	0.397	0.887
37.5	1212.3	3.5	0.06	600	475.1	0.392	0.876

Speed (mph)	Vertical Force (lb)	Slip Angle (degree)	Camber	Curve Radius (ft)	FEA Horizontal Force (lb)	FEA FN	Friction Adjustment Factor
37.5	1200.9	3.7	0.07	600	464.9	0.387	0.865
37.5	1189.4	4	0.08	600	454.9	0.382	0.855
37.5	1177.9	4.2	0.09	600	445.2	0.378	0.845
37.5	1166.2	4.5	0.1	600	435.9	0.374	0.835
40	1304.6	0.6	0	600	529.5	0.406	0.955
40	1294.2	2.2	0.01	600	527.8	0.408	0.959
40	1283.6	2.4	0.02	600	516.6	0.402	0.947
40	1272.9	2.6	0.03	600	505.5	0.397	0.934
40	1262.1	2.8	0.04	600	494.4	0.392	0.921
40	1251.2	3	0.05	600	483.5	0.386	0.909
40	1240.2	3.2	0.06	600	472.8	0.381	0.897
40	1229	3.3	0.07	600	462.3	0.376	0.885
40	1217.8	3.5	0.08	600	452.1	0.371	0.873
40	1206.4	3.7	0.09	600	442.2	0.367	0.862
40	1194.9	3.9	0.1	600	432.5	0.362	0.851
42.5	1332.9	0.5	0	600	528.2	0.396	0.906
42.5	1322.7	2.1	0.01	600	527.3	0.399	0.911
42.5	1312.4	2.3	0.02	600	515.9	0.393	0.898
42.5	1301.9	2.4	0.03	600	504.4	0.387	0.886
42.5	1291.4	2.5	0.04	600	493.1	0.382	0.873
42.5	1280.7	2.7	0.05	600	482	0.376	0.86
42.5	1269.9	2.8	0.06	600	471	0.371	0.848
42.5	1259	3	0.07	600	460.3	0.366	0.836
42.5	1247.9	3.1	0.08	600	449.8	0.36	0.824
42.5	1236.8	3.2	0.09	600	439.6	0.355	0.812
42.5	1225.6	3.4	0.1	600	429.7	0.351	0.801
45	1362.9	0.3	0	600	527.2	0.387	0.898
45	1353	2.1	0.01	600	527.3	0.39	0.905
45	1342.9	2.2	0.02	600	515.6	0.384	0.892
45	1332.7	2.2	0.03	600	503.9	0.378	0.878
45	1322.4	2.3	0.04	600	492.3	0.372	0.865

Speed (mph)	Vertical Force (lb)	Slip Angle (degree)	Camber	Curve Radius (ft)	FEA Horizontal Force (lb)	FEA FN	Friction Adjustment Factor
45	1311.9	2.4	0.05	600	480.9	0.367	0.851
45	1301.4	2.5	0.06	600	469.7	0.361	0.838
45	1290.7	2.5	0.07	600	458.7	0.355	0.825
45	1279.9	2.6	0.08	600	447.9	0.35	0.813
45	1269	2.7	0.09	600	437.5	0.345	0.801
45	1258	2.8	0.1	600	427.3	0.34	0.789
47.5	1394.6	0	0	600	526.7	0.378	0.884
47.5	1384.9	2	0.01	600	527.8	0.381	0.892
47.5	1375.1	2	0.02	600	515.8	0.375	0.878
47.5	1365.2	2	0.03	600	503.8	0.369	0.864
47.5	1355.2	2.1	0.04	600	492	0.363	0.85
47.5	1345	2.1	0.05	600	480.3	0.357	0.836
47.5	1334.7	2.1	0.06	600	468.8	0.351	0.822
47.5	1324.3	2.1	0.07	600	457.6	0.346	0.809
47.5	1313.7	2.1	0.08	600	446.6	0.34	0.796
47.5	1303.1	2.1	0.09	600	435.9	0.334	0.783
47.5	1292.3	2.1	0.1	600	425.5	0.329	0.771
50	1428	-0.2	0	600	526.5	0.369	0.879
50	1418.6	1.9	0.01	600	528.7	0.373	0.888
50	1409.1	1.9	0.02	600	516.4	0.366	0.873
50	1399.5	1.8	0.03	600	504.2	0.36	0.859
50	1389.7	1.8	0.04	600	492.1	0.354	0.844
50	1379.8	1.7	0.05	600	480.2	0.348	0.829
50	1369.8	1.7	0.06	600	468.5	0.342	0.815
50	1359.7	1.6	0.07	600	457	0.336	0.801
50	1349.4	1.6	0.08	600	445.7	0.33	0.787
50	1339	1.5	0.09	600	434.8	0.325	0.774
50	1328.5	1.5	0.1	600	424.2	0.319	0.761
30	1184	1	0	750	532	0.449	0.965
30	1172.5	2.3	0.01	750	528.4	0.451	0.967
30	1160.9	2.6	0.02	750	517.8	0.446	0.957

Speed (mph)	Vertical Force (lb)	Slip Angle (degree)	Camber	Curve Radius (ft)	FEA Horizontal Force (lb)	FEA FN	Friction Adjustment Factor
30	1149.2	2.9	0.03	750	507.2	0.441	0.947
30	1137.4	3.2	0.04	750	496.8	0.437	0.938
30	1125.4	3.5	0.05	750	486.5	0.432	0.928
30	1113.4	3.8	0.06	750	476.3	0.428	0.918
30	1101.3	4.2	0.07	750	466.4	0.424	0.909
30	1089.1	4.5	0.08	750	456.8	0.419	0.9
30	1076.7	4.8	0.09	750	447.4	0.416	0.892
30	1064.4	5.1	0.1	750	438.4	0.412	0.884
32.5	1201.2	0.9	0	750	528.4	0.44	0.959
32.5	1189.8	2.3	0.01	750	525.3	0.441	0.963
32.5	1178.3	2.5	0.02	750	514.4	0.437	0.952
32.5	1166.8	2.8	0.03	750	503.7	0.432	0.941
32.5	1155.1	3.1	0.04	750	493	0.427	0.931
32.5	1143.3	3.4	0.05	750	482.5	0.422	0.92
32.5	1131.4	3.6	0.06	750	472.2	0.417	0.91
32.5	1119.4	3.9	0.07	750	462	0.413	0.9
32.5	1107.3	4.2	0.08	750	452.2	0.408	0.89
32.5	1095.2	4.5	0.09	750	442.6	0.404	0.881
32.5	1082.9	4.7	0.1	750	433.4	0.4	0.873
35	1219.7	0.8	0	750	525.1	0.431	0.956
35	1208.5	2.2	0.01	750	522.6	0.432	0.96
35	1197.2	2.5	0.02	750	511.5	0.427	0.948
35	1185.8	2.7	0.03	750	500.5	0.422	0.937
35	1174.2	2.9	0.04	750	489.6	0.417	0.925
35	1162.6	3.2	0.05	750	478.9	0.412	0.914
35	1150.9	3.4	0.06	750	468.4	0.407	0.903
35	1139	3.7	0.07	750	458	0.402	0.893
35	1127.1	3.9	0.08	750	448	0.397	0.882
35	1115.1	4.1	0.09	750	438.3	0.393	0.872
35	1102.9	4.4	0.1	750	428.8	0.389	0.863
37.5	1239.5	0.7	0	750	522.2	0.421	0.942

Speed (mph)	Vertical Force (lb)	Slip Angle (degree)	Camber	Curve Radius (ft)	FEA Horizontal Force (lb)	FEA FN	Friction Adjustment Factor
37.5	1228.5	2.2	0.01	750	520.3	0.423	0.947
37.5	1217.4	2.4	0.02	750	509	0.418	0.934
37.5	1206.1	2.6	0.03	750	497.8	0.413	0.922
37.5	1194.8	2.8	0.04	750	486.7	0.407	0.91
37.5	1183.3	3	0.05	750	475.7	0.402	0.899
37.5	1171.7	3.2	0.06	750	465	0.397	0.887
37.5	1160.1	3.4	0.07	750	454.5	0.392	0.876
37.5	1148.3	3.6	0.08	750	444.2	0.387	0.865
37.5	1136.4	3.8	0.09	750	434.3	0.382	0.854
37.5	1124.5	4	0.1	750	424.7	0.378	0.844
40	1260.8	0.5	0	750	519.7	0.412	0.97
40	1250	2.2	0.01	750	518.3	0.415	0.975
40	1239	2.3	0.02	750	506.8	0.409	0.962
40	1227.9	2.5	0.03	750	495.4	0.403	0.949
40	1216.8	2.6	0.04	750	484.1	0.398	0.936
40	1205.5	2.8	0.05	750	473	0.392	0.923
40	1194.1	2.9	0.06	750	462	0.387	0.91
40	1182.6	3.1	0.07	750	451.3	0.382	0.898
40	1171	3.2	0.08	750	440.9	0.376	0.886
40	1159.3	3.4	0.09	750	430.7	0.372	0.874
40	1147.5	3.5	0.1	750	420.9	0.367	0.863
42.5	1283.4	0.4	0	750	517.5	0.403	0.922
42.5	1272.8	2.1	0.01	750	516.8	0.406	0.928
42.5	1262	2.2	0.02	750	505.1	0.4	0.915
42.5	1251.1	2.3	0.03	750	493.5	0.394	0.902
42.5	1240.2	2.4	0.04	750	482	0.389	0.888
42.5	1229.1	2.5	0.05	750	470.6	0.383	0.875
42.5	1217.8	2.7	0.06	750	459.5	0.377	0.862
42.5	1206.5	2.8	0.07	750	448.6	0.372	0.85
42.5	1195.1	2.9	0.08	750	438	0.366	0.838
42.5	1183.6	3	0.09	750	427.7	0.361	0.826

Speed (mph)	Vertical Force (lb)	Slip Angle (degree)	Camber	Curve Radius (ft)	FEA Horizontal Force (lb)	FEA FN	Friction Adjustment Factor
42.5	1171.9	3.1	0.1	750	417.7	0.356	0.815
45	1307.4	0.2	0	750	515.7	0.394	0.916
45	1297	2.1	0.01	750	515.8	0.398	0.924
45	1286.4	2.1	0.02	750	503.9	0.392	0.91
45	1275.8	2.2	0.03	750	492	0.386	0.896
45	1265	2.2	0.04	750	480.3	0.38	0.882
45	1254.1	2.3	0.05	750	468.8	0.374	0.868
45	1243	2.4	0.06	750	457.4	0.368	0.855
45	1231.9	2.4	0.07	750	446.4	0.362	0.842
45	1220.7	2.5	0.08	750	435.6	0.357	0.829
45	1209.4	2.6	0.09	750	425.1	0.351	0.816
45	1197.9	2.6	0.1	750	414.9	0.346	0.804
47.5	1332.7	0	0	750	514.2	0.386	0.903
47.5	1322.5	2	0.01	750	515.1	0.389	0.912
47.5	1312.2	2	0.02	750	503	0.383	0.897
47.5	1301.8	2	0.03	750	491	0.377	0.883
47.5	1291.2	2	0.04	750	479.1	0.371	0.868
47.5	1280.5	2.1	0.05	750	467.4	0.365	0.854
47.5	1269.7	2.1	0.06	750	455.9	0.359	0.84
47.5	1258.8	2.1	0.07	750	444.6	0.353	0.827
47.5	1247.7	2.1	0.08	750	433.6	0.348	0.813
47.5	1236.6	2.1	0.09	750	423	0.342	0.801
47.5	1225.4	2.1	0.1	750	412.7	0.337	0.788
50	1359.5	-0.1	0	750	513.2	0.378	0.9
50	1349.5	2	0.01	750	514.8	0.381	0.909
50	1339.4	1.9	0.02	750	502.6	0.375	0.894
50	1329.2	1.9	0.03	750	490.4	0.369	0.879
50	1318.8	1.8	0.04	750	478.3	0.363	0.864
50	1308.4	1.8	0.05	750	466.4	0.356	0.85
50	1297.8	1.7	0.06	750	454.8	0.35	0.835
50	1287.1	1.7	0.07	750	443.3	0.344	0.821

Speed (mph)	Vertical Force (lb)	Slip Angle (degree)	Camber	Curve Radius (ft)	FEA Horizontal Force (lb)	FEA FN	Friction Adjustment Factor
50	1276.3	1.7	0.08	750	432.2	0.339	0.807
50	1265.3	1.6	0.09	750	421.4	0.333	0.794
50	1254.3	1.6	0.1	750	411	0.328	0.781
30	1177.9	1	0	800	530.3	0.45	0.966
30	1166.3	2.3	0.01	800	526.9	0.452	0.97
30	1154.6	2.6	0.02	800	516.2	0.447	0.96
30	1142.9	2.9	0.03	800	505.5	0.442	0.95
30	1131	3.2	0.04	800	494.9	0.438	0.939
30	1119	3.4	0.05	800	484.5	0.433	0.929
30	1106.9	3.7	0.06	800	474.3	0.428	0.92
30	1094.7	4	0.07	800	464.2	0.424	0.91
30	1082.5	4.3	0.08	800	454.5	0.42	0.901
30	1070.1	4.6	0.09	800	445	0.416	0.893
30	1057.7	4.9	0.1	800	435.9	0.412	0.885
32.5	1193.9	0.9	0	800	526.5	0.441	0.962
32.5	1182.5	2.3	0.01	800	523.6	0.443	0.966
32.5	1171	2.5	0.02	800	512.7	0.438	0.955
32.5	1159.3	2.8	0.03	800	501.8	0.433	0.944
32.5	1147.6	3	0.04	800	491	0.428	0.933
32.5	1135.8	3.3	0.05	800	480.4	0.423	0.922
32.5	1123.8	3.5	0.06	800	469.9	0.418	0.912
32.5	1111.8	3.8	0.07	800	459.7	0.414	0.902
32.5	1099.6	4.1	0.08	800	449.8	0.409	0.892
32.5	1087.4	4.3	0.09	800	440.1	0.405	0.883
32.5	1075.1	4.6	0.1	800	430.8	0.401	0.874
35	1211.3	0.7	0	800	523.1	0.432	0.958
35	1200	2.2	0.01	800	520.7	0.434	0.963
35	1188.6	2.4	0.02	800	509.5	0.429	0.951
35	1177.1	2.7	0.03	800	498.4	0.423	0.94
35	1165.5	2.9	0.04	800	487.4	0.418	0.928
35	1153.8	3.1	0.05	800	476.6	0.413	0.917

Speed (mph)	Vertical Force (lb)	Slip Angle (degree)	Camber	Curve Radius (ft)	FEA Horizontal Force (lb)	FEA FN	Friction Adjustment Factor
35	1142	3.3	0.06	800	466	0.408	0.906
35	1130.1	3.6	0.07	800	455.6	0.403	0.895
35	1118.1	3.8	0.08	800	445.5	0.398	0.884
35	1106	4	0.09	800	435.6	0.394	0.874
35	1093.8	4.2	0.1	800	426.1	0.39	0.865
37.5	1229.9	0.6	0	800	519.9	0.423	0.945
37.5	1218.8	2.2	0.01	800	518.2	0.425	0.95
37.5	1207.6	2.4	0.02	800	506.8	0.42	0.938
37.5	1196.3	2.6	0.03	800	495.5	0.414	0.926
37.5	1184.8	2.7	0.04	800	484.3	0.409	0.914
37.5	1173.3	2.9	0.05	800	473.3	0.403	0.902
37.5	1161.6	3.1	0.06	800	462.4	0.398	0.89
37.5	1149.9	3.3	0.07	800	451.9	0.393	0.878
37.5	1138	3.5	0.08	800	441.5	0.388	0.867
37.5	1126.1	3.7	0.09	800	431.5	0.383	0.857
37.5	1114	3.8	0.1	800	421.9	0.379	0.846
40	1249.8	0.5	0	800	517.2	0.414	0.973
40	1238.9	2.1	0.01	800	516	0.416	0.98
40	1227.9	2.3	0.02	800	504.4	0.411	0.966
40	1216.7	2.4	0.03	800	492.9	0.405	0.953
40	1205.4	2.6	0.04	800	481.5	0.399	0.94
40	1194	2.7	0.05	800	470.3	0.394	0.927
40	1182.5	2.9	0.06	800	459.3	0.388	0.914
40	1171	3	0.07	800	448.5	0.383	0.901
40	1159.3	3.2	0.08	800	438.1	0.378	0.889
40	1147.5	3.3	0.09	800	427.9	0.373	0.877
40	1135.6	3.4	0.1	800	418.1	0.368	0.866
42.5	1271	0.3	0	800	514.8	0.405	0.926
42.5	1260.3	2.1	0.01	800	514.2	0.408	0.933
42.5	1249.4	2.2	0.02	800	502.5	0.402	0.919
42.5	1238.4	2.3	0.03	800	490.8	0.396	0.906

Speed (mph)	Vertical Force (lb)	Slip Angle (degree)	Camber	Curve Radius (ft)	FEA Horizontal Force (lb)	FEA FN	Friction Adjustment Factor
42.5	1227.4	2.4	0.04	800	479.2	0.39	0.892
42.5	1216.1	2.5	0.05	800	467.8	0.385	0.879
42.5	1204.8	2.6	0.06	800	456.6	0.379	0.866
42.5	1193.4	2.7	0.07	800	445.7	0.373	0.854
42.5	1181.9	2.8	0.08	800	435	0.368	0.841
42.5	1170.3	2.9	0.09	800	424.7	0.363	0.83
42.5	1158.5	3	0.1	800	414.7	0.358	0.818
45	1293.5	0.2	0	800	512.8	0.396	0.921
45	1283	2.1	0.01	800	512.9	0.4	0.928
45	1272.3	2.1	0.02	800	500.9	0.394	0.914
45	1261.5	2.2	0.03	800	489.1	0.388	0.9
45	1250.6	2.2	0.04	800	477.3	0.382	0.886
45	1239.6	2.3	0.05	800	465.8	0.376	0.873
45	1228.5	2.3	0.06	800	454.4	0.37	0.859
45	1217.2	2.4	0.07	800	443.3	0.364	0.846
45	1205.9	2.5	0.08	800	432.5	0.359	0.833
45	1194.4	2.5	0.09	800	422	0.353	0.821
45	1182.9	2.6	0.1	800	411.8	0.348	0.809
47.5	1317.3	0	0	800	511.1	0.388	0.908
47.5	1306.9	2	0.01	800	511.9	0.392	0.917
47.5	1296.5	2	0.02	800	499.8	0.386	0.902
47.5	1285.9	2	0.03	800	487.8	0.379	0.888
47.5	1275.2	2	0.04	800	475.9	0.373	0.873
47.5	1264.4	2	0.05	800	464.2	0.367	0.859
47.5	1253.4	2.1	0.06	800	452.6	0.361	0.845
47.5	1242.4	2.1	0.07	800	441.4	0.355	0.831
47.5	1231.2	2.1	0.08	800	430.4	0.35	0.818
47.5	1220	2.1	0.09	800	419.8	0.344	0.805
47.5	1208.6	2.1	0.1	800	409.5	0.339	0.793
50	1342.3	-0.1	0	800	509.9	0.38	0.905
50	1332.2	2	0.01	800	511.4	0.384	0.915

Speed (mph)	Vertical Force (lb)	Slip Angle (degree)	Camber	Curve Radius (ft)	FEA Horizontal Force (lb)	FEA FN	Friction Adjustment Factor
50	1322	1.9	0.02	800	499.1	0.378	0.9
50	1311.6	1.9	0.03	800	486.9	0.371	0.885
50	1301.1	1.8	0.04	800	474.9	0.365	0.87
50	1290.5	1.8	0.05	800	463	0.359	0.855
50	1279.8	1.8	0.06	800	451.3	0.353	0.841
50	1268.9	1.7	0.07	800	440	0.347	0.826
50	1258	1.7	0.08	800	428.9	0.341	0.812
50	1246.9	1.6	0.09	800	418.1	0.335	0.799
50	1235.8	1.6	0.1	800	407.7	0.33	0.786
30	1167.6	0.9	0	900	527.4	0.452	0.97
30	1155.9	2.3	0.01	900	524.6	0.454	0.974
30	1144.2	2.5	0.02	900	513.6	0.449	0.964
30	1132.3	2.8	0.03	900	502.7	0.444	0.953
30	1120.4	3	0.04	900	491.9	0.439	0.942
30	1108.3	3.3	0.05	900	481.2	0.434	0.932
30	1096.1	3.5	0.06	900	470.8	0.43	0.922
30	1083.9	3.8	0.07	900	460.6	0.425	0.912
30	1071.5	4.1	0.08	900	450.6	0.421	0.903
30	1059.1	4.3	0.09	900	441	0.416	0.894
30	1046.5	4.6	0.1	900	431.6	0.412	0.885
32.5	1181.9	0.8	0	900	523.3	0.443	0.966
32.5	1170.3	2.2	0.01	900	520.9	0.445	0.971
32.5	1158.7	2.5	0.02	900	509.7	0.44	0.959
32.5	1147	2.7	0.03	900	498.7	0.435	0.948
32.5	1135.1	2.9	0.04	900	487.7	0.43	0.937
32.5	1123.2	3.1	0.05	900	476.9	0.425	0.926
32.5	1111.1	3.4	0.06	900	466.2	0.42	0.915
32.5	1099	3.6	0.07	900	455.8	0.415	0.904
32.5	1086.7	3.8	0.08	900	445.7	0.41	0.894
32.5	1074.4	4.1	0.09	900	435.9	0.406	0.885
32.5	1062	4.3	0.1	900	426.5	0.402	0.876

Speed (mph)	Vertical Force (lb)	Slip Angle (degree)	Camber	Curve Radius (ft)	FEA Horizontal Force (lb)	FEA FN	Friction Adjustment Factor
35	1197.3	0.7	0	900	519.6	0.434	0.963
35	1185.9	2.2	0.01	900	517.6	0.436	0.969
35	1174.4	2.4	0.02	900	506.3	0.431	0.957
35	1162.8	2.6	0.03	900	495	0.426	0.945
35	1151.1	2.8	0.04	900	483.8	0.42	0.933
35	1139.3	3	0.05	900	472.8	0.415	0.921
35	1127.3	3.2	0.06	900	462	0.41	0.91
35	1115.3	3.4	0.07	900	451.5	0.405	0.898
35	1103.2	3.6	0.08	900	441.2	0.4	0.888
35	1091	3.8	0.09	900	431.3	0.395	0.877
35	1078.7	4	0.1	900	421.7	0.391	0.868
37.5	1213.8	0.5	0	900	516.2	0.425	0.95
37.5	1202.6	2.2	0.01	900	514.7	0.428	0.957
37.5	1191.2	2.3	0.02	900	503.1	0.422	0.944
37.5	1179.8	2.5	0.03	900	491.7	0.417	0.931
37.5	1168.2	2.7	0.04	900	480.3	0.411	0.919
37.5	1156.5	2.8	0.05	900	469.2	0.406	0.907
37.5	1144.7	3	0.06	900	458.2	0.4	0.895
37.5	1132.8	3.1	0.07	900	447.5	0.395	0.883
37.5	1120.9	3.3	0.08	900	437.1	0.39	0.872
37.5	1108.8	3.5	0.09	900	427	0.385	0.861
37.5	1096.6	3.6	0.1	900	417.3	0.38	0.85
40	1231.5	0.4	0	900	513.1	0.417	0.98
40	1220.5	2.1	0.01	900	512.1	0.42	0.987
40	1209.3	2.3	0.02	900	500.4	0.414	0.973
40	1197.9	2.4	0.03	900	488.7	0.408	0.96
40	1186.5	2.5	0.04	900	477.3	0.402	0.946
40	1175	2.6	0.05	900	465.9	0.397	0.933
40	1163.3	2.8	0.06	900	454.8	0.391	0.92
40	1151.6	2.9	0.07	900	444	0.386	0.907
40	1139.8	3	0.08	900	433.4	0.38	0.894

Speed (mph)	Vertical Force (lb)	Slip Angle (degree)	Camber	Curve Radius (ft)	FEA Horizontal Force (lb)	FEA FN	Friction Adjustment Factor
40	1127.8	3.2	0.09	900	423.2	0.375	0.883
40	1115.8	3.3	0.1	900	413.3	0.37	0.871
42.5	1250.4	0.3	0	900	510.4	0.408	0.933
42.5	1239.5	2.1	0.01	900	509.9	0.411	0.94
42.5	1228.4	2.2	0.02	900	498	0.405	0.927
42.5	1217.3	2.3	0.03	900	486.2	0.399	0.913
42.5	1206	2.4	0.04	900	474.6	0.394	0.899
42.5	1194.6	2.5	0.05	900	463.1	0.388	0.886
42.5	1183.1	2.5	0.06	900	451.9	0.382	0.873
42.5	1171.6	2.6	0.07	900	440.9	0.376	0.86
42.5	1159.9	2.7	0.08	900	430.2	0.371	0.848
42.5	1148.1	2.8	0.09	900	419.8	0.366	0.836
42.5	1136.2	2.9	0.1	900	409.8	0.361	0.824
45	1270.4	0.2	0	900	508	0.4	0.929
45	1259.6	2.1	0.01	900	508.1	0.403	0.937
45	1248.8	2.1	0.02	900	496.1	0.397	0.923
45	1237.8	2.2	0.03	900	484.1	0.391	0.908
45	1226.7	2.2	0.04	900	472.3	0.385	0.894
45	1215.5	2.3	0.05	900	460.7	0.379	0.88
45	1204.2	2.3	0.06	900	449.3	0.373	0.867
45	1192.7	2.4	0.07	900	438.2	0.367	0.853
45	1181.2	2.4	0.08	900	427.4	0.362	0.84
45	1169.6	2.5	0.09	900	416.9	0.356	0.828
45	1157.8	2.5	0.1	900	406.7	0.351	0.816
47.5	1291.5	0	0	900	506	0.392	0.917
47.5	1280.9	2	0.01	900	506.7	0.396	0.926
47.5	1270.3	2	0.02	900	494.5	0.389	0.911
47.5	1259.5	2	0.03	900	482.4	0.383	0.896
47.5	1248.5	2	0.04	900	470.5	0.377	0.882
47.5	1237.5	2	0.05	900	458.8	0.371	0.868
47.5	1226.4	2.1	0.06	900	447.3	0.365	0.854

Speed (mph)	Vertical Force (lb)	Slip Angle (degree)	Camber	Curve Radius (ft)	FEA Horizontal Force (lb)	FEA FN	Friction Adjustment Factor
47.5	1215.1	2.1	0.07	900	436	0.359	0.84
47.5	1203.7	2.1	0.08	900	425.1	0.353	0.826
47.5	1192.3	2.1	0.09	900	414.5	0.348	0.814
47.5	1180.7	2.1	0.1	900	404.2	0.342	0.801
50	1313.8	-0.1	0	900	504.4	0.384	0.915
50	1303.4	2	0.01	900	505.6	0.388	0.925
50	1292.9	1.9	0.02	900	493.4	0.382	0.909
50	1282.3	1.9	0.03	900	481.2	0.375	0.894
50	1271.6	1.9	0.04	900	469.1	0.369	0.879
50	1260.7	1.8	0.05	900	457.3	0.363	0.864
50	1249.8	1.8	0.06	900	445.7	0.357	0.85
50	1238.7	1.7	0.07	900	434.3	0.351	0.836
50	1227.5	1.7	0.08	900	423.3	0.345	0.822
50	1216.2	1.7	0.09	900	412.5	0.339	0.808
50	1204.8	1.6	0.1	900	402.2	0.334	0.796
30	1155.8	0.7	0	1050	524.1	0.453	0.973
30	1144.1	2.2	0.01	1050	521.8	0.456	0.979
30	1132.2	2.4	0.02	1050	510.6	0.451	0.968
30	1120.3	2.7	0.03	1050	499.5	0.446	0.957
30	1108.2	2.9	0.04	1050	488.4	0.441	0.946
30	1096	3.1	0.05	1050	477.5	0.436	0.935
30	1083.8	3.3	0.06	1050	466.8	0.431	0.925
30	1071.4	3.5	0.07	1050	456.4	0.426	0.914
30	1059	3.8	0.08	1050	446.2	0.421	0.905
30	1046.4	4	0.09	1050	436.4	0.417	0.895
30	1033.8	4.2	0.1	1050	426.8	0.413	0.886
32.5	1168.1	0.7	0	1050	519.7	0.445	0.97
32.5	1156.4	2.2	0.01	1050	517.8	0.448	0.976
32.5	1144.7	2.4	0.02	1050	506.4	0.442	0.965
32.5	1132.8	2.6	0.03	1050	495.1	0.437	0.953
32.5	1120.9	2.8	0.04	1050	483.9	0.432	0.941

Speed (mph)	Vertical Force (lb)	Slip Angle (degree)	Camber	Curve Radius (ft)	FEA Horizontal Force (lb)	FEA FN	Friction Adjustment Factor
32.5	1108.8	3	0.05	1050	472.8	0.426	0.93
32.5	1096.6	3.2	0.06	1050	462	0.421	0.919
32.5	1084.4	3.4	0.07	1050	451.4	0.416	0.908
32.5	1072	3.6	0.08	1050	441.1	0.411	0.897
32.5	1059.6	3.8	0.09	1050	431.1	0.407	0.887
32.5	1047.1	4	0.1	1050	421.5	0.403	0.878
35	1181.3	0.6	0	1050	515.6	0.437	0.969
35	1169.8	2.2	0.01	1050	514.1	0.439	0.975
35	1158.1	2.3	0.02	1050	502.5	0.434	0.963
35	1146.4	2.5	0.03	1050	491	0.428	0.951
35	1134.5	2.7	0.04	1050	479.7	0.423	0.938
35	1122.6	2.8	0.05	1050	468.5	0.417	0.926
35	1110.5	3	0.06	1050	457.5	0.412	0.914
35	1098.4	3.2	0.07	1050	446.8	0.407	0.903
35	1086.1	3.4	0.08	1050	436.4	0.402	0.892
35	1073.8	3.5	0.09	1050	426.3	0.397	0.881
35	1061.4	3.7	0.1	1050	416.5	0.392	0.871
37.5	1195.5	0.5	0	1050	511.9	0.428	0.957
37.5	1184.1	2.1	0.01	1050	510.7	0.431	0.964
37.5	1172.6	2.3	0.02	1050	499	0.426	0.951
37.5	1160.9	2.4	0.03	1050	487.3	0.42	0.938
37.5	1149.2	2.6	0.04	1050	475.8	0.414	0.925
37.5	1137.4	2.7	0.05	1050	464.5	0.408	0.913
37.5	1125.4	2.8	0.06	1050	453.4	0.403	0.901
37.5	1113.4	3	0.07	1050	442.6	0.398	0.889
37.5	1101.3	3.1	0.08	1050	432.1	0.392	0.877
37.5	1089.1	3.3	0.09	1050	421.8	0.387	0.866
37.5	1076.8	3.4	0.1	1050	412	0.383	0.855
40	1210.6	0.4	0	1050	508.4	0.42	0.988
40	1199.4	2.1	0.01	1050	507.6	0.423	0.996
40	1188	2.2	0.02	1050	495.8	0.417	0.982

Speed (mph)	**Vertical Force (lb)**	**Slip Angle (degree)**	**Camber**	**Curve Radius (ft)**	**FEA Horizontal Force (lb)**	**FEA FN**	**Friction Adjustment Factor**
40	1176.5	2.3	0.03	1050	484	0.411	0.968
40	1164.9	2.4	0.04	1050	472.4	0.406	0.954
40	1153.2	2.6	0.05	1050	460.9	0.4	0.94
40	1141.4	2.7	0.06	1050	449.7	0.394	0.927
40	1129.5	2.8	0.07	1050	438.8	0.388	0.914
40	1117.5	2.9	0.08	1050	428.1	0.383	0.901
40	1105.4	3	0.09	1050	417.8	0.378	0.889
40	1093.2	3.1	0.1	1050	407.8	0.373	0.878
42.5	1226.8	0.3	0	1050	505.3	0.412	0.941
42.5	1215.7	2.1	0.01	1050	504.9	0.415	0.949
42.5	1204.4	2.2	0.02	1050	492.9	0.409	0.935
42.5	1193.1	2.2	0.03	1050	481.1	0.403	0.922
42.5	1181.6	2.3	0.04	1050	469.3	0.397	0.908
42.5	1170	2.4	0.05	1050	457.8	0.391	0.894
42.5	1158.4	2.5	0.06	1050	446.4	0.385	0.881
42.5	1146.6	2.5	0.07	1050	435.4	0.38	0.868
42.5	1134.7	2.6	0.08	1050	424.6	0.374	0.855
42.5	1122.7	2.7	0.09	1050	414.2	0.369	0.843
42.5	1110.7	2.8	0.1	1050	404.1	0.364	0.832
45	1243.9	0.1	0	1050	502.5	0.404	0.938
45	1233	2	0.01	1050	502.6	0.408	0.947
45	1221.9	2.1	0.02	1050	490.5	0.401	0.932
45	1210.7	2.1	0.03	1050	478.5	0.395	0.918
45	1199.3	2.2	0.04	1050	466.7	0.389	0.904
45	1187.9	2.2	0.05	1050	455	0.383	0.89
45	1176.4	2.3	0.06	1050	443.6	0.377	0.876
45	1164.7	2.3	0.07	1050	432.4	0.371	0.862
45	1153	2.3	0.08	1050	421.6	0.366	0.849
45	1141.2	2.4	0.09	1050	411.1	0.36	0.837
45	1129.2	2.4	0.1	1050	400.9	0.355	0.825
47.5	1262	0	0	1050	500.1	0.396	0.927

Speed (mph)	Vertical Force (lb)	Slip Angle (degree)	Camber	Curve Radius (ft)	FEA Horizontal Force (lb)	FEA FN	Friction Adjustment Factor
47.5	1251.2	2	0.01	1050	500.6	0.4	0.936
47.5	1240.3	2	0.02	1050	488.5	0.394	0.922
47.5	1229.2	2	0.03	1050	476.4	0.388	0.907
47.5	1218.1	2	0.04	1050	464.4	0.381	0.892
47.5	1206.8	2	0.05	1050	452.7	0.375	0.878
47.5	1195.4	2	0.06	1050	441.2	0.369	0.864
47.5	1183.9	2.1	0.07	1050	429.9	0.363	0.85
47.5	1172.3	2.1	0.08	1050	419	0.357	0.836
47.5	1160.6	2.1	0.09	1050	408.4	0.352	0.824
47.5	1148.8	2.1	0.1	1050	398.2	0.347	0.811
50	1281.1	-0.1	0	1050	498	0.389	0.926
50	1270.5	2	0.01	1050	499.1	0.393	0.936
50	1259.7	1.9	0.02	1050	486.8	0.386	0.921
50	1248.8	1.9	0.03	1050	474.6	0.38	0.906
50	1237.8	1.9	0.04	1050	462.6	0.374	0.891
50	1226.7	1.8	0.05	1050	450.8	0.367	0.876
50	1215.5	1.8	0.06	1050	439.2	0.361	0.861
50	1204.1	1.8	0.07	1050	427.9	0.355	0.847
50	1192.7	1.8	0.08	1050	416.9	0.35	0.833
50	1181.1	1.7	0.09	1050	406.3	0.344	0.82
50	1169.5	1.7	0.1	1050	396	0.339	0.807
30	1149.7	0.7	0	1150	522.4	0.454	0.975
30	1137.9	2.2	0.01	1150	520.4	0.457	0.982
30	1126	2.4	0.02	1150	509.1	0.452	0.97
30	1114	2.6	0.03	1150	497.8	0.447	0.959
30	1101.9	2.8	0.04	1150	486.6	0.442	0.948
30	1089.6	3	0.05	1150	475.6	0.436	0.937
30	1077.3	3.2	0.06	1150	464.8	0.431	0.926
30	1064.9	3.4	0.07	1150	454.2	0.427	0.916
30	1052.4	3.6	0.08	1150	443.9	0.422	0.905
30	1039.8	3.8	0.09	1150	434	0.417	0.896

Speed (mph)	Vertical Force (lb)	Slip Angle (degree)	Camber	Curve Radius (ft)	FEA Horizontal Force (lb)	FEA FN	Friction Adjustment Factor
30	1027.2	4	0.1	1150	424.3	0.413	0.887
32.5	1160.9	0.6	0	1150	517.8	0.446	0.973
32.5	1149.2	2.2	0.01	1150	516.2	0.449	0.979
32.5	1137.4	2.4	0.02	1150	504.7	0.444	0.967
32.5	1125.4	2.5	0.03	1150	493.2	0.438	0.956
32.5	1113.4	2.7	0.04	1150	481.9	0.433	0.944
32.5	1101.3	2.9	0.05	1150	470.8	0.427	0.932
32.5	1089.1	3.1	0.06	1150	459.8	0.422	0.921
32.5	1076.8	3.2	0.07	1150	449.1	0.417	0.91
32.5	1064.3	3.4	0.08	1150	438.7	0.412	0.899
32.5	1051.9	3.6	0.09	1150	428.7	0.408	0.889
32.5	1039.3	3.8	0.1	1150	418.9	0.403	0.879
35	1172.9	0.5	0	1150	513.6	0.438	0.972
35	1161.3	2.2	0.01	1150	512.2	0.441	0.979
35	1149.6	2.3	0.02	1150	500.6	0.435	0.966
35	1137.8	2.5	0.03	1150	489	0.43	0.954
35	1125.9	2.6	0.04	1150	477.5	0.424	0.941
35	1113.9	2.8	0.05	1150	466.3	0.419	0.929
35	1101.8	2.9	0.06	1150	455.2	0.413	0.917
35	1089.5	3.1	0.07	1150	444.4	0.408	0.905
35	1077.2	3.2	0.08	1150	433.9	0.403	0.894
35	1064.8	3.4	0.09	1150	423.7	0.398	0.883
35	1052.4	3.5	0.1	1150	413.9	0.393	0.873
37.5	1185.9	0.4	0	1150	509.6	0.43	0.961
37.5	1174.4	2.1	0.01	1150	508.6	0.433	0.968
37.5	1162.8	2.3	0.02	1150	496.8	0.427	0.955
37.5	1151.1	2.4	0.03	1150	485.1	0.421	0.942
37.5	1139.3	2.5	0.04	1150	473.5	0.416	0.929
37.5	1127.4	2.6	0.05	1150	462.1	0.41	0.916
37.5	1115.4	2.8	0.06	1150	450.9	0.404	0.904
37.5	1103.3	2.9	0.07	1150	440	0.399	0.891

Speed (mph)	**Vertical Force (lb)**	**Slip Angle (degree)**	**Camber**	**Curve Radius (ft)**	**FEA Horizontal Force (lb)**	**FEA FN**	**Friction Adjustment Factor**
37.5	1091.1	3	0.08	1150	429.4	0.394	0.88
37.5	1078.8	3.2	0.09	1150	419.1	0.389	0.868
37.5	1066.4	3.3	0.1	1150	409.2	0.384	0.858
40	1199.8	0.3	0	1150	506	0.422	0.992
40	1188.4	2.1	0.01	1150	505.3	0.425	1
40	1176.9	2.2	0.02	1150	493.4	0.419	0.986
40	1165.3	2.3	0.03	1150	481.5	0.413	0.972
40	1153.6	2.4	0.04	1150	469.8	0.407	0.958
40	1141.8	2.5	0.05	1150	458.4	0.401	0.944
40	1129.9	2.6	0.06	1150	447.1	0.396	0.931
40	1117.9	2.7	0.07	1150	436.1	0.39	0.918
40	1105.8	2.8	0.08	1150	425.4	0.385	0.905
40	1093.7	2.9	0.09	1150	415	0.379	0.893
40	1081.4	3	0.1	1150	405	0.375	0.881
42.5	1214.5	0.2	0	1150	502.6	0.414	0.946
42.5	1203.3	2.1	0.01	1150	502.3	0.417	0.954
42.5	1191.9	2.1	0.02	1150	490.3	0.411	0.94
42.5	1180.5	2.2	0.03	1150	478.4	0.405	0.926
42.5	1168.9	2.3	0.04	1150	466.6	0.399	0.912
42.5	1157.2	2.4	0.05	1150	455	0.393	0.899
42.5	1145.4	2.4	0.06	1150	443.6	0.387	0.885
42.5	1133.6	2.5	0.07	1150	432.5	0.382	0.872
42.5	1121.6	2.6	0.08	1150	421.7	0.376	0.859
42.5	1109.5	2.6	0.09	1150	411.3	0.371	0.847
42.5	1097.4	2.7	0.1	1150	401.2	0.366	0.836
45	1230.1	0.1	0	1150	499.7	0.406	0.943
45	1219.1	2	0.01	1150	499.7	0.41	0.952
45	1207.8	2.1	0.02	1150	487.6	0.404	0.938
45	1196.5	2.1	0.03	1150	475.6	0.397	0.923
45	1185.1	2.2	0.04	1150	463.7	0.391	0.909
45	1173.5	2.2	0.05	1150	452	0.385	0.895

Speed (mph)	Vertical Force (lb)	Slip Angle (degree)	Camber	Curve Radius (ft)	FEA Horizontal Force (lb)	FEA FN	Friction Adjustment Factor
45	1161.9	2.2	0.06	1150	440.6	0.379	0.881
45	1150.1	2.3	0.07	1150	429.4	0.373	0.867
45	1138.3	2.3	0.08	1150	418.5	0.368	0.854
45	1126.3	2.4	0.09	1150	408	0.362	0.841
45	1114.3	2.4	0.1	1150	397.9	0.357	0.829
47.5	1246.7	0	0	1150	497	0.399	0.933
47.5	1235.7	2	0.01	1150	497.5	0.403	0.942
47.5	1224.7	2	0.02	1150	485.3	0.396	0.927
47.5	1213.5	2	0.03	1150	473.2	0.39	0.913
47.5	1202.2	2	0.04	1150	461.3	0.384	0.898
47.5	1190.8	2	0.05	1150	449.5	0.377	0.883
47.5	1179.3	2	0.06	1150	438	0.371	0.869
47.5	1167.6	2	0.07	1150	426.8	0.365	0.855
47.5	1155.9	2.1	0.08	1150	415.8	0.36	0.842
47.5	1144.1	2.1	0.09	1150	405.3	0.354	0.829
47.5	1132.2	2.1	0.1	1150	395.1	0.349	0.817
50	1264.1	-0.1	0	1150	494.8	0.391	0.933
50	1253.3	2	0.01	1150	495.7	0.395	0.943
50	1242.4	1.9	0.02	1150	483.4	0.389	0.927
50	1231.4	1.9	0.03	1150	471.2	0.383	0.912
50	1220.2	1.9	0.04	1150	459.2	0.376	0.897
50	1209	1.9	0.05	1150	447.4	0.37	0.882
50	1197.6	1.8	0.06	1150	435.8	0.364	0.867
50	1186.1	1.8	0.07	1150	424.6	0.358	0.853
50	1174.5	1.8	0.08	1150	413.6	0.352	0.839
50	1162.8	1.7	0.09	1150	403	0.347	0.826
50	1151.1	1.7	0.1	1150	392.8	0.341	0.813
30	1147	0.6	0	1200	521.6	0.455	0.976
30	1135.2	2.2	0.01	1200	519.8	0.458	0.983
30	1123.3	2.4	0.02	1200	508.4	0.453	0.972
30	1111.2	2.6	0.03	1200	497	0.447	0.96

Speed (mph)	Vertical Force (lb)	Slip Angle (degree)	Camber	Curve Radius (ft)	FEA Horizontal Force (lb)	FEA FN	Friction Adjustment Factor
30	1099.1	2.8	0.04	1200	485.8	0.442	0.949
30	1086.8	3	0.05	1200	474.7	0.437	0.938
30	1074.5	3.2	0.06	1200	463.9	0.432	0.927
30	1062.1	3.3	0.07	1200	453.3	0.427	0.916
30	1049.6	3.5	0.08	1200	442.9	0.422	0.906
30	1037	3.7	0.09	1200	432.9	0.417	0.896
30	1024.3	3.9	0.1	1200	423.2	0.413	0.887
32.5	1157.7	0.6	0	1200	517	0.447	0.974
32.5	1146	2.2	0.01	1200	515.5	0.45	0.981
32.5	1134.2	2.3	0.02	1200	503.9	0.444	0.969
32.5	1122.2	2.5	0.03	1200	492.4	0.439	0.957
32.5	1110.2	2.7	0.04	1200	481	0.433	0.945
32.5	1098	2.9	0.05	1200	469.8	0.428	0.933
32.5	1085.8	3	0.06	1200	458.9	0.423	0.921
32.5	1073.4	3.2	0.07	1200	448.1	0.417	0.91
32.5	1061	3.4	0.08	1200	437.7	0.413	0.899
32.5	1048.5	3.5	0.09	1200	427.6	0.408	0.889
32.5	1035.9	3.7	0.1	1200	417.8	0.403	0.879
35	1169.3	0.5	0	1200	512.7	0.438	0.973
35	1157.7	2.1	0.01	1200	511.4	0.442	0.981
35	1145.9	2.3	0.02	1200	499.7	0.436	0.968
35	1134.1	2.4	0.03	1200	488.1	0.43	0.955
35	1122.1	2.6	0.04	1200	476.6	0.425	0.943
35	1110.1	2.7	0.05	1200	465.3	0.419	0.93
35	1097.9	2.9	0.06	1200	454.2	0.414	0.918
35	1085.7	3	0.07	1200	443.3	0.408	0.906
35	1073.3	3.2	0.08	1200	432.8	0.403	0.895
35	1060.9	3.3	0.09	1200	422.6	0.398	0.884
35	1048.4	3.5	0.1	1200	412.7	0.394	0.874
37.5	1181.7	0.4	0	1200	508.6	0.43	0.962
37.5	1170.2	2.1	0.01	1200	507.7	0.434	0.97

Speed (mph)	Vertical Force (lb)	Slip Angle (degree)	Camber	Curve Radius (ft)	FEA Horizontal Force (lb)	FEA FN	Friction Adjustment Factor
37.5	1158.6	2.2	0.02	1200	495.8	0.428	0.957
37.5	1146.8	2.4	0.03	1200	484.1	0.422	0.943
37.5	1135	2.5	0.04	1200	472.5	0.416	0.93
37.5	1123	2.6	0.05	1200	461.1	0.411	0.918
37.5	1111	2.7	0.06	1200	449.9	0.405	0.905
37.5	1098.8	2.9	0.07	1200	438.9	0.399	0.893
37.5	1086.6	3	0.08	1200	428.3	0.394	0.881
37.5	1074.3	3.1	0.09	1200	418	0.389	0.87
37.5	1061.8	3.2	0.1	1200	408	0.384	0.859
40	1195	0.3	0	1200	504.9	0.423	0.994
40	1183.6	2.1	0.01	1200	504.3	0.426	1.002
40	1172.1	2.2	0.02	1200	492.3	0.42	0.988
40	1160.4	2.3	0.03	1200	480.5	0.414	0.974
40	1148.7	2.4	0.04	1200	468.7	0.408	0.96
40	1136.9	2.5	0.05	1200	457.2	0.402	0.946
40	1124.9	2.6	0.06	1200	445.9	0.396	0.932
40	1112.9	2.7	0.07	1200	434.9	0.391	0.919
40	1100.8	2.8	0.08	1200	424.2	0.385	0.906
40	1088.5	2.9	0.09	1200	413.8	0.38	0.894
40	1076.2	3	0.1	1200	403.8	0.375	0.882
42.5	1209.1	0.2	0	1200	501.5	0.415	0.948
42.5	1197.8	2.1	0.01	1200	501.2	0.418	0.956
42.5	1186.5	2.1	0.02	1200	489.1	0.412	0.942
42.5	1174.9	2.2	0.03	1200	477.2	0.406	0.928
42.5	1163.3	2.3	0.04	1200	465.4	0.4	0.914
42.5	1151.6	2.3	0.05	1200	453.8	0.394	0.901
42.5	1139.8	2.4	0.06	1200	442.4	0.388	0.887
42.5	1127.9	2.5	0.07	1200	431.3	0.382	0.874
42.5	1115.8	2.5	0.08	1200	420.5	0.377	0.861
42.5	1103.7	2.6	0.09	1200	410	0.371	0.849
42.5	1091.5	2.7	0.1	1200	399.9	0.366	0.837

Speed (mph)	Vertical Force (lb)	Slip Angle (degree)	Camber	Curve Radius (ft)	FEA Horizontal Force (lb)	FEA FN	Friction Adjustment Factor
45	1224.1	0.1	0	1200	498.4	0.407	0.946
45	1213	2	0.01	1200	498.5	0.411	0.955
45	1201.7	2.1	0.02	1200	486.3	0.405	0.94
45	1190.3	2.1	0.03	1200	474.3	0.398	0.925
45	1178.8	2.2	0.04	1200	462.4	0.392	0.911
45	1167.2	2.2	0.05	1200	450.7	0.386	0.897
45	1155.5	2.2	0.06	1200	439.3	0.38	0.883
45	1143.7	2.3	0.07	1200	428.1	0.374	0.869
45	1131.8	2.3	0.08	1200	417.2	0.369	0.856
45	1119.8	2.3	0.09	1200	406.7	0.363	0.844
45	1107.8	2.4	0.1	1200	396.6	0.358	0.831
47.5	1240	0	0	1200	495.7	0.4	0.936
47.5	1229	2	0.01	1200	496.1	0.404	0.945
47.5	1217.8	2	0.02	1200	483.9	0.397	0.93
47.5	1206.6	2	0.03	1200	471.8	0.391	0.915
47.5	1195.2	2	0.04	1200	459.9	0.385	0.9
47.5	1183.8	2	0.05	1200	448.1	0.379	0.886
47.5	1172.2	2	0.06	1200	436.6	0.372	0.872
47.5	1160.5	2	0.07	1200	425.4	0.367	0.858
47.5	1148.7	2.1	0.08	1200	414.5	0.361	0.844
47.5	1136.9	2.1	0.09	1200	403.9	0.355	0.831
47.5	1124.9	2.1	0.1	1200	393.7	0.35	0.819
50	1256.7	-0.1	0	1200	493.3	0.393	0.936
50	1245.8	2	0.01	1200	494.2	0.397	0.945
50	1234.8	1.9	0.02	1200	481.9	0.39	0.93
50	1223.7	1.9	0.03	1200	469.7	0.384	0.915
50	1212.5	1.9	0.04	1200	457.7	0.378	0.9
50	1201.2	1.9	0.05	1200	445.9	0.371	0.885
50	1189.7	1.8	0.06	1200	434.4	0.365	0.87
50	1178.2	1.8	0.07	1200	423.1	0.359	0.856
50	1166.6	1.8	0.08	1200	412.2	0.353	0.842

Speed (mph)	Vertical Force (lb)	Slip Angle (degree)	Camber	Curve Radius (ft)	FEA Horizontal Force (lb)	FEA FN	Friction Adjustment Factor
50	1154.8	1.8	0.09	1200	401.6	0.348	0.829
50	1143	1.7	0.1	1200	391.3	0.342	0.816
30	1140.2	0.6	0	1350	519.7	0.456	0.978
30	1128.3	2.2	0.01	1350	518.2	0.459	0.986
30	1116.3	2.3	0.02	1350	506.6	0.454	0.974
30	1104.2	2.5	0.03	1350	495.1	0.448	0.963
30	1092	2.7	0.04	1350	483.8	0.443	0.951
30	1079.7	2.9	0.05	1350	472.6	0.438	0.94
30	1067.3	3	0.06	1350	461.6	0.432	0.928
30	1054.8	3.2	0.07	1350	450.8	0.427	0.917
30	1042.3	3.4	0.08	1350	440.4	0.423	0.907
30	1029.6	3.5	0.09	1350	430.2	0.418	0.897
30	1016.9	3.7	0.1	1350	420.4	0.413	0.888
32.5	1149.7	0.5	0	1350	514.9	0.448	0.977
32.5	1137.9	2.2	0.01	1350	513.7	0.451	0.984
32.5	1126	2.3	0.02	1350	501.9	0.446	0.972
32.5	1114	2.5	0.03	1350	490.3	0.44	0.96
32.5	1101.8	2.6	0.04	1350	478.8	0.435	0.948
32.5	1089.6	2.8	0.05	1350	467.5	0.429	0.936
32.5	1077.3	2.9	0.06	1350	456.4	0.424	0.924
32.5	1064.9	3.1	0.07	1350	445.6	0.418	0.912
32.5	1052.4	3.2	0.08	1350	435	0.413	0.901
32.5	1039.8	3.4	0.09	1350	424.8	0.409	0.891
32.5	1027.2	3.5	0.1	1350	414.9	0.404	0.881
35	1160	0.4	0	1350	510.4	0.44	0.977
35	1148.3	2.1	0.01	1350	509.4	0.444	0.985
35	1136.4	2.3	0.02	1350	497.5	0.438	0.972
35	1124.5	2.4	0.03	1350	485.8	0.432	0.959
35	1112.5	2.5	0.04	1350	474.2	0.426	0.946
35	1100.3	2.7	0.05	1350	462.8	0.421	0.933
35	1088.1	2.8	0.06	1350	451.6	0.415	0.921

Speed (mph)	Vertical Force (lb)	Slip Angle (degree)	Camber	Curve Radius (ft)	FEA Horizontal Force (lb)	FEA FN	Friction Adjustment Factor
35	1075.8	2.9	0.07	1350	440.6	0.41	0.909
35	1063.4	3.1	0.08	1350	430	0.404	0.897
35	1050.9	3.2	0.09	1350	419.7	0.399	0.886
35	1038.3	3.3	0.1	1350	409.7	0.395	0.876
37.5	1171	0.4	0	1350	506.1	0.432	0.966
37.5	1159.4	2.1	0.01	1350	505.4	0.436	0.974
37.5	1147.7	2.2	0.02	1350	493.4	0.43	0.961
37.5	1135.8	2.3	0.03	1350	481.6	0.424	0.948
37.5	1123.9	2.4	0.04	1350	469.9	0.418	0.934
37.5	1111.9	2.5	0.05	1350	458.4	0.412	0.921
37.5	1099.7	2.7	0.06	1350	447.1	0.407	0.909
37.5	1087.5	2.8	0.07	1350	436.1	0.401	0.896
37.5	1075.2	2.9	0.08	1350	425.3	0.396	0.884
37.5	1062.7	3	0.09	1350	415	0.39	0.873
37.5	1050.3	3.1	0.1	1350	405	0.386	0.862
40	1182.8	0.3	0	1350	502.2	0.425	0.999
40	1171.3	2.1	0.01	1350	501.7	0.428	1.007
40	1159.7	2.2	0.02	1350	489.6	0.422	0.993
40	1147.9	2.3	0.03	1350	477.7	0.416	0.979
40	1136.1	2.3	0.04	1350	465.9	0.41	0.965
40	1124.2	2.4	0.05	1350	454.3	0.404	0.951
40	1112.1	2.5	0.06	1350	443	0.398	0.937
40	1100	2.6	0.07	1350	431.9	0.393	0.924
40	1087.8	2.7	0.08	1350	421.1	0.387	0.911
40	1075.4	2.8	0.09	1350	410.7	0.382	0.898
40	1063	2.9	0.1	1350	400.6	0.377	0.886
42.5	1195.4	0.2	0	1350	498.5	0.417	0.953
42.5	1184	2.1	0.01	1350	498.3	0.421	0.962
42.5	1172.5	2.1	0.02	1350	486.2	0.415	0.948
42.5	1160.8	2.2	0.03	1350	474.2	0.408	0.934
42.5	1149.1	2.2	0.04	1350	462.3	0.402	0.92

Speed (mph)	Vertical Force (lb)	Slip Angle (degree)	Camber	Curve Radius (ft)	FEA Horizontal Force (lb)	FEA FN	Friction Adjustment Factor
42.5	1137.3	2.3	0.05	1350	450.7	0.396	0.906
42.5	1125.3	2.4	0.06	1350	439.2	0.39	0.892
42.5	1113.3	2.4	0.07	1350	428.1	0.385	0.879
42.5	1101.2	2.5	0.08	1350	417.3	0.379	0.866
42.5	1088.9	2.5	0.09	1350	406.8	0.374	0.854
42.5	1076.6	2.6	0.1	1350	396.7	0.368	0.842
45	1208.7	0.1	0	1350	495.2	0.41	0.952
45	1197.4	2	0.01	1350	495.3	0.414	0.961
45	1186	2.1	0.02	1350	483.1	0.407	0.946
45	1174.5	2.1	0.03	1350	471	0.401	0.931
45	1162.9	2.1	0.04	1350	459.1	0.395	0.917
45	1151.2	2.2	0.05	1350	447.4	0.389	0.903
45	1139.3	2.2	0.06	1350	435.9	0.383	0.889
45	1127.4	2.2	0.07	1350	424.7	0.377	0.875
45	1115.4	2.3	0.08	1350	413.9	0.371	0.862
45	1103.3	2.3	0.09	1350	403.3	0.366	0.849
45	1091.1	2.3	0.1	1350	393.2	0.36	0.837
47.5	1222.8	0	0	1350	492.3	0.403	0.942
47.5	1211.6	2	0.01	1350	492.7	0.407	0.952
47.5	1200.3	2	0.02	1350	480.4	0.4	0.937
47.5	1189	2	0.03	1350	468.3	0.394	0.922
47.5	1177.5	2	0.04	1350	456.3	0.388	0.907
47.5	1165.9	2	0.05	1350	444.6	0.381	0.892
47.5	1154.1	2	0.06	1350	433.1	0.375	0.878
47.5	1142.3	2	0.07	1350	421.8	0.369	0.864
47.5	1130.4	2	0.08	1350	410.9	0.364	0.851
47.5	1118.4	2.1	0.09	1350	400.4	0.358	0.838
47.5	1106.3	2.1	0.1	1350	390.2	0.353	0.826
50	1237.6	-0.1	0	1350	489.6	0.396	0.943
50	1226.6	2	0.01	1350	490.4	0.4	0.953
50	1215.5	2	0.02	1350	478.1	0.393	0.937

Speed (mph)	Vertical Force (lb)	Slip Angle (degree)	Camber	Curve Radius (ft)	FEA Horizontal Force (lb)	FEA FN	Friction Adjustment Factor
50	1204.2	1.9	0.03	1350	465.9	0.387	0.922
50	1192.8	1.9	0.04	1350	453.9	0.381	0.907
50	1181.3	1.9	0.05	1350	442.2	0.374	0.892
50	1169.7	1.9	0.06	1350	430.6	0.368	0.877
50	1158	1.8	0.07	1350	419.4	0.362	0.863
50	1146.3	1.8	0.08	1350	408.5	0.356	0.849
50	1134.4	1.8	0.09	1350	397.9	0.351	0.836
50	1122.4	1.8	0.1	1350	387.8	0.345	0.823
30	1134.7	0.5	0	1500	518.2	0.457	0.98
30	1122.8	2.2	0.01	1500	517	0.46	0.988
30	1110.7	2.3	0.02	1500	505.3	0.455	0.976
30	1098.6	2.5	0.03	1500	493.6	0.449	0.965
30	1086.3	2.6	0.04	1500	482.2	0.444	0.953
30	1074	2.8	0.05	1500	470.8	0.438	0.941
30	1061.5	2.9	0.06	1500	459.7	0.433	0.93
30	1049	3.1	0.07	1500	448.9	0.428	0.919
30	1036.4	3.2	0.08	1500	438.3	0.423	0.908
30	1023.7	3.4	0.09	1500	428.1	0.418	0.898
30	1010.9	3.5	0.1	1500	418.2	0.414	0.888
32.5	1143.2	0.5	0	1500	513.3	0.449	0.979
32.5	1131.4	2.1	0.01	1500	512.2	0.453	0.987
32.5	1119.4	2.3	0.02	1500	500.4	0.447	0.975
32.5	1107.4	2.4	0.03	1500	488.7	0.441	0.962
32.5	1095.2	2.5	0.04	1500	477.1	0.436	0.95
32.5	1082.9	2.7	0.05	1500	465.6	0.43	0.938
32.5	1070.5	2.8	0.06	1500	454.4	0.424	0.926
32.5	1058.1	3	0.07	1500	443.5	0.419	0.914
32.5	1045.5	3.1	0.08	1500	432.9	0.414	0.903
32.5	1032.9	3.2	0.09	1500	422.6	0.409	0.892
32.5	1020.2	3.4	0.1	1500	412.6	0.404	0.882
35	1152.5	0.4	0	1500	508.6	0.441	0.979

Speed (mph)	Vertical Force (lb)	Slip Angle (degree)	Camber	Curve Radius (ft)	FEA Horizontal Force (lb)	FEA FN	Friction Adjustment Factor
35	1140.7	2.1	0.01	1500	507.7	0.445	0.988
35	1128.8	2.2	0.02	1500	495.8	0.439	0.975
35	1116.9	2.4	0.03	1500	483.9	0.433	0.962
35	1104.8	2.5	0.04	1500	472.3	0.427	0.949
35	1092.6	2.6	0.05	1500	460.8	0.422	0.936
35	1080.3	2.7	0.06	1500	449.5	0.416	0.923
35	1067.9	2.8	0.07	1500	438.5	0.411	0.911
35	1055.4	2.9	0.08	1500	427.8	0.405	0.9
35	1042.9	3.1	0.09	1500	417.4	0.4	0.888
35	1030.2	3.2	0.1	1500	407.4	0.395	0.878
37.5	1162.4	0.3	0	1500	504.1	0.434	0.969
37.5	1150.7	2.1	0.01	1500	503.5	0.438	0.978
37.5	1139	2.2	0.02	1500	491.5	0.432	0.964
37.5	1127	2.3	0.03	1500	479.6	0.425	0.951
37.5	1115	2.4	0.04	1500	467.8	0.42	0.938
37.5	1102.9	2.5	0.05	1500	456.2	0.414	0.925
37.5	1090.7	2.6	0.06	1500	444.9	0.408	0.912
37.5	1078.4	2.7	0.07	1500	433.8	0.402	0.899
37.5	1066	2.8	0.08	1500	423	0.397	0.887
37.5	1053.5	2.9	0.09	1500	412.6	0.392	0.875
37.5	1041	3	0.1	1500	402.5	0.387	0.864
40	1173.1	0.3	0	1500	500	0.426	1.003
40	1161.5	2.1	0.01	1500	499.6	0.43	1.012
40	1149.8	2.2	0.02	1500	487.5	0.424	0.997
40	1137.9	2.2	0.03	1500	475.5	0.418	0.983
40	1126	2.3	0.04	1500	463.7	0.412	0.969
40	1114	2.4	0.05	1500	452	0.406	0.954
40	1101.9	2.5	0.06	1500	440.6	0.4	0.941
40	1089.7	2.5	0.07	1500	429.5	0.394	0.927
40	1077.4	2.6	0.08	1500	418.6	0.389	0.914
40	1065	2.7	0.09	1500	408.2	0.383	0.902

Speed (mph)	Vertical Force (lb)	Slip Angle (degree)	Camber	Curve Radius (ft)	FEA Horizontal Force (lb)	FEA FN	Friction Adjustment Factor
40	1052.5	2.8	0.1	1500	398.1	0.378	0.89
42.5	1184.4	0.2	0	1500	496.2	0.419	0.958
42.5	1172.9	2.1	0.01	1500	496	0.423	0.967
42.5	1161.3	2.1	0.02	1500	483.8	0.417	0.952
42.5	1149.5	2.2	0.03	1500	471.8	0.41	0.938
42.5	1137.7	2.2	0.04	1500	459.9	0.404	0.924
42.5	1125.8	2.3	0.05	1500	448.2	0.398	0.91
42.5	1113.8	2.3	0.06	1500	436.7	0.392	0.896
42.5	1101.6	2.4	0.07	1500	425.6	0.386	0.883
42.5	1089.4	2.4	0.08	1500	414.7	0.381	0.87
42.5	1077.1	2.5	0.09	1500	404.2	0.375	0.858
42.5	1064.7	2.5	0.1	1500	394.1	0.37	0.846
45	1196.4	0.1	0	1500	492.7	0.412	0.957
45	1185	2	0.01	1500	492.8	0.416	0.966
45	1173.5	2.1	0.02	1500	480.5	0.41	0.951
45	1161.9	2.1	0.03	1500	468.4	0.403	0.936
45	1150.1	2.1	0.04	1500	456.5	0.397	0.922
45	1138.3	2.2	0.05	1500	444.8	0.391	0.907
45	1126.4	2.2	0.06	1500	433.3	0.385	0.893
45	1114.3	2.2	0.07	1500	422.1	0.379	0.88
45	1102.2	2.2	0.08	1500	411.2	0.373	0.866
45	1090	2.3	0.09	1500	400.7	0.368	0.854
45	1077.7	2.3	0.1	1500	390.5	0.362	0.842
47.5	1209	0	0	1500	489.5	0.405	0.948
47.5	1197.8	2	0.01	1500	489.9	0.409	0.957
47.5	1186.4	2	0.02	1500	477.6	0.403	0.942
47.5	1174.9	2	0.03	1500	465.5	0.396	0.927
47.5	1163.2	2	0.04	1500	453.5	0.39	0.912
47.5	1151.5	2	0.05	1500	441.8	0.384	0.898
47.5	1139.7	2	0.06	1500	430.2	0.378	0.884
47.5	1127.8	2	0.07	1500	419	0.372	0.87

Speed (mph)	Vertical Force (lb)	Slip Angle (degree)	Camber	Curve Radius (ft)	FEA Horizontal Force (lb)	FEA FN	Friction Adjustment Factor
47.5	1115.7	2	0.08	1500	408.1	0.366	0.856
47.5	1103.6	2	0.09	1500	397.6	0.36	0.843
47.5	1091.4	2.1	0.1	1500	387.5	0.355	0.831
50	1222.4	-0.1	0	1500	486.7	0.398	0.949
50	1211.2	2	0.01	1500	487.3	0.402	0.959
50	1200	2	0.02	1500	475	0.396	0.943
50	1188.6	1.9	0.03	1500	462.9	0.389	0.928
50	1177.1	1.9	0.04	1500	450.9	0.383	0.913
50	1165.5	1.9	0.05	1500	439.2	0.377	0.898
50	1153.7	1.9	0.06	1500	427.6	0.371	0.883
50	1141.9	1.8	0.07	1500	416.4	0.365	0.869
50	1130	1.8	0.08	1500	405.5	0.359	0.855
50	1118	1.8	0.09	1500	395	0.353	0.842
50	1105.9	1.8	0.1	1500	384.9	0.348	0.829
30	1085.3	0	0	Infinity	505.6	0.466	1
32.5	1085.3	0	0	Infinity	497.8	0.459	1
35	1085.3	0	0	Infinity	489	0.451	1
37.5	1085.3	0	0	Infinity	485.6	0.447	1
40	1085.3	0	0	Infinity	461.4	0.425	1
42.5	1085.3	0	0	Infinity	474.8	0.437	1
45	1085.3	0	0	Infinity	467.3	0.431	1
47.5	1085.3	0	0	Infinity	463.7	0.427	1
50	1085.3	0	0	Infinity	455.4	0.42	1

Table D.2 *Friction Numbers by Speed, Vertical Force, Slip Angle, and Camber Angle on the Outer Tire.*

Speed (mph)	Vertical Force (lbs)	Slip Angle (degree)	Camber	Curve Radius (ft)	FEA Horizontal Force (lbs)	FEA FN	Friction Adjustment Factor
30	591.9	5.1	0	150	292.5	0.494	1.061
30	607	3.5	0.01	150	303.2	0.5	1.072
30	621.9	5.1	0.02	150	305	0.49	1.053
30	636.8	6.6	0.03	150	307.9	0.483	1.038
30	651.7	8.2	0.04	150	310.6	0.477	1.023
30	666.4	9.7	0.05	150	312.7	0.469	1.007
30	681.1	11.2	0.06	150	314.4	0.462	0.991
30	695.7	12.8	0.07	150	315.8	0.454	0.975
30	710.1	14.3	0.08	150	316.9	0.446	0.958
30	724.5	15.8	0.09	150	317.5	0.438	0.941
30	738.8	17.4	0.1	150	317.5	0.43	0.922
32.5	506.3	4.6	0	150	252.4	0.498	1.07
32.5	521.8	3.4	0.01	150	262.8	0.504	1.081
32.5	537.2	4.7	0.02	150	265.5	0.494	1.061
32.5	552.6	6.1	0.03	150	269.5	0.488	1.047
32.5	568	7.5	0.04	150	273.8	0.482	1.035
32.5	583.2	8.8	0.05	150	277.5	0.476	1.021
32.5	598.4	10.2	0.06	150	280.7	0.469	1.007
32.5	613.5	11.6	0.07	150	283.5	0.462	0.992
32.5	628.6	12.9	0.08	150	285.9	0.455	0.976
32.5	643.5	14.3	0.09	150	287.9	0.447	0.96
32.5	658.4	15.7	0.1	150	289.4	0.44	0.944
35	413.8	3.9	0	150	208.5	0.504	1.082
35	429.8	3.2	0.01	150	218.5	0.508	1.091
35	445.8	4.4	0.02	150	222.4	0.499	1.071
35	461.7	5.5	0.03	150	227.6	0.493	1.058
35	477.6	6.7	0.04	150	233.3	0.488	1.049
35	493.4	7.9	0.05	150	238.7	0.484	1.039
35	509.2	9.1	0.06	150	243.5	0.478	1.027
35	524.9	10.3	0.07	150	247.8	0.472	1.013
35	540.5	11.5	0.08	150	251.5	0.465	0.999

Speed (mph)	Vertical Force (lbs)	Slip Angle (degree)	Camber	Curve Radius (ft)	FEA Horizontal Force (lbs)	FEA FN	Friction Adjustment Factor
35	556	12.6	0.09	150	254.7	0.458	0.984
35	571.5	13.8	0.1	150	257.5	0.451	0.967
37.5	314.4	3.3	0	150	161	0.512	1.099
37.5	331	3	0.01	150	170.2	0.514	1.104
37.5	347.5	4	0.02	150	175.4	0.505	1.083
37.5	364.1	5	0.03	150	181.8	0.499	1.072
37.5	380.5	5.9	0.04	150	189	0.497	1.066
37.5	396.9	6.9	0.05	150	196.3	0.494	1.061
37.5	413.3	7.9	0.06	150	202.9	0.491	1.054
37.5	429.6	8.9	0.07	150	208.8	0.486	1.043
37.5	445.8	9.9	0.08	150	213.9	0.48	1.03
37.5	462	10.9	0.09	150	218.3	0.473	1.014
37.5	478.1	11.8	0.1	150	222.2	0.465	0.998
40	208.2	2.6	0	150	110.3	0.53	1.138
40	225.4	2.8	0.01	150	118	0.524	1.124
40	242.5	3.5	0.02	150	124.4	0.513	1.101
40	259.7	4.3	0.03	150	132.2	0.509	1.093
40	276.8	5.1	0.04	150	140.7	0.508	1.091
40	293.8	5.9	0.05	150	149.5	0.509	1.093
40	310.8	6.6	0.06	150	158.1	0.509	1.092
40	327.8	7.4	0.07	150	165.9	0.506	1.087
40	344.7	8.2	0.08	150	172.8	0.501	1.076
40	361.5	8.9	0.09	150	178.8	0.494	1.061
40	378.3	9.7	0.1	150	183.9	0.486	1.044
42.5	95.1	1.8	0	150	58	0.61	1.309
42.5	112.9	2.5	0.01	150	63	0.558	1.197
42.5	130.7	3.1	0.02	150	70.4	0.538	1.155
42.5	148.5	3.6	0.03	150	79	0.532	1.142
42.5	166.3	4.2	0.04	150	88.6	0.532	1.143
42.5	184	4.7	0.05	150	98.6	0.536	1.15
42.5	201.7	5.3	0.06	150	108.6	0.539	1.156

Speed (mph)	Vertical Force (lbs)	Slip Angle (degree)	Camber	Curve Radius (ft)	FEA Horizontal Force (lbs)	FEA FN	Friction Adjustment Factor
42.5	219.4	5.8	0.07	150	118.3	0.539	1.158
42.5	237	6.4	0.08	150	127.2	0.537	1.152
42.5	254.6	6.9	0.09	150	135.2	0.531	1.14
42.5	272.1	7.5	0.1	150	142.1	0.522	1.121
45	-24.8	1	0	150			
45	-6.3	2.3	0.01	150			
45	12.2	2.6	0.02	150	14.9	1.224	2.628
45	30.7	2.9	0.03	150	24.2	0.788	1.692
45	49.1	3.2	0.04	150	34.3	0.698	1.499
45	67.6	3.5	0.05	150	45	0.666	1.43
45	86	3.8	0.06	150	56	0.651	1.397
45	104.4	4.1	0.07	150	66.8	0.64	1.374
45	122.8	4.4	0.08	150	77.2	0.629	1.35
45	141.1	4.8	0.09	150	87	0.617	1.323
45	159.4	5.1	0.1	150	95.9	0.601	1.291
47.5	-151.6	0.2	0	150			
47.5	-132.4	2.1	0.01	150			
47.5	-113.2	2.1	0.02	150			
47.5	-93.9	2.2	0.03	150			
47.5	-74.7	2.2	0.04	150			
47.5	-55.5	2.3	0.05	150			
47.5	-36.3	2.3	0.06	150			
47.5	-17.1	2.4	0.07	150			
47.5	2.1	2.4	0.08	150	26.1	12.583	27.011
47.5	21.2	2.5	0.09	150	36.8	1.734	3.721
47.5	40.3	2.5	0.1	150	46.8	1.161	2.491
50	-285.2	-0.7	0	150			
50	-265.3	1.8	0.01	150			
50	-245.3	1.6	0.02	150			
50	-225.3	1.4	0.03	150			
50	-205.2	1.1	0.04	150			

Speed (mph)	Vertical Force (lbs)	Slip Angle (degree)	Camber	Curve Radius (ft)	FEA Horizontal Force (lbs)	FEA FN	Friction Adjustment Factor
50	-185.2	0.9	0.05	150			
50	-165.2	0.7	0.06	150			
50	-145.2	0.5	0.07	150			
50	-125.2	0.3	0.08	150			
50	-105.2	0.1	0.09	150			
50	-85.2	-0.1	0.1	150			
30	838.6	2.6	0	300	397.5	0.474	1.017
30	852.3	2.8	0.01	300	401	0.471	1.01
30	865.8	3.5	0.02	300	402.7	0.465	0.998
30	879.3	4.3	0.03	300	404.9	0.461	0.989
30	892.7	5.1	0.04	300	406.5	0.455	0.978
30	905.9	5.8	0.05	300	407	0.449	0.964
30	919.1	6.6	0.06	300	406.6	0.442	0.95
30	932.1	7.4	0.07	300	405.3	0.435	0.933
30	945.1	8.2	0.08	300	403.5	0.427	0.917
30	957.9	8.9	0.09	300	401.4	0.419	0.9
30	970.6	9.7	0.1	300	399.2	0.411	0.883
32.5	795.8	2.3	0	300	376.6	0.473	1.016
32.5	809.7	2.7	0.01	300	379.3	0.468	1.005
32.5	823.5	3.4	0.02	300	381.3	0.463	0.994
32.5	837.2	4.1	0.03	300	383.9	0.459	0.984
32.5	850.8	4.7	0.04	300	386.1	0.454	0.974
32.5	864.3	5.4	0.05	300	387.4	0.448	0.962
32.5	877.8	6.1	0.06	300	387.8	0.442	0.948
32.5	891.1	6.8	0.07	300	387.2	0.435	0.933
32.5	904.3	7.5	0.08	300	385.8	0.427	0.916
32.5	917.4	8.2	0.09	300	383.9	0.419	0.898
32.5	930.4	8.8	0.1	300	381.9	0.41	0.881
35	749.5	2	0	300	354.8	0.473	1.016
35	763.7	2.6	0.01	300	356.3	0.467	1.001
35	777.8	3.2	0.02	300	358.5	0.461	0.989

Speed (mph)	Vertical Force (lbs)	Slip Angle (degree)	Camber	Curve Radius (ft)	FEA Horizontal Force (lbs)	FEA FN	Friction Adjustment Factor
35	791.7	3.8	0.03	300	361.1	0.456	0.979
35	805.6	4.4	0.04	300	363.7	0.451	0.969
35	819.4	5	0.05	300	365.8	0.446	0.958
35	833.1	5.5	0.06	300	367.2	0.441	0.946
35	846.7	6.1	0.07	300	367.6	0.434	0.932
35	860.2	6.7	0.08	300	366.9	0.427	0.916
35	873.6	7.3	0.09	300	365.5	0.418	0.898
35	886.9	7.9	0.1	300	363.7	0.41	0.88
37.5	699.9	1.6	0	300	332.4	0.475	1.036
37.5	714.3	2.5	0.01	300	332.1	0.465	1.014
37.5	728.6	3	0.02	300	334.5	0.459	1.001
37.5	742.9	3.5	0.03	300	337.1	0.454	0.989
37.5	757.1	4	0.04	300	339.8	0.449	0.979
37.5	771.2	4.5	0.05	300	342.5	0.444	0.968
37.5	785.2	5	0.06	300	344.7	0.439	0.957
37.5	799.1	5.4	0.07	300	346.3	0.433	0.945
37.5	812.9	5.9	0.08	300	346.7	0.427	0.93
37.5	826.6	6.4	0.09	300	346.2	0.419	0.913
37.5	840.3	6.9	0.1	300	344.9	0.41	0.895
40	646.8	1.3	0	300	309.1	0.478	1.042
40	661.5	2.4	0.01	300	306.7	0.464	1.011
40	676.1	2.8	0.02	300	309.5	0.458	0.998
40	690.7	3.2	0.03	300	312.4	0.452	0.986
40	705.2	3.5	0.04	300	315.5	0.447	0.975
40	719.6	3.9	0.05	300	318.6	0.443	0.965
40	734	4.3	0.06	300	321.5	0.438	0.955
40	748.2	4.7	0.07	300	323.9	0.433	0.944
40	762.4	5.1	0.08	300	325.4	0.427	0.931
40	776.4	5.5	0.09	300	325.9	0.42	0.915
40	790.4	5.9	0.1	300	325.3	0.412	0.897
42.5	590.2	0.9	0	300	284.6	0.482	1.051

Speed (mph)	Vertical Force (lbs)	Slip Angle (degree)	Camber	Curve Radius (ft)	FEA Horizontal Force (lbs)	FEA FN	Friction Adjustment Factor
42.5	605.3	2.3	0.01	300	279.9	0.462	1.008
42.5	620.2	2.5	0.02	300	283.6	0.457	0.997
42.5	635.1	2.8	0.03	300	287.3	0.452	0.986
42.5	650	3.1	0.04	300	291.1	0.448	0.977
42.5	664.7	3.4	0.05	300	294.9	0.444	0.967
42.5	679.4	3.6	0.06	300	298.5	0.439	0.958
42.5	694	3.9	0.07	300	301.6	0.435	0.948
42.5	708.5	4.2	0.08	300	303.9	0.429	0.935
42.5	722.9	4.5	0.09	300	305	0.422	0.92
42.5	737.2	4.7	0.1	300	305.1	0.414	0.902
45	530.3	0.5	0	300	258.2	0.487	1.062
45	545.6	2.2	0.01	300	251.4	0.461	1.005
45	561	2.3	0.02	300	256.3	0.457	0.996
45	576.2	2.5	0.03	300	261.3	0.453	0.989
45	591.4	2.6	0.04	300	266.2	0.45	0.982
45	606.5	2.8	0.05	300	271.1	0.447	0.974
45	621.6	2.9	0.06	300	275.5	0.443	0.967
45	636.5	3.1	0.07	300	279.4	0.439	0.957
45	651.4	3.2	0.08	300	282.2	0.433	0.945
45	666.2	3.4	0.09	300	283.9	0.426	0.929
45	680.9	3.5	0.1	300	284.4	0.418	0.911
47.5	466.9	0.1	0	300	229.9	0.492	1.074
47.5	482.6	2	0.01	300	221.1	0.458	0.999
47.5	498.3	2.1	0.02	300	227.4	0.456	0.995
47.5	513.9	2.1	0.03	300	233.7	0.455	0.992
47.5	529.5	2.1	0.04	300	240	0.453	0.988
47.5	545	2.1	0.05	300	245.9	0.451	0.984
47.5	560.4	2.2	0.06	300	251.4	0.449	0.978
47.5	575.8	2.2	0.07	300	256.1	0.445	0.97
47.5	591	2.2	0.08	300	259.6	0.439	0.958
47.5	606.2	2.2	0.09	300	261.9	0.432	0.942

Speed (mph)	Vertical Force (lbs)	Slip Angle (degree)	Camber	Curve Radius (ft)	FEA Horizontal Force (lbs)	FEA FN	Friction Adjustment Factor
47.5	621.4	2.3	0.1	300	262.8	0.423	0.922
50	400	-0.4	0	300	199.8	0.5	1.089
50	416.2	1.9	0.01	300	188.9	0.454	0.99
50	432.2	1.8	0.02	300	196.6	0.455	0.992
50	448.2	1.7	0.03	300	204.3	0.456	0.994
50	464.2	1.6	0.04	300	211.8	0.456	0.995
50	480.1	1.5	0.05	300	218.9	0.456	0.994
50	495.9	1.4	0.06	300	225.3	0.454	0.991
50	511.7	1.2	0.07	300	230.8	0.451	0.984
50	527.4	1.1	0.08	300	235.1	0.446	0.972
50	543	1	0.09	300	238.1	0.438	0.956
50	558.6	0.9	0.1	300	239.8	0.429	0.936
30	920.9	1.7	0	450	433	0.47	1.025
30	934	2.5	0.01	450	432.6	0.463	1.01
30	947.1	3	0.02	450	434.5	0.459	1
30	960.1	3.5	0.03	450	436.8	0.455	0.992
30	973	4.1	0.04	450	438.6	0.451	0.983
30	985.8	4.6	0.05	450	439.1	0.445	0.971
30	998.4	5.1	0.06	450	438.6	0.439	0.958
30	1011	5.6	0.07	450	437.2	0.433	0.943
30	1023.4	6.1	0.08	450	435.2	0.425	0.927
30	1035.7	6.6	0.09	450	432.5	0.418	0.911
30	1047.9	7.1	0.1	450	429.4	0.41	0.894
32.5	892.3	1.5	0	450	417.3	0.468	1.02
32.5	905.7	2.5	0.01	450	416.2	0.46	1.002
32.5	918.9	2.9	0.02	450	418.3	0.455	0.993
32.5	932	3.4	0.03	450	420.9	0.452	0.985
32.5	945.1	3.8	0.04	450	423.1	0.448	0.976
32.5	958	4.3	0.05	450	424.2	0.443	0.966
32.5	970.9	4.7	0.06	450	424.2	0.437	0.953
32.5	983.6	5.2	0.07	450	423.3	0.43	0.938

Speed (mph)	Vertical Force (lbs)	Slip Angle (degree)	Camber	Curve Radius (ft)	FEA Horizontal Force (lbs)	FEA FN	Friction Adjustment Factor
32.5	996.2	5.6	0.08	450	421.5	0.423	0.923
32.5	1008.7	6.1	0.09	450	418.8	0.415	0.905
32.5	1021.1	6.6	0.1	450	415.6	0.407	0.887
35	861.5	1.3	0	450	401.3	0.466	1.016
35	875	2.4	0.01	450	399	0.456	0.994
35	888.4	2.8	0.02	450	401.3	0.452	0.985
35	901.7	3.2	0.03	450	403.8	0.448	0.976
35	915	3.6	0.04	450	406	0.444	0.968
35	928.1	4	0.05	450	407.4	0.439	0.957
35	941.1	4.4	0.06	450	408	0.434	0.945
35	954	4.8	0.07	450	407.8	0.427	0.932
35	966.8	5.2	0.08	450	406.6	0.42	0.917
35	979.5	5.5	0.09	450	404.2	0.413	0.9
35	992.1	5.9	0.1	450	401	0.404	0.881
37.5	828.4	1.1	0	450	385.3	0.465	1.014
37.5	842.1	2.3	0.01	450	381.3	0.453	0.987
37.5	855.7	2.7	0.02	450	383.4	0.448	0.977
37.5	869.2	3	0.03	450	385.5	0.443	0.967
37.5	882.6	3.3	0.04	450	387.3	0.439	0.957
37.5	895.9	3.6	0.05	450	388.8	0.434	0.946
37.5	909.2	4	0.06	450	389.8	0.429	0.935
37.5	922.3	4.3	0.07	450	390.3	0.423	0.923
37.5	935.3	4.6	0.08	450	389.9	0.417	0.909
37.5	948.2	5	0.09	450	388.3	0.409	0.893
37.5	961	5.3	0.1	450	385.7	0.401	0.875
40	792.9	0.9	0	450	369.3	0.466	1.015
40	806.8	2.3	0.01	450	363	0.45	0.981
40	820.7	2.5	0.02	450	365	0.445	0.97
40	834.4	2.8	0.03	450	366.8	0.44	0.959
40	848	3	0.04	450	368.4	0.434	0.947
40	861.6	3.3	0.05	450	369.8	0.429	0.936

Speed (mph)	Vertical Force (lbs)	Slip Angle (degree)	Camber	Curve Radius (ft)	FEA Horizontal Force (lbs)	FEA FN	Friction Adjustment Factor
40	875	3.5	0.06	450	371.2	0.424	0.925
40	888.3	3.8	0.07	450	372.2	0.419	0.914
40	901.6	4.1	0.08	450	372.3	0.413	0.9
40	914.7	4.3	0.09	450	371.3	0.406	0.885
40	927.7	4.6	0.1	450	369.2	0.398	0.868
42.5	755.3	0.6	0	450	353	0.467	1.019
42.5	769.4	2.2	0.01	450	344.2	0.447	0.975
42.5	783.4	2.4	0.02	450	346.4	0.442	0.964
42.5	797.3	2.5	0.03	450	348.4	0.437	0.953
42.5	811.2	2.7	0.04	450	350.3	0.432	0.942
42.5	825	2.9	0.05	450	352.1	0.427	0.931
42.5	838.6	3.1	0.06	450	353.9	0.422	0.92
42.5	852.2	3.3	0.07	450	355.1	0.417	0.909
42.5	865.7	3.5	0.08	450	355.4	0.41	0.895
42.5	879	3.6	0.09	450	354.4	0.403	0.879
42.5	892.3	3.8	0.1	450	352.4	0.395	0.861
45	715.3	0.3	0	450	335.9	0.47	1.042
45	729.6	2.1	0.01	450	324.7	0.445	0.988
45	743.9	2.2	0.02	450	327.6	0.44	0.977
45	758.1	2.3	0.03	450	330.3	0.436	0.967
45	772.2	2.4	0.04	450	333	0.431	0.957
45	786.2	2.5	0.05	450	335.6	0.427	0.947
45	800.1	2.6	0.06	450	337.7	0.422	0.937
45	813.9	2.7	0.07	450	339.2	0.417	0.925
45	827.6	2.8	0.08	450	339.5	0.41	0.91
45	841.2	2.9	0.09	450	338.3	0.402	0.893
45	854.7	3	0.1	450	336	0.393	0.873
47.5	673	0.1	0	450	317.1	0.471	1.046
47.5	687.6	2	0.01	450	304.4	0.443	0.982
47.5	702.1	2	0.02	450	308.2	0.439	0.974
47.5	716.5	2.1	0.03	450	312	0.435	0.966

Speed (mph)	Vertical Force (lbs)	Slip Angle (degree)	Camber	Curve Radius (ft)	FEA Horizontal Force (lbs)	FEA FN	Friction Adjustment Factor
47.5	730.9	2.1	0.04	450	315.7	0.432	0.959
47.5	745.1	2.1	0.05	450	319	0.428	0.95
47.5	759.3	2.1	0.06	450	321.7	0.424	0.94
47.5	773.4	2.1	0.07	450	323.3	0.418	0.928
47.5	787.4	2.1	0.08	450	323.5	0.411	0.912
47.5	801.3	2.2	0.09	450	322.2	0.402	0.893
47.5	815	2.2	0.1	450	319.8	0.392	0.871
50	628.5	-0.2	0	450	296.7	0.472	1.048
50	643.3	1.9	0.01	450	282.8	0.44	0.976
50	658.1	1.9	0.02	450	287.9	0.437	0.971
50	672.7	1.8	0.03	450	292.7	0.435	0.966
50	687.4	1.7	0.04	450	297.3	0.433	0.96
50	701.9	1.6	0.05	450	301.4	0.429	0.953
50	716.3	1.6	0.06	450	304.6	0.425	0.944
50	730.7	1.5	0.07	450	306.6	0.42	0.931
50	744.9	1.4	0.08	450	307	0.412	0.915
50	759.1	1.4	0.09	450	305.9	0.403	0.894
50	773.2	1.3	0.1	450	303.7	0.393	0.872
30	962	1.3	0	600	450.9	0.469	1.04
30	974.9	2.4	0.01	600	448.3	0.46	1.021
30	987.8	2.8	0.02	600	450.3	0.456	1.012
30	1000.5	3.2	0.03	600	452.5	0.452	1.004
30	1013.2	3.5	0.04	600	454.3	0.448	0.995
30	1025.7	3.9	0.05	600	455	0.444	0.985
30	1038.1	4.3	0.06	600	454.5	0.438	0.972
30	1050.4	4.7	0.07	600	453.1	0.431	0.957
30	1062.5	5.1	0.08	600	451.1	0.425	0.942
30	1074.6	5.5	0.09	600	448.5	0.417	0.926
30	1086.5	5.8	0.1	600	445.3	0.41	0.91
32.5	940.6	1.1	0	600	437.7	0.465	1.033
32.5	953.6	2.3	0.01	600	434.4	0.455	1.011

Speed (mph)	Vertical Force (lbs)	Slip Angle (degree)	Camber	Curve Radius (ft)	FEA Horizontal Force (lbs)	FEA FN	Friction Adjustment Factor
32.5	966.6	2.7	0.02	600	436.6	0.452	1.003
32.5	979.5	3	0.03	600	439.1	0.448	0.995
32.5	992.2	3.4	0.04	600	441.2	0.445	0.987
32.5	1004.9	3.7	0.05	600	442.2	0.44	0.977
32.5	1017.4	4.1	0.06	600	442.2	0.435	0.965
32.5	1029.9	4.4	0.07	600	441.1	0.428	0.951
32.5	1042.2	4.7	0.08	600	439.3	0.421	0.935
32.5	1054.3	5.1	0.09	600	436.6	0.414	0.919
32.5	1066.4	5.4	0.1	600	433.2	0.406	0.902
35	917.4	1	0	600	424.2	0.462	1.026
35	930.6	2.3	0.01	600	419.9	0.451	1.001
35	943.7	2.6	0.02	600	422.2	0.447	0.993
35	956.7	2.9	0.03	600	424.6	0.444	0.985
35	969.6	3.2	0.04	600	426.6	0.44	0.976
35	982.4	3.5	0.05	600	427.7	0.435	0.966
35	995.1	3.8	0.06	600	428	0.43	0.955
35	1007.7	4.1	0.07	600	427.4	0.424	0.941
35	1020.1	4.4	0.08	600	426	0.418	0.927
35	1032.5	4.7	0.09	600	423.5	0.41	0.91
35	1044.7	5	0.1	600	420.1	0.402	0.893
37.5	892.6	0.8	0	600	411	0.46	1.022
37.5	905.9	2.2	0.01	600	405.1	0.447	0.992
37.5	919.2	2.5	0.02	600	407.1	0.443	0.983
37.5	932.3	2.7	0.03	600	409	0.439	0.974
37.5	945.4	3	0.04	600	410.5	0.434	0.964
37.5	958.3	3.2	0.05	600	411.5	0.429	0.953
37.5	971.1	3.5	0.06	600	411.9	0.424	0.941
37.5	983.9	3.7	0.07	600	411.7	0.418	0.929
37.5	996.5	4	0.08	600	410.7	0.412	0.915
37.5	1009	4.2	0.09	600	408.6	0.405	0.899
37.5	1021.3	4.5	0.1	600	405.7	0.397	0.882

Speed (mph)	Vertical Force (lbs)	Slip Angle (degree)	Camber	Curve Radius (ft)	FEA Horizontal Force (lbs)	FEA FN	Friction Adjustment Factor
40	866	0.6	0	600	398	0.46	1.02
40	879.5	2.2	0.01	600	389.9	0.443	0.984
40	892.9	2.4	0.02	600	391.6	0.439	0.973
40	906.2	2.6	0.03	600	393	0.434	0.963
40	919.4	2.8	0.04	600	394.1	0.429	0.951
40	932.5	3	0.05	600	394.8	0.423	0.94
40	945.5	3.2	0.06	600	395.3	0.418	0.928
40	958.4	3.3	0.07	600	395.4	0.413	0.916
40	971.2	3.5	0.08	600	394.6	0.406	0.902
40	983.8	3.7	0.09	600	392.7	0.399	0.886
40	996.4	3.9	0.1	600	390	0.391	0.869
42.5	837.8	0.5	0	600	385.1	0.46	1.02
42.5	851.4	2.1	0.01	600	374.3	0.44	0.976
42.5	865	2.3	0.02	600	375.9	0.435	0.965
42.5	878.4	2.4	0.03	600	377.3	0.43	0.953
42.5	891.8	2.5	0.04	600	378.5	0.424	0.942
42.5	905.1	2.7	0.05	600	379.4	0.419	0.93
42.5	918.3	2.8	0.06	600	380.1	0.414	0.919
42.5	931.3	3	0.07	600	380.2	0.408	0.906
42.5	944.3	3.1	0.08	600	379.3	0.402	0.892
42.5	957.1	3.2	0.09	600	377.3	0.394	0.875
42.5	969.8	3.4	0.1	600	374.4	0.386	0.857
45	807.8	0.3	0	600	371.7	0.46	1.021
45	821.6	2.1	0.01	600	358.6	0.436	0.969
45	835.3	2.2	0.02	600	360.5	0.432	0.958
45	849	2.2	0.03	600	362.3	0.427	0.947
45	862.5	2.3	0.04	600	363.9	0.422	0.937
45	876	2.4	0.05	600	365.4	0.417	0.926
45	889.3	2.5	0.06	600	366.4	0.412	0.914
45	902.6	2.5	0.07	600	366.5	0.406	0.901
45	915.7	2.6	0.08	600	365.3	0.399	0.885

Speed (mph)	Vertical Force (lbs)	Slip Angle (degree)	Camber	Curve Radius (ft)	FEA Horizontal Force (lbs)	FEA FN	Friction Adjustment Factor
45	928.7	2.7	0.09	600	362.8	0.391	0.867
45	941.7	2.8	0.1	600	359.5	0.382	0.847
47.5	776.1	0	0	600	357.2	0.46	1.021
47.5	790.1	2	0.01	600	342.4	0.433	0.962
47.5	804	2	0.02	600	345	0.429	0.952
47.5	817.8	2	0.03	600	347.5	0.425	0.943
47.5	831.6	2.1	0.04	600	350	0.421	0.934
47.5	845.2	2.1	0.05	600	352	0.416	0.924
47.5	858.8	2.1	0.06	600	353.2	0.411	0.913
47.5	872.2	2.1	0.07	600	353.2	0.405	0.899
47.5	885.5	2.1	0.08	600	351.6	0.397	0.881
47.5	898.8	2.1	0.09	600	348.6	0.388	0.861
47.5	911.9	2.1	0.1	600	344.9	0.378	0.839
50	742.7	-0.2	0	600	341.3	0.459	1.02
50	756.9	1.9	0.01	600	325.6	0.43	0.955
50	771	1.9	0.02	600	329.1	0.427	0.947
50	785	1.8	0.03	600	332.4	0.423	0.94
50	798.9	1.8	0.04	600	335.5	0.42	0.932
50	812.8	1.7	0.05	600	338.1	0.416	0.923
50	826.5	1.7	0.06	600	339.5	0.411	0.912
50	840.2	1.6	0.07	600	339.4	0.404	0.897
50	853.7	1.6	0.08	600	337.7	0.396	0.878
50	867.2	1.5	0.09	600	334.7	0.386	0.857
50	880.5	1.5	0.1	600	330.9	0.376	0.834
30	986.7	1	0	750	461.7	0.468	1.046
30	999.5	2.3	0.01	750	457.7	0.458	1.024
30	1012.2	2.6	0.02	750	459.7	0.454	1.015
30	1024.8	2.9	0.03	750	461.9	0.451	1.008
30	1037.3	3.2	0.04	750	463.7	0.447	0.999
30	1049.6	3.5	0.05	750	464.4	0.442	0.989
30	1061.9	3.8	0.06	750	464	0.437	0.977

Speed (mph)	Vertical Force (lbs)	Slip Angle (degree)	Camber	Curve Radius (ft)	FEA Horizontal Force (lbs)	FEA FN	Friction Adjustment Factor
30	1074	4.2	0.07	750	462.7	0.431	0.963
30	1086	4.5	0.08	750	460.6	0.424	0.948
30	1097.9	4.8	0.09	750	458.1	0.417	0.933
30	1109.7	5.1	0.1	750	455	0.41	0.916
32.5	969.5	0.9	0	750	449.8	0.464	1.037
32.5	982.4	2.3	0.01	750	445.2	0.453	1.013
32.5	995.2	2.5	0.02	750	447.5	0.45	1.005
32.5	1007.9	2.8	0.03	750	449.9	0.446	0.998
32.5	1020.5	3.1	0.04	750	451.9	0.443	0.99
32.5	1033	3.4	0.05	750	452.9	0.438	0.98
32.5	1045.4	3.6	0.06	750	452.8	0.433	0.968
32.5	1057.6	3.9	0.07	750	451.7	0.427	0.955
32.5	1069.7	4.2	0.08	750	449.8	0.42	0.94
32.5	1081.7	4.5	0.09	750	447.2	0.413	0.924
32.5	1093.6	4.7	0.1	750	443.8	0.406	0.907
35	951	0.8	0	750	437.8	0.46	1.029
35	964	2.2	0.01	750	432.3	0.448	1.002
35	976.9	2.5	0.02	750	434.6	0.445	0.994
35	989.7	2.7	0.03	750	436.9	0.441	0.987
35	1002.4	2.9	0.04	750	438.8	0.438	0.978
35	1015	3.2	0.05	750	439.7	0.433	0.968
35	1027.5	3.4	0.06	750	439.8	0.428	0.957
35	1039.9	3.7	0.07	750	439	0.422	0.944
35	1052.1	3.9	0.08	750	437.4	0.416	0.929
35	1064.2	4.1	0.09	750	434.9	0.409	0.913
35	1076.2	4.4	0.1	750	431.5	0.401	0.896
37.5	931.1	0.7	0	750	426.2	0.458	1.023
37.5	944.3	2.2	0.01	750	419.1	0.444	0.992
37.5	957.3	2.4	0.02	750	421.1	0.44	0.983
37.5	970.2	2.6	0.03	750	422.9	0.436	0.974
37.5	983	2.8	0.04	750	424.3	0.432	0.965

Speed (mph)	Vertical Force (lbs)	Slip Angle (degree)	Camber	Curve Radius (ft)	FEA Horizontal Force (lbs)	FEA FN	Friction Adjustment Factor
37.5	995.7	3	0.05	750	424.9	0.427	0.954
37.5	1008.3	3.2	0.06	750	425	0.421	0.942
37.5	1020.8	3.4	0.07	750	424.4	0.416	0.929
37.5	1033.2	3.6	0.08	750	422.9	0.409	0.915
37.5	1045.4	3.8	0.09	750	420.5	0.402	0.899
37.5	1057.5	4	0.1	750	417.4	0.395	0.882
40	909.9	0.5	0	750	414.8	0.456	1.019
40	923.1	2.2	0.01	750	405.6	0.439	0.982
40	936.3	2.3	0.02	750	407.2	0.435	0.972
40	949.3	2.5	0.03	750	408.5	0.43	0.962
40	962.3	2.6	0.04	750	409.4	0.425	0.951
40	975.1	2.8	0.05	750	409.7	0.42	0.939
40	987.8	2.9	0.06	750	409.7	0.415	0.927
40	1000.5	3.1	0.07	750	409.1	0.409	0.914
40	1013	3.2	0.08	750	407.6	0.402	0.899
40	1025.3	3.4	0.09	750	405.3	0.395	0.884
40	1037.6	3.5	0.1	750	402.2	0.388	0.866
42.5	887.3	0.4	0	750	403.8	0.455	1.017
42.5	900.7	2.1	0.01	750	391.9	0.435	0.973
42.5	913.9	2.2	0.02	750	393.2	0.43	0.962
42.5	927.1	2.3	0.03	750	394.3	0.425	0.951
42.5	940.2	2.4	0.04	750	395	0.42	0.939
42.5	953.2	2.5	0.05	750	395.5	0.415	0.927
42.5	966	2.7	0.06	750	395.6	0.41	0.915
42.5	978.8	2.8	0.07	750	395	0.404	0.902
42.5	991.4	2.9	0.08	750	393.3	0.397	0.887
42.5	1003.9	3	0.09	750	390.7	0.389	0.87
42.5	1016.3	3.1	0.1	750	387.3	0.381	0.852
45	863.3	0.2	0	750	392.3	0.454	1.016
45	876.8	2.1	0.01	750	378.2	0.431	0.964
45	890.2	2.1	0.02	750	379.5	0.426	0.953

Speed (mph)	Vertical Force (lbs)	Slip Angle (degree)	Camber	Curve Radius (ft)	FEA Horizontal Force (lbs)	FEA FN	Friction Adjustment Factor
45	903.5	2.2	0.03	750	380.8	0.421	0.942
45	916.8	2.2	0.04	750	381.9	0.417	0.931
45	929.9	2.3	0.05	750	382.8	0.412	0.92
45	942.9	2.4	0.06	750	383	0.406	0.908
45	955.8	2.4	0.07	750	382.3	0.4	0.894
45	968.6	2.5	0.08	750	380.2	0.393	0.877
45	981.2	2.6	0.09	750	377	0.384	0.859
45	993.8	2.6	0.1	750	373.1	0.375	0.839
47.5	837.9	0	0	750	380	0.453	1.014
47.5	851.6	2	0.01	750	364.2	0.428	0.956
47.5	865.2	2	0.02	750	366.1	0.423	0.946
47.5	878.6	2	0.03	750	367.9	0.419	0.936
47.5	892	2	0.04	750	369.6	0.414	0.926
47.5	905.3	2.1	0.05	750	370.9	0.41	0.916
47.5	918.4	2.1	0.06	750	371.2	0.404	0.903
47.5	931.5	2.1	0.07	750	370.1	0.397	0.888
47.5	944.4	2.1	0.08	750	367.5	0.389	0.87
47.5	957.3	2.1	0.09	750	363.7	0.38	0.849
47.5	970	2.1	0.1	750	359.4	0.37	0.828
50	811.2	-0.1	0	750	366.5	0.452	1.01
50	825	2	0.01	750	349.8	0.424	0.948
50	838.7	1.9	0.02	750	352.5	0.42	0.939
50	852.3	1.9	0.03	750	354.9	0.416	0.931
50	865.9	1.8	0.04	750	357.2	0.413	0.922
50	879.3	1.8	0.05	750	358.8	0.408	0.912
50	892.6	1.7	0.06	750	359.1	0.402	0.899
50	905.9	1.7	0.07	750	357.8	0.395	0.883
50	919	1.7	0.08	750	354.9	0.386	0.863
50	932	1.6	0.09	750	350.8	0.376	0.841
50	944.9	1.6	0.1	750	346.3	0.366	0.819
30	992.8	1	0	800	464.4	0.468	1.045

Speed (mph)	Vertical Force (lbs)	Slip Angle (degree)	Camber	Curve Radius (ft)	FEA Horizontal Force (lbs)	FEA FN	Friction Adjustment Factor
30	1005.6	2.3	0.01	800	460	0.457	1.022
30	1018.3	2.6	0.02	800	462.1	0.454	1.014
30	1030.8	2.9	0.03	800	464.3	0.45	1.007
30	1043.3	3.2	0.04	800	466	0.447	0.998
30	1055.6	3.4	0.05	800	466.7	0.442	0.988
30	1067.8	3.7	0.06	800	466.3	0.437	0.976
30	1079.9	4	0.07	800	465	0.431	0.962
30	1091.9	4.3	0.08	800	463	0.424	0.948
30	1103.8	4.6	0.09	800	460.5	0.417	0.933
30	1115.5	4.9	0.1	800	457.4	0.41	0.917
32.5	976.8	0.9	0	800	452.9	0.464	1.036
32.5	989.6	2.3	0.01	800	447.9	0.453	1.012
32.5	1002.4	2.5	0.02	800	450.2	0.449	1.004
32.5	1015	2.8	0.03	800	452.6	0.446	0.997
32.5	1027.6	3	0.04	800	454.5	0.442	0.989
32.5	1040	3.3	0.05	800	455.5	0.438	0.979
32.5	1052.3	3.5	0.06	800	455.4	0.433	0.967
32.5	1064.5	3.8	0.07	800	454.3	0.427	0.954
32.5	1076.6	4.1	0.08	800	452.4	0.42	0.939
32.5	1088.6	4.3	0.09	800	449.8	0.413	0.924
32.5	1100.4	4.6	0.1	800	446.5	0.406	0.907
35	959.4	0.7	0	800	441.2	0.46	1.028
35	972.4	2.2	0.01	800	435.4	0.448	1.001
35	985.2	2.4	0.02	800	437.7	0.444	0.993
35	998	2.7	0.03	800	440	0.441	0.985
35	1010.6	2.9	0.04	800	441.8	0.437	0.977
35	1023.2	3.1	0.05	800	442.7	0.433	0.967
35	1035.6	3.3	0.06	800	442.7	0.428	0.956
35	1047.9	3.6	0.07	800	441.9	0.422	0.943
35	1060.1	3.8	0.08	800	440.2	0.415	0.928
35	1072.2	4	0.09	800	437.7	0.408	0.912

Speed (mph)	Vertical Force (lbs)	Slip Angle (degree)	Camber	Curve Radius (ft)	FEA Horizontal Force (lbs)	FEA FN	Friction Adjustment Factor
35	1084.1	4.2	0.1	800	434.3	0.401	0.895
37.5	940.8	0.6	0	800	429.9	0.457	1.075
37.5	953.9	2.2	0.01	800	422.6	0.443	1.042
37.5	966.8	2.4	0.02	800	424.6	0.439	1.033
37.5	979.7	2.6	0.03	800	426.4	0.435	1.024
37.5	992.4	2.7	0.04	800	427.7	0.431	1.014
37.5	1005.1	2.9	0.05	800	428.3	0.426	1.002
37.5	1017.6	3.1	0.06	800	428.2	0.421	0.99
37.5	1030.1	3.3	0.07	800	427.5	0.415	0.976
37.5	1042.4	3.5	0.08	800	425.9	0.409	0.961
37.5	1054.5	3.7	0.09	800	423.5	0.402	0.945
37.5	1066.6	3.8	0.1	800	420.2	0.394	0.927
40	920.9	0.5	0	800	419	0.455	1.07
40	934	2.1	0.01	800	409.5	0.438	1.031
40	947.1	2.3	0.02	800	411.1	0.434	1.021
40	960.1	2.4	0.03	800	412.4	0.429	1.01
40	973	2.6	0.04	800	413.2	0.425	0.999
40	985.8	2.7	0.05	800	413.4	0.419	0.986
40	998.4	2.9	0.06	800	413.3	0.414	0.974
40	1011	3	0.07	800	412.5	0.408	0.96
40	1023.4	3.2	0.08	800	410.9	0.402	0.944
40	1035.7	3.3	0.09	800	408.4	0.394	0.928
40	1047.9	3.4	0.1	800	405.2	0.387	0.91
42.5	899.7	0.3	0	800	408.4	0.454	1.068
42.5	913	2.1	0.01	800	396.3	0.434	1.021
42.5	926.2	2.2	0.02	800	397.5	0.429	1.01
42.5	939.3	2.3	0.03	800	398.5	0.424	0.998
42.5	952.3	2.4	0.04	800	399.2	0.419	0.986
42.5	965.2	2.5	0.05	800	399.5	0.414	0.974
42.5	978	2.6	0.06	800	399.5	0.408	0.961
42.5	990.6	2.7	0.07	800	398.6	0.402	0.947

Speed (mph)	Vertical Force (lbs)	Slip Angle (degree)	Camber	Curve Radius (ft)	FEA Horizontal Force (lbs)	FEA FN	Friction Adjustment Factor
42.5	1003.2	2.8	0.08	800	396.8	0.396	0.93
42.5	1015.6	2.9	0.09	800	394	0.388	0.912
42.5	1028	3	0.1	800	390.5	0.38	0.893
45	877.2	0.2	0	800	397.4	0.453	1.066
45	890.6	2.1	0.01	800	383	0.43	1.012
45	903.9	2.1	0.02	800	384.2	0.425	1
45	917.2	2.2	0.03	800	385.4	0.42	0.988
45	930.3	2.2	0.04	800	386.3	0.415	0.977
45	943.3	2.3	0.05	800	387.1	0.41	0.965
45	956.3	2.3	0.06	800	387.1	0.405	0.952
45	969.1	2.4	0.07	800	386.1	0.398	0.937
45	981.8	2.5	0.08	800	383.9	0.391	0.92
45	994.4	2.5	0.09	800	380.5	0.383	0.9
45	1006.8	2.6	0.1	800	376.5	0.374	0.88
47.5	853.4	0	0	800	385.6	0.452	1.063
47.5	867	2	0.01	800	369.6	0.426	1.003
47.5	880.4	2	0.02	800	371.3	0.422	0.992
47.5	893.8	2	0.03	800	372.9	0.417	0.981
47.5	907.1	2	0.04	800	374.4	0.413	0.971
47.5	920.3	2	0.05	800	375.5	0.408	0.96
47.5	933.3	2.1	0.06	800	375.6	0.402	0.947
47.5	946.3	2.1	0.07	800	374.3	0.396	0.93
47.5	959.2	2.1	0.08	800	371.4	0.387	0.911
47.5	971.9	2.1	0.09	800	367.4	0.378	0.889
47.5	984.5	2.1	0.1	800	363	0.369	0.867
50	828.4	-0.1	0	800	372.7	0.45	1.058
50	842.1	2	0.01	800	355.8	0.423	0.994
50	855.7	1.9	0.02	800	358.2	0.419	0.985
50	869.2	1.9	0.03	800	360.4	0.415	0.975
50	882.6	1.8	0.04	800	362.5	0.411	0.966
50	895.9	1.8	0.05	800	363.8	0.406	0.955

Speed (mph)	Vertical Force (lbs)	Slip Angle (degree)	Camber	Curve Radius (ft)	FEA Horizontal Force (lbs)	FEA FN	Friction Adjustment Factor
50	909.2	1.8	0.06	800	363.9	0.4	0.942
50	922.3	1.7	0.07	800	362.3	0.393	0.924
50	935.3	1.7	0.08	800	359.1	0.384	0.903
50	948.2	1.6	0.09	800	354.8	0.374	0.88
50	961	1.6	0.1	800	350.1	0.364	0.857
30	1003.1	0.9	0	900	468.9	0.467	1.099
30	1015.8	2.3	0.01	900	463.9	0.457	1.074
30	1028.4	2.5	0.02	900	466	0.453	1.066
30	1040.9	2.8	0.03	900	468.2	0.45	1.058
30	1053.3	3	0.04	900	469.9	0.446	1.049
30	1065.6	3.3	0.05	900	470.6	0.442	1.039
30	1077.8	3.5	0.06	900	470.3	0.436	1.026
30	1089.8	3.8	0.07	900	469	0.43	1.012
30	1101.7	4.1	0.08	900	467	0.424	0.997
30	1113.5	4.3	0.09	900	464.5	0.417	0.981
30	1125.1	4.6	0.1	900	461.5	0.41	0.965
32.5	988.8	0.8	0	900	457.9	0.463	1.089
32.5	1001.6	2.2	0.01	900	452.4	0.452	1.062
32.5	1014.3	2.5	0.02	900	454.7	0.448	1.055
32.5	1026.9	2.7	0.03	900	457.1	0.445	1.047
32.5	1039.4	2.9	0.04	900	459	0.442	1.039
32.5	1051.7	3.1	0.05	900	459.9	0.437	1.029
32.5	1064	3.4	0.06	900	459.8	0.432	1.016
32.5	1076.1	3.6	0.07	900	458.7	0.426	1.003
32.5	1088.1	3.8	0.08	900	456.8	0.42	0.988
32.5	1100	4.1	0.09	900	454.2	0.413	0.971
32.5	1111.7	4.3	0.1	900	450.8	0.406	0.954
35	973.4	0.7	0	900	446.9	0.459	1.08
35	986.3	2.2	0.01	900	440.5	0.447	1.051
35	999.1	2.4	0.02	900	442.8	0.443	1.043
35	1011.7	2.6	0.03	900	445	0.44	1.035

Speed (mph)	Vertical Force (lbs)	Slip Angle (degree)	Camber	Curve Radius (ft)	FEA Horizontal Force (lbs)	FEA FN	Friction Adjustment Factor
35	1024.3	2.8	0.04	900	446.8	0.436	1.026
35	1036.8	3	0.05	900	447.6	0.432	1.016
35	1049.1	3.2	0.06	900	447.6	0.427	1.004
35	1061.3	3.4	0.07	900	446.7	0.421	0.99
35	1073.4	3.6	0.08	900	444.9	0.414	0.975
35	1085.4	3.8	0.09	900	442.3	0.407	0.959
35	1097.2	4	0.1	900	438.9	0.4	0.941
37.5	956.8	0.5	0	900	436.2	0.456	1.072
37.5	969.8	2.2	0.01	900	428.4	0.442	1.039
37.5	982.7	2.3	0.02	900	430.3	0.438	1.03
37.5	995.5	2.5	0.03	900	432.1	0.434	1.021
37.5	1008.1	2.7	0.04	900	433.3	0.43	1.011
37.5	1020.7	2.8	0.05	900	433.8	0.425	1
37.5	1033.1	3	0.06	900	433.6	0.42	0.987
37.5	1045.5	3.1	0.07	900	432.7	0.414	0.974
37.5	1057.7	3.3	0.08	900	431	0.407	0.959
37.5	1069.7	3.5	0.09	900	428.4	0.4	0.942
37.5	1081.7	3.6	0.1	900	425	0.393	0.924
40	939.1	0.4	0	900	426	0.454	1.067
40	952.2	2.1	0.01	900	416	0.437	1.028
40	965.2	2.3	0.02	900	417.5	0.433	1.018
40	978.1	2.4	0.03	900	418.7	0.428	1.007
40	990.8	2.5	0.04	900	419.4	0.423	0.996
40	1003.5	2.6	0.05	900	419.6	0.418	0.983
40	1016	2.8	0.06	900	419.2	0.413	0.97
40	1028.5	2.9	0.07	900	418.2	0.407	0.956
40	1040.8	3	0.08	900	416.3	0.4	0.941
40	1053	3.2	0.09	900	413.6	0.393	0.924
40	1065.1	3.3	0.1	900	410.2	0.385	0.906
42.5	920.3	0.3	0	900	416	0.452	1.063
42.5	933.5	2.1	0.01	900	403.5	0.432	1.017

Speed (mph)	**Vertical Force (lbs)**	**Slip Angle (degree)**	**Camber**	**Curve Radius (ft)**	**FEA Horizontal Force (lbs)**	**FEA FN**	**Friction Adjustment Factor**
42.5	946.6	2.2	0.02	900	404.6	0.427	1.005
42.5	959.5	2.3	0.03	900	405.4	0.423	0.994
42.5	972.4	2.4	0.04	900	406	0.417	0.982
42.5	985.2	2.5	0.05	900	406.2	0.412	0.97
42.5	997.9	2.5	0.06	900	405.8	0.407	0.957
42.5	1010.4	2.6	0.07	900	404.7	0.401	0.942
42.5	1022.8	2.7	0.08	900	402.6	0.394	0.926
42.5	1035.2	2.8	0.09	900	399.5	0.386	0.908
42.5	1047.3	2.9	0.1	900	395.8	0.378	0.889
45	900.3	0.2	0	900	405.8	0.451	1.03
45	913.6	2.1	0.01	900	391	0.428	0.978
45	926.8	2.1	0.02	900	392	0.423	0.967
45	939.9	2.2	0.03	900	392.9	0.418	0.956
45	952.9	2.2	0.04	900	393.7	0.413	0.944
45	965.8	2.3	0.05	900	394.1	0.408	0.933
45	978.6	2.3	0.06	900	393.9	0.403	0.92
45	991.3	2.4	0.07	900	392.6	0.396	0.905
45	1003.8	2.4	0.08	900	390	0.388	0.888
45	1016.3	2.5	0.09	900	386.3	0.38	0.869
45	1028.6	2.5	0.1	900	382.1	0.372	0.849
47.5	879.2	0	0	900	394.7	0.449	1.026
47.5	892.6	2	0.01	900	378.4	0.424	0.969
47.5	905.9	2	0.02	900	379.9	0.419	0.958
47.5	919.1	2	0.03	900	381.2	0.415	0.948
47.5	932.3	2	0.04	900	382.4	0.41	0.938
47.5	945.3	2	0.05	900	383.1	0.405	0.926
47.5	958.2	2.1	0.06	900	382.9	0.4	0.913
47.5	971	2.1	0.07	900	381.1	0.393	0.897
47.5	983.7	2.1	0.08	900	377.9	0.384	0.878
47.5	996.3	2.1	0.09	900	373.6	0.375	0.857
47.5	1008.7	2.1	0.1	900	368.9	0.366	0.836

Speed (mph)	Vertical Force (lbs)	Slip Angle (degree)	Camber	Curve Radius (ft)	FEA Horizontal Force (lbs)	FEA FN	Friction Adjustment Factor
50	856.9	-0.1	0	900	382.7	0.447	1.021
50	870.4	2	0.01	900	365.6	0.42	0.96
50	883.9	1.9	0.02	900	367.6	0.416	0.951
50	897.2	1.9	0.03	900	369.5	0.412	0.941
50	910.5	1.9	0.04	900	371.2	0.408	0.932
50	923.7	1.8	0.05	900	372.1	0.403	0.921
50	936.7	1.8	0.06	900	371.8	0.397	0.907
50	949.7	1.7	0.07	900	369.7	0.389	0.89
50	962.5	1.7	0.08	900	366	0.38	0.869
50	975.2	1.7	0.09	900	361.4	0.371	0.847
50	987.8	1.6	0.1	900	356.4	0.361	0.825
30	1014.9	0.7	0	1050	474	0.467	1.068
30	1027.5	2.2	0.01	1050	468.3	0.456	1.042
30	1040	2.4	0.02	1050	470.5	0.452	1.034
30	1052.5	2.7	0.03	1050	472.6	0.449	1.026
30	1064.8	2.9	0.04	1050	474.3	0.445	1.018
30	1077	3.1	0.05	1050	475	0.441	1.008
30	1089.1	3.3	0.06	1050	474.7	0.436	0.996
30	1101.1	3.5	0.07	1050	473.5	0.43	0.983
30	1112.9	3.8	0.08	1050	471.6	0.424	0.969
30	1124.6	4	0.09	1050	469.2	0.417	0.954
30	1136.2	4.2	0.1	1050	466.1	0.41	0.938
32.5	1002.6	0.7	0	1050	463.7	0.462	1.057
32.5	1015.3	2.2	0.01	1050	457.5	0.451	1.03
32.5	1027.9	2.4	0.02	1050	459.9	0.447	1.023
32.5	1040.5	2.6	0.03	1050	462.2	0.444	1.015
32.5	1052.8	2.8	0.04	1050	464	0.441	1.007
32.5	1065.1	3	0.05	1050	464.9	0.436	0.998
32.5	1077.3	3.2	0.06	1050	464.7	0.431	0.986
32.5	1089.3	3.4	0.07	1050	463.7	0.426	0.973
32.5	1101.2	3.6	0.08	1050	461.8	0.419	0.958

Speed (mph)	Vertical Force (lbs)	Slip Angle (degree)	Camber	Curve Radius (ft)	FEA Horizontal Force (lbs)	FEA FN	Friction Adjustment Factor
32.5	1113	3.8	0.09	1050	459.1	0.413	0.943
32.5	1124.7	4	0.1	1050	455.8	0.405	0.926
35	989.4	0.6	0	1050	453.3	0.458	1.047
35	1002.2	2.2	0.01	1050	446.4	0.445	1.018
35	1014.9	2.3	0.02	1050	448.7	0.442	1.01
35	1027.5	2.5	0.03	1050	450.8	0.439	1.003
35	1039.9	2.7	0.04	1050	452.4	0.435	0.994
35	1052.3	2.8	0.05	1050	453.2	0.431	0.985
35	1064.5	3	0.06	1050	453.1	0.426	0.973
35	1076.7	3.2	0.07	1050	452.1	0.42	0.96
35	1088.7	3.4	0.08	1050	450.2	0.414	0.945
35	1100.5	3.5	0.09	1050	447.5	0.407	0.929
35	1112.3	3.7	0.1	1050	444	0.399	0.912
37.5	975.2	0.5	0	1050	443.4	0.455	1.039
37.5	988.1	2.1	0.01	1050	435	0.44	1.006
37.5	1000.8	2.3	0.02	1050	436.9	0.437	0.998
37.5	1013.5	2.4	0.03	1050	438.6	0.433	0.989
37.5	1026.1	2.6	0.04	1050	439.7	0.429	0.98
37.5	1038.5	2.7	0.05	1050	440.1	0.424	0.969
37.5	1050.8	2.8	0.06	1050	439.8	0.418	0.957
37.5	1063	3	0.07	1050	438.7	0.413	0.943
37.5	1075.1	3.1	0.08	1050	436.7	0.406	0.928
37.5	1087.1	3.3	0.09	1050	433.9	0.399	0.912
37.5	1098.9	3.4	0.1	1050	430.4	0.392	0.895
40	960	0.4	0	1050	433.9	0.452	1.033
40	973	2.1	0.01	1050	423.4	0.435	0.995
40	985.8	2.2	0.02	1050	424.8	0.431	0.985
40	998.6	2.3	0.03	1050	425.9	0.427	0.975
40	1011.2	2.4	0.04	1050	426.6	0.422	0.964
40	1023.8	2.6	0.05	1050	426.5	0.417	0.952
40	1036.2	2.7	0.06	1050	425.9	0.411	0.94

Speed (mph)	Vertical Force (lbs)	Slip Angle (degree)	Camber	Curve Radius (ft)	FEA Horizontal Force (lbs)	FEA FN	Friction Adjustment Factor
40	1048.5	2.8	0.07	1050	424.6	0.405	0.926
40	1060.7	2.9	0.08	1050	422.5	0.398	0.91
40	1072.7	3	0.09	1050	419.5	0.391	0.894
40	1084.7	3.1	0.1	1050	415.8	0.383	0.876
42.5	943.9	0.3	0	1050	424.6	0.45	1.028
42.5	956.9	2.1	0.01	1050	411.7	0.43	0.983
42.5	969.9	2.2	0.02	1050	412.6	0.425	0.973
42.5	982.7	2.2	0.03	1050	413.4	0.421	0.961
42.5	995.5	2.3	0.04	1050	413.7	0.416	0.95
42.5	1008.1	2.4	0.05	1050	413.7	0.41	0.938
42.5	1020.6	2.5	0.06	1050	413.1	0.405	0.925
42.5	1033	2.5	0.07	1050	411.6	0.398	0.911
42.5	1045.3	2.6	0.08	1050	409.1	0.391	0.895
42.5	1057.5	2.7	0.09	1050	405.8	0.384	0.877
42.5	1069.5	2.8	0.1	1050	401.8	0.376	0.859
45	926.7	0.1	0	1050	415.2	0.448	1.024
45	939.9	2	0.01	1050	400	0.426	0.973
45	952.9	2.1	0.02	1050	400.9	0.421	0.962
45	965.9	2.1	0.03	1050	401.5	0.416	0.95
45	978.7	2.2	0.04	1050	402	0.411	0.939
45	991.5	2.2	0.05	1050	402.2	0.406	0.927
45	1004.1	2.3	0.06	1050	401.6	0.4	0.914
45	1016.6	2.3	0.07	1050	399.9	0.393	0.899
45	1029	2.3	0.08	1050	396.9	0.386	0.882
45	1041.3	2.4	0.09	1050	393	0.377	0.863
45	1053.4	2.4	0.1	1050	388.6	0.369	0.843
47.5	908.6	0	0	1050	405.1	0.446	1.019
47.5	921.9	2	0.01	1050	388.4	0.421	0.963
47.5	935	2	0.02	1050	389.5	0.417	0.952
47.5	948.1	2	0.03	1050	390.6	0.412	0.942
47.5	961	2	0.04	1050	391.4	0.407	0.931

Speed (mph)	Vertical Force (lbs)	Slip Angle (degree)	Camber	Curve Radius (ft)	FEA Horizontal Force (lbs)	FEA FN	Friction Adjustment Factor
47.5	973.9	2	0.05	1050	391.8	0.402	0.92
47.5	986.6	2	0.06	1050	391.1	0.396	0.906
47.5	999.2	2.1	0.07	1050	388.9	0.389	0.89
47.5	1011.7	2.1	0.08	1050	385.2	0.381	0.87
47.5	1024.1	2.1	0.09	1050	380.7	0.372	0.85
47.5	1036.4	2.1	0.1	1050	375.8	0.363	0.829
50	889.5	-0.1	0	1050	394.1	0.443	1.013
50	902.9	2	0.01	1050	376.6	0.417	0.953
50	916.2	1.9	0.02	1050	378.2	0.413	0.944
50	929.3	1.9	0.03	1050	379.7	0.409	0.934
50	942.4	1.9	0.04	1050	380.9	0.404	0.924
50	955.3	1.8	0.05	1050	381.4	0.399	0.913
50	968.2	1.8	0.06	1050	380.6	0.393	0.898
50	980.9	1.8	0.07	1050	377.9	0.385	0.881
50	993.6	1.8	0.08	1050	373.8	0.376	0.86
50	1006.1	1.7	0.09	1050	368.8	0.367	0.838
50	1018.5	1.7	0.1	1050	363.7	0.357	0.816
30	1021	0.7	0	1150	476.6	0.467	1.084
30	1033.6	2.2	0.01	1150	470.6	0.455	1.058
30	1046.1	2.4	0.02	1150	472.8	0.452	1.05
30	1058.5	2.6	0.03	1150	475	0.449	1.042
30	1070.8	2.8	0.04	1150	476.6	0.445	1.034
30	1083	3	0.05	1150	477.3	0.441	1.024
30	1095	3.2	0.06	1150	477.1	0.436	1.012
30	1106.9	3.4	0.07	1150	475.9	0.43	0.999
30	1118.7	3.6	0.08	1150	474	0.424	0.984
30	1130.4	3.8	0.09	1150	471.6	0.417	0.969
30	1141.9	4	0.1	1150	468.5	0.41	0.953
32.5	1009.8	0.6	0	1150	466.7	0.462	1.073
32.5	1022.5	2.2	0.01	1150	460.2	0.45	1.045
32.5	1035.1	2.4	0.02	1150	462.6	0.447	1.038

Speed (mph)	**Vertical Force (lbs)**	**Slip Angle (degree)**	**Camber**	**Curve Radius (ft)**	**FEA Horizontal Force (lbs)**	**FEA FN**	**Friction Adjustment Factor**
32.5	1047.5	2.5	0.03	1150	464.8	0.444	1.031
32.5	1059.9	2.7	0.04	1150	466.6	0.44	1.022
32.5	1072.1	2.9	0.05	1150	467.5	0.436	1.013
32.5	1084.2	3.1	0.06	1150	467.3	0.431	1.001
32.5	1096.2	3.2	0.07	1150	466.2	0.425	0.988
32.5	1108.1	3.4	0.08	1150	464.3	0.419	0.973
32.5	1119.8	3.6	0.09	1150	461.7	0.412	0.958
32.5	1131.4	3.8	0.1	1150	458.3	0.405	0.941
35	997.7	0.5	0	1150	456.7	0.458	1.063
35	1010.5	2.2	0.01	1150	449.4	0.445	1.033
35	1023.1	2.3	0.02	1150	451.7	0.441	1.025
35	1035.7	2.5	0.03	1150	453.8	0.438	1.018
35	1048.1	2.6	0.04	1150	455.4	0.434	1.009
35	1060.4	2.8	0.05	1150	456.1	0.43	0.999
35	1072.6	2.9	0.06	1150	456	0.425	0.987
35	1084.7	3.1	0.07	1150	454.9	0.419	0.974
35	1096.6	3.2	0.08	1150	453	0.413	0.959
35	1108.4	3.4	0.09	1150	450.2	0.406	0.943
35	1120.1	3.5	0.1	1150	446.7	0.399	0.926
37.5	984.8	0.4	0	1150	447.1	0.454	1.054
37.5	997.6	2.1	0.01	1150	438.4	0.439	1.021
37.5	1010.3	2.3	0.02	1150	440.3	0.436	1.012
37.5	1022.9	2.4	0.03	1150	442	0.432	1.003
37.5	1035.4	2.5	0.04	1150	443.1	0.428	0.994
37.5	1047.8	2.6	0.05	1150	443.4	0.423	0.983
37.5	1060.1	2.8	0.06	1150	443	0.418	0.97
37.5	1072.2	2.9	0.07	1150	441.7	0.412	0.957
37.5	1084.3	3	0.08	1150	439.7	0.405	0.942
37.5	1096.2	3.2	0.09	1150	436.8	0.398	0.925
37.5	1107.9	3.3	0.1	1150	433.1	0.391	0.908
40	970.9	0.3	0	1150	438	0.451	1.048

Speed (mph)	Vertical Force (lbs)	Slip Angle (degree)	Camber	Curve Radius (ft)	FEA Horizontal Force (lbs)	FEA FN	Friction Adjustment Factor
40	983.8	2.1	0.01	1150	427.2	0.434	1.008
40	996.6	2.2	0.02	1150	428.6	0.43	0.999
40	1009.3	2.3	0.03	1150	429.7	0.426	0.989
40	1021.9	2.4	0.04	1150	430.3	0.421	0.978
40	1034.4	2.5	0.05	1150	430.1	0.416	0.966
40	1046.7	2.6	0.06	1150	429.4	0.41	0.953
40	1058.9	2.7	0.07	1150	428	0.404	0.939
40	1071.1	2.8	0.08	1150	425.7	0.397	0.923
40	1083.1	2.9	0.09	1150	422.5	0.39	0.906
40	1094.9	3	0.1	1150	418.8	0.383	0.888
42.5	956.2	0.2	0	1150	429.1	0.449	1.042
42.5	969.2	2.1	0.01	1150	415.9	0.429	0.997
42.5	982	2.1	0.02	1150	416.8	0.424	0.986
42.5	994.8	2.2	0.03	1150	417.5	0.42	0.975
42.5	1007.5	2.3	0.04	1150	417.8	0.415	0.963
42.5	1020	2.4	0.05	1150	417.6	0.409	0.951
42.5	1032.5	2.4	0.06	1150	416.8	0.404	0.938
42.5	1044.8	2.5	0.07	1150	415.2	0.397	0.923
42.5	1057	2.6	0.08	1150	412.5	0.39	0.906
42.5	1069.1	2.6	0.09	1150	409	0.383	0.889
42.5	1081.1	2.7	0.1	1150	405	0.375	0.87
45	940.5	0.1	0	1150	420.1	0.447	1.037
45	953.6	2	0.01	1150	404.7	0.424	0.986
45	966.6	2.1	0.02	1150	405.4	0.419	0.974
45	979.4	2.1	0.03	1150	406	0.415	0.963
45	992.2	2.2	0.04	1150	406.3	0.41	0.951
45	1004.9	2.2	0.05	1150	406.4	0.404	0.939
45	1017.4	2.2	0.06	1150	405.6	0.399	0.926
45	1029.8	2.3	0.07	1150	403.7	0.392	0.91
45	1042.1	2.3	0.08	1150	400.5	0.384	0.893
45	1054.3	2.4	0.09	1150	396.4	0.376	0.873

Speed (mph)	Vertical Force (lbs)	Slip Angle (degree)	Camber	Curve Radius (ft)	FEA Horizontal Force (lbs)	FEA FN	Friction Adjustment Factor
45	1066.4	2.4	0.1	1150	391.9	0.368	0.854
47.5	924	0	0	1150	410.4	0.444	1.032
47.5	937.2	2	0.01	1150	393.6	0.42	0.975
47.5	950.2	2	0.02	1150	394.5	0.415	0.964
47.5	963.2	2	0.03	1150	395.4	0.411	0.953
47.5	976	2	0.04	1150	396.1	0.406	0.942
47.5	988.8	2	0.05	1150	396.2	0.401	0.931
47.5	1001.4	2	0.06	1150	395.3	0.395	0.917
47.5	1014	2	0.07	1150	392.9	0.387	0.9
47.5	1026.4	2.1	0.08	1150	389	0.379	0.88
47.5	1038.7	2.1	0.09	1150	384.3	0.37	0.859
47.5	1050.8	2.1	0.1	1150	379.3	0.361	0.838
50	906.6	-0.1	0	1150	399.9	0.441	1.024
50	919.8	2	0.01	1150	382.3	0.416	0.965
50	933	1.9	0.02	1150	383.7	0.411	0.955
50	946.1	1.9	0.03	1150	385	0.407	0.945
50	959	1.9	0.04	1150	386	0.402	0.935
50	971.9	1.9	0.05	1150	386.2	0.397	0.923
50	984.6	1.8	0.06	1150	385.1	0.391	0.908
50	997.3	1.8	0.07	1150	382.2	0.383	0.89
50	1009.8	1.8	0.08	1150	377.9	0.374	0.869
50	1022.2	1.7	0.09	1150	372.7	0.365	0.847
50	1034.4	1.7	0.1	1150	367.4	0.355	0.825
30	1023.7	0.6	0	1200	477.8	0.467	1.084
30	1036.3	2.2	0.01	1200	471.6	0.455	1.057
30	1048.8	2.4	0.02	1200	473.9	0.452	1.049
30	1061.1	2.6	0.03	1200	476	0.449	1.042
30	1073.4	2.8	0.04	1200	477.6	0.445	1.033
30	1085.6	3	0.05	1200	478.3	0.441	1.023
30	1097.6	3.2	0.06	1200	478.1	0.436	1.012
30	1109.5	3.3	0.07	1200	476.9	0.43	0.998

Speed (mph)	Vertical Force (lbs)	Slip Angle (degree)	Camber	Curve Radius (ft)	FEA Horizontal Force (lbs)	FEA FN	Friction Adjustment Factor
30	1121.3	3.5	0.08	1200	475.1	0.424	0.984
30	1132.9	3.7	0.09	1200	472.6	0.417	0.969
30	1144.5	3.9	0.1	1200	469.6	0.41	0.953
32.5	1013	0.6	0	1200	468	0.462	1.073
32.5	1025.6	2.2	0.01	1200	461.4	0.45	1.045
32.5	1038.2	2.3	0.02	1200	463.7	0.447	1.037
32.5	1050.6	2.5	0.03	1200	466	0.444	1.03
32.5	1062.9	2.7	0.04	1200	467.7	0.44	1.022
32.5	1075.2	2.9	0.05	1200	468.6	0.436	1.012
32.5	1087.3	3	0.06	1200	468.5	0.431	1.001
32.5	1099.2	3.2	0.07	1200	467.4	0.425	0.988
32.5	1111.1	3.4	0.08	1200	465.5	0.419	0.973
32.5	1122.8	3.5	0.09	1200	462.8	0.412	0.957
32.5	1134.4	3.7	0.1	1200	459.5	0.405	0.941
35	1001.4	0.5	0	1200	458.1	0.458	1.063
35	1014.1	2.1	0.01	1200	450.7	0.444	1.032
35	1026.7	2.3	0.02	1200	453	0.441	1.025
35	1039.2	2.4	0.03	1200	455.1	0.438	1.017
35	1051.6	2.6	0.04	1200	456.7	0.434	1.009
35	1063.9	2.7	0.05	1200	457.4	0.43	0.999
35	1076.1	2.9	0.06	1200	457.3	0.425	0.987
35	1088.2	3	0.07	1200	456.2	0.419	0.974
35	1100.1	3.2	0.08	1200	454.2	0.413	0.959
35	1111.9	3.3	0.09	1200	451.4	0.406	0.943
35	1123.5	3.5	0.1	1200	447.8	0.399	0.926
37.5	989	0.4	0	1200	448.7	0.454	1.054
37.5	1001.8	2.1	0.01	1200	439.9	0.439	1.028
37.5	1014.5	2.2	0.02	1200	441.8	0.435	1.019
37.5	1027	2.4	0.03	1200	443.4	0.432	1.01
37.5	1039.5	2.5	0.04	1200	444.5	0.428	1.001
37.5	1051.9	2.6	0.05	1200	444.8	0.423	0.99

Speed (mph)	Vertical Force (lbs)	Slip Angle (degree)	Camber	Curve Radius (ft)	FEA Horizontal Force (lbs)	FEA FN	Friction Adjustment Factor
37.5	1064.1	2.7	0.06	1200	444.3	0.418	0.977
37.5	1076.2	2.9	0.07	1200	443.1	0.412	0.964
37.5	1088.2	3	0.08	1200	441	0.405	0.948
37.5	1100.1	3.1	0.09	1200	438	0.398	0.932
37.5	1111.9	3.2	0.1	1200	434.4	0.391	0.914
40	975.7	0.3	0	1200	439.8	0.451	1.055
40	988.6	2.1	0.01	1200	428.9	0.434	1.015
40	1001.3	2.2	0.02	1200	430.2	0.43	1.006
40	1014	2.3	0.03	1200	431.3	0.425	0.995
40	1026.5	2.4	0.04	1200	431.9	0.421	0.985
40	1039	2.5	0.05	1200	431.7	0.416	0.972
40	1051.3	2.6	0.06	1200	430.9	0.41	0.959
40	1063.5	2.7	0.07	1200	429.4	0.404	0.945
40	1075.6	2.8	0.08	1200	427.1	0.397	0.929
40	1087.6	2.9	0.09	1200	423.9	0.39	0.912
40	1099.4	3	0.1	1200	420.1	0.382	0.894
42.5	961.6	0.2	0	1200	431.1	0.448	1.049
42.5	974.5	2.1	0.01	1200	417.8	0.429	1.003
42.5	987.4	2.1	0.02	1200	418.6	0.424	0.992
42.5	1000.1	2.2	0.03	1200	419.3	0.419	0.981
42.5	1012.7	2.3	0.04	1200	419.5	0.414	0.969
42.5	1025.3	2.3	0.05	1200	419.3	0.409	0.957
42.5	1037.7	2.4	0.06	1200	418.5	0.403	0.944
42.5	1050	2.5	0.07	1200	416.7	0.397	0.929
42.5	1062.1	2.5	0.08	1200	414	0.39	0.912
42.5	1074.2	2.6	0.09	1200	410.5	0.382	0.894
42.5	1086.1	2.7	0.1	1200	406.4	0.374	0.876
45	946.6	0.1	0	1200	422.2	0.446	1.044
45	959.6	2	0.01	1200	406.7	0.424	0.992
45	972.5	2.1	0.02	1200	407.4	0.419	0.98
45	985.4	2.1	0.03	1200	407.9	0.414	0.969

Speed (mph)	Vertical Force (lbs)	Slip Angle (degree)	Camber	Curve Radius (ft)	FEA Horizontal Force (lbs)	FEA FN	Friction Adjustment Factor
45	998.1	2.2	0.04	1200	408.2	0.409	0.957
45	1010.7	2.2	0.05	1200	408.2	0.404	0.945
45	1023.2	2.2	0.06	1200	407.3	0.398	0.932
45	1035.6	2.3	0.07	1200	405.3	0.391	0.916
45	1047.9	2.3	0.08	1200	402.1	0.384	0.898
45	1060	2.3	0.09	1200	398	0.375	0.879
45	1072	2.4	0.1	1200	393.4	0.367	0.859
47.5	930.7	0	0	1200	412.7	0.443	1.038
47.5	943.8	2	0.01	1200	395.8	0.419	0.981
47.5	956.9	2	0.02	1200	396.7	0.415	0.97
47.5	969.8	2	0.03	1200	397.5	0.41	0.959
47.5	982.6	2	0.04	1200	398.1	0.405	0.948
47.5	995.3	2	0.05	1200	398.2	0.4	0.936
47.5	1007.9	2	0.06	1200	397.2	0.394	0.922
47.5	1020.4	2	0.07	1200	394.6	0.387	0.905
47.5	1032.8	2.1	0.08	1200	390.7	0.378	0.885
47.5	1045	2.1	0.09	1200	385.9	0.369	0.864
47.5	1057.1	2.1	0.1	1200	380.9	0.36	0.843
50	914	-0.1	0	1200	402.4	0.44	1.03
50	927.2	2	0.01	1200	384.8	0.415	0.971
50	940.4	1.9	0.02	1200	386.1	0.411	0.961
50	953.4	1.9	0.03	1200	387.3	0.406	0.951
50	966.3	1.9	0.04	1200	388.2	0.402	0.94
50	979.1	1.9	0.05	1200	388.3	0.397	0.928
50	991.8	1.8	0.06	1200	387.1	0.39	0.913
50	1004.4	1.8	0.07	1200	384.1	0.382	0.895
50	1016.9	1.8	0.08	1200	379.6	0.373	0.874
50	1029.2	1.8	0.09	1200	374.4	0.364	0.851
50	1041.4	1.7	0.1	1200	369.1	0.354	0.829
30	1030.5	0.6	0	1350	480.8	0.467	1.092
30	1043.1	2.2	0.01	1350	474.2	0.455	1.064

Speed (mph)	Vertical Force (lbs)	Slip Angle (degree)	Camber	Curve Radius (ft)	FEA Horizontal Force (lbs)	FEA FN	Friction Adjustment Factor
30	1055.5	2.3	0.02	1350	476.5	0.451	1.056
30	1067.9	2.5	0.03	1350	478.6	0.448	1.049
30	1080.1	2.7	0.04	1350	480.2	0.445	1.04
30	1092.2	2.9	0.05	1350	480.9	0.44	1.03
30	1104.2	3	0.06	1350	480.7	0.435	1.019
30	1116.1	3.2	0.07	1350	479.6	0.43	1.006
30	1127.8	3.4	0.08	1350	477.7	0.424	0.991
30	1139.4	3.5	0.09	1350	475.3	0.417	0.976
30	1150.9	3.7	0.1	1350	472.2	0.41	0.96
32.5	1021	0.5	0	1350	471.4	0.462	1.08
32.5	1033.6	2.2	0.01	1350	464.3	0.449	1.051
32.5	1046.1	2.3	0.02	1350	466.7	0.446	1.044
32.5	1058.5	2.5	0.03	1350	468.9	0.443	1.037
32.5	1070.8	2.6	0.04	1350	470.6	0.44	1.029
32.5	1083	2.8	0.05	1350	471.5	0.435	1.019
32.5	1095	2.9	0.06	1350	471.3	0.43	1.007
32.5	1106.9	3.1	0.07	1350	470.2	0.425	0.994
32.5	1118.7	3.2	0.08	1350	468.3	0.419	0.98
32.5	1130.4	3.4	0.09	1350	465.6	0.412	0.964
32.5	1142	3.5	0.1	1350	462.3	0.405	0.947
35	1010.7	0.4	0	1350	461.9	0.457	1.07
35	1023.4	2.1	0.01	1350	454.1	0.444	1.039
35	1036	2.3	0.02	1350	456.4	0.441	1.031
35	1048.4	2.4	0.03	1350	458.5	0.437	1.023
35	1060.8	2.5	0.04	1350	460	0.434	1.015
35	1073	2.7	0.05	1350	460.6	0.429	1.005
35	1085.1	2.8	0.06	1350	460.4	0.424	0.993
35	1097.1	2.9	0.07	1350	459.3	0.419	0.98
35	1109	3.1	0.08	1350	457.3	0.412	0.965
35	1120.7	3.2	0.09	1350	454.4	0.405	0.949
35	1132.3	3.3	0.1	1350	450.8	0.398	0.932

Speed (mph)	Vertical Force (lbs)	Slip Angle (degree)	Camber	Curve Radius (ft)	FEA Horizontal Force (lbs)	FEA FN	Friction Adjustment Factor
37.5	999.7	0.4	0	1350	452.9	0.453	1.06
37.5	1012.4	2.1	0.01	1350	443.7	0.438	1.026
37.5	1025	2.2	0.02	1350	445.6	0.435	1.017
37.5	1037.6	2.3	0.03	1350	447.2	0.431	1.009
37.5	1050	2.4	0.04	1350	448.2	0.427	0.999
37.5	1062.3	2.5	0.05	1350	448.4	0.422	0.988
37.5	1074.5	2.7	0.06	1350	447.9	0.417	0.976
37.5	1086.5	2.8	0.07	1350	446.5	0.411	0.962
37.5	1098.4	2.9	0.08	1350	444.3	0.404	0.947
37.5	1110.2	3	0.09	1350	441.2	0.397	0.93
37.5	1121.9	3.1	0.1	1350	437.5	0.39	0.913
40	987.9	0.3	0	1350	444.3	0.45	1.053
40	1000.7	2.1	0.01	1350	433.1	0.433	1.013
40	1013.4	2.2	0.02	1350	434.4	0.429	1.003
40	1026	2.3	0.03	1350	435.5	0.424	0.993
40	1038.4	2.3	0.04	1350	436	0.42	0.983
40	1050.8	2.4	0.05	1350	435.7	0.415	0.97
40	1063.1	2.5	0.06	1350	434.8	0.409	0.957
40	1075.2	2.6	0.07	1350	433.2	0.403	0.943
40	1087.2	2.7	0.08	1350	430.6	0.396	0.927
40	1099.1	2.8	0.09	1350	427.3	0.389	0.91
40	1110.8	2.9	0.1	1350	423.4	0.381	0.892
42.5	975.3	0.2	0	1350	436.1	0.447	1.046
42.5	988.2	2.1	0.01	1350	422.5	0.428	1.001
42.5	1001	2.1	0.02	1350	423.3	0.423	0.99
42.5	1013.6	2.2	0.03	1350	423.8	0.418	0.979
42.5	1026.2	2.2	0.04	1350	424	0.413	0.967
42.5	1038.6	2.3	0.05	1350	423.7	0.408	0.955
42.5	1050.9	2.4	0.06	1350	422.7	0.402	0.941
42.5	1063.2	2.4	0.07	1350	420.7	0.396	0.926
42.5	1075.2	2.5	0.08	1350	417.8	0.389	0.909

Speed (mph)	Vertical Force (lbs)	Slip Angle (degree)	Camber	Curve Radius (ft)	FEA Horizontal Force (lbs)	FEA FN	Friction Adjustment Factor
42.5	1087.2	2.5	0.09	1350	414.1	0.381	0.892
42.5	1099	2.6	0.1	1350	410	0.373	0.873
45	962	0.1	0	1350	427.7	0.445	1.059
45	974.9	2	0.01	1350	411.9	0.423	1.007
45	987.8	2.1	0.02	1350	412.5	0.418	0.995
45	1000.5	2.1	0.03	1350	412.9	0.413	0.984
45	1013.2	2.1	0.04	1350	413	0.408	0.972
45	1025.7	2.2	0.05	1350	412.8	0.402	0.959
45	1038.1	2.2	0.06	1350	411.8	0.397	0.945
45	1050.4	2.2	0.07	1350	409.5	0.39	0.929
45	1062.5	2.3	0.08	1350	406.1	0.382	0.911
45	1074.6	2.3	0.09	1350	401.8	0.374	0.891
45	1086.5	2.3	0.1	1350	397.2	0.366	0.871
47.5	947.9	0	0	1350	418.6	0.442	1.052
47.5	960.9	2	0.01	1350	401.5	0.418	0.996
47.5	973.9	2	0.02	1350	402.3	0.413	0.984
47.5	986.7	2	0.03	1350	402.9	0.408	0.973
47.5	999.4	2	0.04	1350	403.3	0.404	0.962
47.5	1012	2	0.05	1350	403.1	0.398	0.949
47.5	1024.5	2	0.06	1350	401.9	0.392	0.935
47.5	1036.9	2	0.07	1350	399.1	0.385	0.917
47.5	1049.1	2	0.08	1350	395	0.376	0.897
47.5	1061.3	2.1	0.09	1350	390.1	0.368	0.876
47.5	1073.3	2.1	0.1	1350	384.9	0.359	0.855
50	933.1	-0.1	0	1350	408.8	0.438	1.044
50	946.2	2	0.01	1350	391.1	0.413	0.985
50	959.2	2	0.02	1350	392.2	0.409	0.974
50	972.1	1.9	0.03	1350	393.1	0.404	0.964
50	984.9	1.9	0.04	1350	393.7	0.4	0.953
50	997.6	1.9	0.05	1350	393.6	0.395	0.94
50	1010.2	1.9	0.06	1350	392.1	0.388	0.925

Speed (mph)	Vertical Force (lbs)	Slip Angle (degree)	Camber	Curve Radius (ft)	FEA Horizontal Force (lbs)	FEA FN	Friction Adjustment Factor
50	1022.6	1.8	0.07	1350	388.8	0.38	0.906
50	1035	1.8	0.08	1350	384.2	0.371	0.885
50	1047.2	1.8	0.09	1350	378.8	0.362	0.862
50	1059.3	1.8	0.1	1350	373.3	0.352	0.84
30	1036	0.5	0	1500	483.1	0.466	1.111
30	1048.5	2.2	0.01	1500	476.2	0.454	1.082
30	1060.9	2.3	0.02	1500	478.5	0.451	1.075
30	1073.3	2.5	0.03	1500	480.6	0.448	1.067
30	1085.5	2.6	0.04	1500	482.2	0.444	1.059
30	1097.5	2.8	0.05	1500	483	0.44	1.049
30	1109.5	2.9	0.06	1500	482.7	0.435	1.037
30	1121.3	3.1	0.07	1500	481.6	0.43	1.024
30	1133	3.2	0.08	1500	479.8	0.423	1.009
30	1144.6	3.4	0.09	1500	477.4	0.417	0.994
30	1156	3.5	0.1	1500	474.4	0.41	0.978
32.5	1027.4	0.5	0	1500	474	0.461	1.1
32.5	1040	2.1	0.01	1500	466.7	0.449	1.07
32.5	1052.5	2.3	0.02	1500	469.1	0.446	1.062
32.5	1064.8	2.4	0.03	1500	471.3	0.443	1.055
32.5	1077.1	2.5	0.04	1500	473	0.439	1.047
32.5	1089.2	2.7	0.05	1500	473.8	0.435	1.037
32.5	1101.2	2.8	0.06	1500	473.6	0.43	1.025
32.5	1113.1	3	0.07	1500	472.5	0.424	1.012
32.5	1124.9	3.1	0.08	1500	470.6	0.418	0.997
32.5	1136.5	3.2	0.09	1500	467.9	0.412	0.981
32.5	1148	3.4	0.1	1500	464.5	0.405	0.964
35	1018.2	0.4	0	1500	464.9	0.457	1.088
35	1030.8	2.1	0.01	1500	456.8	0.443	1.056
35	1043.3	2.2	0.02	1500	459.1	0.44	1.049
35	1055.7	2.4	0.03	1500	461.1	0.437	1.041
35	1068.1	2.5	0.04	1500	462.6	0.433	1.032

Speed (mph)	Vertical Force (lbs)	Slip Angle (degree)	Camber	Curve Radius (ft)	FEA Horizontal Force (lbs)	FEA FN	Friction Adjustment Factor
35	1080.2	2.6	0.05	1500	463.2	0.429	1.022
35	1092.3	2.7	0.06	1500	463	0.424	1.01
35	1104.2	2.8	0.07	1500	461.8	0.418	0.997
35	1116.1	2.9	0.08	1500	459.7	0.412	0.982
35	1127.8	3.1	0.09	1500	456.8	0.405	0.965
35	1139.3	3.2	0.1	1500	453.1	0.398	0.948
37.5	1008.2	0.3	0	1500	456.2	0.452	1.078
37.5	1020.9	2.1	0.01	1500	446.7	0.438	1.043
37.5	1033.5	2.2	0.02	1500	448.6	0.434	1.034
37.5	1046	2.3	0.03	1500	450.2	0.43	1.026
37.5	1058.3	2.4	0.04	1500	451.1	0.426	1.016
37.5	1070.6	2.5	0.05	1500	451.3	0.422	1.005
37.5	1082.7	2.6	0.06	1500	450.7	0.416	0.992
37.5	1094.7	2.7	0.07	1500	449.2	0.41	0.978
37.5	1106.6	2.8	0.08	1500	446.9	0.404	0.962
37.5	1118.4	2.9	0.09	1500	443.8	0.397	0.946
37.5	1130	3	0.1	1500	439.9	0.389	0.928
40	997.6	0.3	0	1500	447.9	0.449	1.07
40	1010.4	2.1	0.01	1500	436.5	0.432	1.03
40	1023	2.2	0.02	1500	437.8	0.428	1.02
40	1035.5	2.2	0.03	1500	438.8	0.424	1.01
40	1048	2.3	0.04	1500	439.2	0.419	0.999
40	1060.3	2.4	0.05	1500	438.9	0.414	0.987
40	1072.5	2.5	0.06	1500	437.9	0.408	0.973
40	1084.5	2.5	0.07	1500	436.2	0.402	0.958
40	1096.5	2.6	0.08	1500	433.5	0.395	0.942
40	1108.3	2.7	0.09	1500	430.1	0.388	0.925
40	1120	2.8	0.1	1500	426.1	0.38	0.907
42.5	986.3	0.2	0	1500	440	0.446	1.063
42.5	999.1	2.1	0.01	1500	426.2	0.427	1.017
42.5	1011.8	2.1	0.02	1500	427	0.422	1.006

Speed (mph)	Vertical Force (lbs)	Slip Angle (degree)	Camber	Curve Radius (ft)	FEA Horizontal Force (lbs)	FEA FN	Friction Adjustment Factor
42.5	1024.4	2.2	0.03	1500	427.5	0.417	0.994
42.5	1036.9	2.2	0.04	1500	427.5	0.412	0.983
42.5	1049.3	2.3	0.05	1500	427.1	0.407	0.97
42.5	1061.6	2.3	0.06	1500	426	0.401	0.956
42.5	1073.7	2.4	0.07	1500	423.9	0.395	0.941
42.5	1085.7	2.4	0.08	1500	420.9	0.388	0.924
42.5	1097.6	2.5	0.09	1500	417.1	0.38	0.906
42.5	1109.4	2.5	0.1	1500	412.8	0.372	0.887
45	974.3	0.1	0	1500	432	0.443	1.057
45	987.2	2	0.01	1500	416.1	0.421	1.004
45	1000	2.1	0.02	1500	416.6	0.417	0.993
45	1012.6	2.1	0.03	1500	416.8	0.412	0.981
45	1025.2	2.1	0.04	1500	416.9	0.407	0.969
45	1037.7	2.2	0.05	1500	416.5	0.401	0.957
45	1050	2.2	0.06	1500	415.3	0.396	0.943
45	1062.2	2.2	0.07	1500	412.9	0.389	0.926
45	1074.3	2.2	0.08	1500	409.3	0.381	0.908
45	1086.3	2.3	0.09	1500	404.9	0.373	0.888
45	1098.1	2.3	0.1	1500	400.2	0.364	0.869
47.5	961.6	0	0	1500	423.2	0.44	1.049
47.5	974.6	2	0.01	1500	406.1	0.417	0.993
47.5	987.4	2	0.02	1500	406.7	0.412	0.982
47.5	1000.2	2	0.03	1500	407.2	0.407	0.97
47.5	1012.8	2	0.04	1500	407.4	0.402	0.959
47.5	1025.3	2	0.05	1500	407	0.397	0.946
47.5	1037.8	2	0.06	1500	405.6	0.391	0.931
47.5	1050.1	2	0.07	1500	402.6	0.383	0.914
47.5	1062.2	2	0.08	1500	398.4	0.375	0.894
47.5	1074.3	2	0.09	1500	393.3	0.366	0.873
47.5	1086.2	2.1	0.1	1500	388.1	0.357	0.852
50	948.3	-0.1	0	1500	413.8	0.436	1.04

Speed (mph)	Vertical Force (lbs)	Slip Angle (degree)	Camber	Curve Radius (ft)	FEA Horizontal Force (lbs)	FEA FN	Friction Adjustment Factor
50	961.3	2	0.01	1500	396.1	0.412	0.982
50	974.2	2	0.02	1500	397	0.407	0.971
50	987.1	1.9	0.03	1500	397.8	0.403	0.96
50	999.8	1.9	0.04	1500	398.1	0.398	0.949
50	1012.4	1.9	0.05	1500	397.8	0.393	0.936
50	1024.9	1.9	0.06	1500	396.1	0.386	0.921
50	1037.2	1.8	0.07	1500	392.6	0.378	0.902
50	1049.5	1.8	0.08	1500	387.8	0.369	0.881
50	1061.6	1.8	0.09	1500	382.3	0.36	0.858
50	1073.6	1.8	0.1	1500	376.7	0.351	0.836
30	1085.3	0	0	Infinity	505.6	0.466	1
32.5	1085.3	0	0	Infinity	497.8	0.459	1
35	1085.3	0	0	Infinity	489	0.451	1
37.5	1085.3	0	0	Infinity	485.6	0.447	1
40	1085.3	0	0	Infinity	461.4	0.425	1
42.5	1085.3	0	0	Infinity	474.8	0.437	1
45	1085.3	0	0	Infinity	467.3	0.431	1
47.5	1085.3	0	0	Infinity	463.7	0.427	1
50	1085.3	0	0	Infinity	455.4	0.42	1

Appendix E. Assessment and Comparison of LWST and SCRIM Field Test Route Details

Figure E.1 provides an overview of highway routes from R1 to R11, detailing route identifiers, locations, and segments between specific mile markers. Each entry includes starting and ending points marked by latitude and longitude coordinates, along with intersecting roadways at these points where applicable. The length of each route segment is also indicated in miles. The routes cover highways and state roads, offering insights into specific stretches, from rural areas to intersections with notable cross streets or avenues. This information can be used for route planning, traffic analysis, or geographic studies of roadway infrastructure.

Table E.1 *Highway Route Segments Overview.*

Route ID	Route	Start LAT	Start LONG	Start Intersecting Roadway	End LAT	End LONG	End Intersecting Roadway	Length (miles)
1	US-52	40.31591	-86.76662	E 700 S	40.17042	-86.60915	Sugar Creek Ave	13
2	SR-32a	40.05413	-86.58190	N 600 W	40.04660	-86.50660	S 200 W	5
3	SR-32b	40.03921	-86.44449	East of Indianapolis Ave	40.04130	-86.26028	1100 E	9
4	SR-39	39.48270	-86.43980	SR 67	39.73128	-86.52707	CR 200 S	19
5	SR-46a	39.16302	-86.41455	N Gettys Creek Rd	39.20916	-86.24697	Mound St	12
6	SR-135	39.20916	-86.24697	Mound St	39.27041	-86.24938	North of SR 45	5
7	SR-46b	39.31254	-86.86615	SR 246	39.25967	-86.65752	W Chafin Chapel Rd	13
8	SR-46c	39.19926	-86.04647	W Old Nashville Rd	39.19942	-85.97740	Carlos Folger Rd	4
9	SR-240	39.64051	-86.77668	N CR 450 E	39.63044	-86.68742	S CR 900 E	5
10	I-65a	40.05832	-86.49366		40.13949	-86.52464		5
11	I-65b	40.36132	-86.77743		40.44908	-86.84552		5

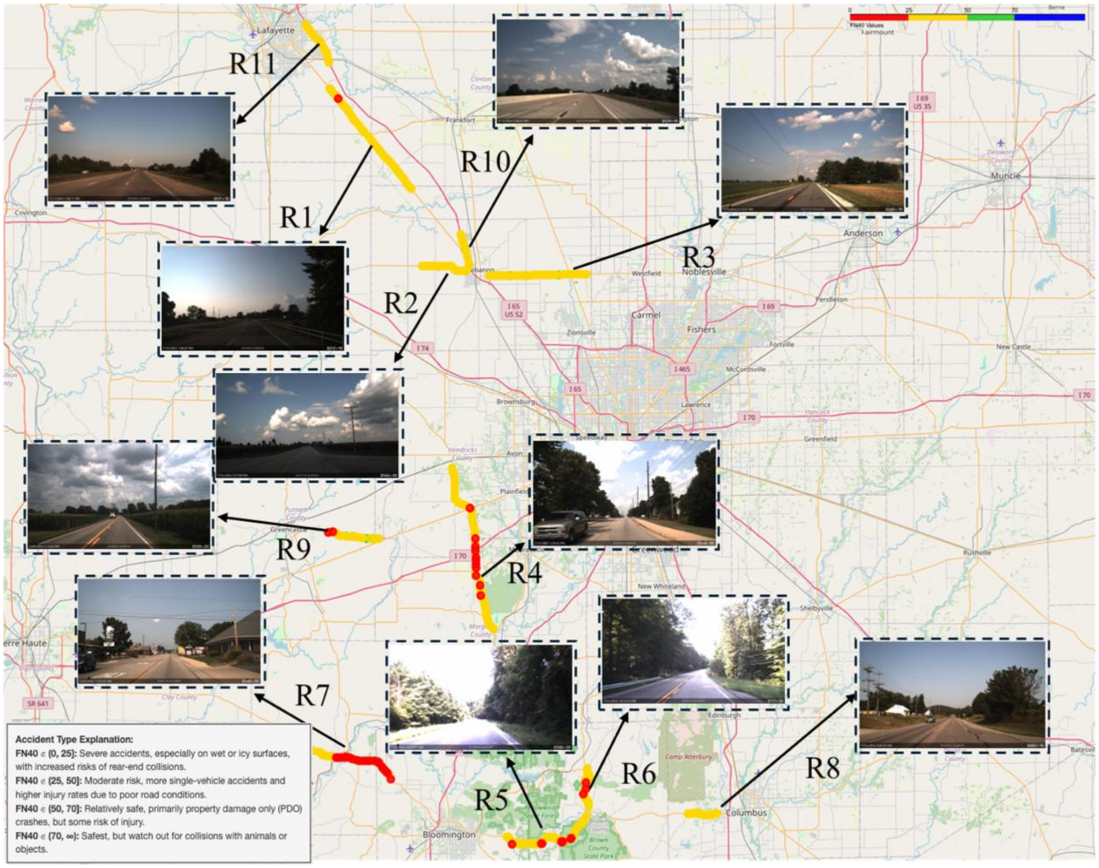

Figure E.1 *Overview of Route Tracks From R1 to R11 on Map.*

The images labeled R1 through R11 from Figure E.2 to Figure E. 12 offer a comprehensive visual representation of a designated route, illustrating the routes from the "Starting point" to the "End point." This series of images captures various perspectives along the route, providing a detailed overview of both geographical context and on-the-ground features. The details are as follows:

- (a): A map overview that illustrates the entire route path, with the starting and ending points clearly marked. The dashed line indicates the general direction and progression of the road, allowing viewers to understand the overall layout of the route in relation to the surrounding area.
- (b) and (d): These images from Google Maps focus on the starting point of the route, presenting it from two perspectives (terrain view and site view). The terrain view gives a broader understanding of the geographical and topographical features surrounding the

starting point, while the site view provides a close-up, on-the-ground look at the road surface and nearby environment.

- (c) and (e): These images of Google Maps capture the end point of the route, again from both terrain view and site view. The terrain view shows the topographical context at the end of the journey, including natural features and land contours. The site view offers a direct visual of the road surface and adjacent surroundings, highlighting any specific road characteristics or environmental elements present near the end point.
- (f) and (g) are real-time captures taken during the test drive using the dashcam. These images showcase the actual road conditions, weather, and visibility at the time of testing

This collection of images provides a layered perspective on the route, combining broad geographical insights with detailed, site-specific views, making it a useful tool for analyzing both the layout and conditions of the road.

E.1. R1 Route Details and Visual Analysis

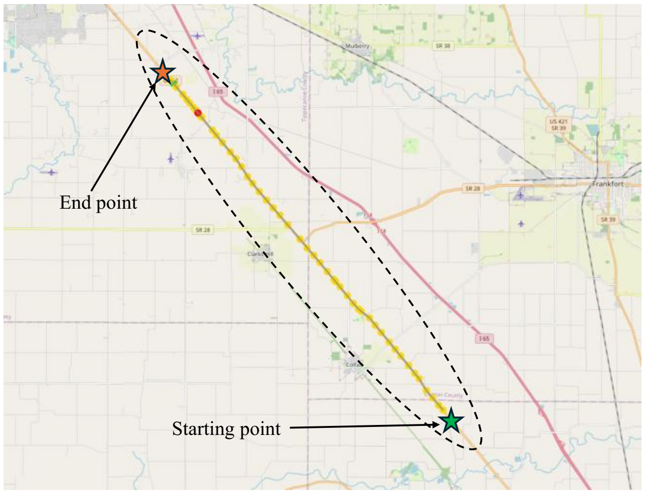

(a)

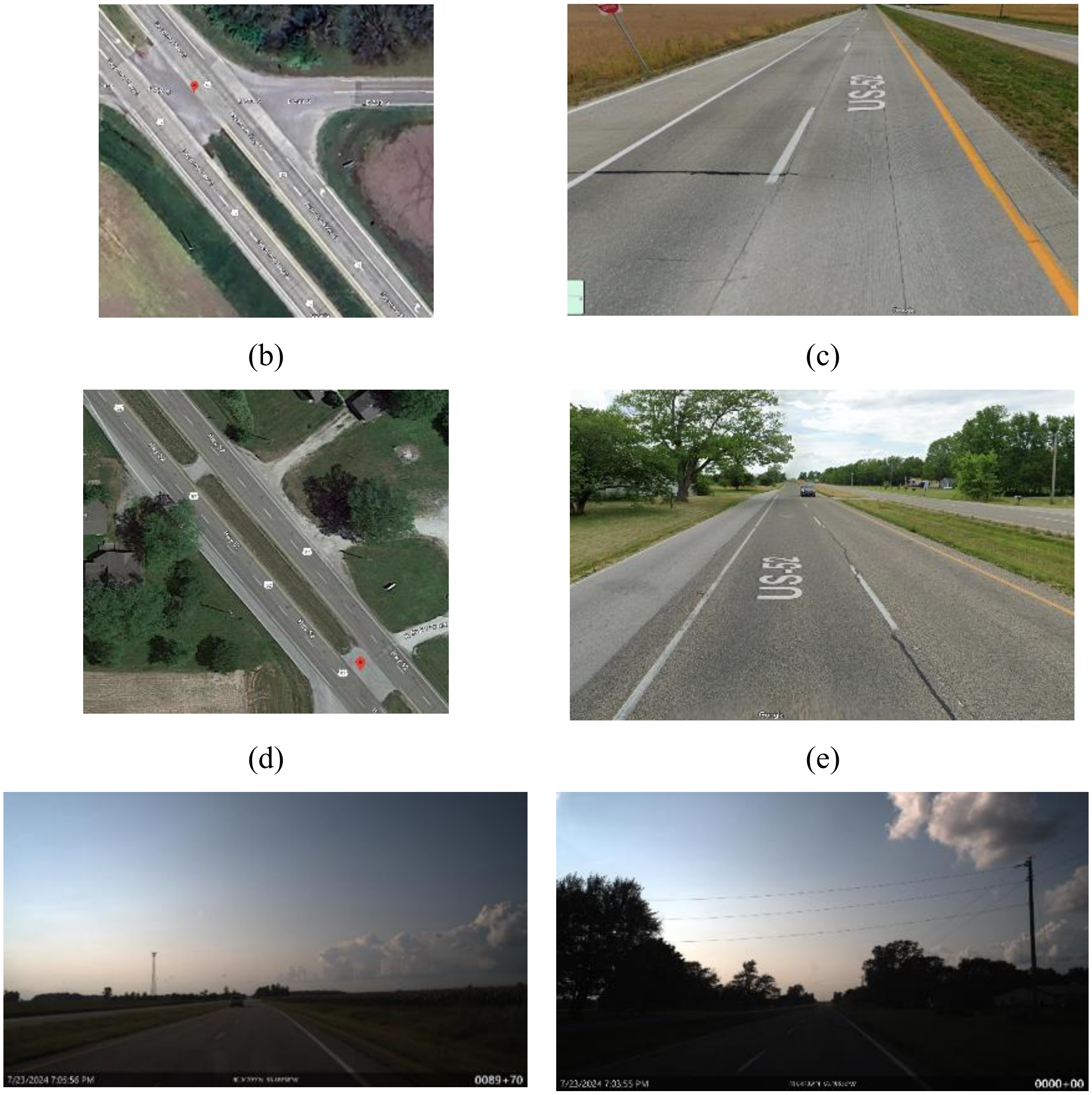

(b) (c)

(d) (e)

(f) (g)

Figure E.2 *R1 Route Details: (a) Route Overview on Map; (b) Terrain View at Starting Point From Google Maps; (c) Site View at Starting Point From Google Maps; (d) Terrain View at End Point From Google Maps; (e) Site View at End Point From Google Maps; (f) and (g): Real-Time Capture From The Testing Vehicle.*

The road surface appears to be a concrete pavement at the starting point, as there are distinct joint lines, which are typical of concrete roads. The visible lines on the concrete surface appear to be longitudinal and transverse (parallel and perpendicular to the direction of travel). It appears to be an asphalt pavement at the end point. The texture of the road looks continuous and smooth, which is typical of asphalt.

E.2. R2 Route Details and Visual Analysis

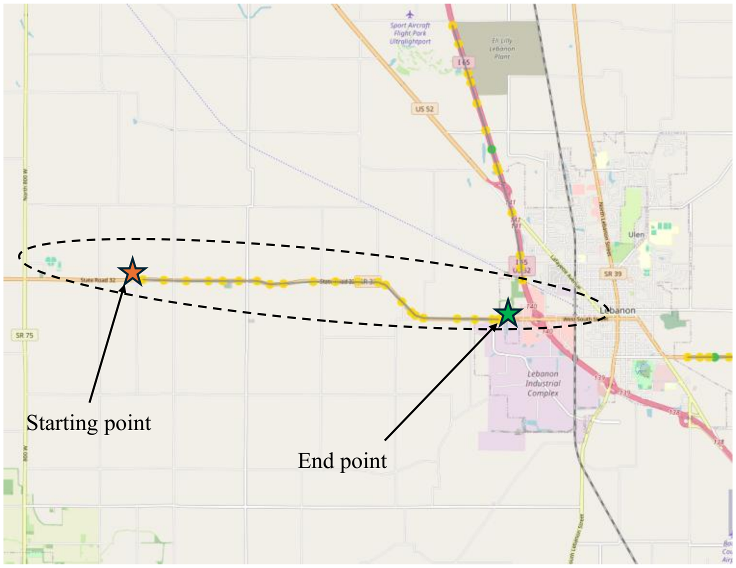

(a)

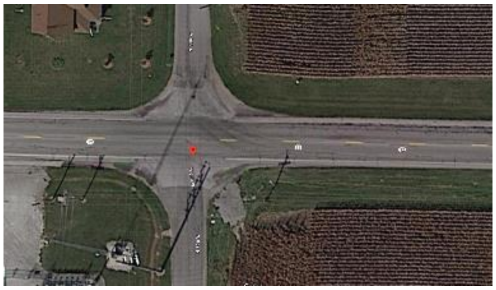

(b)

(c)

(d)

(e)

(f) (g)

Figure E 3 *R2 Route Details: (a) Route Overview on Map; (b) Terrain View at Starting Point From Google Maps; (c) Site View at Starting Point From Google Maps; (d) Terrain View at End Point From Google Maps; (e) Site View at End Point From Google Maps; (f) and (g): Real-Time Capture From The Testing Vehicle.*

This road appears to be an asphalt pavement. The texture of the road looks continuous and smooth, which is typical of asphalt.

E.3. R3 Route Details and Visual Analysis

(a)

(b) (c)

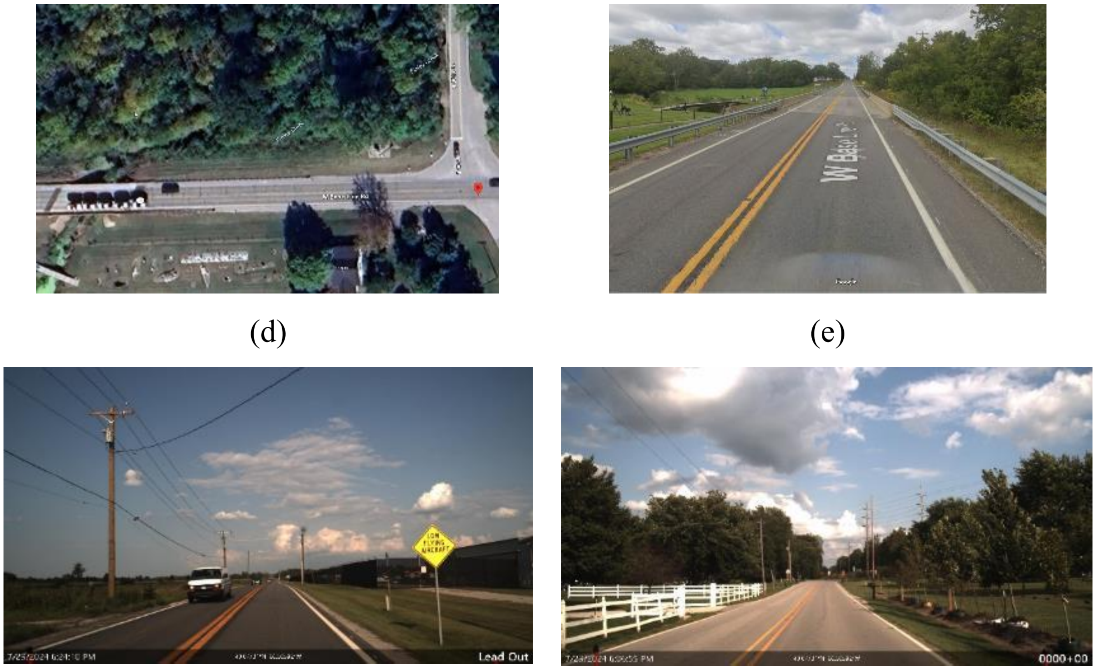

(d) (e)

(f) (g)

Figure E.4 *R3 Route Details: (a) Route Overview on Map; (b) Terrain View at Starting Point From Google Maps; (c) Site View at Starting Point From Google Maps; (d) Terrain View at End Point From Google Maps; (e) Site View at End Point From Google Maps; (f) and (g): Real-Time Capture From the Testing Vehicle.*

The road surface at the starting point appears to be concrete pavement. The texture of the road surface appears to have transverse lines. This road appears to be an asphalt pavement. The texture of the road looks continuous and smooth, which is typical of asphalt.

E.4. R4 Route Details and Visual Analysis

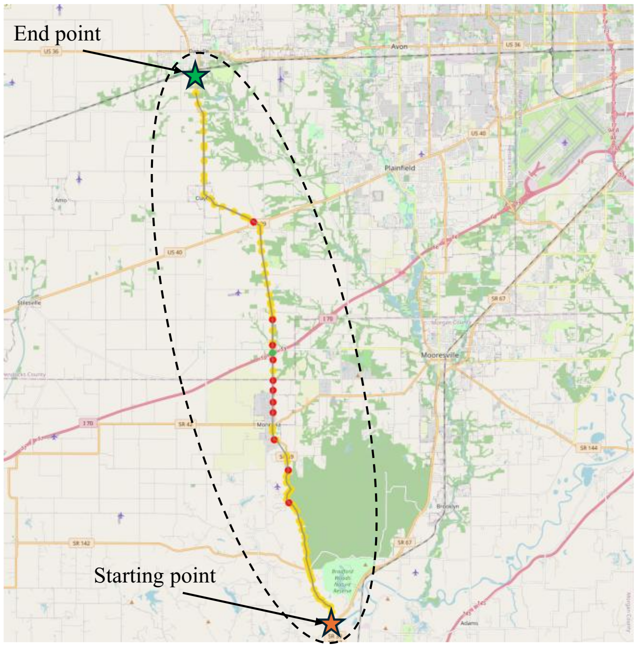

(a)

(b)

(c)

(d)

(e)

(f) (g)

Figure E.5 *R4 Route Details: (a) Route Overview on Map; (b) Terrain View at Starting Point From Google Maps; (c) Site View at Starting Point From Google Maps; (d) Terrain View at End Point From Google Maps; (e) Site View at End Point From Google Maps; (f) and (g): Real-Time Capture From the Testing Vehicle.*

This road appears to be an asphalt pavement. The texture of the road looks continuous and smooth, which is typical of asphalt.

E.5. R5 Route Details and Visual Analysis

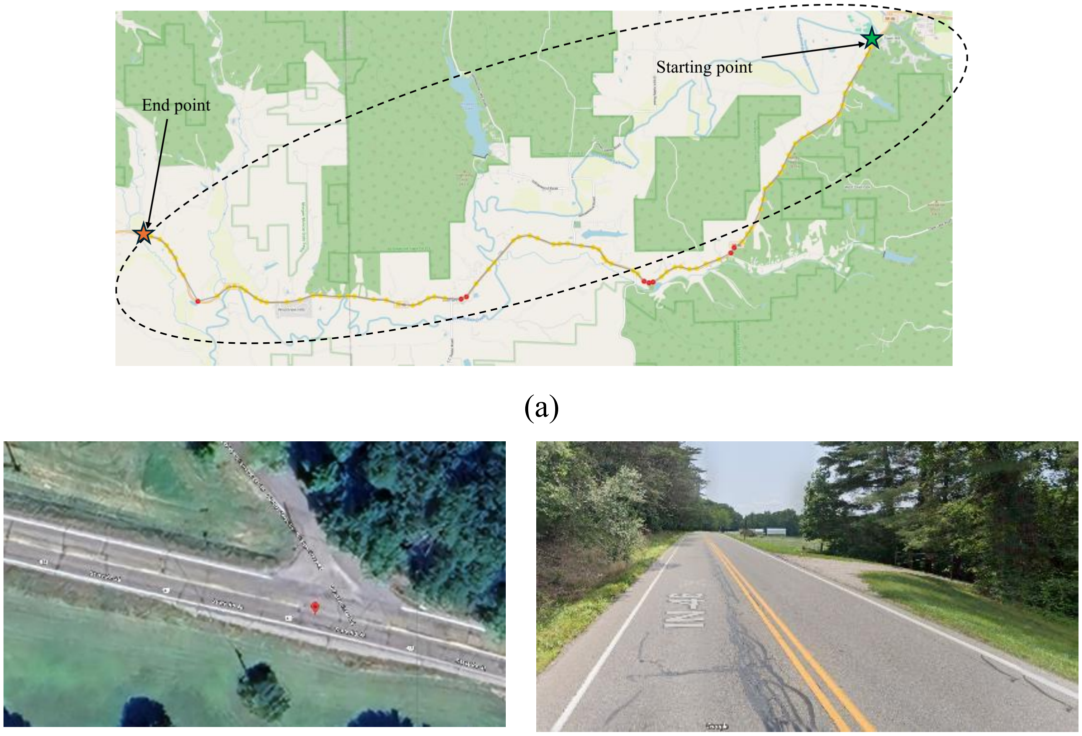

(a)

(b) (c)

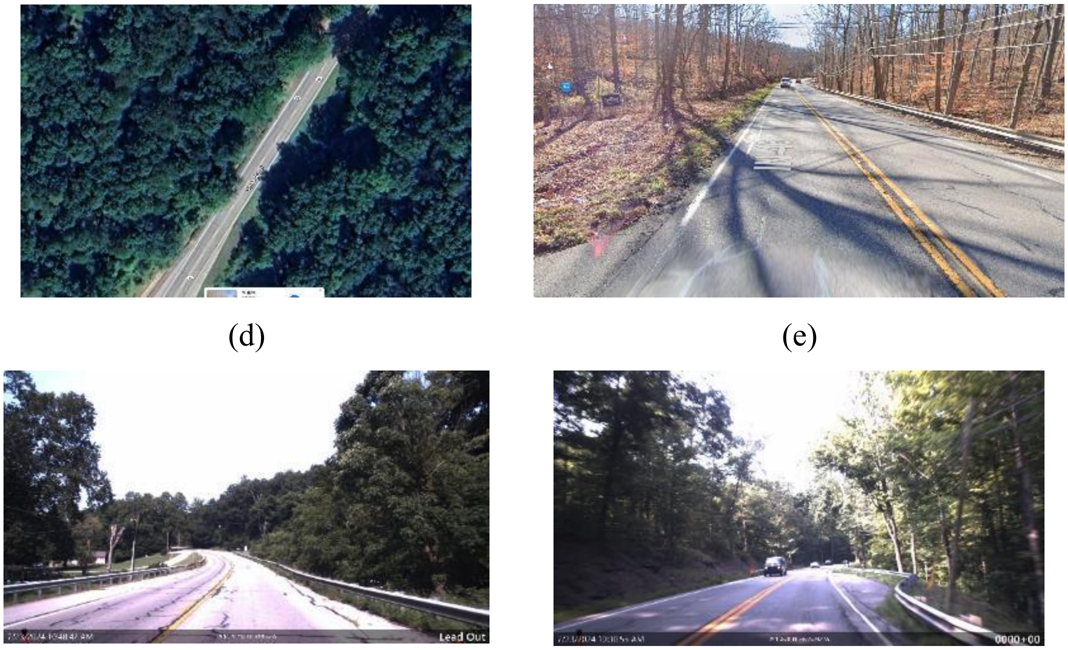

(d) (e)

(f) (g)

Figure E.6 *R5 Route Details: (a) Route Overview on Map; (b) Terrain View at Starting Point From Google Maps; (c) Site View at Starting Point From Google Maps; (d) Terrain View at End Point From Google Maps; (e) Site View at End Point From Google Maps; (f) and (g): real-Time Capture From the Testing Vehicle.*

This road appears to be an asphalt pavement. The texture of the road looks continuous and smooth, which is typical of asphalt.

E.6. R6 Route Details and Visual Analysis

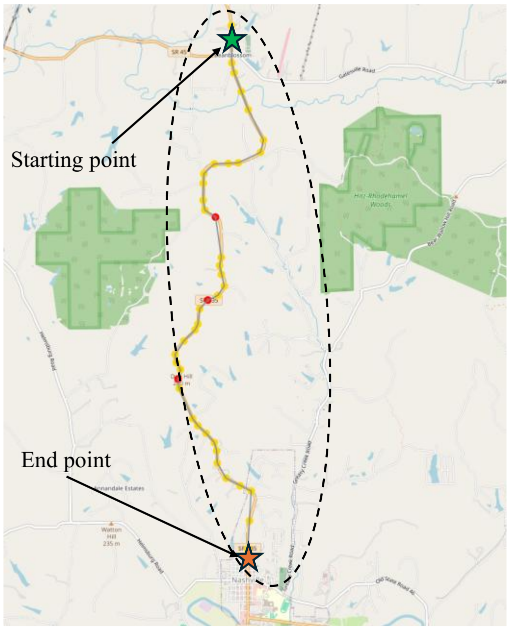

(a)

(b)

(c)

(d)

(e)

(f) (g)

Figure E.7 *R6 Route Details: (a) Route Overview on Map; (b) Terrain View at Starting Point From Google Maps; (c) Site View at Starting Point From Google Maps; (d) Terrain View at End Point From Google Maps; (e) Site View at End Point From Google Maps; (f) and (g): Real-Time Capture From the Testing Vehicle.*

This road appears to be an asphalt pavement. The texture of the road looks continuous and smooth, which is typical of asphalt.

E.7. R7 Route Details and Visual Analysis

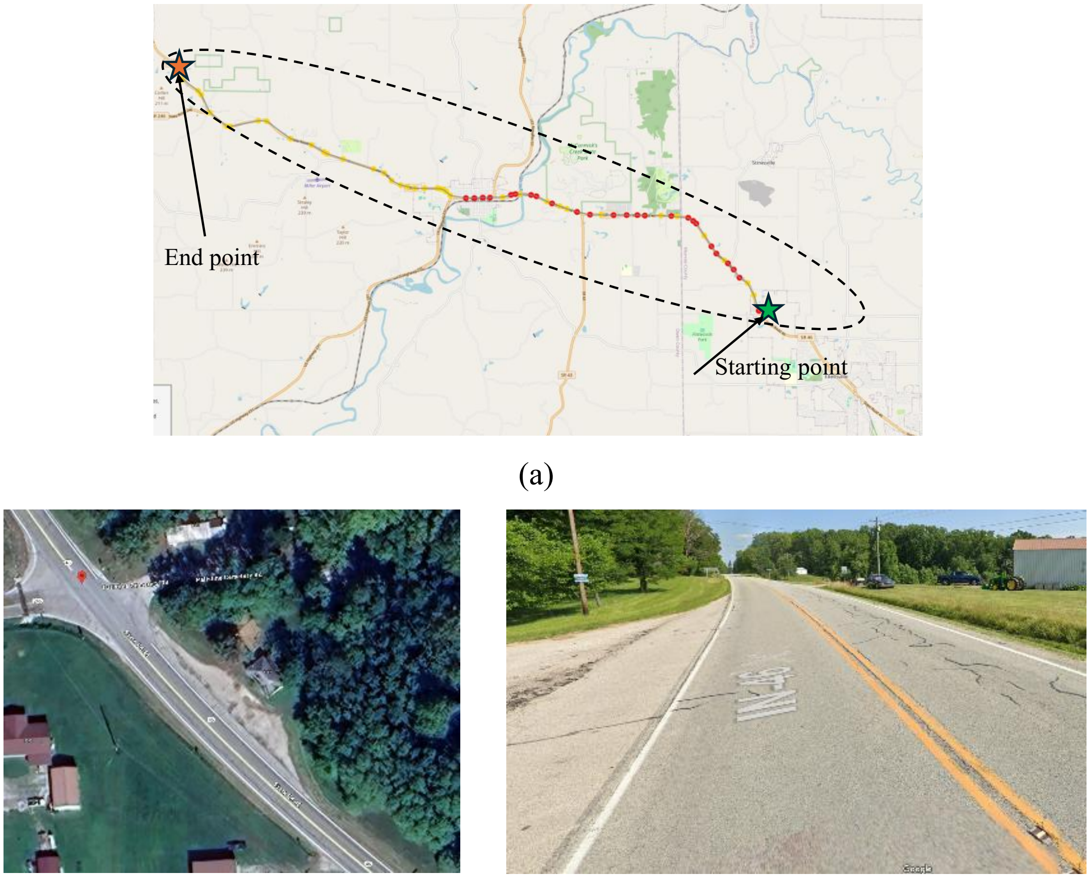

(a)

(b) (c)

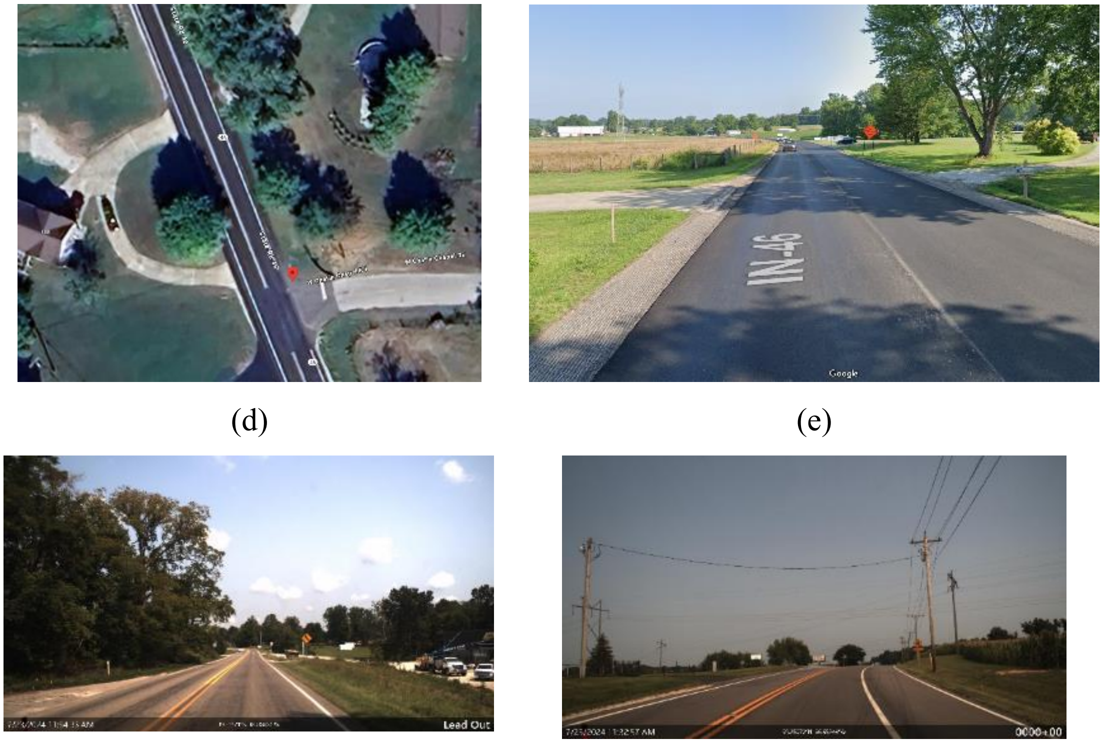

(d) (e)

(f) (g)

Figure E.8 *R7 Route Details: (a) Route overview on map; (b) Terrain view at starting point from Google Maps; (c) Site view at Starting Point From Google Maps; (d) Terrain View at End Point From Google Maps; (e) Site View at End Point From Google Maps; (f) and (g): real-Time Capture From the Testing Vehicle.*

This road appears to be an asphalt pavement. The texture of the road looks continuous and smooth, which is typical of asphalt. However, some road sections have a noticeable longitudinal crack on the asphalt surface.

E.8. R8 Route Details and Visual Analysis

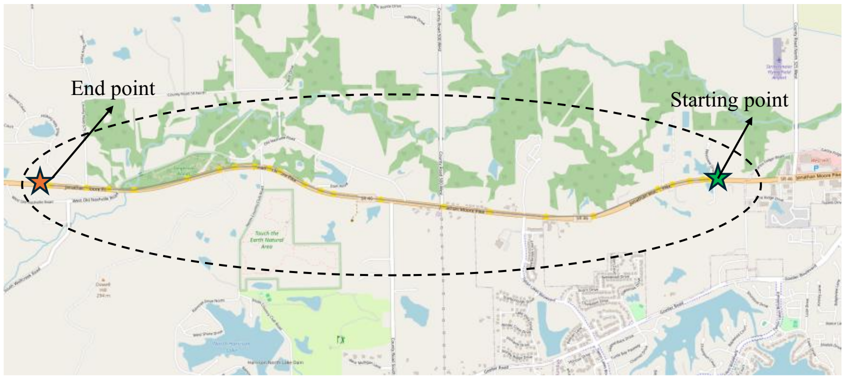

(a)

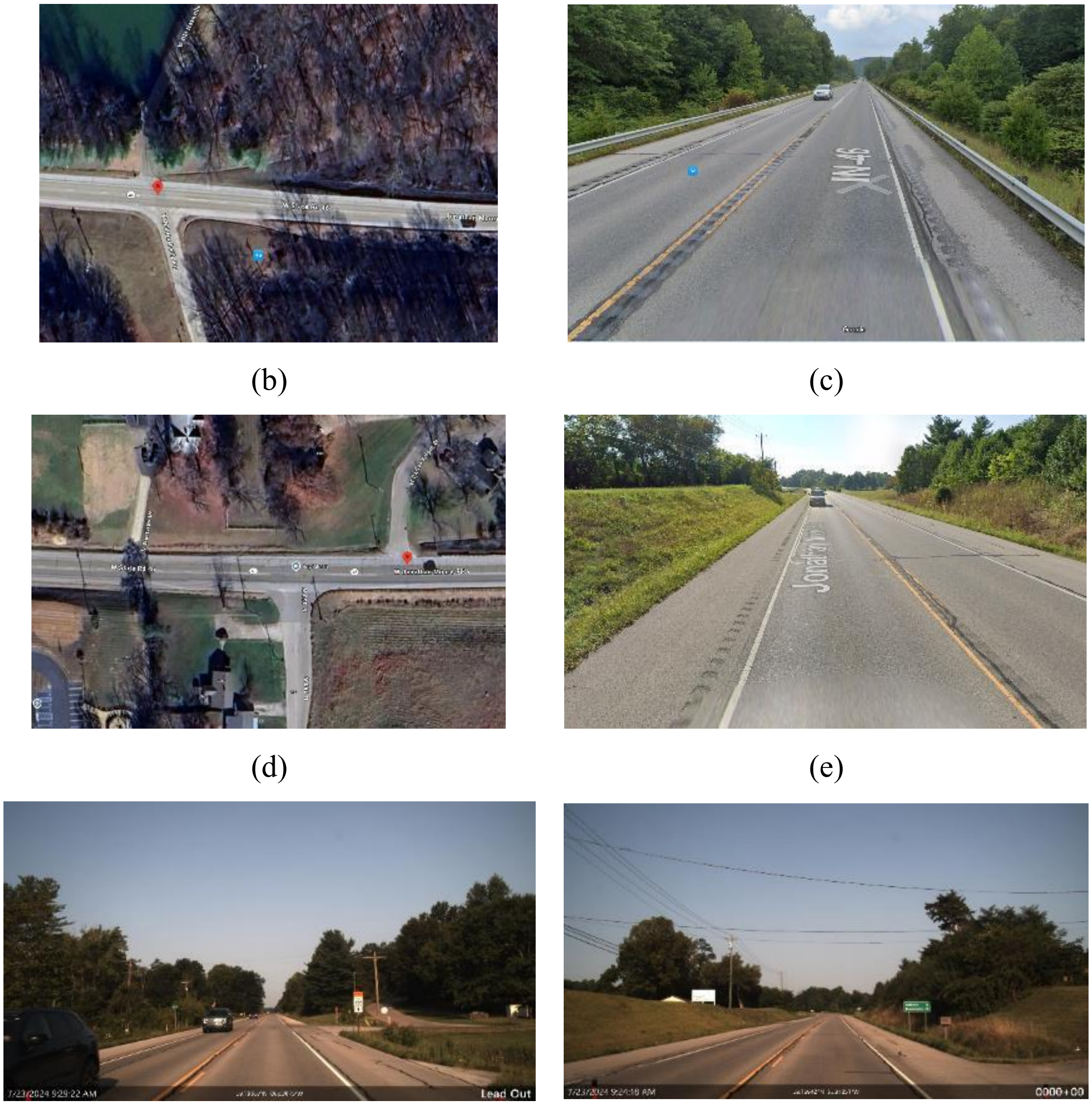

(b) (c)

(d) (e)

(f) (g)

Figure E.9 *R8 Route Details: (a) Route Overview on Map; (b) Terrain View at Starting Point From Google Maps; (c) Site View at Starting Point From Google Maps; (d) Terrain View at End Point From Google Maps; (e) Site View at End Point From Google Maps; (f) and (g): Real-Time Capture From the Testing Vehicle.*

This road appears to be an asphalt pavement. The texture of the road looks continuous and smooth, which is typical of asphalt

E.9 R9 Route Details and Visual Analysis

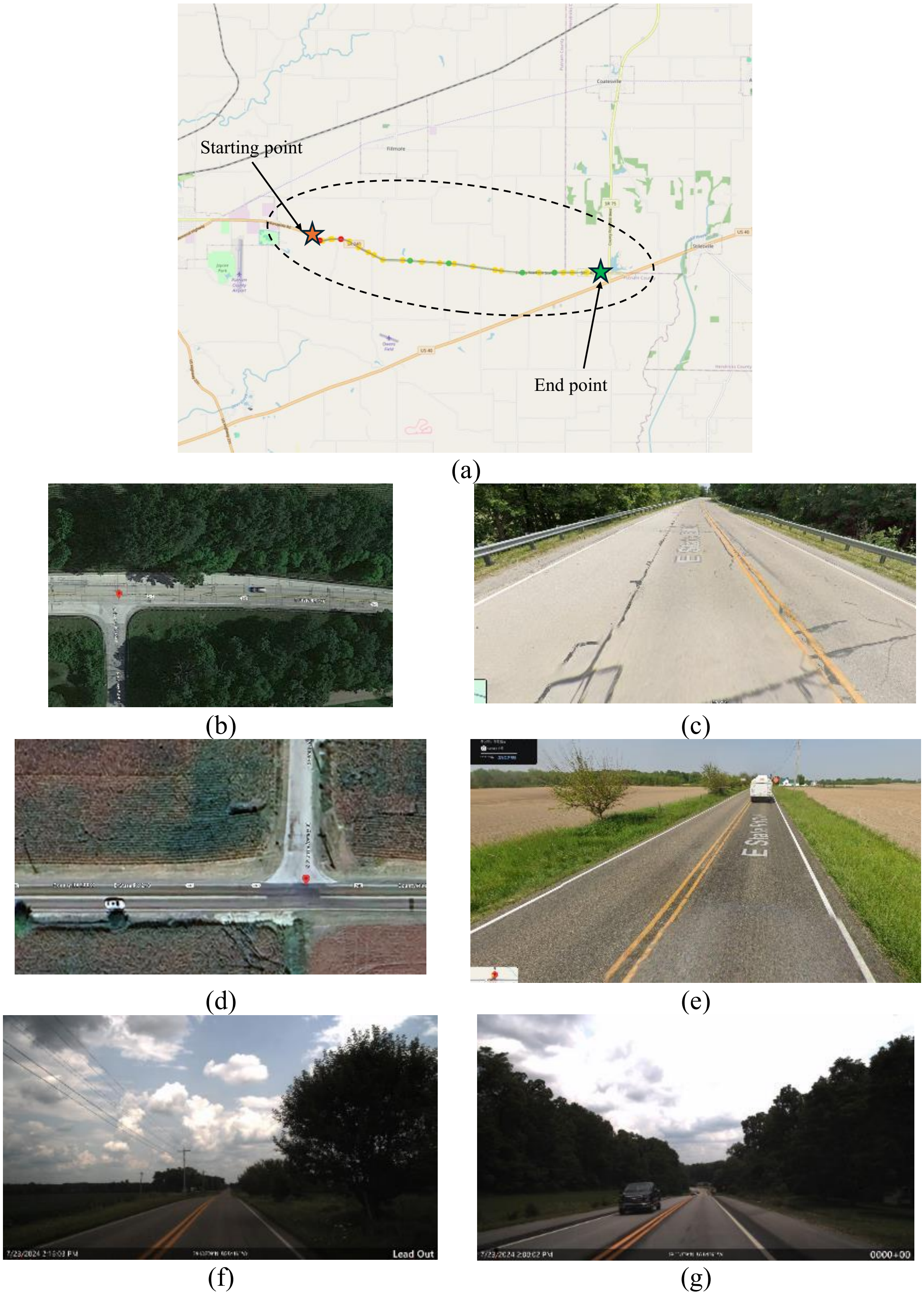

Figure E.10 *R9 Route Details: (a) Route Overview on Map; (b) Terrain View at Starting Point From Google Maps; (c) Site View at Starting Point From Google Maps; (d) Terrain View at End Point From Google Maps; (e) Site View at End Point From Google Maps; (f) and (g): Real-Time Capture From the Testing Vehicle.*

The road surface at the starting point appears to be concrete pavement. The texture of the road surface appears to have no groove and transverse groove lines. The road appears to be asphalt pavement at the end point. The texture of the road looks continuous and smooth, which is typical of asphalt.

E.10. R10 Route Details and Visual Analysis

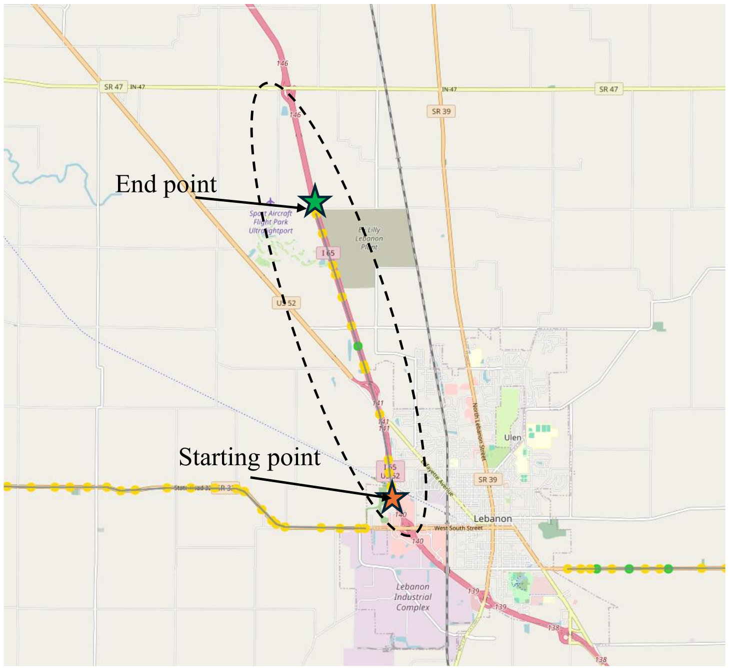

(a)

(b)

(c)

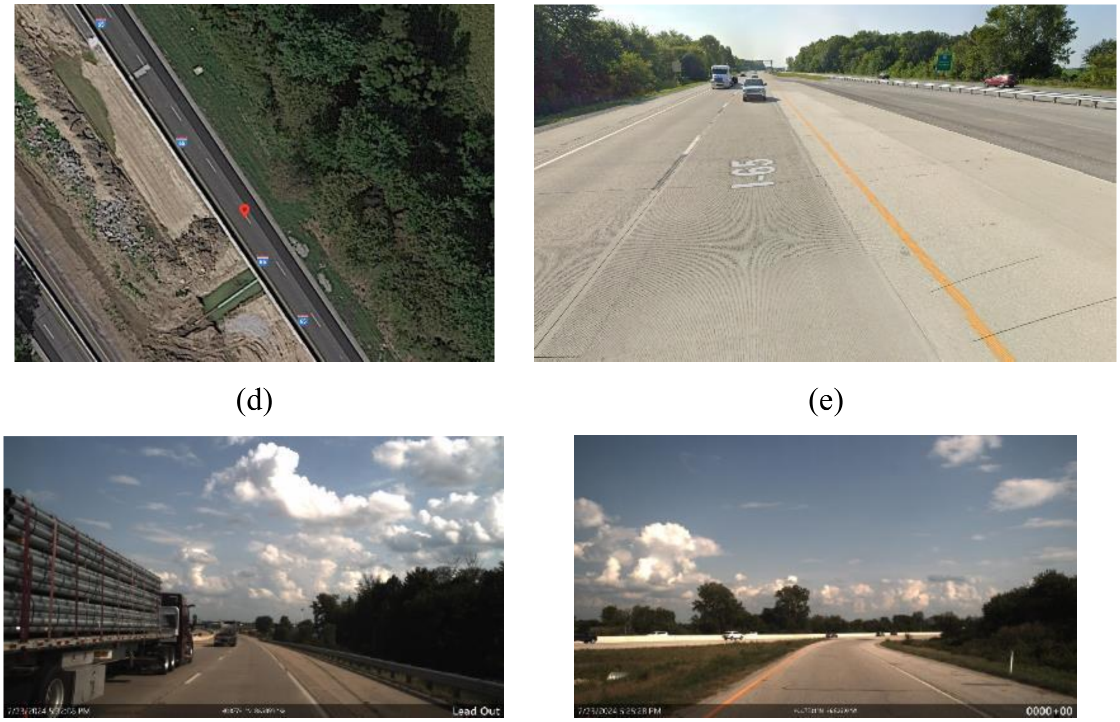

(d) (e)

(f) (g)

Figure E.11 *R10 Route Details: (a) Route Overview on Map; (b) Terrain View at Starting Point From Google Maps; (c) Site View at Starting Point From Google Maps; (d) Terrain View at End Point From Google Maps; (e) Site View at End Point From Google Maps; (f) and (g): Real-Time Capture From the Testing Vehicle.*

The road surface appears to be concrete pavement, as there are distinct joint lines, which are typical of concrete roads. The visible lines on the surface appear to be longitudinal and transverse.

E.11. R11 Route Details and Visual Analysis

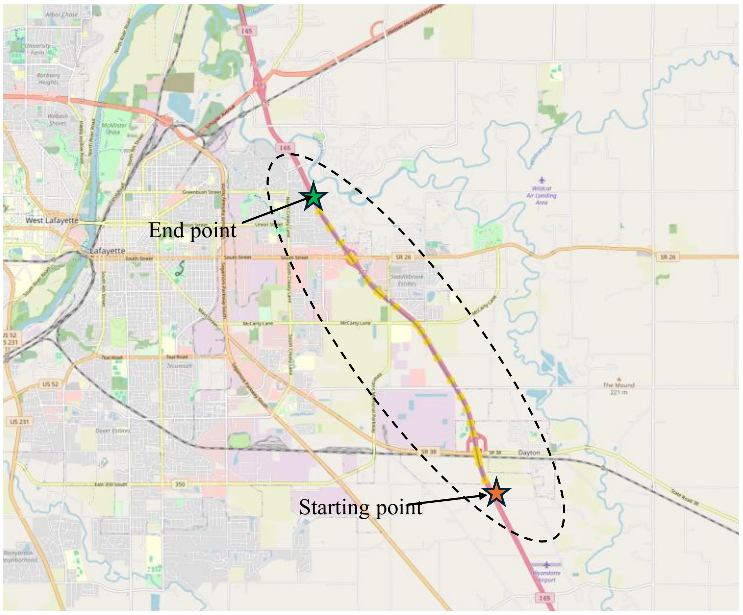

(a)

(b)

(c)

(d)

(e)

(f) (g)

Figure E.12 R11 Route Details: (a) Route Overview on Map; (b) Terrain View at Starting Point From Google Maps; (c) Site View at Starting Point From Google Maps; (d) Terrain View at End Point From Google Maps; (e) Site View at End Point From Google Maps; (f) and (g): Real-Time Capture From the Testing Vehicle.

This road appears to be asphalt pavement at the starting point, with a continuous and smooth texture typical of asphalt. Further along, the road surface appears to transition to concrete pavement, with a mixed longitudinal and transverse texture.

E.12. Data Preprocessing

1. SR and MPD

1)Correlation analysis of SR and MPD

Correlation analysis quantifies the relationship between two parameters, including the direction and strength of the relationship. Through significance testing, the correlations obtained from the sample can be generalized to the overall population. First, histograms of the parameters and related distribution metrics are calculated to check whether the SR and MPD from R1 to R11 conform to a normal distribution. Secondly, according to the data distribution, the appropriate correlation coefficient calculation method is selected to analyze the correlation between SR and MPD of the sample. Finally, statistical significance testing is conducted to evaluate the significance of the sample when generalized to the overall population, supplementing the analysis and supporting the reliability of the patterns observed in the sample being effectively replicated in more data.

Histograms of SR and MPD are shown in Figure E.13, Figure E.14 and Figure E.15. For further understanding the distribution features, statistical values of SR and MPD are given, including the average value, standard deviation, the minimum and maximum values of the data, median, skewness, kurtosis. Skewness indicates complete symmetry, the positive value indicates the right bias, and the negative value indicates the left bias. Kurtosis describes the sharpness of the data distribution. The higher peak indicates that the data is concentrated near the mean, and the lower peak indicates that the data is scattered. The summary of the index is given in Table E.2 and Table E.3.

As shown in the results, the distribution of SR and MPD from R1 to R11 obviously deviates from the normal distribution. If the distribution obviously deviates from the normal distribution (such as right or left), the Pearson correlation coefficient may give misleading results, which requires that the data conforms to the normal distribution. According to the distribution of two parameters, Spearman correlation efficient is more suitable to analyze the relationship between SR and MPD, which is non-parametric measure that assesses how well the relationship between two variables can be described by a monotonic function. The Spearman correlation coefficient is more robust and suitable for uneven data distribution or contains out-of-group values, especially for nonlinear relationship. If the distribution of data does not satisfy the normality assumption, the Spearman correlation coefficient is a more appropriate choice.

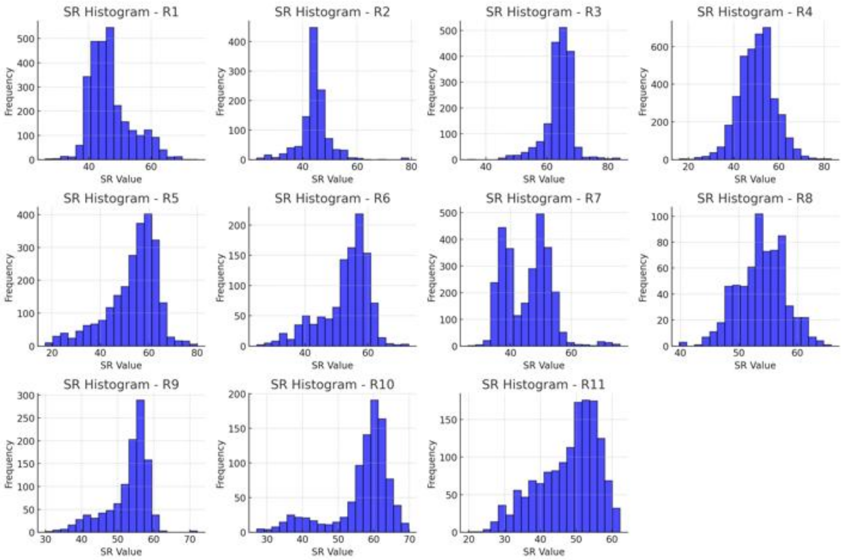

__Figure E.13__ Histogram of SR From R1 To R11.

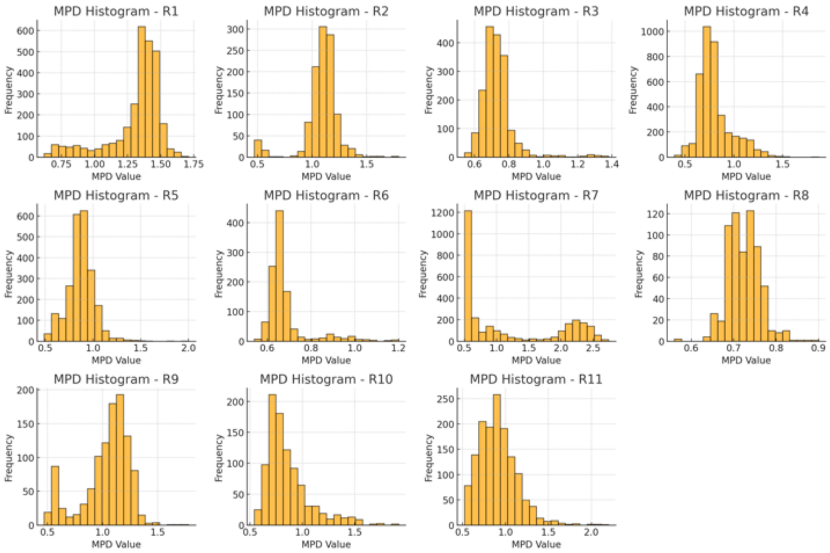

Figure E.14 *Histogram of MPD From R1 To R11.*

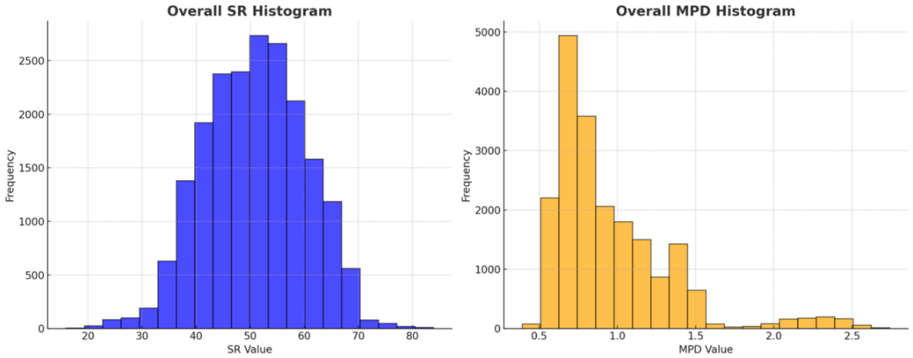

Figure E.15 *Histogram of SR and MPD in Total Data.*

Table E.2 *Data Distribution Summary of SR From R1 to R11.*

Road	SR Mean	SR Std Dev	SR Min	SR Max	SR Median	SR Skewness	SR Kurtosis
R1	46.80	6.64	26.00	74.80	45.60	0.90	0.61
R2	44.35	5.80	23.00	78.90	44.00	0.64	7.49
R3	64.13	4.60	34.10	83.90	64.90	-0.93	4.47
R4	50.13	8.08	15.90	83.10	50.40	-0.05	0.81
R5	53.25	10.62	17.20	80.00	55.80	-1.00	0.81
R6	52.79	7.73	24.60	72.90	54.80	-1.00	0.59
R7	45.40	7.51	26.00	75.90	46.75	0.45	0.31
R8	53.82	4.07	39.80	65.80	53.80	-0.16	-0.01
R9	52.99	5.89	29.90	72.10	54.90	-1.21	1.23
R10	56.50	8.24	27.10	69.80	59.30	-1.47	1.54
R11	47.73	8.15	19.70	62.20	49.90	-0.67	-0.36
Total	50.84	9.27	15.90	83.90	50.90	-0.08	-0.25

Table E.3 *Data Distribution Summary of MPD From R1 to R11.*

Road	MPD Mean	MPD Std Dev	MPD Min	MPD Max	MPD Median	MPD Skewness	MPD Kurtosis
R1	1.31	0.20	0.62	1.71	1.37	-1.60	1.99
R2	1.08	0.16	0.47	1.79	1.1	-1.62	5.74
R3	0.73	0.10	0.54	1.38	0.71	3.06	14.57
R4	0.80	0.17	0.39	1.87	0.76	1.24	1.86
R5	0.87	0.14	0.49	2.00	0.87	0.55	4.22
R6	0.68	0.10	0.54	1.20	0.65	2.66	7.57
R7	1.19	0.75	0.50	2.74	0.71	0.69	-1.30
R8	0.72	0.04	0.56	0.90	0.72	0.36	1.60
R9	1.03	0.22	0.47	1.78	1.08	-0.86	0.30
R10	0.86	0.22	0.54	1.92	0.79	1.64	3.03
R11	0.91	0.22	0.52	2.20	0.89	1.15	3.11
Total	0.96	0.39	2.74	0.83	0.83	1.82	3.89

The resulting correlation conclusions need to be generalized from the sample to the whole to provide evidence of whether the same trend can be obtained in more data. By calculating the p-value, the judgement whether the correlation between SR and MPD is significant can be effectively given. In statistical analysis, the p value is a probability used to evaluate the appearance of the observation results under the condition that the original hypothesis is true. The original hypothesis

(Null Hypothesis, H_0) is usually a general hypothesis, indicating that there is no effect, no difference or no correlation. When conducting statistical tests, the significance level (α) is first determined, which is usually set to 0.05. This level represents a 5% risk of accepting the original hypothesis of incorrect rejection. In this case, the original hypothesis is expressed that there is no linear or nonlinear correlation between SR and MPD for Pearson correlation and Spearman correlation coefficient. If the p value < 0.05, reject the original hypothesis and consider that the correlation between SR and MPD is significant.

Table E.4 *Data Distribution Summary for R1 to R11.*

	Pearson correlation	**p-value**	**Spearman correlation**	**p-value**
R7	-0.605	<0.05	-0.481	<0.05
R1	-0.58	<0.05	-0.413	<0.05
R6	-0.119	<0.05	-0.037	0.217
R8	-0.037	0.343	-0.035	0.368
R3	0.197	<0.05	0.272	<0.05
R10	0.221	<0.05	0.283	<0.05
R2	0.241	<0.05	0.089	0.003
R4	0.373	<0.05	0.527	<0.05
R5	0.502	<0.05	0.416	<0.05
R11	0.521	<0.05	0.56	<0.05
R9	0.706	<0.05	0.651	<0.05
Total	-0.285	<0.05	-0.145	<0.05

2) Conclusion of the relationship between SR with MPD in R1 to R11

Through the analysis of the correlation between SR and MPD, some conclusion of their relationship and significance of each road, as well as the total data, can be clarified. Here, 0.5, which is commonly used in statistics and engineering analysis, is used as the boundary between the strength of the correlation and the strength of the relationship. High Pearson value tends to be linear. High Spearman value and low Pearson value may tend to be nonlinear relationships or indicate the existence of nonlinear monotonous relationships.

(a) Significant positive correlation (R4, R5, R9)

Significant positive correlation of SR and MPD can be observed in R4, R5 and R9. For example, In R4 and R5, the calculated Pearson correlation coefficients are 0.37 and 0.50 respectively, and the Spearman correlation coefficients are 0.53 and 0.42, indicating that there is a medium-strong positive correlation between the two, and with the increase of SR, the MPD also increases accordingly. The p-value is also extremely small, which supports the significance of the result, indicating that this relationship can be generalized to the whole.

(b) Significant negative correlation (R1, R7)

Significant positive correlation of SR and MPD can be observed in R1 and R7. Specifically, in R1, Pearson's correlation coefficient is -0.58 and Spearman's correlation coefficient is -0.41, indicating that there is a moderate-intensity negative correlation between SR and MPD, which means that when SR increases, MPD tends to decrease. Similarly, in R7, the correlation coefficient is -0.61 and -0.48, showing significant negative correlation. The p-value of the two is extremely small, which further confirms the significance and generalizability of the results.

(c) Weak positive correlation (R2, R10)

Significant positive correlation of SR and MPD can be observed in R2 and R10. For example, in R2, Pearson's correlation coefficient is 0.24 and Spearman's correlation coefficient is 0.09. It shows that there is a weak positive correlation between SR and MPD. Although it is statistically significant, the intensity of the relationship is not enough for widespread promotion.

(d) No significant correlation (R6, R8, R11)

In R6, R8 and R11, the correlation coefficient between SR and MPD is close to zero, and the p value has not reached a significant level, indicating that there is not enough evidence to support the relationship between SR and MPD. These results cannot be generalized as a whole, reflecting that there may be other influencing factors on these roads.

3) Conclusion of the relationship between SR with MPD in total data

After analyzing the overall data set, there is a mild negative correlation between SR and MPD. Specifically, Pearson's correlation coefficient is -0.28 and Spearman's correlation coefficient is -0.15, which shows that when SR increases, MPD tends to show a decreasing trend. However, this correlation is relatively weak, suggesting that the relationship between the two is not strong. It is worth noting that the calculated p value is extremely small (close to 0), indicating that the observed negative correlation is statistically significant, which means that this relationship is not accidental. Although there is a negative correlation between SR and MPD, due to the low correlation, it may mean that there are other influencing factors in the actual situation. Therefore, when conducting further research and decision-making on traffic engineering, it is necessary to consider more potential influencing factors to fully understand the relationship between road surface conditions and slopes.

4) Results of SR regression with MPD using linear regression methods

The relationship between SR and MPD was analyzed first using linear regression model. Through regression analysis of multiple worksheets (R1 to R11) of SCRIM test data, the results containing multiple evaluation indicators to evaluate the fitting effect and predictive ability of the model are generated, as shown in Figure E.16 and Table E.5

In the data preprocessing stage, first perform logarithmic transformation or Box-Cox transformation of SR to ensure the normality and linear relationship of the data. Subsequently, standardized technology is used to normalize MPD and SR to eliminate the impact of different frameworks. By using the OLS (ordinary least squares method) fitting model, the regression results, including mean square error (MSE), root mean square error (RMSE), F statistics and Coverage Probability are calculated.

To better demonstrate the predictive ability of the model, the scatter plot of each worksheet is drawn, and regression lines and confidence intervals are added to the diagram. The blue dot is used to represent the actual observation value, the red line represents the fitted regression line, and the yellow points represent the outliers of 95% forecast interval. In this way, the relationship between actual data and model predictions can be intuitively observed, and abnormal points outside the confidence interval can be identified.

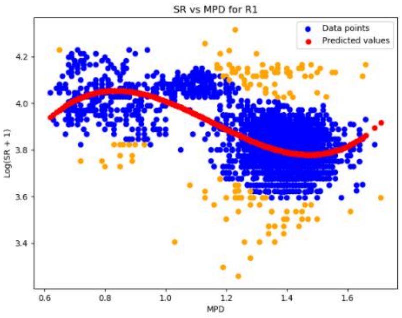

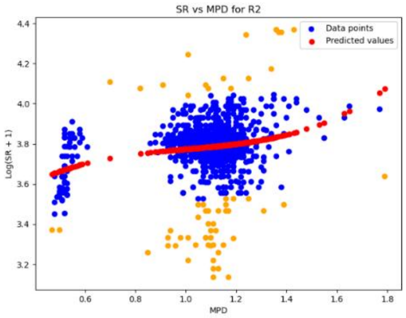

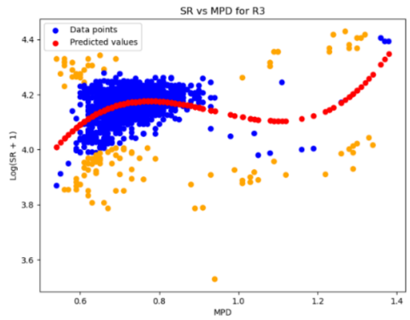
SR vs MPD for R3
Data points
Predicted values
Log(SR + 1)
MPD
3.6
3.8
4.0
4.2
4.4
0.6
0.8
1.0
1.2
1.4

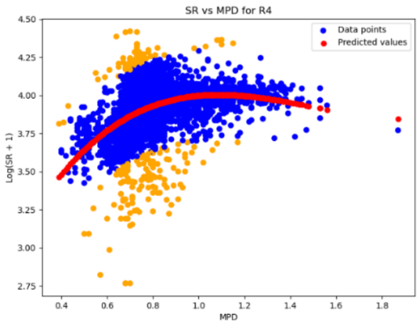
SR vs MPD for R4
Data points
Predicted values
Log(SR + 1)
MPD
2.75
3.00
3.25
3.50
3.75
4.00
4.25
4.50
0.4
0.6
0.8
1.0
1.2
1.4
1.6
1.8

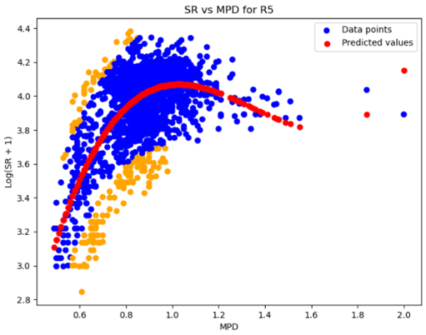
SR vs MPD for R5
Data points
Predicted values
Log(SR + 1)
MPD
2.8
3.0
3.2
3.4
3.6
3.8
4.0
4.2
4.4
0.6
0.8
1.0
1.2
1.4
1.6
1.8
2.0

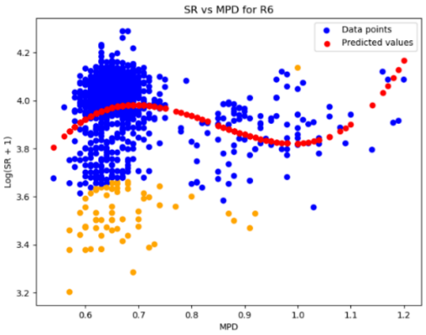
SR vs MPD for R6
Data points
Predicted values
Log(SR + 1)
MPD
3.2
3.4
3.6
3.8
4.0
4.2
0.6
0.7
0.8
0.9
1.0
1.1
1.2

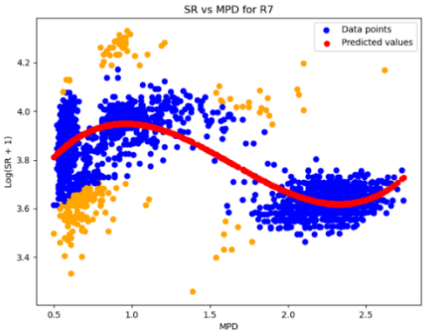
SR vs MPD for R7
Data points
Predicted values
Log(SR + 1)
MPD
3.4
3.6
3.8
4.0
4.2
0.5
1.0
1.5
2.0
2.5

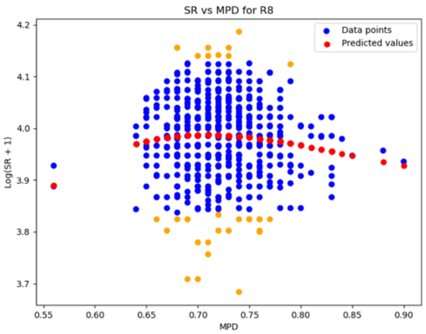
SR vs MPD for R8
Data points
Predicted values
Log(SR + 1)
MPD
3.7
3.8
3.9
4.0
4.1
4.2
0.55
0.60
0.65
0.70
0.75
0.80
0.85
0.90

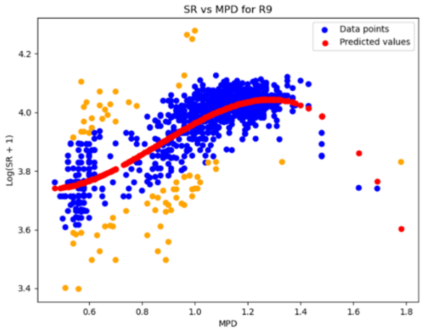
SR vs MPD for R9
Data points
Predicted values
Log(SR + 1)
MPD
3.4
3.6
3.8
4.0
4.2
0.6
0.8
1.0
1.2
1.4
1.6
1.8

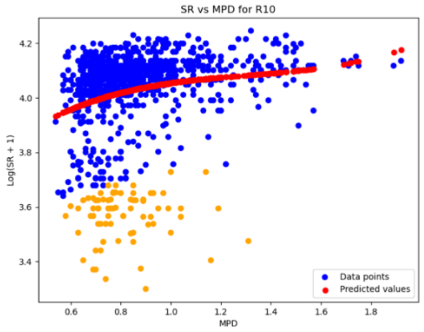
SR vs MPD for R10
Data points
Predicted values
Log(SR + 1)
MPD
3.4
3.6
3.8
4.0
4.2
0.6
0.8
1.0
1.2
1.4
1.6
1.8

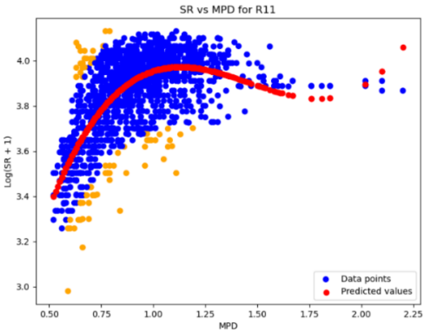

Figure E.16 *Histogram of SR and MPD in Total Data.*

Table E.5 *Regression Summary for R1 to R11 With Linear Regression Methods.*

Sheet	MSE	RMSE	F score	Coverage Probability
R1	0.012012	0.109601	518.4217	0.951845
R2	0.016934	0.130131	22.75948	0.94573
R3	0.005091	0.07135	67.75037	0.937674
R4	0.022908	0.151354	344.8277	0.947996
R5	0.030947	0.175917	662.1933	0.931513
R6	0.025062	0.158311	21.32365	0.939891
R7	0.013386	0.115697	952.8722	0.917493
R8	0.005792	0.076106	2.619124	0.950076
R9	0.00636	0.079748	470.783	0.929564
R10	0.027224	0.164997	14.61584	0.922587
R11	0.017872	0.133686	458.7236	0.94212

Due to the limitations of linear models, which tend to exhibit poor convergence effects but are relatively simple to adjust, a 95% confidence interval was established based on regression predictions. The probability of data points falling within this interval was calculated. If the coverage probability exceeds 90%, it indicates that most points fall within the predicted range at the 95% confidence level. The indicators in the table demonstrate that the model exhibits good convergence and fitting performance across multiple worksheets.

From the results in the table, it is evident that all coverage probabilities exceed 90%, indicating that the model performs well in terms of convergence and achieves relatively accurate regression results within an adjustable range. In particular, the relatively low values of MSE and RMSE highlight the model's predictive capability. Meanwhile, future research should focus on additional influencing factors, consider the boundary effects of outliers, and analyze the cumulative impact to obtain a more accurate regression model.

Appendix F. Pavement Markings Lab Test Results and Photos

Table F.1 *MPD Measurements by LST before Polishing.*

Group No.	MPD (mm)		
	Specimen 1	Specimen 2	Avg.
No.11 (Bao et al., 2024)	0.46	0.39	0.42
No.12 (Bao et al., 2024)	0.87	0.63	0.75
No.25	1.35	1.43	1.39
No.26	0.44	0.60	0.52
No.27	0.58	0.56	0.57
No.28	0.60	0.53	0.57
No.29	0.88	1.27	1.07

Table F.2 *Dry BPN Measurements Before Polishing.*

Group No.	BPN			
	Specimen 1	Specimen 2	S.D	Avg.
No.11 (Bao et al., 2024)	78.0	68.0	7.07	73.00
No.12 (Bao et al., 2024)	83.0	80.0	1.84	81.30
No.25	100.0	100.0	0.00	100.00
No.26	92.0	96.0	2.00	94.00
No.27	90.0	90.0	0.00	90.00
No.28	84.0	85.0	0.50	84.50
No.29	90.0	100.0	5.00	95.00

Table F.3 *Wet BPN Measurements Before Polishing.*

Group No.	BPN			
	Specimen 1	Specimen 2	S.D.	Avg.
No.11 (Bao et al., 2024)	37	34	1.98	35.5
No.12 (Bao et al., 2024)	32	36	3.11	33.8
No.25	85.0	79.0	3.00	82.00
No.26	76.0	85.0	4.50	80.50
No.27	60.0	65.0	2.50	62.50
No.28	56.0	60.0	2.00	58.00
No.29	55.0	67.0	6.00	61.00

Table F.4 *MPD Measurements by CTM Before and After Polishing.*

Group No.	**Polishing Cycles**	**MPD (mm)**		
		Specimen 1	**Specimen 2**	**Avg.**
No.11 (Bao et al., 2024)	0	0.59	0.42	0.50
	500	0.51	0.43	0.47
	2000	0.48	0.47	0.47
	5000	0.50	0.43	0.46
	10000	0.48	0.41	0.45
	15000	0.51	0.43	0.47
	25000	0.48	0.42	0.45
	40000	0.46	0.42	0.44
	60000	0.48	0.45	0.46
No.12 (Bao et al., 2024)	0	0.72	0.64	0.68
	500	0.59	0.63	0.61
	1500	0.57	0.60	0.58
	5000	0.55	0.62	0.58
	10000	0.59	0.56	0.57
	20000	0.57	0.60	0.58
No.25	0	1.55	1.43	1.49
	500	1.17	1.14	1.15
	5000	1.22	1.18	1.20
	25000	1.18	1.07	1.12
	55000	-	1.11	1.11
No.26	0	0.65	0.48	0.56
	500	0.51	0.42	0.47
	5000	0.53	0.47	0.50
	55000	0.51	0.43	0.47
No.27	0	0.93		0.93
	1500	0.61		0.61
	5000	0.53		0.53
	25000	0.52		0.52
	55000	0.46		0.46
No.28	0	0.68		0.68
	1500	0.49		0.49
	5000	0.54		0.54
	25000	0.60		0.60
	55000	0.55		0.55
No.29	0	1.31	1.05	1.18
	1500	1.11	0.96	1.03
	5000	1.02	0.93	0.97
	25000	0.91	0.88	0.89
	55000	0.85	0.83	0.83

Table F.5 DF20 Measurements Before and After Polishing.

Group No.	Polishing Cycles	DF 20		
		Specimen 1	Specimen 2	Avg.
No.11 (Bao et al., 2024)	0	0.38	0.35	0.36
	500	0.34	0.31	0.33
	2000	0.33	0.30	0.31
	5000	0.33	0.29	0.31
	10000	0.26	0.22	0.24
	15000	0.22	0.24	0.23
	25000	0.28	0.22	0.25
	40000	0.25	0.19	0.22
	60000	0.29	0.24	0.26
No.12 (Bao et al., 2024)	0	0.18	0.23	0.21
	500	0.18	0.25	0.21
	1500	0.10	0.21	0.15
	5000	0.11	0.19	0.16
	10000	0.14	0.19	0.16
	20000	0.07	0.07	0.07
No.25	0	0.56	0.58	0.57
	500	0.47	0.44	0.45
	5000	0.47	0.44	0.46
	25000	0.44	0.36	0.40
	55000	0.42	0.41	0.42
No.26	0	0.74	0.37	0.55
	500	0.64	0.45	0.55
	5000	0.57	0.35	0.46
	55000	0.44	0.35	0.39
No.27	0	0.63		0.63
	1500	0.44		0.44
	5000	0.44		0.44
	25000	0.43		0.43
	55000	0.43		0.43
No.28	0	0.56		0.56
	1500	0.45		0.45
	5000	0.44		0.44
	25000	0.43		0.43
	55000	0.41		0.41
No.29	0	0.49	0.60	0.54
	1500	0.44	0.51	0.48
	5000	0.47	0.41	0.44
	25000	0.45	0.43	0.44
	55000	0.47	0.45	0.46

Table F.6 *DF40 Measurements Before and After Polishing.*

Group No.	**Polishing Cycles**	**DF 40**		
		Specimen 1	**Specimen 2**	**Avg.**
No.11 (Bao et al., 2024)	0	0.39	0.36	0.37
	500	0.35	0.32	0.33
	2000	0.33	0.30	0.32
	5000	0.33	0.30	0.32
	10000	0.30	0.28	0.29
	15000	0.29	0.28	0.28
	25000	0.29	0.26	0.27
	40000	0.30	0.26	0.28
	60000	0.29	0.22	0.25
No.12 (Bao et al., 2024)	0	0.23	0.27	0.25
	500	0.22	0.26	0.24
	1500	0.20	0.24	0.22
	5000	0.21	0.23	0.22
	10000	0.22	0.22	0.22
	20000	0.18	0.16	0.17
No.25	0	0.63	0.65	0.64
	500	0.55	0.53	0.54
	5000	0.54	0.51	0.52
	25000	0.53	0.42	0.47
	55000	0.53	0.50	0.50
No.26	0	0.77		0.77
	500	0.68		0.68
	5000	0.59		0.59
	55000	0.46		0.46
No.27	0	0.68		0.68
	1500	0.54		0.54
	5000	0.50		0.50
	25000	0.45		0.45
	55000	0.45		0.45
No.28	0	0.58		0.58
	1500	0.49		0.49
	5000	0.46		0.46
	25000	0.45		0.45
	55000	0.41		0.41
No.29	0	0.63	0.49	0.56
	1500	0.45	0.45	0.45
	5000	0.44	0.44	0.44
	25000	0.44	0.42	0.43
	55000	0.47	0.43	0.43

***Table F.**7 F60 Measurements Before and After Polishing.*

Group No.	Polishing Cycles	F60		
		Specimen 1	Specimen 2	Avg.
No.11 (Bao et al., 2024)	0	0.39	0.36	0.37
	500	0.22		0.22
	2000	0.20		0.20
	5000	0.20		0.20
	10000	0.19		0.19
	15000	0.18		0.18
	25000	0.18		0.18
	40000	0.18		0.18
	60000	0.18		0.18
No.12 (Bao et al., 2024)	0	0.19		0.19
	500	0.18		0.18
	1500	0.17		0.17
	5000	0.17		0.17
	10000	0.17		0.17
	20000	0.15		0.15
No.25	0	0.43	0.44	0.44
	500	0.37	0.35	0.36
	5000	0.37	0.35	0.36
	25000	0.36	0.30	0.33
	55000		0.34	0.34
No.26	0	0.40		0.40
	500	0.34		0.34
	5000	0.31		0.31
	55000	0.25		0.25
No.27	0	0.41		0.41
	1500	0.30		0.30
	5000	0.27		0.27
	25000	0.25		0.25
	55000	0.24		0.24
No.28	0	0.33		0.33
	1500	0.26		0.26
	5000	0.26		0.26
	25000	0.27		0.27
	55000	0.24		0.24
No.29	0	0.42	0.33	0.37
	1500	0.31	0.30	0.31
	5000	0.30	0.29	0.30
	25000	0.29	0.28	0.29
	55000	0.30	0.28	0.28

References

Bao, J., Hu, X., Peng, C., Duan, J., Lin, Y., Tao, C., Jiang, Y., & Li, S. (2024). *Advancing INDOT's friction test program for seamless coverage of system: Pavement markings, typical aggregates, color surface treatment, and horizontal curves* (Joint Transportation Research Program Publication No. FHWA/IN/JTRP-2024/09). Purdue University. https://doi.org/10.5703/1288284317734

About the Joint Transportation Research Program (JTRP)

On March 11, 1937, the Indiana Legislature passed an act which authorized the Indiana State Highway Commission to cooperate with and assist Purdue University in developing the best methods of improving and maintaining the highways of the state and the respective counties thereof. That collaborative effort was called the Joint Highway Research Project (JHRP). In 1997 the collaborative venture was renamed as the Joint Transportation Research Program (JTRP) to reflect the state and national efforts to integrate the management and operation of various transportation modes.

The first studies of JHRP were concerned with Test Road No. 1—evaluation of the weathering characteristics of stabilized materials. After World War II, the JHRP program grew substantially and was regularly producing technical reports. Over 1,600 technical reports are now available, published as part of the JHRP and subsequently JTRP collaborative venture between Purdue University and what is now the Indiana Department of Transportation.

Free online access to all reports is provided through a unique collaboration between JTRP and Purdue Libraries. These are available at docs.lib.purdue.edu/jtrp/.

Further information about JTRP and its current research program is available at engineering.purdue.edu/JTRP.

About This Report

An open access version of this publication is available online. See the URL in the citation below.

Tao, C., Lin, Y., Duan, J., Peng, C., Bao, J., Jiang, Y., & Li, S. (2025). *Implementing an advanced friction testing program for seamless coverage of INDOT system* (Joint Transportation Research Program Publication No. FHWA/IN/JTRP-2025/22). West Lafayette, IN: Purdue University. https://doi.org/10.5703/1288284317908